Long-Range Interactions, weak magnetic fields amplification, and End states for Quantum Computing

INAUGURALDISSERTATION

zur

Erlangung der Würde eines Doktors der Philosophie

vorgelegt der

Philosophisch-Naturwissenschaftlichen Fakultät

der Universität Basel

von

Luka Trifunovic

aus Belgrad, Serbien

Basel, 2015

Originaldokument gespeichert auf dem Dokumentenserver der Universität Basel
edoc.unibas.ch

Dieses Werk ist unter dem Vertrag „Creative Commons Namensnennung-Keine kommerzielle Nutzung-Keine Bearbeitung 2.5 Schweiz“ lizenziert. Die vollständige Lizenz kann unter
creativecommons.org/licences/by-nc-nd/2.5/ch
eingesehen werden.

creative commons

Namensnennung-Keine kommerzielle Nutzung-Keine Bearbeitung 2.5 Schweiz

---

Sie dürfen:

das Werk vervielfältigen, verbreiten und öffentlich zugänglich machen

Zu den folgenden Bedingungen:

Namensnennung. Sie müssen den Namen des Autors/Rechteinhabers in der von ihm festgelegten Weise nennen (wodurch aber nicht der Eindruck entstehen darf, Sie oder die Nutzung des Werkes durch Sie würden entlohnt).

Keine kommerzielle Nutzung. Dieses Werk darf nicht für kommerzielle Zwecke verwendet werden.

Keine Bearbeitung. Dieses Werk darf nicht bearbeitet oder in anderer Weise verändert werden.

- Im Falle einer Verbreitung müssen Sie anderen die Lizenzbedingungen, unter welche dieses Werk fällt, mitteilen. Am Einfachsten ist es, einen Link auf diese Seite einzubinden.
- Jede der vorgenannten Bedingungen kann aufgehoben werden, sofern Sie die Einwilligung des Rechteinhabers dazu erhalten.
- Diese Lizenz lässt die Urheberpersönlichkeitsrechte unberührt.

Die gesetzlichen Schranken des Urheberrechts bleiben hiervon unberührt.

Die Commons Deed ist eine Zusammenfassung des Lizenzvertrags in allgemeinverständlicher Sprache: http://creativecommons.org/licenses/by-nc-nd/2.5/ch/legalcode.de

Haftungsausschluss:
Die Commons Deed ist kein Lizenzvertrag. Sie ist lediglich ein Referenztext, der den zugrundeliegenden Lizenzvertrag übersichtlich und in allgemeinverständlicher Sprache wiedergibt. Die Deed selbst entfaltet keine juristische Wirkung und erscheint im eigentlichen Lizenzvertrag nicht. Creative Commons ist keine Rechtsanwaltsgesellschaft und leistet keine Rechtsberatung. Die Weitergabe und Verlinkung des Commons Deeds führt zu keinem Mandatsverhältnis.

Quelle: http://creativecommons.org/licenses/by-nc-nd/2.5/ch/ Datum: 3.4.2009

Genehmigt von der Philosophisch-Naturwissenschaftlichen Fakultät auf Antrag von

Prof. Dr. Daniel Loss

Prof. Dr. Guido Burkard

Basel, den 14. Oktober 2014

Prof. Dr. Jörg Schibler
Dekan

Acknowledgments

See print version.

Summary

It was Richard Feynman who first proposed, in 1982, the far-reaching concept of a "quantum computer"—a device more powerful than classical computers. The idea of a quantum computer is to employ the fascinating and often counterintuitive laws of quantum mechanics to process information. It is far from obvious that the proposed concept of a quantum computer is more powerful than its classical counterpart, it was only in 1994 when Peter Shor theoretically demonstrated the existence of a quantum algorithm for factorizing integers into prime factors that runs in polynomial time unlike its classical counterpart which works in sub-exponential time. The factorization of integers into prime factors is the basis of asymmetric cryptography. These early theoretical results lunched an immense interest of the scientific community. Already during '90s, the first proposals for the physical implementation of quantum computation emerged. Ever since, many experimental groups around the world pursued different physical implementations of quantum bits (qubits). The first decade of the new century saw a steady improvement in the control and decoherence time (the time over which the information carried by the qubit is lost) for various qubits by many orders of magnitude. The natural next step in this context is to answer the question of how to scale the system up to include many qubits and thus build a quantum computer? One of the main parts of this thesis addresses exactly this question, namely the question of architecture and scalability of future quantum computer.

Among various different physical realizations of qubits, the idea of using electron spins trapped in electrostatic semiconductor quantum dots as the building blocks of a quantum computer (the so-called spin qubits), put forward by Daniel Loss and David DiVincenzo in 1997, triggered tremendous interest in scientific community. Nevertheless, the implementation of the original Loss-DiVincenzo proposal posed a considerable technical challenge. It used quantum tunneling between qubits to enable their communication with each other, and thus required that the qubits to

be placed very close to each other. This requirement not only leaves little space for the placement of the vast amount of gates and wirings needed to define the electrostatic quantum dots, but also makes it challenging to control the local magnetic field needed for single-qubit operations. For these reasons, no system with more than a couple of spin qubits has been successfully implemented thus far. In the first part of this thesis, we leap over this long-standing problem with an entirely different strategy of using metallic floating gates or ferromagnets to couple together qubits that are separated over a long distance. Our scheme works for any type of spin qubits, including the qubits based on nitrogen-vacancy center (NV-center) in diamond and technologically very important silicon qubits.

The main topic of this thesis is related to quantum computer. Still, quite unexpectedly, some of the ideas we employed in order to tackle the problem of quantum computer scalability can be utilized in a completely different field of research, namely, in the field of magnetic field sensing. Qubit are not only a necessary ingredient of quantum computer but they also provide a way to measure very accurately magnetic fields. The magnetometer build upon the qubit based on NV-center, so-called NV-magnetometer, emerged in recent years as most sensitive magnetic moment sensor. These magnetometers are able to detect about hundred nuclear spins within a minute of acquisition time. In the second part of this thesis, we propose an entirely novel experimental realization of NV-magnetometers which increases present NV-center sensitivities by four orders of magnitude at room temperature. This unprecedented amplification of sensitivity will render magnetometers capable of detecting individual nuclear spins. This amplification is achieved by introducing a ferromagnetic particle between the nuclear spin that needs to be detected and the NV-magnetometer. Our setup, in contrast to existing schemes, is particularly advantageous because, due to the large amplification of sensitivity, the nuclear spin need not lie within a few nanometers of the surface but rather can be detectable at a distance of 30 nm. With these novelties, our scheme provides chemically sensitive spin detection under ambient conditions allowing nanoscale resolution of nuclear magnetic moments in biological systems—the holy grail of nuclear magnetic resonance.

In the last part of the thesis we focus our attention to a new direction in quantum computer implementation that deals with topological quantum computer introduced by Alexei Kitaev in 1997; in this approach the idea is to use quasiparticles with "fractional" statistics and to perform the single- and two-qubit gates by merely exchanging these quasiparticles. Additionally, information in this system is stored non-locally thus

it mitigates the problem of decoherence caused by local noise from the environment. Majorana fermions are one of the most well known examples of such excitations. We analyze transport signatures of different topological states in one-dimensional systems, like Majorana fermions and fractionally charged states. We envision an Aharonov-Bohm setup wherein conductance measurement provides a clear signature of presence of fractionally charged fermionic states, since oscillations with double period emerge in this case. Additionally, we propose a very simple setup that enables existence of degenerate mid-gap states, so-called Tamm-Shockley states that are characterized by fractional charge and discuss possible ways of detecting these states experimentally.

Contents

Contents **vii**

1 Introduction **1**
1.1 The "Loss-DiVincenzo" proposal 1
1.2 Qubits based on nitrogen-vacancy centers 5
1.3 Topological quantum computation by anyons 9

I Long-Range Indirect Interaction of Spins Qubits

2 Introduction **14**

3 Long-Distance Spin-Spin Coupling via Floating Gates **17**
3.1 Electrostatics of the floating gate 18
3.2 Qubit-qubit coupling 20
3.3 Scalable Architecture 25
3.4 Implementation of two-qubit gates 31
3.5 Numeric Modeling of Realistic Devices 32
3.6 Conclusions 35
3.7 Acknolwedgment 36
3.A SPIN-SPIN COUPLING - singly occupied double-dots . . . 36
3.B SPIN-SPIN COUPLING - the hybrid system 39
3.C Implementation of two-qubit gates 41

4 Long-Distance Entanglement of Spin-Qubits via Ferromagnet **44**
4.1 Model 44
4.2 Decoherence 50
4.3 Estimates 55
4.4 Conclusions 56
4.5 Acknowledgements 56
4.A Holstein-Primakoff transformation 56

4.B Transverse correlators $\langle S^+_{\boldsymbol{q}}(t)S^-_{-\boldsymbol{q}}(0)\rangle$ 57
4.C Longitudinal correlators $\langle S^z_{\boldsymbol{q}}(t)S^z_{-\boldsymbol{q}}(0)\rangle$ 61
4.D Exchange coupling to the ferromagnet 64
4.E Fourth order contributions to decoherence 68

5 Long-Range Interaction of Spin-Qubits via Ferromagnets 72
5.1 Ferromagnet 73
5.2 Coupling between ST-qubits 73
5.3 Coupling between spin-$1/2$ qubits 79
5.4 Coupling between spin-$1/2$ and ST-qubits 85
5.5 Validity of the effective Hamiltonian 87
5.6 Switching mechanisms 88
5.7 Coupling strengths and operation times 88
5.8 Conclusions 90
5.9 Acknowledgment 91
5.A Rotated Hamiltonian for CNOT gate 91

II Weak magnetic field amplification for room-temperature magnetometry

6 Introduction 94

7 High-efficiency resonant amplification of weak magnetic fields for single spin magnetometry 96
7.1 Setup 97
7.2 Proposed magnetometer sensitivity 100
7.3 Conclusions 107
7.4 Acknowledgments 108
7.5 Methods 108
7.A Cramer-Rao Bound 111
7.B Sensitivity of an NV-center 112
7.C AC sensitivity for $\theta = 0$ 114
7.D Calculation of $\varphi_{NV}(t_i)$ and $\beta(t_i, \tau)$ 115
7.E Stray field from a uniformly magnetized cuboid 119

III End states in one-dimensional systems

8 Introduction 124

9 Localized end states in density modulated quantum wires and rings 128
9.1 Lattice model 129
9.2 Disorder effects 130
9.3 Continuum model 132

9.4 Interaction effects 133
9.5 Detection 135
9.6 Effective quantum dot 138
9.7 Conclusions 139
9.8 Acknowledgements 139

10 Realistic transport modeling for a superconducting nanowire with Majorana fermions 140
10.1 Model 141
10.2 Discussion 144
10.3 Conclusions 152
10.4 Acknowledgments 152

11 Transport signatures of fractional Fermions in Rashba nanowires 153
11.1 Model 154
11.2 Method 155
11.3 Results 157
11.4 Experimental feasibility 160
11.5 Conclusions 161
11.6 Acknowledgements 162

Bibliography 163

CHAPTER 1

Introduction

In this section we introduce several concepts that are used as a starting point for the work presented in this thesis. Since the main part of the thesis deals with physical implementations of quantum computer and quantum bits (qubits) we start by reviewing Loss-DiVincenzo proposal and DiVincenzo criteria, see Sec. 1.1. We then describe another implementation of qubits using defects in diamond. Even tough the term qubit is mainly used in context of quantum computing, it can also be a powerful tool to for magnetic field sensing as described in Sec. 1.2. Finally in Sec. 1.3, we turn our attention to a new paradigm of quantum computation by introducing the basic concepts needed to understand advantages of *topological* quantum computation.

1.1 The "Loss-DiVincenzo" proposal

The first proposals for the physical implementation of quantum computation appeared in the '90s. Among those, the idea of using electron spins trapped in lateral electrostatic semiconductor quantum dots as the building blocks of a quantum computer, put forward by Daniel Loss and David DiVincenzo in 1997 [1], emerged as the most propitious one [2, 3, 4]. In order to define a lateral quantum dot, one starts with two-dimensional electron gas (2DEG) that is confined between two semiconductor sheets such as GaAs and InAs. Once the 2DEG is defined, one places gates on top of the two-sheet structure (see Fig. 1.1) and applies voltage in order to define an electrostatic well that will trap a single elec-

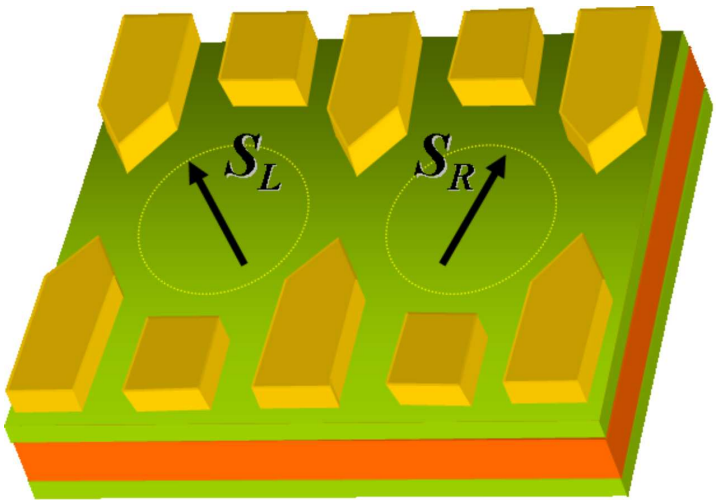

Figure 1.1: Scheme of the Loss-DiVincenzo proposal. The yellow gates on the top that give rise to an electrostatic potential that defines wells (quantum dots) as well as control the tunneling between the wells. The black arrows denote electron's spin degree of freedom.

tron. Since a single electron is spatially separated from the rest of the 2DEG, its spin can be used to define a two-level system, i.e., a qubit.

In order for a qubit to be used as a building block of a quantum computer, it has to satisfy the stringent requirements know as DiVincenzo criteria [5], that can be summarized as follows:

- Reliable initialization in a predefined state of the qubit
- Coherent quantum control of a single qubit (single-qubit gates) and controlled entangling interaction between the pairs of adjacent qubits (two-qubit gates)
- The coherent superposition of the two states of the qubit has to be longer lived than the single- and two-qubit operation times
- Possibility to readout the qubit state within the time shorter than the qubit relaxation time
- Scalability, i.e., the possibility to scale up the number of qubits

Figure 1.1 illustrates the Loss-DiVincenzo proposal. Each qubit is encoded in the spin (arrow) of an electron that is trapped in a lateral quan-

tum dot. Formally, the two basis states of the qubit are defined as

$$|0\rangle = |\uparrow\rangle \qquad \text{and} \qquad |1\rangle = |\downarrow\rangle\,, \tag{1.1}$$

with $|\uparrow\rangle$ and $|\downarrow\rangle$ being the two states of the electron spin with opposite spin projection along the certain axis defined by an externally applied magnetic field. A general qubit state is then an arbitrary superposition of the basis states

$$|\psi\rangle = \alpha|0\rangle + \beta|1\rangle\,, \tag{1.2}$$

with $|\alpha|^2 + |\beta|^2 = 1$.

We now clarify why Loss-DiVincenzo proposal satisfies most of DiVincenzo criteria. The qubit initialization can be achieved by externally applying magnetic field B_z along z-axis (the choice of axis is arbitrary), which causes the $|\uparrow\rangle$ and $|\downarrow\rangle$ states of the qubit to split up with energy difference $E_Z = \hbar\mu_B g B_z$, with Landé factor $g = -0.44$ for GaAs and μ_B being the Bohr magneton. Assuming that the applied magnetic field is big enough $|E_Z| \gg k_B T$ (k_B is Boltzmann constant), the initialization is achieved by waiting for electron spins to reach their thermodynamic equilibrium.[1]

Next, the single-qubit gates can be performed by applying AC magnetic field in xy-plane. When the frequency of the applied AC magnetic field matches the qubit Zeeman splitting, it will cause the transitions that are periodic in time between the two qubit states—so-called Rabi oscillations. By varying the duration of applied AC magnetic field any single-qubit gate can be achieved. This scheme is know as electron spin resonance (ESR). It is worth noting at this point that one needs in principle to apply AC magnetic field locally on the qubit which is experimentally very challenging task. An alternative approach is to use spatially varying g-factor—the qubit we want to address is pulled into a layer with higher g-factor thus only this qubit satisfies the resonant condition with the applied AC field. Additionally, making use of spin-orbit interaction allows an all-electrical implementation of single-qubit gates. Furthermore, the two-qubit gates can be performed by using the exchange coupling between the neighbouring spins, where the strength of this interaction can be tuned electrically by adjusting the gate voltage that controls the barrier height between two neighbouring potential wells. The time-dependent interaction Hamiltonian is of Heisenberg type

[1] In this scheme, the initialization time is given by the qubit relaxation time and therefore it is slow. We note that there exist fast initialization schemes.

$$H_{12} = J(t)\boldsymbol{S}_1 \cdot \boldsymbol{S}_2 \,, \tag{1.3}$$

and it was demonstrated [1] that this type of interaction is enough to produce entanglement between the interacting qubits.

Finally, it is possible to readout spin state of the qubit by converting spin state into charge state and using quantum point contact to detect charge [6].

The scalability of Loss-DiVincenzo proposal is experimentally very challenging, since—with present day technology—there is hardly enough space to place the large amount of metallic gates and wires needed to define and to address the spin qubits. A promising strategy to meet this challenge is to implement long-range interactions between the qubits which allows the quantum dots to be moved apart and to create space for the wirings.

In this thesis we extend Loss-DiVincenzo proposal such that the scalability requirement is satisfied. We achieve this by proposing a long-range electrostatic interaction between the qubits mediated via a dog-bone shaped floating metallic gate. In order for the scheme to work, the spin degree of freedom has to be coupled to charge which is achieved through the spin orbit interaction (SOI). Furthermore, we argue that inclusion of a floating gate does not induce detrimental source of decoherence since the system already contains the gates that define the quantum dots. We construct explicitly a controlled-NOT (CNOT) two-qubit gate and obtain the operation time of a few tens of nanoseconds for GaAs quantum dots—significantly below the typical coherence time of the quantum dot defined qubit. Thus the extended Loss-DiVincenzo proposal satisfies all DiVincenzo criteria. The details of our proposal can be found in Chapter 3.

Certain semiconductors have very weak or practically no SOI (for e.g. silicon, a technologically very important material). In such materials the previously described electrostatic coupler would yield too small coupling. In order to provide a scheme that would mediate a long-range interaction also in this kind of material, we propose a setup that consist of a dog-bone shaped ferromagnet (FM). Herein, no SOI is needed since the qubit spin degree of freedom is directly coupled to the FM spins via dipolar interaction. This scheme applied to semiconductor lateral quantum dots is described in Chapter 5.

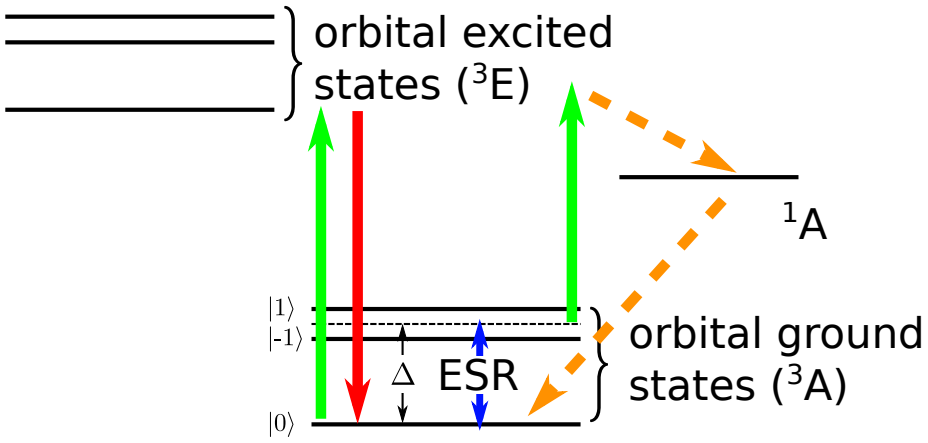

Figure 1.2: Schematic energy level diagram of a single nitrogen vacancy (NV) center in diamond. The levels shown here lie within the band gap of the diamond. The red arrow denotes the fluorescence that NV-center emits when off-resonantly excited with green laser (green arrows). Once the states $|\pm 1\rangle$ of the NV-center orbital ground state are off-resonantly excited, they decay nonradiately through ^{1}A singlet state to $|0\rangle$ (orange arrows). This enable NV-center to be optically initialized and also readout of the spin state. One can drive the transitions between $|0\rangle$ and $|\pm 1\rangle$ with help of electron spin resonance ESR (blue arrow). The NV-center zero-field splitting in the orbital ground state is denoted by $\Delta \sim 2.87$ GHz.

1.2 Qubits based on nitrogen-vacancy centers

The nitrogen-vacancy (NV) center is one of many possible point defects in diamond. A diamond is an insulator (depending on the diamond type, it can be also a semiconductor) with a band gap of 5.5 eV. One typically uses a pure diamond (i.e. type II) that has little if any nitrogen impurities. The NV-center consists of substitutional nitrogen impurity with a vacancy at its nearest neighbour lattice site. There are two types for NV-center defects that have different charge, a neutral one denoted by NV^0 and a negatively charged one denoted by NV^-. In this thesis we will only consider NV^- centers and for simplicity we denote them by NV throughout the thesis.

The energy level diagram of a negatively charged NV-center is illustrated in Fig. 1.2. The orbital part of the NV-center electronic state has C_{3V} symmetry, thus the states can be labeled by the irreducible representations of C_{3V} symmetry group (A and E). The orbital ground state has ^{3}A

symmetry, which means that the orbital part has A symmetry (i.e. it is invariant under C_{3V} group operations) and there are 3 states with different spin projections. Even in the absence of an externally applied magnetic field, the ground state $|0\rangle$ and the excited states $|\pm 1\rangle$ are split by energy Δ—so-called zero-field splitting, while the states $|\pm 1\rangle$ are degenerate. This crystal field splitting quantized the spin projection along the N-V symmetry axis. Since the energy difference between $|0\rangle$ and $|\pm 1\rangle$ states lies in microwave region, one can drive transition between these states (i.e. Rabi oscillations) with microwave radiation.

There are several optical properties of the NV-centers that make them very attractive for various applications in the field of quantum information processing; here we mention the most important ones. Firstly, the orbital ground states of the NV-center can be off-resonantly excited with a green laser. If the NV-center was initially in $|0\rangle$ state, then due to selection rules, it decays back to $|0\rangle$ state with emission of an photon (photoluminescence). On the other hand, if the initial state of the NV-center is $|\pm 1\rangle$, then the predominant channel for the relaxation is through nonradiant decay via metastable singlet state (^{1}A, see Fig. 1.2) into the $|0\rangle$ state. Thus we see that the NV-center can be initialized into $|0\rangle$ state by simply shining the green laser onto it. Furthermore, by detecting the photons from spin-dependent photoluminescence, we can determine the state of the NV-center, i.e., perform the readout of the NV-center state; if the NV-center was initially in $|0\rangle$ photon is detected, otherwise no photon is detected. This readout scheme is limited by photon detection efficiency and photon shot noise. We stress that quite remarkably both initialization and the readout[2] can be performed at room temperature. We note herein that the described spin-dependent fluorescence readout scheme is spoiled when there is a component of an externally applied magnetic field that is perpendicular to the N-V axis. Namely, such a magnetic field component mixes $|0\rangle$ and $|\pm 1\rangle$ states which in turn affects the above mentioned selection rules. In practice, perpendicular magnetic field up to 10 mT can be tolerated [9].

When an external magnetic field is applied along the N-V symmetry axis, the $|\pm 1\rangle$ states split and one can use $|0\rangle$ and $|-1\rangle$ states to define a qubit. We already mentioned that such a qubit can be readout and initialized optically at room temperature. Additionally, one can also per-

[2] At low temperature it is also possible to perform a resonant single-shot readout [7]. At room temperature a single-shot readout is still possible with help of a nuclear spin in vicinity of the NV-center [8].

form single-qubit gates by using microwave drive (ESR) [10]. Probably one of the most remarkable features of the NV-centers is their long coherence time even at room temperature, $T_2^* \approx 20\,\mu s$ and $T_2 \approx 1.8\,ms$ [11]. We see that the qubit defined by two states of a NV-center satisfies almost all of DiVincenzo criteria. The only ingredient missing in order to use NV-center as a building block of a quantum computer is the possibility to perform two-qubit gates, i.e., possibility of having a controlled interaction between the NV-centers. We note that two-qubit gates on NV-centers have been experimentally demonstrated [12], but unfortunately this scheme is not scalable. In this thesis we tackle this important problem by proposing a way to mediate a controlled long-range coupling between two NV-centers. The proposed coupling is mediated by virtual magnons, a virtual excitations that propagate through a dog-bone shaped ferromagnet that is placed between the two NV-centers that need to be coupled. The details of our scheme are presented in Chapter 4.

Scanning magnetometry with a single NV-center

In this section we explain why qubits are useful not only in the context of quantum computation and quantum information processing, but also provide possibility of very accurate magnetic field sensing by making use of Ramsey type measurements. We focus here on NV-centers, but any long-lived qubit can be used instead.

We start by initializing the NV-center in the state $|0\rangle$. Then, a $\pi/2$ pulse is applied to the NV-center which leaves it in a superposition state $(|0\rangle + |1\rangle)/\sqrt{2}$, then we wait for the NV-center to accumulate the phase during the interrogation time t, this phase is proportional the magnetic field component along the N-V axis B_{NV}. After the interrogation time t has passed, the NV-center is in the state $(|0\rangle + e^{i\varphi_{\mathrm{NV}}}|1\rangle)/\sqrt{2}$, where $\varphi_{\mathrm{NV}} = \gamma B_{\mathrm{NV}} t$. Finally, another $\pi/2$ pulse is applied to the NV-center which transfers the phase difference between the $|0\rangle$ and $|1\rangle$ states into the occupation of these two states, which is given by following probability distribution

$$p(n|\varphi_{\mathrm{NV}}(t)) = \frac{1}{2}\left(1 + n\cos(\varphi_{\mathrm{NV}}(t))e^{-\langle(\delta\varphi_{\mathrm{NV}}(t))^2\rangle}\right). \tag{1.4}$$

Here, $n = \pm 1$ are the two possible outcomes when the state of the NV-center is measured. We also included dephasing in the NV-center via term $\langle(\delta\varphi_{\mathrm{NV}}(t))^2\rangle$ that describes the fluctuations of the accumulated phase

due to NV-center environment, where $\langle \cdots \rangle$ is the expectation value in the Gibbs state. Because the accumulated phase itself depends on B_{NV}, a measurement of the NV-center is a measurement of B_{NV}. The variance in the measured value of the NV-center can be reduced by repeating the measurement.

Typically NV-center dephasing can be described by $\langle (\delta\varphi_{\mathrm{NV}}(t))^2 \rangle = (t/T_2)^2$, where T_2 is the NV-center dephasing time mentioned earlier.[3] From Eq. 1.4 we see immediately that the interrogation time should not exceed the dephasing time of the NV-center, and the bigger the interrogation time the bigger the phase accumulated thus more precise the measurement of the magnetic field. From this reasoning it is clear why NV-centers are good magnetometers—they are unique qubits with such a long dephasing time at room temperature. Additional advantage of NV-magnetometers stems from the fact that they are point defects which allows for very small sample-to-probe separation (see Fig. 1.3) unlike for e.g. superconducting quantum interference device (SQUID) magnetometers.

The best NV-magnetometers allow for sensitivities[4] up to a few $\mathrm{nT}/\mathrm{Hz}^{\frac{1}{2}}$ at room temperature [13, 14, 15, 16, 17, 18] and sub-nanometer spatial resolution, permitting three-dimensional imaging of nanostructures [14]. Although impressive, current state-of-the-art technology [19] is unable to detect a single nuclear spin; achieving such sensitivity would revolutionize magnetic imaging in chemical and biological systems by facilitating atomic resolution of molecules.

In this thesis, we propose an entirely novel experimental realization of NV-magnetometers which increases present NV-center sensitivities by four orders of magnitude at room temperature. This unprecedented amplification of sensitivity will enable magnetometers capable of detecting individual nuclear spins. This amplification is achieved by introducing a ferromagnetic particle between the nuclear spin that needs to be detected, and the NV-magnetometer. When excited on resonance by the driven nuclear spin, the macroscopic ferromagnetic spin begins to precess which, in turn, amplifies the magnetic field felt by the NV-center. By resonantly addressing the nuclear spin and using a ferromagnetic resonator as a lever, our setup, in contrast to existing schemes, is particularly advantageous because, due to the large amplification of sensitiv-

[3] For DC magnetometry the relevant time is T_2^* rather than T_2.

[4] Sensitivity S of a magnetometer is a quantity that gives the smallest magnetic field $S/\sqrt{t_a}$ that can be sensed for a given acquisition time t_a.

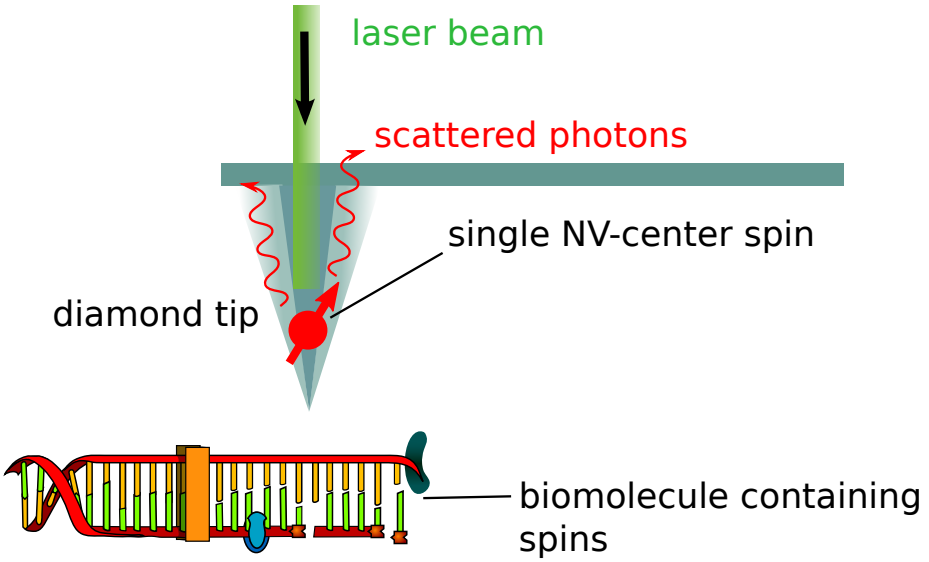

Figure 1.3: Schematic of scanning NV-magnetometry. The NV-center is placed on an atomic force microscopy probe that is used to scan over the sample in order to get spatial image of the magnetic field from the sample. The green laser is used for off-resonant excitation of the NV-center. The fluorescence photons are depicted by red arrows.

ity, the nuclear spin need not lie within a few nanometers of the surface but rather can be detectable at a distance of 30 nm. With these novelties, our scheme provides chemically sensitive spin detection needed for nanoscale nuclear magnetic resonance (NMR) on biological tissue under ambient conditions—the holy grail of NMR. The details of our proposal are presented in Chapter 7.

1.3 Topological quantum computation by anyons

So far we have discussed several possible physical implementations of quantum computer. The common property of all the mentioned proposals is that the single- and two-qubit gates are typically performed by applying microwave pulses on the qubit and by controlling the pulse duration. Any imperfections in pulse sequence applied leads to an error in the gates. It is possible to correct for these error only if the errors of a gate operations are not too big, i.e., there exist a threshold above which

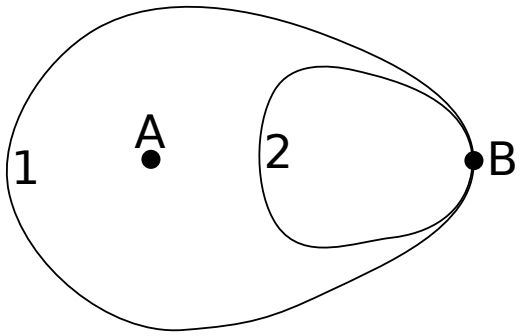

Figure 1.4: The path 1 cannot be continuously deformed into path 2 within two-dimensional space, since path 1 contains point A whereas path 2 does not. On the other had, in three-dimensions two paths are topologically equivalent.

it is no longer possible to do error correction. The value of the error threshold depends on the error correction scheme employed; the surface code error correction—the most powerful fault-tolerant quantum-error-correction scheme known, has an exceptionally large error threshold of 1.1% [20, 21].

Yet there is another approach to quantum computer implementation, so-called topological quantum computer—a theoretical concept that exploits quasiparticle excitations, living in two-dimensional (2D) space, called anyons. Anyons are excitations with "fractional" statistics, the term was coined by Wilzceck [22], see also Ref. [23]. It can be easily seen that the quasiparticle statistic in three dimensions must be either bosonic or fermionic. Namely, two exchanges of the quasiparticles makes a loop, and in three-dimensions closed loop is equivalent to a point. Thus as a result of two consecutive exchanges the wavefunction of the quasiparticles under the consideration has to be unchanged. This argument leaves only two possibilities for the phase that the wavefunction acquires after a single exchange, the phase can be either 0 or π corresponding to bosonic or fermionic statistics, respectively. Since in 2D space, the closed loop in not necessarily equivalent to a point (see Fig. 1.4), we conclude that the aforementioned argument does not hold. Therefore, excitations in 2D space can acquire arbitrary phase factor $e^{i\varphi}$ under the exchange—these excitations are called *abelian anyons*. The excitations in 2D space can have even more complicated exchange statistics. Let us consider three anyons labeled 1, 2, and 3. The most general way to describe the result of the exchange $1 \leftrightarrow 2$ is by 2×2 unitary matrix U_{12} that acts in the space spanned

by the particles 1 and 2. Similarly, the exchange $2 \leftrightarrow 3$ corresponds to the unitary matrix U_{23}. These matrices generally do not mutually commute, i.e. $[U_{12}, U_{23}] \neq 0$, which explains the adjective *non-abelian* used to describe these anyons. It is important to note that the form of unitary matrices U_{ij} does not depend on the exact shape of the path used for the exchange but only on the topology of the path, hence the name topological quantum computation. Thus local errors induced by the environment during the exchange process do not cause errors in the resulting state. Additionally, the space used for the computation has to be degenerate since the braiding of the particles cannot change the energy of the initial state. From here we immediately see the potential use of these anyonic excitations, the quantum gates can be performed by merely performing braiding of certain anyons. Unfortunately, it is not always possible to obtain the universal set of quantum gates[5] in topologically protected manner described above. An example of anyon is Majorana fermion (MFs) described below that allows for error-free implementation only of certain gates from universal set of quantum gates.

When it comes to physical implementation of a topological quantum computer, the study of MFs that emerge as end-states in various solid-state systems has recently attracted a lot of attention [24, 25, 26, 27, 28, 29, 30]. These theoretical efforts motivated the experimental quest for MFs, since they required quite simple ingredients—superconductivity, spin-orbit interaction and magnetic fields. This quest in turn gave rise to lot of controversy over whether MFs are actually observed in the recent experiments [31, 32, 33] or not. In the Chapter 10 of this thesis we contribute to clarification of some of these controversies by analyzing the transport signatures of MFs in a realistic model that corresponds well to the setup used in Ref. [31].

In Chapter 9 we introduce a simple model that allows for mid-gap end-states that are characterised by fractional charge. Further research showed that this model can be extended in order to support phases with MFs and a complementary phase characterized by fractionally charged fermions (FF) [34]. These FF can exhibit non-Abelian braiding statistics [35], but they exist both with and without superconductivity. In Chapter 11 we analyze the transport signatures of FF and discuss the

[5]One example of the universal set of quantum gates is the set consisting of Hadamard gate, a phase rotation gate and the controlled-NOT gate. By repeated application of these gates, where the number of steps scales at most polynomially with the desired accuracy, one can reach any desired state within the Hilbert space of the quantum computer memory within desired accuracy.

possible detection schemes that bare relevance for designing future experiments.

Part I

Long-Range Indirect Interaction of Spins Qubits

CHAPTER 2

Introduction

Quantum coherence and entanglement lie at the heart of quantum information processing. One of the basic requirements for implementing quantum computing is to generate, control, and measure entanglement in a given quantum system. This is a rather challenging task, as it requires to overcome several obstacles, the most important one being decoherence processes. These negative effects have their origin in the unavoidable coupling of the quantum systems to the environment they are residing in.

A guiding principle in the search for a good system to encode qubits is the smaller the system the more coherence, or, more precisely, the fewer degrees of freedom the weaker the coupling to the environment. Simultaneously, one needs to be able to coherently manipulate the individual quantum objects, which is more efficient for larger systems. This immediately forces us to compromise between manipulation and decoherence requirements.

Following this principle, among the most promising candidates for encoding a qubit we find *atomistic* two-level systems, such as NV-centers and silicon-based spin qubits [36, 37, 38, 39, 40, 41, 42, 43, 44, 45, 46, 47]. The latter are composed of nuclear (electron) spins of phosphorus atoms in a silicon nanostructure. They have very long T_2 times of $60\,ms$ [48] for nuclei and of $200\mu s$ for electrons [49]. Recently, high fidelity single qubit gates and readout have been demonstrated experimentally [49]. Nitrogen-vacancy centers [50] in diamond have also been demonstrated experimentally to be very stable with long decoherence times of $T_2^* \approx 20\,\mu s$ and $T_2 \approx 1.8\,ms$ [11]. Both types of spin qubits have the additional

advantage that noise due to surrounding nuclear spins can be avoided by isotopically purifying the material.

Unfortunately, it is hardly possible to make these spin qubits interact with each other in a controlled and scalable fashion. They are very localized and their position in the host material is given and cannot be adjusted easily. Therefore, if during their production two qubits turn out to lie close to each other they will always be coupled, while if they are well-isolated from each other they will never interact. It is thus of high interest to propose a scheme to couple such atomistic qubits in a way that allows a high degree of control. While there have been various proposals over the last years in order to couple spin qubits over large distances [51, 52, 53, 54, 55, 56, 57, 58, 59, 60, 61, 62], none of these methods apply straightforwardly to atomisitc qubits such as silicon-based qubits and N-V centers.

Alternative successful candidates for encoding a qubit are an electron spin localized in a semiconductor quantum dot, gate-defined or self-assembled, or a singlet-triplet qubit with two electrons in a double quantum well [4, 63]. These natural two-level systems are very long-lived (relaxation time $T_1 \sim 1s$ [64], and decoherence time $T_2 > 200\mu s$ [65]), they can be controlled efficiently by both electric and magnetic fields [66, 67, 68], and, eventually, may be scaled into a large network. It has been experimentally demonstrated that qubit-qubit couplings can be generated and controlled efficiently for these systems [61].

A large-scale quantum computer must be capable of reaching a system size of thousands of qubits, in particular to accommodate the overhead for quantum error correction [69]. This poses serious architectural challenges for the exchange-based quantum dot scheme [1], since—with present day technology—there is hardly enough space to place the large amount of metallic gates and wires needed to define and to address the spin qubits. A promising strategy to meet this challenge is to implement long-range interactions between the qubits which allows the quantum dots to be moved apart and to create space for the wirings. Based on such a design we propose a quantum computer architecture that consists of a two-dimensional lattice of spin-qubits, with nearest neighbor (and beyond) qubit-qubit interaction. Such an architecture provides the platform to implement the surface code–the most powerful fault-tolerant quantum error correction scheme known with an exceptionally large error threshold of 1.1% [70, 20].

To achieve such long-range interactions we propose a mechanism for entangling spin qubits in quantum dots (QDs) based on floating gates

and spin-orbit interaction. The actual system we analyze is composed of two double-QDs which are not tunnel coupled. The number of electrons in each double-QD can be controlled efficiently by tuning the potential on the nearby gates. Moreover, the electrons can be moved from the left to the right dot within each double-QD by applying strong bias voltage. Thus, full control over the double-QD is possible by only electrical means. The double-QDs are separated by a large distance compared to their own size so that they can interact only capacitively. An electromagnetic cavity [52, 53] can be used to create a long-range qubit-qubit coupling [58, 71]. Here we consider the classical limit thereof, i.e., a metallic floating gate [72, 73, 74, 75, 59] suspended over the two double-QDs, or a shared 2DEG lead between the qubits. The strength of the coupling mediated by this gate depends on its geometry, as well as on the position and orientation of the double-QDs underneath the gate. Finally, we show that spin-qubits based on spins-1/2 [1] and on singlet-triplet states [63] can be coupled, and thus hybrid systems can be formed that combine the advantages of both spin-qubit types.

We propose additional mechanism of long-range coherent interaction also in the absence of any spin-orbit interaction, thus enabling the coupling between *any kind of spin qubits*. The idea is to use the dipolar coupling of spin qubits to the spins of a dogbone-shaped ferromagnet. We show that coupling strengths of about $10^{-8}eV$ are achievable between spin qubits separated by a distance of about $1\,\mu m$. Our scheme is demonstrated to be applicable to singlet-triplet qubits as well. Furthermore, we explicitly construct the required sequences to implement a CNOT gate and estimate the corresponding operation times. The additional decoherence induced by the coupling to the ferromagnet is studied and we find a regime where fluctuations are under control and no significant additional decoherence is introduced. A particularly promising application of our proposal is to atomistic spin-qubits such as silicon-based qubits and NV-centers in diamond to which previous coupling schemes do not apply.

CHAPTER 3

Long-Distance Spin-Spin Coupling via Floating Gates

Adapted from:
Luka Trifunovic, Oliver Dial, Mircea Trif, James R. Wootton, Rediet Abebe, Amir Yacoby, and Daniel Loss
"Long-Distance Spin-Spin Coupling via Floating Gates",
Phys. Rev. X **2**, 011006 (2012)

The electron spin is a natural two level system that allows a qubit to be encoded. When localized in a gate defined quantum dot, the electron spin provides a promising platform for a future functional quantum computer. The essential ingredient of any quantum computer is entanglement—for the case of electron spin qubits considered here—commonly achieved via the exchange interaction. Nevertheless, there is an immense challenge as to how to scale the system up to include many qubits. Here we propose a novel architecture of a large scale quantum computer based on a realization of long-distance quantum gates between electron spins localized in quantum dots. The crucial ingredients of such a long-distance coupling are floating metallic gates that mediate electrostatic coupling over large distances. We show, both analytically and numerically, that distant electron spins in an array of quantum dots can be coupled selectively, with coupling strengths that are larger than the electron spin decay and with switching times on the order of nanoseconds.

3.1 Electrostatics of the floating gate

The Coulomb interaction and spin-orbit interaction (SOI) enable coupling between spin-qubits of different QD systems in the complete absence of tunneling [56, 57, 76, 77]. However, the Coulomb interaction is screened at large distances by electrons of the 2DEG and of the metal gates. Thus, the long-distance coupling between two spin-qubits is not feasible via direct Coulomb interaction. However, by exploiting long-range electrostatic forces, it was demonstrated experimentally [72, 74] that QDs can be coupled and controlled capacitively via floating metallic gates over long distances. The optimal geometric design of such floating gates should be such that the induced charge stays as close as possible to the nearest QDs, and does not spread out uniformly over the entire gate surface. In other words, the dominant contributions to the total gate-capacitance should come from the gate-regions that are near the QDs. To achieve a strong qubit-qubit coupling there is one more requirement: the electric field induced on one QD needs to be sensitive to the changes of the charge distribution of the other QD. Thus, the charge gradient, $(\partial q_{ind}/\partial \boldsymbol{r})_{\boldsymbol{r}=0}$, needs to be large, where $\boldsymbol{r}$ is the position-vector of the point charge with the respect to the center of the respective QD. To fulfill these requirements we assume the floating gates consist of two metallic discs of radius R joined by a thin wire of length L.

Let us now investigate the optimal design by modeling the electrostatics of the floating gates. The electron charge in the QD induces an image charge of opposite sign on the nearby disc (ellipsoid), see Fig. 3.1. By virtue of the gate voltage being floating with respect to the ground, the excess charge is predominantly distributed on the distant metallic ellipsoid, thus producing an electric field acting on the second QD. In order to carry out the quantitative analysis of the electrostatic coupling, we make use of the expression for an induced charge on the grounded ellipsoidal conductor in the field of a point charge [78]. Electrostatic considerations imply that the coupling (gradient) is enhanced by implementing a flat-disc design of the gate. Thus, in what follows, we set the disc height to zero; to reach this regime in practice one only has to ensure that the disc height be much smaller than its radius. The expression for the induced charge (in the units of the electron charge) is then given by [78]

$$q_{ind}(\boldsymbol{r}) \;=\; \frac{2}{\pi}\arcsin(R/\xi_{\boldsymbol{r}}), \tag{3.1}$$

where R is the radius of the disc, and a_0 is the distance between the QD

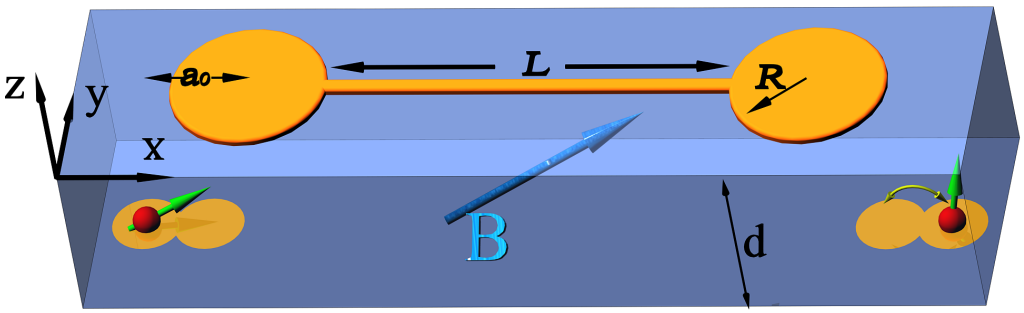

Figure 3.1: Model system consisting of two identical double-QDs in the xy-plane and the floating gate between them. The gate consists of two metallic discs of radius R connected by a thin wire of length L. Each double-QD can accommodate one or two electrons, defining the corresponding qubit. Absence of tunneling between the separate double-QD is assumed; the purely electrostatic interaction between the electrons in the double-QDs leads to an effective qubit-qubit coupling. For the spin-$1/2$ qubit the coupling depends sensitively on the orientation of the magnetic field B. Here a_0 is the in-plane distance between a QD and the corresponding disc center, while d is vertical distance between the QD and the gate.

and the ellipsoid centers (see Fig. 3.1). The ellipsoidal coordinate $\xi_{\boldsymbol{r}}$ is given by

$$\begin{aligned} 2\xi_{\boldsymbol{r}}^2 &= R^2 + d^2 + |\boldsymbol{a}_0 + \boldsymbol{r}|^2 \\ &\quad + \sqrt{(R^2 + d^2 + |\boldsymbol{a}_0 + \boldsymbol{r}|^2)^2 - 4R^2|\boldsymbol{a}_0 + \boldsymbol{r}|^2}. \end{aligned} \tag{3.2}$$

We emphasize that the induced charge depends only on the coordinate $\xi_{\boldsymbol{r}}$ of the external charge, as is readily seen from Eq. (3.1). This is one of the crucial points for the experimental realization of the qubit-qubit coupling. Thus, positioning the QD below the gate as in previous setups [72] is not useful for the qubit-qubit proposed considered here, since $\partial q_{ind}/\partial \boldsymbol{r} \approx 0$. This fact, however, can be exploited to turn *on* and *off* the effective coupling between the qubits. Alternatively, one can use a switch that interrupts the charge displacement current through the floating gate and thus disables the build-up of charge gradients at the other disc.

Figure 3.2 depicts both the induced charged q_{ind}, as well as the charge variation $\partial q_{ind}/\partial r$ as a function of the horizontal distance a_0 between the center of the QD and the center of the gate. We see that for very small vertical distances $d \ll R$ the variation of the induced charge peaks at

$a_0 \approx R$, reaching values as high as unity for $d = 0.1R$, and falls down quickly for a_0 larger or smaller than R. As mentioned above, this could be used as an efficient switching mechanism. However, as d increases to higher values, comparable to the disc radius R, the charge variation $\partial q_{ind}/\partial r$ flattens out over a wide range of in-plane distances a_0. This means that for larger depths $d \gtrsim \lambda$ of the quantum dot the switching mechanism turns out to be rather inefficient, even though the magnitude of the coupling is only weakly reduced ($\partial q_{ind}/\partial r \approx 0.3$ for $r \approx R$ and $d = 0.5R$). Nevertheless, the gates confining the QDs, as well as the 2DEG itself could lead to screening of the interaction between the QD and the floating gate, allowing for an improved switching even in this case.

Finally, by utilizing the expression for the electrostatic potential of a charged thin disc [78] we arrive at the expression for the electrostatic coupling

$$V(\boldsymbol{r}_1, \boldsymbol{r}_2) = \frac{\pi \alpha_q}{\kappa} \frac{e^2 q_{ind}(\boldsymbol{r}_1) q_{ind}(\boldsymbol{r}_2)}{R}, \tag{3.3}$$

where κ is the dielectric constant, $\alpha_q = \frac{C_d}{C_w + 2C_d}$ is the charge distribution factor of the gate, and C_d and C_w are the capacitances of the discs and wire, respectively (see Appendix 3.A). We mention that Eq. (3.3) is derived in the limit when the floating gate is immersed in the dielectric, and it provides a lower bound for $V(\boldsymbol{r}_1, \boldsymbol{r}_2)$ in the realistic case when the floating gate sits on top of the dielectric.

3.2 Qubit-qubit coupling

Next, we consider the coupling between qubits. These can be for either single- or double-QDs. The two-qubit system with the floating gate is well described by the Hamiltonian

$$H = V + \sum_{i=1,2} H^i_{qubit}\,, \tag{3.4}$$

where V describes the electrostatic coupling between the distant charges in the qubits and is given by Eq. (3.3), and H^i_{qubit} stands for either the single-QD or double-QD Hamiltonian [79, 57]

$$H_{QD} = H_0 + H_Z + H_{SO}, \tag{3.5}$$

$$H_{DQD} = J\, \boldsymbol{S}_1 \cdot \boldsymbol{S}_2 + H^1_Z + H^2_Z\,. \tag{3.6}$$

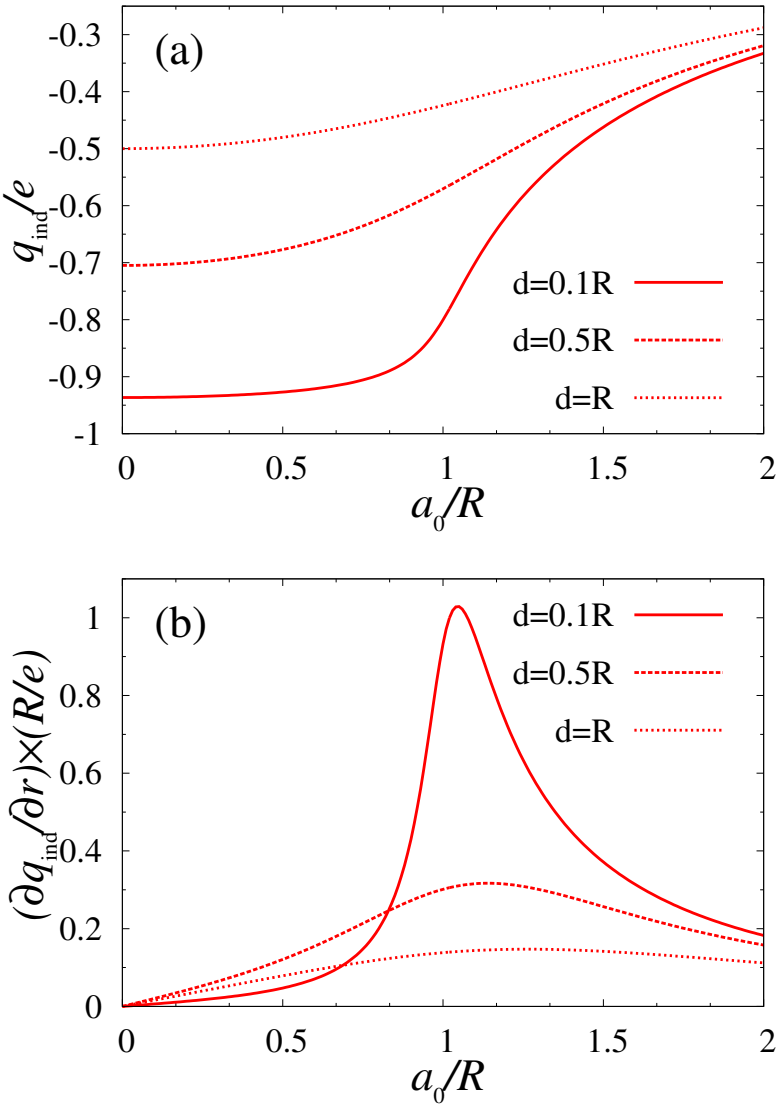

Figure 3.2: (a) The dependence of the induced charge, q_{ind}, and (b) of the derivative of the induced charge, $\partial q_{ind}/\partial r$, on a_0 at $r = 0$, i.e. the in-plane distance from the center of the cylindrical gate to the center of the QD. We plot these two quantities for several vertical distances d between the QD and the gate: $d/R = 0.1,\ 0.5,\ 1$, corresponding to the full, dashed and dotted lines, *resp.*.

Here, $H_0 = p_i^2/2m^* + m^*(\omega_x^2 x_i^2 + \omega_y^2 y_i^2)/2$ is the energy of an electron in dot i described by a harmonic confinement potential, m^* being the effective mass and $\hbar\omega_{x,y}$ the corresponding single-particle level spacings. For a single-QD $H_Z = g\mu_B \boldsymbol{B}\cdot\boldsymbol{\sigma}/2$, stands for the Zeeman coupling, with $\boldsymbol{\sigma}$ the Pauli matrix for the spin-1/2, and both Rashba and Dresselhaus spin-orbit interactions

$$H_{SO} = \alpha(p_x\sigma_y - p_y\sigma_x) + \beta(-p_x\sigma_x + p_y\sigma_y), \tag{3.7}$$

where α (β) is the Rashba (Dresselhauss) spin-orbit interaction strength. The double-QD is described by an effective Heisenberg model [79], see Eq. (3.6), with $\boldsymbol{S}_i$ being the spin in the double-QD. In what follows we assume the floating gate to be aligned along the x-axis, see Fig. 3.1.

Singly occupied double-QDs

We start by considering two single-QD qubits. Let us first give a physical description of the qubit-qubit coupling. The purely electrostatic coupling between the QDs involves only the charge degrees of freedom of the electrons. Within each QD the spin degree of freedom is then coupled to the one of the charge via spin-orbit interaction. Hence, we expect the effective spin-spin coupling to be second order in the SOI and first order in the electrostatic interaction. In fact, one has also to assume Zeeman splitting to be present on at least one QD in order to remove the van Vleck cancellation [80, 81]. Such a cancellation occurs due to linearity in the momentum of the SOI—for the SOI cubic in momentum (as for e.g. the self-assembled QDs), one obtains a spin-spin coupling even in the absence of magnetic fields[1].

Proceeding to a quantitative description, we assume the spin-orbit strength to be small compared to the QD confinement energies $\hbar\omega_{x,y}$. Following Refs. [81, 57], we apply a unitary Schrieffer-Wolff transformation to remove the first order SOI terms. The resulting Hamiltonian has decoupled spin and orbital degrees of freedom (to second order in SOI), with the effective qubit-qubit coupling (see Appendix 3.A), with

$$H_{S-S} = J_{12}(\boldsymbol{\sigma}_1\cdot\boldsymbol{\gamma})(\boldsymbol{\sigma}_2\cdot\boldsymbol{\gamma}) \tag{3.8}$$

$$J_{12} = \frac{m^*\omega_{x,12}^2 E_Z^2}{2(\omega_x^2 - E_Z^2)^2}, \tag{3.9}$$

[1]We have checked that for the SOI given by $\sigma_x p_x^3$, the spin-spin coupling of the form $J_{xx} = -(5\pi^3/2)m^3\alpha^2\alpha_q^3\alpha_c^3(\partial q_{ind}/\partial x)^6\omega_x^6$ is obtained in the absence of the magnetic field.

where $\boldsymbol{\gamma} = (\beta \cos 2\gamma, -\alpha - \beta \sin 2\gamma, 0)$; γ being the angle between the crystallographic axes of the 2DEG and the xyz-coordinate system defined in Fig. 3.1. Here we assumed for simplicity that the magnetic field is perpendicular to the 2DEG substrate, with $E_Z = g\mu_B B$ the corresponding Zeeman energy (assumed also the same for both dots). However, neither the orientation nor the possible difference in the Zeeman splittings in the two dots affect the functionality of our scheme (see Appendix 3.A for the most general coupling case). We mention that the spin-spin interaction in Eq. (3.8) is of Ising type, which, together with single qubit gates forms a set of universal gates (see below).

All information about the floating gate coupling is embodied in the quantity

$$\omega_{x,12}^2 = \pi \alpha_q \alpha_C \left(\frac{\partial q_{ind}}{\partial \tilde{x}} \right)^2_{\boldsymbol{r}=0} \omega_x^2, \tag{3.10}$$

where $\alpha_C = e^2/(\kappa R \hbar \omega_x)$, and $\tilde{x} = x/\lambda$ (λ is the QD size).[2] Remarkably, the coupling has only a weak dependence on the wire length L—through the capacitance ratio α_q.

Next, we give estimates for the qubit-qubit coupling for GaAs and InAs QDs. Taking the spin-orbit strength for GaAs semiconductors $\lambda \simeq 0.1\lambda_{SO}$ ($\lambda_{SO} = \hbar/(m^*\alpha)$), and assuming $E_{Z1} \simeq E_{Z2} \equiv E_Z \simeq 0.5\hbar\omega_x$ ($B = 2T$ and $\hbar\omega_x \simeq 1meV$), we obtain $H_{s-s} \simeq \alpha_q \alpha_C (\partial q_{ind}/\partial \tilde{x})^2_{\boldsymbol{r}=0} \times 10^{-7} eV$. The electrostatic coupling strongly depends (like d^{-2}) on the vertical distance between the gate and the QDs. Typically, $d \simeq \lambda$, and one obtains using Eq. (3.1) maximal coupling $H_{s-s} \simeq 10^{-11} - 10^{-10} eV$ (for $R = 1.6\lambda$, $L = 10\mu m$, and $R_w = 30nm$ leading to $\alpha_q = 0.02$; $a_0 = 1.9\lambda$). Although, it is experimentally challenging to decrease d to a value of about $10nm$, the gain would be a significantly stronger coupling $10^{-9} - 10^{-8} eV$ (for $R = 0.17\lambda$ and $a_0 = 0.2\lambda$). Moreover, if a semiconductor with larger spin-orbit coupling is used—such as InAs ($\lambda/\lambda_{SO} \simeq 1$)—the coupling is increased by two orders of magnitude compared to GaAs, reaching the μeV-regime. Quite remarkably, these values almost reach within the exchange strengths range, $J_{exc} \sim 10 - 100\mu eV$ ($10 - 100ps$), occurring in typical GaAs double quantum dots [1, 82]. Actually, for realistic devices—as presented in the Sec. 3.5—the coupling is almost two orders of magnitude larger then the estimates presented herein, and thus operation times are well below the decoherence times for QD. This discrepancy is not

[2] It is interesting to note that the derived coupling, Eq. (3.8), is independent of the orbital states of the QDs, and thus, insensitive to the fluctuations of a QD electron charge distribution.

very surprising and it is mainly due to our conservative treatment of the dielectric, and the sensitivity of the electric field gradient to geometry of the surrounding gates.

Hybrid spin-qubits

A number of different spin-based qubits in quantum dots have been investigated over the years [83], each with its own advantages and challenges. The most prominent ones are spin-1/2 and singlet-triplet spin qubits. Here, we show that these qubits can be cross-coupled to each other and thus hybrid spin-qubits can be formed which open up the possibility to take advantage of the 'best of both worlds'.

We model the hybrid system by a single- and a double-QD qubit, described by Eqs. (3.5) and (3.6), respectively. The single-QD and the floating gate act as an electric field, leading to the change in the splitting between the logical states of the double-QD spin-qubit, $J \to J + \tilde{x}_e \delta\tilde{J}$ [79], with $x_e = \tilde{x}_e \lambda$ being the x-coordinate of the electron in the single-QD and

$$\delta\tilde{J} = \frac{3}{\sinh(2\tilde{l})} \frac{\omega_{x,12}^2}{\tilde{l}\omega_D^2} \epsilon \,. \tag{3.11}$$

Here, ω_D is the confinement energy in the DQD, $\tilde{l}$ is the distance between the double-QD minima measured in units of a QD size λ. The previous formula is valid for the regime $\epsilon \gtrsim \omega_D$.

In order to decouple spin and orbital degrees of freedom, we again employ a Schrieffer-Wolff transformation and obtain the hybrid coupling in lowest order (see Appendix 3.B)

$$H_{hybrid} = \frac{3\mu g \; \delta\tilde{J}(\boldsymbol{\gamma} \times \boldsymbol{B}) \cdot \boldsymbol{\sigma}}{4(\omega_x^2 - E_{Z1}^2)\lambda} \tau_z \,. \tag{3.12}$$

Here, τ_z is a Pauli matrix acting in the pseudo-spin space spanned by the logical states of the singlet-triplet qubit. It should be noted that the sign of this coupling can be manipulated by changing the sign of the detuning voltage ϵ. As an estimate, we can write $H_{hybrid} \simeq \left(\frac{\omega_{x,12}}{\omega_x}\right)^2 \frac{E_Z}{\omega_D} \frac{a_B}{\lambda_{SO}} \epsilon$. Assuming the parameters cited in the previous section for the GaAs-QDs we obtain the estimate $H_{S-s} \simeq 10^{-10} - 10^{-9} eV$. Reducing the distance d or using InAs-QDs we can gain one order of magnitude more in the coupling.

Doubly occupied double-QDs

To complete our discussion about the qubit-qubit couplings, we now consider two double-QDs coupled via the floating gate. As already noted, owing to the different charge distributions of the logical states in the double-QD, the SOI term is not needed for the qubit-qubit coupling [76]. Certainly, the SOI exists in double-QDs but its effect on the ST splitting can be neglected [84]. Below only a rough estimate of the coupling is provided, while the detailed analysis can be found in Ref. [76].

We assume both double-QDs to be strongly detuned, thereupon the singlet logic state is almost entirely localized on the lower potential well of the double-QD. The electrostatic energy difference between the singlet-singlet and triplet-triplet system configurations gives the rough estimate of the qubit-qubit coupling, $H_{S-S} \simeq V(R,R) - V(R+l,R+l)$. Taking the distance between the double-QD minima $l \simeq R$ and the same GaAs parameters as before, we finally obtain the estimate $H_{S-S} \simeq 10^{-5} - 10^{-6} eV$. As can be seen from Fig. 3.2, reducing d to $10nm$ increases the coupling five times.

3.3 Scalable Architecture

One central issue in quantum computing is scalability, meaning that the basic operations such as initialization, readout, single- and two-qubit gates should not depend on the total number of qubits. In particular, this enables the implementation of fault-tolerant quantum error correction [69], such as surface codes where error thresholds are as large as 1.1% [70, 20].

To this end, the architecture of the qubit system becomes of central importance [85]. Making use of the electrostatic long-distance gates presented above, we now discuss two illustrative examples for such scalable architectures.

Design with floating metal gates

In the first design we propose here, the metallic gates above the 2DEG are utilized for qubit-qubit coupling, while the switching of the coupling is achieved by moving the QDs (see Fig. 3.3). Only the coupling between adjacent QDs is possible in this design. Without this constraint, the induced charge due to nearby QDs would be spread over the whole system, resulting in an insufficient qubit-qubit coupling.

The actual virtue of the setup is its experimental feasibility, as suggested by recent experiments [72, 74]. However, as explained in Sec. II, a minor but crucial difference here is that the qubit-qubit coupling depends not on the charge itself but rather on its gradient, in contrast to earlier designs [72, 74]. This requires the dots to be positioned off the disc-center.

In order to complete our quantum computer design, we have to equip our system with a fast switch. The discussion in Sec. II is relevant therefore, because the coupling can be turned *off* (*on*) by moving a QD away (towards) the corresponding floating gate, see Fig. 3.2. The spatial change of the quantum dot induces an electric response in the metallic floating gate on a time scale roughly given by the elastic mean free time (at low temperatures). This is the time it takes to reach the new electronic equilibrium configuration that minimizes the electrostatic energy. Since for a typical metal this time is on the order of tens of femtoseconds, this response time poses no limitations, being much faster than the effective switching times obtained in the previous sections.

All-in-2DEG design

We now consider a setup where are all elements of the qubit-network, including the floating connector gates, are implemented in the 2DEG itself. This will allow us to extend the above design in an essential way, namely to implement a switching mechanism inside the connectors themselves which is potentially fast and efficient (with a large on/off ratio). There are two attractive features coming with such a design. First, the qubit-qubit coupling is now controlled by the connector switch only, while the quantum dots with the spin-qubits can be left fixed, thereby reducing the source of gate errors. Second, this design allows for coupling beyond nearest neighbor qubits, which is beneficial for the error threshold in fault-tolerant quantum error correction schemes [85].

The proposed network is shown in Fig. 3.4 where the floating gates are formed within the 2DEG in form of discs connected by quantum wires. The discs themselves can be considered as large quantum dots containing many electrons ($\sim 50 - 100$) so that (quantum) fluctuations are negligibly small. Parts of the network are then connected or disconnected by locally depleting these wires with the help of a standard quantum point contact [82]. This suppresses the displacement of charges very quickly and efficiently. The electrostatics of such semiconductor gates is essentially the same as the previously discussed metallic one. Indeed, the

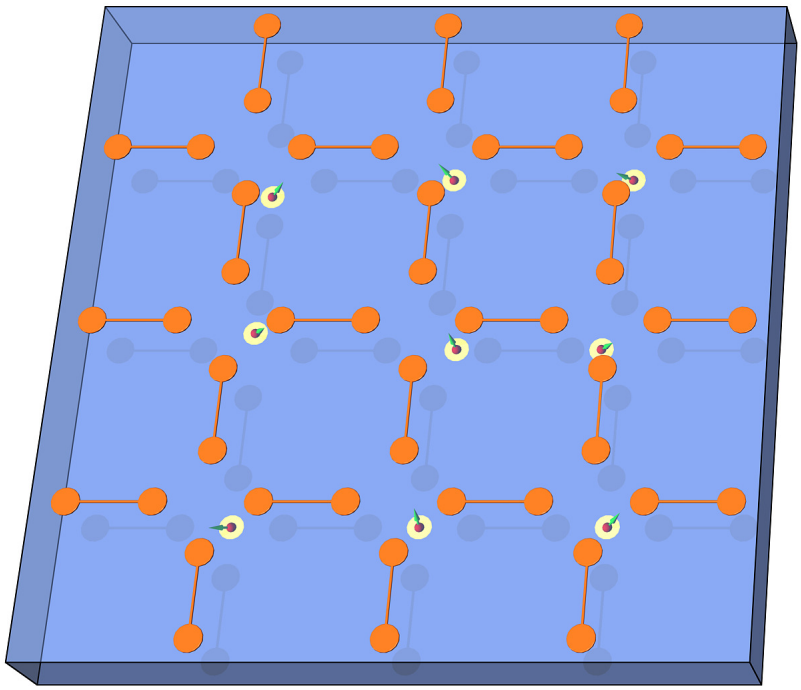

Figure 3.3: Quantum computer architecture using metallic floating gates on top of a 2DEG. The electrostatic long-range coupling is confined to adjacent qubits. Turning on (off) the qubit-qubit interaction is achieved by moving a qubit close to (away from) the corresponding metal disc. This architecture allows for parallel switching.

number of electrons in the 2DEG-defined network can be fixed, thus the gate behaves as floating. Again, the minimal switching time is limited roughly by the elastic mean free time (at low temperatures), which for a typical GaAs 2DEG is on the order of tens of picoseconds.

The single spin control required for completing the universal set of gates in our proposal can be implemented in both setups through ESR [86], or purely electrically via EDSR [87, 88, 89], which is more convenient for our electrostatic scheme. The time scales achieved are on the order of 50 ns, much shorter than the spin relaxation and decoherence times [87, 88, 89].

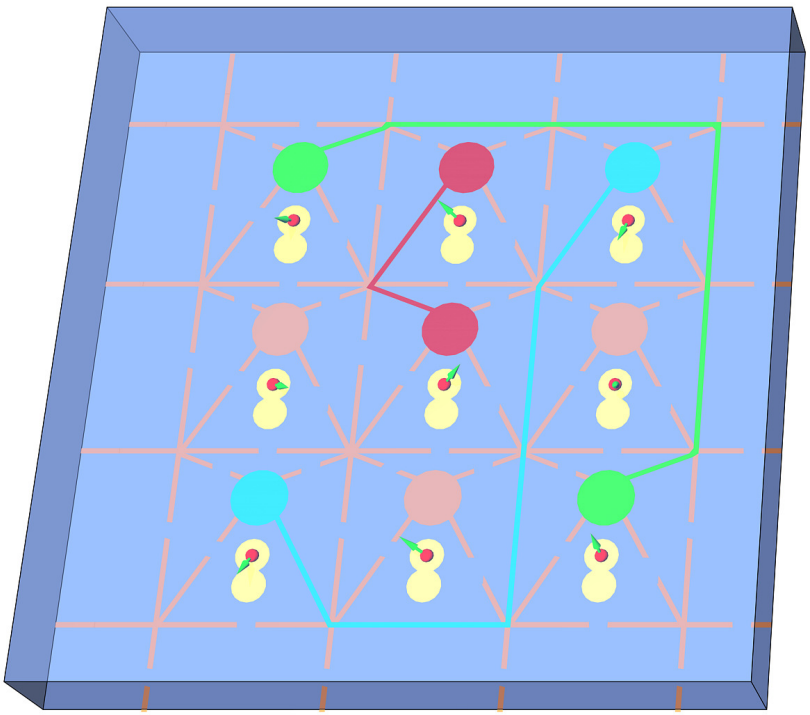

Figure 3.4: All-in-2DEG design: the qubits and the floating connector gates are all implemented within the same 2DEG. The spin-qubits (green arrow) are confined to double quantum dots (small yellow double circles) and are at a fixed position with maximum coupling strength to the floating gate (big disc) (see Fig. 3.2). The network consists of quantum channels (lines) that enable the electrostatic coupling between discs (large circles) so that two individual qubits at or beyond nearest neighbor sites can be selectively coupled to each other. In the figure shown are four pairs of particular discs that are connected by quantum channels (full lines), while the remaining discs (red) are disconnected from the network (interrupted red lines) The discs can be considered as large quantum dots containing many electrons. The quantum wires can be efficiently disconnected (interrupted lines) by depleting the single-channel with a metallic top gate (not shown). This architecture allows for parallel switching.

Design based on 1D nanowire quantum dots

The floating gate architecture efficiency is strongly dependent on the strength of the SOI experienced by the electrons in the QDs, which have to be large enough to overcome the spin decoherence rates. InAs nanowires are such strong SOI materials, with strengths larger by an order of magnitude than in GaAs 2DEG [90]. Moreover, the electron spins in QDs created in these nanowires show long coherence times [89] and can be controlled (electrically) on times scales comparable to those found for the electron spin manipulation in GaAs gate defined QDs [89].

In Fig. 3.5 we show a sketch of an architecture based on nanowires containing single or double QDs. Typical examples for such wires are InAs [90, 89] or Ge/Si [75, 91] nanowires, Carbon nanotubes [74, 92, 93, 94], etc. The default position of a QD is chosen so that the coupling to any of the surrounding gates is minimal. Neighboring QDs in the same nanowire are coupled by a vertical metal gate, while QDs in adjacent nanowires by a horizontal metal gate. The electron in a given QD can be selectively coupled to only two of the surrounding gates by moving it (via the gates that confine the electrons) in regions where the electric field gradient for the induced charge is maximum on these two 'active' gates, while negligible for the others two 'passive' gates. The other QD partner in the coupling is moved towards one of the 'active' gates thus resulting in a qubit-qubit coupling. Note that there are in total three 'active' gates, but only one of them is shared by both QDs, thus allowing selective coupling of any nearest neighbor pair in the network.

The spin coupling mechanism as well as the 2D geometry are similar to the previous 2DEG GaAs QDs designs, showing the great flexibility of the floating gate architecture. As before, the spin-qubits can be manipulated purely electrically, via the same gates that confine the QDs [89]. We mention also that the gate geometry (dog-bone like) shown in Fig. 3.5 is not optimized to achieve the best switching ratio, more asymmetric gate geometries possibly leading to better results.

Spin qubit decoherence and relaxation

Decoherence and relaxation are ones of the main obstacles to overcome in building a quantum computer. The main source of qubit decay in typical GaAs quantum dots comes from nuclear spins and phonons (via spin orbit interaction), and has been studied in great detail theoretically and experimentally, see e.g. Ref. [95]. The longest relaxation and decoherence

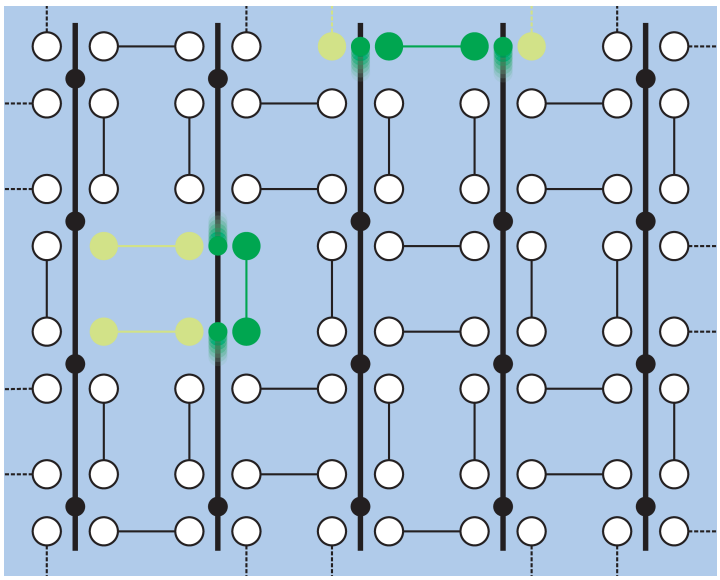

Figure 3.5: Architecture based on nanowire QDs coupled by metallic gates. The spin qubits are confined to QDs (black dots) on nanowires. The nanowires form a parallel array (vertical black lines). The coupling between neighboring spin-qubits is enabled by floating metal gates (white) positioned either parallel to the wires thus coupling QDs created in the same wire, or perpendicular to the wires thus coupling QDs created in adjacent nanowires. By using external gates (not shown) to move the dots along the nanowires (shaded colors) it is then possible to selectively couple one particular QD to only two surrounding gates ('active' gates; green and yellow). The other QD partner couple to one of these 'active' gates also (green), thus resulting in a selective coupling of the desired nearest neighbor pair.

times measured are about $T_1 \sim 1s$ [64] and $T_2 \sim 270\mu s$ [65], respectively. Exactly the same qubit decay mechanisms also apply here, except one new source coming from the Nyquist noise of the floating metallic gates. However, this problem has been studied in great detail in Ref. [96] and no major impact on the decoherence time was found. Even if Nyquist noise were a problem, it could be further reduced by using superconducting gates in lieu of normal metal ones.

3.4 Implementation of two-qubit gates

Since the Hamiltonian of Eq. (3.8) is entangling, it can be used to implement two-qubit gates. Here we consider the CNOT gate, widely used in schemes for quantum computation [70, 20]. The Hamiltonian for two single-QD qubits interacting via the floating gate is the sum of H_{S-S} and the Zeeman terms. The strength of the latter in comparison to the former allows us to approximate the Hamiltonian by $H' = J_{12}|\boldsymbol{\gamma}|^2(\sigma_x^1\sigma_x^2 + \sigma_y^1\sigma_y^2)/2 + E_z(\sigma_z^1 + \sigma_z^2)/2$, for which qubit-qubit interaction and Zeeman terms commute. The CNOT gate, C, may then be realized with the following sequences,

$$\begin{aligned} C &= \sqrt{\sigma_z^1}\,\sqrt{\sigma_x^2}\,\mathcal{H}^1 e^{i(\sigma_z^1+\sigma_z^2)E_z t} e^{-iH't} \\ &\quad \sigma_x^1\, e^{i(\sigma_z^1+\sigma_z^2)E_z t} e^{-iH't}\, \sigma_x^1\, \mathcal{H}^1, \qquad (3.13) \\ C &= \sqrt{\sigma_z^1}\,\sqrt{\sigma_x^2}\,\mathcal{H}^1\, \sigma_x^2\, e^{-iH't/2}\, \sigma_x^1\sigma_x^2\, e^{-iH't/2} \\ &\quad \sigma_x^2\, e^{-iH't/2}\, \sigma_x^1\sigma_x^2\, e^{-iH't/2}\, \mathcal{H}^1 \qquad (3.14) \end{aligned}$$

where $t = \pi/(4J_{12}|\boldsymbol{\gamma}_x|^2)$ and $\mathcal{H}$ denotes the single qubit Hadamard rotation. These sequences require two and four applications of the floating gate, respectively. More details on their construction can be found in Appendix 3.C. The time t is the bottleneck process in the sequence, and so the time taken to implement the gates will be on the order of this value. For a realistic value of $J_{12}|\boldsymbol{\gamma}|^2 = 10\mu eV$, this gives a time of around a nanosecond.

Since H' is only an approximation of the total Hamiltonian, these sequences will yield approximate CNOTs. Their success can be characterized by the fidelity which depends only on the relative strengths of the parameters. For a realistic device we can expect the Zeeman terms to be an order of magnitude stronger than the qubit-qubit coupling. The above sequences then yield fidelities of 99.33% and 99.91% respectively. For realistic parameters, with the Zeeman terms an order of magnitude stronger than the qubit-qubit coupling, the above sequences yield fidelities of 99.33% and 99.91% respectively. For two orders of magnitude between the Zeeman terms and qubit-qubit coupling the approximation improves, giving fidelities of 99.993% and 99.998%, respectively. These are all well above the fidelity of 99.17%, corresponding to the threshold for noisy CNOTs in the surface code [20]. Hence, despite the difference in error models, we can be confident that the gates of our scheme are equally useful for quantum computation.

3.5 Numeric Modeling of Realistic Devices

In the previous sections, a number of practical concerns related to the construction of working devices were neglected; most notably, the existence of the metallic gates used to define the quantum dots themselves and the presence of undepleted 2DEG outside of the quantum dots. These have finite capacitances to the coupler, shunting away some of the charge that would otherwise contribute to the inter-qubit interaction. To confirm that substantial couplings can still be attained at large distances with these limitations, we have performed numeric simulations of devices with realistic geometries similar to currently in-use ST spin qubits. A typical simulated geometry is included in Fig. 3.6. The gate and heterostructure design is identical to a functional device currently being characterized, and the boundaries of the 2DEG and placement of the electrons within the dot are estimates guided by experimentally measured parameters. Each quantum dot is modeled as a fixed charge metallic disc 50 nm in diameter within the 2DEG. While unsophisticated, this suffices to estimate the practicality of this scheme.

We define the coupling between two ST qubits as the change in detuning in one ST qubit induced by the transfer of a full electron from one dot to the other dot in a second ST qubit. For our reference ST qubit design with the two qubits physically adjacent to each other and no coupler (680 nm center-to-center), we calculate a coupling of 20μeV. As the qubits are separated, the coupling vanishes rapidly as the 2DEG in between the qubits screens the electric field; it is reduced by an order of magnitude if the dots are separated by an additional 250 nm. This rapid falloff makes the gate density needed for large scale integration of these qubits problematic.

Addition of a floating metallic coupler of the type described herein increases the coupling at zero separation to 70μeV and allows the qubits to be separated by more than $6\mu m$ before the coupling drops to the level seen for two directly adjacent qubits. We can further improve upon this coupling by etching the device in the vicinity of the coupler, reducing the shunt capacitance of the coupler to the grounded 2DEG between the devices.

For the case of single spins this metallic coupler is modified to place the quantum dots at the edges of the coupler rather than under the discs. We define the coupling in this case as the electric field in V/m induced on one qubit in response to 1nm of motion of the electron on the other qubit. We continue to find substantial couplings even at large separa-

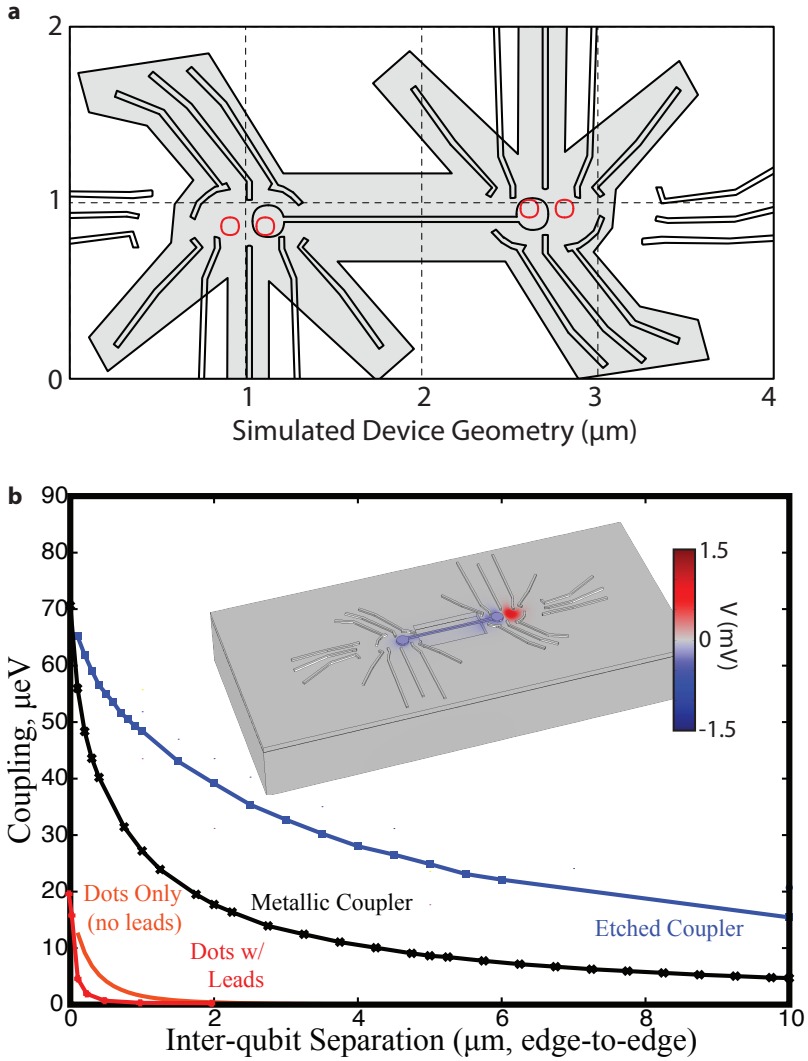

Figure 3.6: Numeric simulation confirm the efficacy of the design for S-T qubits; addition of a metallic coupler (crosses) increases coupling more than 3-fold for closely spaced dots, and greatly extends the range of the coupling. (a) The simulated device with a separation of 1 μm and an etched coupler. 2DEG underneath the shaded region is treated as depleted, while red circles show the locations of the individual quantum dots within the simulation. (b) Coupling strength as a function of separation for the ST qubits in free space (smooth curve), qubits including leads and 2DEG but without a coupler (red +), including a metallic coupler (black crosses), and additionally etching a trench around the coupler to deplete the 2DEG underneath (blue squares). Inset: Electrostatic potential (color scale) at the sample surface shows the impact of the coupler on a device with a 1 μm separation.

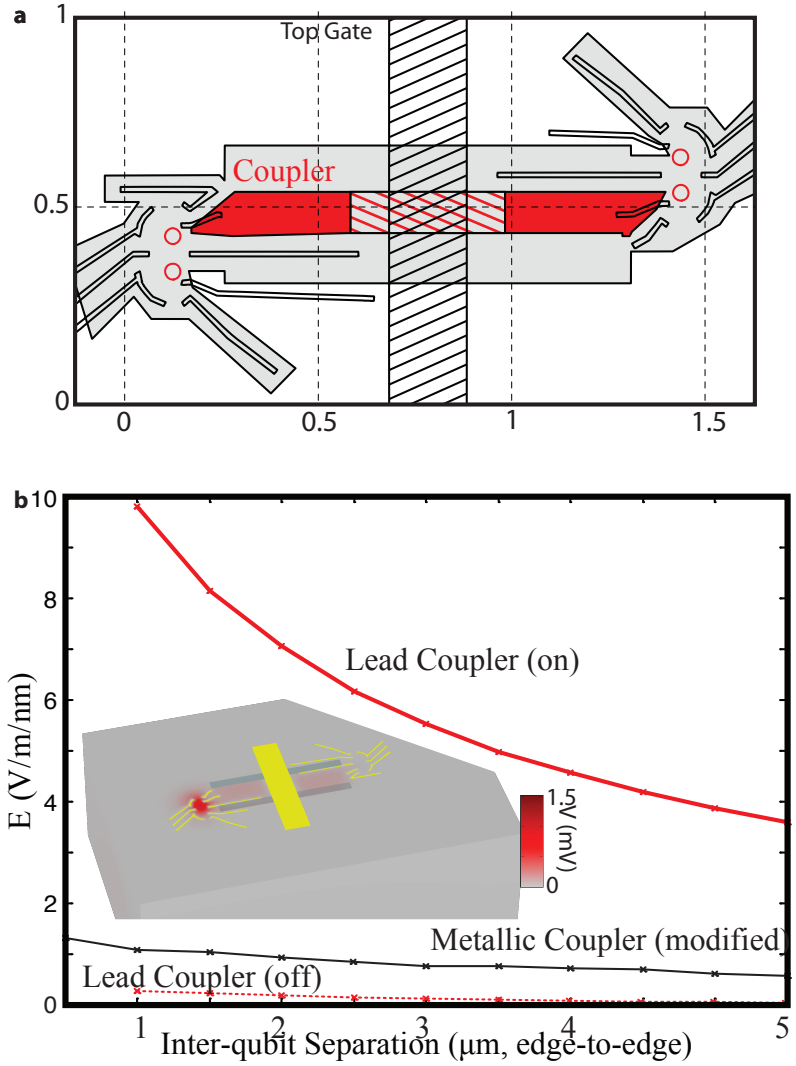

Figure 3.7: Simulations of single-spin qubits show appreciable coupling strengths, even over distances of several microns. While the metallic coupler design of Fig. 3.6 modified to place the quantum dots at the edges of the couplers is effective (black crosses in b), an all-in-2DEG design where one of the leads of the qubit acts as a coupler (red region in a) provides dramatically enhanced coupling (solid red lines in b). The coupler is deactivated by a metallic top gate (black hatched region in a), modeled by removing the hatched section of the coupler. Doing so reduces inter-qubit coupling by over an order of magnitude (dashed red lines in b).

tions (Fig. 3.7). However, in this case we find we can further improve couplings by moving to the all-in-2DEG design where one of the leads of the quantum dot is used as the coupler (Fig. 3.7 a). Using the lead in this fashion should be harmless; no current is driven into the lead during qubit manipulations. The lead (colored region) is modeled as a metallic strip at the level of the 2DEG. Due to the close proximity of the lead to the qubit as well as the sharp electric field gradients near the point of the lead, we find strongly enhanced coupling for this lead coupler over the floating metallic coupler for single spin qubits. By depleting part of the lead coupler using a metallic top gate (yellow region), it is possible to selectively turn this coupling on and off. The reduction in coupling in the off state is more than an order of magnitude, and can be further improved by increasing the size of the depleted region.

3.6 Conclusions

We proposed and analyzed an experimentally feasible setup for implementing quantum gates in an array of spin qubits localized in gate-defined quantum dots based on the interplay of the Coulomb repulsion between the electrons, SOI and externally applied magnetic fields. As opposed to the current schemes based on direct exchange, here there is no need for electron tunneling between the quantum dots, thus bringing the scheme within experimental reach based only on current spin-qubit technology.

We showed, both analytically and numerically, that using either metallic floating gates in the shape of a dog-bone, or the 2DEG itself acting as a metallic gate, long-range spin-spin coupling is achieved, with coupling strengths exceeding the spin decay rates. Moreover, the coupling can be selectively switched *on* and *off* between any pairs of qubits by only local qubit manipulation, allowing entangling quantum gates such as the CNOT to be performed accurately and efficiently. The two-dimensional architecture based on the design provides a platform for implementing the powerful surface code.

The electrostatic scheme proposed here is a step forward towards an efficient implementation of gates also between hybrid qubits, like ST qubit, hole-spin qubits, or even superconducting qubits. This opens up new avenues for a future working hybrid quantum computer based not on one, but several types of qubits.

3.7 Acknolwedgment

We thank C. Marcus and D. Stepanenko for helpful discussions and acknowledge support from the Swiss NF, NCCRs Nanoscience and QSIT, and DARPA. This research was partially supported by IARPA/MQCO program and the U. S. Army Research Office under Contract No. W911NF-11-1-0068. MT acknowledges financial support from NSF under Grant No. DMR-0840965.

3.A SPIN-SPIN COUPLING - singly occupied double-dots

In this section we derive explicitly the effective spin-spin coupling. The spin-orbit interaction (SOI) Hamiltonian H_{SO} is assumed to be small compared to both the orbital Hamiltonian $H_0 + V$ and the Zeeman coupling H_Z, so that we can treat it in perturbation theory. The method of choice for the perturbation theory is based on the Schrieffer-Wolff (SW) transformation, following Refs. [81, 57]. This method is very suitable for deriving effective Hamiltonians, as we aim at herein. We first perform a unitary transformation on the full Hamiltonian, i.e. $H \to e^S H e^{-S} \equiv H_{SW}$, with S an anti-unitary operator so that we get

$$\begin{aligned} H_{SW} &= H_d + H_{SO} + [S, H_d + H_{SO}] \\ &\quad + \frac{1}{2}[S, [S, H_d + H_{SO}]] + \ldots, \end{aligned} \tag{3.15}$$

where $H_d = H_0 + V + H_Z$. We look for the transformation S so that this diagonalizes the full Hamiltonian H in the basis of H_d. In leading order in H_{SO}, we choose S so that $[S, H_0 + V + H_Z] = -(1 - \mathcal{P})H_{SO}$, with the projector operator $\mathcal{P}$ satisfying $\mathcal{P}A = \sum_{E_n = E_m} A_{nm}|m\rangle\langle n|$, $\forall A$, i.e. it projects onto the diagonal part of the Hamiltonian H_d. Keeping the lowest order terms in α and β in the SW transformation, we are left with the effective interaction Hamiltonian H_{SW} that contains the desired spin-spin coupling in the basis of H_d

$$H_{SW} = H_d - \frac{1}{2}\mathcal{P}[S, H_{SO}], \tag{3.16}$$

where $S = (1 - \mathcal{P})L_d^{-1} H_{SO}$, with L_d being the Liouvillian superoperator ($L_d A = [H_d, A], \forall A$).

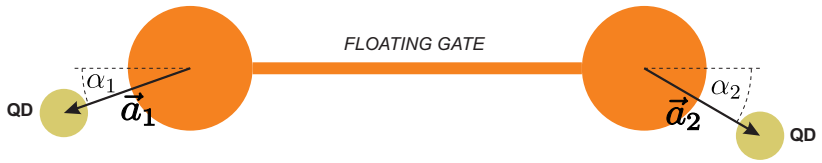

Figure 3.8: The misalignment angle α of the two QDs (yellow), defined with respect to the metallic floating gate (orange).

Next we find the explicit expression for the spin-spin coupling due to the second-order term in SOI in Eq. (3.16), i.e. $U \equiv \frac{1}{2}[S, H_{SO}]$. We make use of the explicit time-dependent (integral) representation of the Liouvillian $L_d^{-1} = -i\int_0^\infty dt e^{i(L_d+i\eta)t}$ and arrive at

$$U = -\frac{i}{2}\int_0^\infty dt e^{-\eta t}[H_{SO}(t), H_{SO}], \tag{3.17}$$

where $H_{SO}(t) = e^{iL_d t}H_n = e^{iH_d t}H_n e^{-iH_d t}$, and $\eta \to 0^+$ ensures the convergence of the time integration. Heisenberg operators, $\boldsymbol{\sigma}_i(t)$ and $\boldsymbol{p}_i(t)$, are needed in order to calculate U. The former is easy to obtain $\boldsymbol{\sigma}_i(t) = \widehat{\Sigma}_i(t)\boldsymbol{\sigma}_i$, with $\widehat{\Sigma}_i(t)$ given by

$$\begin{aligned}(\widehat{\Sigma}_i)_{mn}(t) &= \delta_{mn}\boldsymbol{l}_i^2\cos\frac{E_{Zi}t}{2\hbar} + 2(\boldsymbol{l}_i)_m(\boldsymbol{l}_i)_n\sin^2\frac{E_{Zi}t}{4\hbar} \\ &\quad -\varepsilon_{nmk}(\boldsymbol{l}_i)_k\sin\frac{E_{Zn}t}{2\hbar},\end{aligned} \tag{3.18}$$

with $\boldsymbol{l}_i = \boldsymbol{B}_i/B$. The calculation of $\boldsymbol{p}_i(t)$ consists of solving the system of ordinary differential equations (ODEs)

$$\frac{d}{dt}\boldsymbol{p}_i(t) = -m^*\omega_0^2\boldsymbol{r}_i(t) - \frac{\partial}{\partial\boldsymbol{r}_i}V(\boldsymbol{r}_1(t), \boldsymbol{r}_2(t)), \tag{3.19}$$

$$\frac{d}{dt}\boldsymbol{r}_i(t) = \boldsymbol{p}_i(t)/m^*. \tag{3.20}$$

In order to solve this system we expand the electrostatic potential, given in Eq. (3.3), around the minima to second order in $\boldsymbol{r}_i(t)$. The system

of ODEs now reads

$$\frac{d^2}{dt^2}\begin{pmatrix} \boldsymbol{p}_1(t) \\ \boldsymbol{p}_2(t) \end{pmatrix} = -\widehat{\Omega}\begin{pmatrix} \boldsymbol{p}_1(t) \\ \boldsymbol{p}_2(t) \end{pmatrix}, \tag{3.21}$$

$$\widehat{\Omega} = \begin{pmatrix} \omega_x^2 & 0 & \hat{\Omega}_{12} \\ 0 & \omega_y^2 & \\ \hat{\Omega}_{12}^{\dagger} & & \begin{matrix} \omega_x^2 & 0 \\ 0 & \omega_y^2 \end{matrix} \end{pmatrix}. \tag{3.22}$$

In this approximation only terms $O(\boldsymbol{r}_i^2)$ are retained—this is valid for low lying levels. We ignore the renormalization of the frequencies (ω_x and ω_y) because it gives higher order (in the Coulomb energy) contribution to the effective spin-spin coupling. The coupling between the QDs ($\hat{\Omega}_{12}$) is given by

$$(\hat{\Omega}_{12})_{ij} = \pi\alpha_q\alpha_C\left(\frac{\partial q_{ind}}{\partial\tilde{\boldsymbol{r}}_i}\right)\left(\frac{\partial q_{ind}}{\partial\tilde{\boldsymbol{r}}_j}\right)\omega_i\omega_j, \tag{3.23}$$

$$(\partial q_{ind}/\partial\boldsymbol{r}_i)_{\boldsymbol{r}=0} = \frac{2R\sqrt{\xi_0^2 - R^2}\boldsymbol{a}_i}{\pi\xi_0^2(2\xi_0^2 - a_0^2 - R^2 - d^2)}, \tag{3.24}$$

where $\alpha_q = C_d/(C_d + C_w)$, $\alpha_C = e^2/(\kappa R\hbar\omega_x)$, and $\tilde{\boldsymbol{r}}_i = \boldsymbol{r}_i/\lambda_i$ (λ_i is the QD size along the i-th direction). $\boldsymbol{a}_i$ are the vectors that define the position of the QDs with respect to the nearby disc center, see Fig. 3.8. Note that the expressions for the disc (C_d) and wire (C_w) capacitances, *resp.* are given by

$$C_d = 2R/\pi, \tag{3.25}$$

$$C_w = \frac{L}{2\ln(L/R_w)}, \tag{3.26}$$

where R is the radius of the disk, R_w is the radius of the wire and L is the length of the wire.

In order to obtain the solution of Eq. (3.22), we note that even a slight ellipticity ($|\omega_x^2 - \omega_y^2| \gg \max[(\hat{\Omega}_{12})_{xy}^2, (\hat{\Omega}_{12})_{yx}^2]$) of the QDs causes the motion in the x- and y-direction to be decoupled. Having in mind that $(\hat{\Omega}_{12})_{yx,xy}^2/\omega_{x,y}^2 \sim 10^{-3} - 10^{-4}$, we conclude that such a ellipticity is unavoidable in realistic experimental devices. Thus, we put off-diagonal elements of the $\hat{\Omega}_{12}$ matrix to zero and obtain the solutions

$$\begin{aligned} \boldsymbol{p}_{1,2}^i(t) = {} & \pm\boldsymbol{p}_a^i\cos(\boldsymbol{\omega}_+^i t) + \boldsymbol{p}_s^i\cos(\boldsymbol{\omega}_-^i t) \mp \\ & \mp m^*\boldsymbol{r}_a^i\boldsymbol{\omega}_+^i\sin(\boldsymbol{\omega}_+^i t) - m^*\boldsymbol{r}_s^i\boldsymbol{\omega}_-^i\sin(\boldsymbol{\omega}_-^i t), \end{aligned} \tag{3.27}$$

herein the notation $\boldsymbol{r}_{s,a} = (\boldsymbol{r}_1 \pm \boldsymbol{r}_2)/2$, $\boldsymbol{p}_{s,a} = (\boldsymbol{p}_1 \pm \boldsymbol{p}_2)/2$ and $\boldsymbol{\omega}_\pm = \left(\sqrt{\omega_x^2 \pm (\hat{\Omega}_{12})^2_{xx}}, \sqrt{\omega_y^2 \pm (\hat{\Omega}_{12})^2_{yy}}\right)$ has been introduced. In the previous formula, a superscript of a vector denotes the corresponding component of the vector.

Next, the obtained solutions are inserted into Eq. (3.17). Finally, after performing the integration over time one obtains the effective spin-spin coupling for arbitrary orientation of the magnetic field

$$\begin{aligned} H_{s-s} &= \sum_{i=x,y} \frac{m^* \omega_{i,12}^2 E_{Z1}^2 (\boldsymbol{l}_1 \times (\boldsymbol{l}_1 \times \boldsymbol{\gamma}_i)) \cdot \boldsymbol{\sigma}_1 (\boldsymbol{\sigma}_2 \cdot \boldsymbol{\gamma}_i)}{4(\omega_x^2 - E_{Z1}^2)(\omega_x^2 - E_{Z2}^2)} \\ &\quad +1 \leftrightarrow 2, \end{aligned} \tag{3.28}$$

where $\boldsymbol{\gamma}_x = (\beta \cos 2\gamma, -\alpha - \beta \cos 2\gamma, 0)$, $\boldsymbol{\gamma}_y = (\alpha - \beta \sin 2\gamma, -\beta \cos 2\gamma, 0)$, and $\boldsymbol{l}_i = \boldsymbol{B}_i/B$. For simplicity of notation, $\boldsymbol{\gamma}_x$ is referred to as $\boldsymbol{\gamma}$ in the main text.

Few remarks should be made herein for the result in Eq. (3.28). First of all, from Eq. (3.24) we see that $\hat{\Omega}_{12} \propto \boldsymbol{a}_1 \otimes \boldsymbol{a}_2$, accordingly, the two terms in the sum of Eq. (3.28) are proportional to $\cos\alpha_1 \cos\alpha_2$ and $\sin\alpha_1 \sin\alpha_2$— the angles α_i are being depicted in Fig. 3.8. When only Rashba SOI is present in the material, the coefficients in front of the two terms are equal and the coupling is proportional to $\boldsymbol{a}_1 \cdot \boldsymbol{a}_2$. This gives yet another efficient switching mechanism thereby, when the QDs are rotated in such a way that the two vectors are orthogonal ($\boldsymbol{a}_1 \cdot \boldsymbol{a}_2 = 0$).[3]

3.B SPIN-SPIN COUPLING - the hybrid system

We start from the Hamiltonian of the system and then apply the Schrieffer-Wolff transformation to remove the first order SOI term (present only in the single QD). The electrostatic potential V is again expanded around the minimum

$$\begin{aligned} V(\boldsymbol{r}_e, \boldsymbol{r}_1, \boldsymbol{r}_2) &= V(\boldsymbol{r}_e, \boldsymbol{r}_1) + V(\boldsymbol{r}_e, \boldsymbol{r}_2) \\ &\approx m^* \sum_{i=e,1,2} (\delta\omega_x^2 x_i^2 + \delta\omega_y^2 y_i^2) \\ &\quad + m^* \omega_{x,12}^2 x_e (x_1 + x_2), \end{aligned} \tag{3.29}$$

[3] coupling is zero up to the small terms $O\left((\hat{\Omega}_{12})^2_{xy,yx}/|\omega_x^2 - \omega_y^2|\right)$

where $\boldsymbol{r}_e$, $\boldsymbol{r}_1$, and $\boldsymbol{r}_2$ are the coordinates with respect to the local minima for the electron in the single QD, and the two electrons in the DQD, respectively. The terms under the sum only renormalize the frequencies, we do not take them into account, they give only higher order (in the Coulomb energy) contributions to the final results. The last term acts as an electric field on the DQD; as has been shown in the Ref. [79], this leads to a change in the exchange splitting between the singlet and triplet states in the DQD.

$$H = H_0 + H_Z + H_{SO} + \delta\tilde{J}\tilde{x}_e \boldsymbol{S}_1 \cdot \boldsymbol{S}_2, \tag{3.30}$$

where $\delta\tilde{J}$ is given by

$$\delta\tilde{J} = \frac{3}{\sinh(2\tilde{l}^2)} \frac{\omega_{x,12}^2}{\tilde{l}\omega_D^2}\epsilon. \tag{3.31}$$

ω_D is the confinement energy in the DQD, $\tilde{l}$ is the distance between the DQD minima measured in units of a QD size. We assumed that the detuning ϵ is applied to the DQD in order to get the coupling linear in electrostatic coupling.

The Schrieffer-Wolff transformation S is given by the following expression $S = (L_0 + L_Z + L_H)^{-1} H_{SO}$. Similarly to the previous section, in order to find the inverse Liouvillian we have to solve the system of ODEs

$$\begin{aligned}
\frac{d}{dt}p_{e,x}(t) &= -m^*\omega_x^2 x_e(t) - m^*\tilde{J}\boldsymbol{S}_1 \cdot \boldsymbol{S}_2, && (3.32)\\
\frac{d}{dt}p_{e,y}(t) &= -m^*\omega_y^2 y_e(t), && (3.33)\\
\frac{d}{dt}\boldsymbol{r}_e(t) &= \boldsymbol{p}_e(t)/m^*. && (3.34)
\end{aligned}$$

The solution is easily obtained

$$\begin{aligned}
p_e^x(t) &= p_e^x \cos(\omega_x t) && (3.35)\\
&\quad -m^*\left(x_e\omega_x + \frac{\tilde{J}}{m^*\omega_x\lambda}\boldsymbol{S}_1 \cdot \boldsymbol{S}_2\right)\sin(\omega_x t),\\
p_e^y(t) &= p_e^y \cos(\omega_y t) - m^* y_e \omega_y \sin(\omega_y t). && (3.36)
\end{aligned}$$

After integration over time, the S transformation is obtained

$$\begin{aligned} -iS &= \sum_{i=x,y} \frac{m^* r_{e,i}\,(\mu^2 g^2 (\boldsymbol{B}\cdot\boldsymbol{\gamma}_i)(\boldsymbol{B}\cdot\boldsymbol{\sigma}) - 4\omega_i^2 \boldsymbol{\gamma}_i\cdot\boldsymbol{\sigma})}{8(\omega_i^2 - E_Z^2)} \\ &\quad + \frac{\mu g (\boldsymbol{B}\times\boldsymbol{\sigma})\cdot\boldsymbol{\gamma}_i p_{e,i}}{4(\omega_i^2 - E_Z^2)} \\ &\quad + \frac{\mu^2 g^2 (\boldsymbol{B}\cdot\boldsymbol{\gamma}_x)(\boldsymbol{B}\cdot\boldsymbol{\sigma}) - 4\omega_x^2 \boldsymbol{\gamma}_x\cdot\boldsymbol{\sigma}}{8\omega_x^2(\omega_x^2 - E_Z^2)\lambda} \delta\tilde{J}\boldsymbol{S}_1\cdot\boldsymbol{S}_2, \end{aligned} \tag{3.37}$$

The coupling is contained in the $[S, H_Z + \delta\tilde{J}\tilde{x}_e \boldsymbol{S}_1\cdot\boldsymbol{S}_2]$ term

$$H_{S-s} = \frac{3\mu g\ \delta\tilde{J}(\boldsymbol{\gamma}_x\times\boldsymbol{B})\cdot\boldsymbol{\sigma}}{4(\omega_x^2 - E_Z^2)\lambda}(\boldsymbol{S}_1\cdot\boldsymbol{S}_2). \tag{3.38}$$

By rewriting the last equation in the pseudo-spin space the generalization for Eq. (3.12) for arbitrary magnetic field orientation is obtained.

3.C Implementation of two-qubit gates

Two qubits interacting via the floating gate evolve according to the Hamiltonian $H = H_{S-S} + E_Z(\sigma_z^1 + \sigma_z^2)$, the sum of the qubit-qubit coupling and Zeeman term. In general these contributions do not commute, making it difficult to use the evolution to implement standard entangling gates. However, when the field is perpendicular to the 2DEG substrate, H_{S-S} takes the form of Eq. (3.8) which can be decomposed into two terms as follows,

$$\begin{aligned} H_{S-S} &= J_{12}(\Gamma_1 - i\Gamma_2\sigma_z^1)(\sigma_x^1\sigma_x^2 - \sigma_y^1\sigma_y^2)/2 \\ &+ J_{12}|\boldsymbol{\gamma}_x|^2(\sigma_x^1\sigma_x^2 + \sigma_y^1\sigma_y^2)/2. \end{aligned} \tag{3.39}$$

Here $\Gamma_1 = ((\boldsymbol{\gamma}_x)_x^2 - (\boldsymbol{\gamma}_x)_y^2)$ and $\Gamma_2 = (\boldsymbol{\gamma}_x)_x(\boldsymbol{\gamma}_x)_y$. The first of these two terms anticommutes with the Zeeman term, whereas the second commutes. As such, when $E_Z \gg J_{12}|\boldsymbol{\gamma}_x|^2$, H_{S-S} can be approximated by the second term alone,

$$H_{S-S} \approx H'_{S-S} = \frac{J_{12}|\boldsymbol{\gamma}_x|^2}{2}(\sigma_x^1\sigma_x^2 + \sigma_y^1\sigma_y^2), \tag{3.40}$$

$$H \approx H' = H'_{S-S} + E_z(\sigma_z^1 + \sigma_z^2)/2. \tag{3.41}$$

With this approximation, the coupling and Zeeman terms in H' now commute.

We consider the implementation of the gate $\sqrt{\sigma_x\sigma_x} = \exp(-i\sigma_x^1\sigma_x^2\pi/4)$, which is locally equivalent to a CNOT. The Hamiltonian H' already contains a $\sigma_x^1\sigma_x^2$ term, so implementation of the $\sqrt{\sigma_x\sigma_x}$ gate requires only that the effects of the other terms be removed by appropriate local rotations. Two possible sequences that can be used to achieve this are,

$$\begin{aligned}\sqrt{\sigma_x\sigma_x} = \quad & e^{i(\sigma_z^1+\sigma_z^2)E_z t}e^{-iH't} \\ & \sigma_x^1 e^{i(\sigma_z^1+\sigma_z^2)E_z t}e^{-iH't}\sigma_x^1, \qquad (3.42)\\ \sqrt{\sigma_x\sigma_x} = \quad & \sigma_x^2\, e^{-iH't/2}\, \sigma_x^1\sigma_x^2\, e^{-iH't/2} \\ & \sigma_x^2\, e^{-iH't/2}\, \sigma_x^1\sigma_x^2\, e^{-iH't/2}, \qquad (3.43)\end{aligned}$$

where $t = \pi/(4J_{12}|\boldsymbol{\gamma}|^2)$. The first sequence requires two applications of the qubit-qubit coupling, whereas the second requires four. The main difference is that the former removes the effects of the field through the application of corresponding z-rotations after each application of H', where the latter uses x-rotations to negate the sign of the field terms and additional applications of H' to cancel them out. The former is therefore simpler to implement, however the latter method will also cancel terms not taken into account in the approximation.

Once the $\sqrt{\sigma_x\sigma_x}$ has been implemented using either of the above sequences, the CNOT gate, C, may be applied using the appropriate local rotations,

$$C = \sqrt{\sigma_z^1}\,\sqrt{\sigma_x^2}\,\mathcal{H}^1\ \sqrt{\sigma_x\sigma_x}\ \mathcal{H}^1. \qquad (3.44)$$

Here $\mathcal{H}$ denotes the single qubit Hadamard rotation.

Since H' is an approximation of H, the above sequences will yield approximate CNOTs, C', when used with the full Hamiltonian. The success of the sequences therefore depends on the fidelity of the gates, $F(C')$. Ideally this would be defined using a minimization over all possible states of two qubits. However, to characterize the fidelity of an imperfect CNOT it is sufficient to consider the following four logical states of two qubits: $|+,0\rangle, |+,1\rangle, |-,0\rangle$, and $|-,1\rangle$. These are product states which, when acted upon by a perfect CNOT, become the four maximally entangled Bell states $|\Phi^+\rangle, |\Psi^+\rangle, |\Phi^-\rangle$, and $|\Psi^-\rangle$, respectively. As such, the fidelity of an imperfect CNOT may be defined,

$$F(C') = \min_{i\in\{+,-\},j\in\{0,1\}} |\langle i,j|C^\dagger C'|i,j\rangle|^2. \qquad (3.45)$$

The choice of basis used here ensures that $F(C')$ gives a good characterization of the properties of C' in comparison to a perfect CNOT, especially for the required task of generating entanglement.

In a realistic parameter regime it can be expected that $(\boldsymbol{\gamma}_x)_x$ and $(\boldsymbol{\gamma}_x)_y$ will be of the same order, and the qubit-qubit coupling will be a few orders of magnitude less than the Zeeman terms. To get a rough idea of what fidelities can be achieved in such cases using the schemes proposed, we average over 10^4 samples for which $(\boldsymbol{\gamma}_x)_y$ is randomly assigned values between $(\boldsymbol{\gamma}_x)_x/2$ and $3(\boldsymbol{\gamma}_x)_x/2$ according to the uniform distribution, and $J_{12}(\boldsymbol{\gamma}_x)_x/E_Z = 0.1$. This yields values of 99.33% and 99.91% for the sequences of Eq. (3.42) and Eq. (3.43), respectively. For $J_{12}(\boldsymbol{\gamma}_x)_x/E_Z = 0.01$ these improve, becoming 99.993% and 99.998%, respectively.

To compare these values to the thresholds found in schemes for quantum computation, we must first note that imperfect CNOTs in these cases are usually modelled by the perfect implementation of the gate followed by depolarizing noise at a certain probability. It is known that such noisy CNOTs can be used for quantum computation in the surface code if the depolarizing probability is less than 1.1% [20]. This corresponds to a fidelity, according to the definition above, of 99.17%. The fidelities that may be achieved in the schemes proposed here are well above this value and hence, though they do not correspond to the same noise model, we can expect these gates to be equally suitable for fault-tolerant quantum computation.

CHAPTER 4

Long-Distance Entanglement of Spin-Qubits via Ferromagnet

Adapted from:
Luka Trifunovic, Fabio L. Pedrocchi, and Daniel Loss,
"Long-Distance Entanglement of Spin-Qubits via Ferromagnet",
Phys. Rev. X **3**, 041023 (2013)

We propose a mechanism of coherent coupling between distant spin qubits interacting dipolarly with a ferromagnet. We derive an effective two-spin interaction Hamiltonian and find a regime where dynamics is coherent. Finally, we present a sequence for the implementation of the entangling CNOT gate and estimate the corresponding operation time to be a few tens of nanoseconds. A particularly promising application of our proposal is to atomistic spin-qubits such as silicon-based qubits and NV-centers in diamond to which existing coupling schemes do not apply.

4.1 Model

The system we consider consists of two spin-$\frac{1}{2}$ qubits coupled dipolarly to the ferromagnet

$$H = H_\sigma + H_\mathrm{F} + H_\mathrm{I}, \tag{4.1}$$

where H_F is for the moment unspecified Hamiltonian of the dog-bone shaped ferromagnet that is assumed to be polarized along the x-axis. We

first assume that the qubits are also polarized along the x-axis, $H_\sigma = \sum_{i=1,2} \frac{\Delta_i}{2}\sigma_i^x$, while the ferromagnet disc axes are along z, see Fig. 4.1. The magnetic dipole coupling between the ferromagnet and the spin-qubits can be written as

$$\begin{aligned} H_{\rm I} &= \frac{\mu_0\mu_b\mu}{4\pi a^3}\sum_{i=1,2}\int d\boldsymbol{r} S^x_{\boldsymbol{r}}\left[\left(\frac{3iA'_{i,\boldsymbol{r}}}{2}+\frac{3C''_{i,\boldsymbol{r}}}{4}\right)\sigma_i^+ + \text{h.c.}\right. \\ &\qquad \left. + \frac{1}{2}\left(B_{i,\boldsymbol{r}} - 3C'_{i,\boldsymbol{r}}\right)\sigma_i^x\right] \\ &\quad + S^+_{\boldsymbol{r}}\left[\left(\frac{3}{8}C'_{i,\boldsymbol{r}} - \frac{3i}{2}A''_{i,\boldsymbol{r}} + \frac{3}{8}B_{i,\boldsymbol{r}}\right)\sigma_i^+\right. \\ &\quad \left. -\frac{1}{8}\left(B_{i,\boldsymbol{r}} - 3C'_{i,\boldsymbol{r}}\right)\sigma_i^- + \left(\frac{3C''_{i,\boldsymbol{r}}}{4}+\frac{3iA'_{i,\boldsymbol{r}}}{2}\right)\sigma_i^x\right] \\ &\quad + \text{h.c}, \end{aligned} \tag{4.2}$$

where $A_{\boldsymbol{r}}$, $B_{\boldsymbol{r}}$, $C_{\boldsymbol{r}}$ are given by

$$A_{\boldsymbol{r}} = \frac{1}{a^3}\frac{r^z r^+}{r^5}\,, \tag{4.3}$$

$$C_{\boldsymbol{r}} = \frac{1}{a^3}\frac{(r^+)^2}{r^5}\,, \tag{4.4}$$

$$B_{\boldsymbol{r}} = \frac{1}{a^3}\frac{1}{r^3}\left(2 - \frac{3r^+r^-}{r^2}\right)\,, \tag{4.5}$$

with $S^\pm_{\boldsymbol{r}} = S^y_{\boldsymbol{r}} \pm iS^z_{\boldsymbol{r}}$, $\sigma^\pm = \sigma^y \pm i\sigma^z$, and lattice constant a. Here we denote the real part of a complex number with prime and the imaginary part with double prime. The operator $\boldsymbol{S}_{\boldsymbol{r}}$ describes the spin of the ferromagnet at the position $\boldsymbol{r}$.

Next, we release the assumptions about the mutual orientation of the disc axes, the axes of polarization of the ferromagnet, and the direction of the qubits splitting and assume that these can take arbitrary directions. Now the interaction Hamiltonian reads

$$\begin{aligned} H_{\rm I} =& \frac{\mu_0\mu_b\mu}{4\pi a^3}\sum_{i=1,2}\int d\boldsymbol{r} S^{\tilde{z}}_{\boldsymbol{r}}\left[a_{i,\boldsymbol{r}}\sigma_i^z + b_{i,\boldsymbol{r}}\sigma_i^+ + \text{h.c.}\right] + \\ & S^{\tilde{+}}_{\boldsymbol{r}}\left[c_{i,\boldsymbol{r}}\sigma_i^z + d_{i,\boldsymbol{r}}\sigma_i^+ + e_{i,\boldsymbol{r}}\sigma_i^-\right] + \text{h.c}, \end{aligned} \tag{4.6}$$

where $\boldsymbol{S}_{\boldsymbol{r}}$ has quantization axis along $\widetilde{z}$ and $\boldsymbol{\sigma}_{\boldsymbol{r}}$ along z. The coordinate systems (x, y, z) for the qubit $\boldsymbol{\sigma}$ and $(\widetilde{x}, \widetilde{y}, \widetilde{z})$ for the ferromagnet can be different. The expressions of the coefficients in Eq. (4.6) are now more

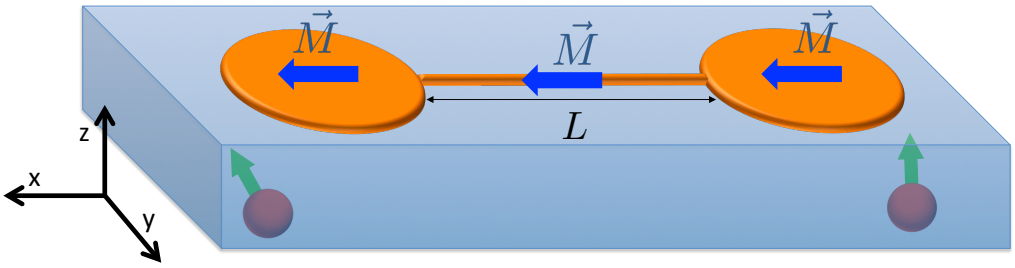

Figure 4.1: The schematics of the ferromagnetic coupler setup. The orange dog-bone shape denotes the ferromagnet that is coupled via magnetic dipole interaction to spins of nearby quantum dots (red sphere with green arrow). The ferromagnet is assumed to be a monodomain and its magnetization is denoted by blue arrows ($\boldsymbol{M}$) that can take arbitrary orientation. L is the length of the quasi-1D ferromagnetic channel that is approximately equal to the distance between the qubits. The shape of the ferromagnetic coupler is chosen such that it enables strong coupling to the spin-qubits while maintaining the spatially slowly decaying 1D susceptibility between the two discs.

complicated, nevertheless it is important to note that the integrals of these coefficients are *experimentally accessible*. The qubits can be used to measure the stray field of the ferromagnet which is given by $\boldsymbol{B}_s = (b_i', b_i'', a_i)$, where $\{a_i, \ldots, e_i\} = \frac{\mu_0 \mu}{4\pi a^3} \int d\boldsymbol{r} \{a_i, \ldots, e_i\}_{\boldsymbol{r}}$. In order to measure the remaining coefficients, one needs to apply the magnetic field externally in order to polarize sequentially the ferromagnet along the two perpendicular directions to the ferromagnet easy axis. The coefficients are obtained then by measuring again the stray fields (with the aid of the qubits) which now are given by $(d' + e', d'' - e'', c')$ and $(d'' + e'', d' - e', c'')$. Furthermore, all the results that we are going to obtain for the qubit-qubit coupling as well as for the decoherence time will depend only on the integrals of the coefficients, i.e., on $\{a_i, \ldots, e_i\}$ rather than $\{a_i, \ldots, e_i\}_{\boldsymbol{r}}$. We point out that the stray field $\boldsymbol{B}_s$ induces a splitting on the qubits that is incorporated into H_σ.

Coherent coupling

We proceed to derive the effective qubit-qubit coupling by performing a Schrieffer-Wolff (SW) transformation [97]. We assume that the excitations in the ferromagnet are gapped due to some magnetic anisotropy

(e.g. shape-anisotropy) or externally applied magnetic field, with the gap being denoted by Δ_F (for FMR dependence on externally applied magnetic field see Kittel [98]). This is important because when the qubit splitting Δ is below FMR frequency, flipping the qubit spin cannot excite magnons in the ferromagnet, thus there are only virtual magnons excited via coupling to the qubits—otherwise such a coupling would lead to strong decoherence in the qubits. Due to presence of the gap in the ferromagnet, its transversal susceptibility $\chi_\perp(\omega, \boldsymbol{r})$ decays exponentially below FMR ($\omega < \Delta_F$) with the characteristic length $l_F \propto 1/\sqrt{\Delta_F - \omega}$, thus we take into account only terms with $\omega \sim \Delta_F$, see Eqs. (4.72) and (4.74) in Appendix 4.B. Straightforward application of lowest order SW transformation accompanied by tracing out the degrees of freedom of the ferromagnet yields the effective qubit-qubit coupling Hamiltonian

$$H_{eff} = H_\sigma + \chi_\perp^{1D}(\Delta_1, L) e_1 \sigma_1^- (c_2 \sigma_2^z + d_2 \sigma_2^+ + e_2 \sigma_2^-)^\dagger + 1 \leftrightarrow 2 + \text{h.c.}, \tag{4.7}$$

where $\chi_\perp^{1D}$ is the transverse susceptibility (i.e. transverse to the $\widetilde{z}$ direction) of a quasi-1D ferromagnet, since we assumed a dog-bone shaped ferromagnet. We have neglected the longitudinal susceptibility $\chi_\parallel$ since it is suppressed by temperature. It can be seen from the above expression that in order to obtain a sizable coupling between the qubits we have to tune both the qubits close to resonance, $\Delta_i \sim \Delta_F$ (see Sec. 4.1). This can be achieved by applying an external magnetic field. Since the g-factor of the ferromagnet is generally not the same as the g-factor of the qubit, it is possible to tune the system on resonance with an external homogeneous magnetic field. The fine tuning can then be achieved by applying locally a small external magnetic field from a coil. The on-resonance requirement offers an elegant way to switch on/off the coupling between the qubits. The idea is to tune the qubit splitting close to resonance for switching on the mediated interaction and to tune it off resonance to switch off the mediated interaction.

The expression for the transverse susceptibility of a ferromagnet is given in Eq. (4.74) of Appendix 4.B assuming H_F to be of Heisenberg type. The derivation given therein relays on the fact that dispersion of low-laying ferromagnetic excitations (i.e. spin waves) is quadratic [99]. Note that for very long wave lengths (bigger than a micron) the excitations are so-called *dipolar spin waves* with dispersion very different from quadratic one and dependent on concrete boundary conditions [100]. Since we are considering ferromagnets with dimensions not exceeding

micron, the relevant excitations are *exchange spin waves* with quadratic dispersion which is practically independent of specific boundary conditions [100]. We note here that the FMR can increase toward the edges of the sample [101], in this case one should use ferromagnetic coupler with lateral dimensions bigger than the one quoted in Sec. 4.3 in order to have a middle region with nearly spatially independent FMR.

Special care has to be taken for the validity of the perturbation theory employed herein, since we are working close to FMR, i.e., $\Delta - \Delta_F$ has to be small but still much larger than the coupling of a qubit to an individual spin of the ferromagnet. For the perturbation theory to be valid we require the tilt of each ferromagnet spin to be sufficiently small (i.e. $\langle S^{\pm}_{\boldsymbol{r}} \rangle \ll 1$). The tilt of the central spin of the ferromagnetic disk can be estimated by the integral over the dogbone disk D

$$\langle S^{\pm}_{\boldsymbol{r}} \rangle = \int_D \chi_{\perp}(\boldsymbol{r}) B_{\perp}(\boldsymbol{r}) d\boldsymbol{r}\,, \tag{4.8}$$

where $B_{\perp}(\boldsymbol{r})$ is the perpendicular (to the magnetization direction) component of the field produced at position $\boldsymbol{r}$ by the qubit. Using cylindrical coordinates we then obtain

$$\langle S^{\pm}_{\boldsymbol{r}} \rangle \sim \frac{\mu_0 \mu_B^2}{2a} \int_0^R \rho d\rho \frac{1}{(\rho^2 + h^2)^{3/2}} \frac{S}{D\rho}, \tag{4.9}$$

where $\frac{S}{D\rho}$ is the spatial decay of the transversal susceptibility and $\frac{1}{(\rho^2+h^2)^{3/2}}$ is the decay of the dipolar field causing the perturbation of the ferromagnet. For our choice of parameters, we obtain a tilt $\langle S^{\pm}_{\boldsymbol{r}} \rangle < 10^{-7} \ll 1$. Even though each spin is just slightly tilted, we obtain a sizable coupling due to big number of spins involved in mediating the coupling.

For the sake of completeness, in Appendix 4.D we present a detailed discussion of the effective coupling mediated by the dog-bone when the qubits are exchange coupled to the ferromagnet which requires a tunnel coupling between spin qubit and ferromagnet.

Implementation of two-qubit gates

Two qubits interacting via the ferromagnet evolve according to the Hamiltonian H_{eff}, see Eq. (4.7). The Hamiltonian is therefore the sum of Zeeman terms and qubit-qubit interaction. These terms, by and large, do not commute, making it difficult to use the evolution to implement standard entangling gates. In order to obtain sizable coupling we need to assume

that the two qubits are on-resonance with each other, $\Delta_1 \simeq \Delta_2$. Now H_σ acts only in the subspace spanned by $\{|\uparrow,\uparrow\rangle, |\downarrow,\downarrow\rangle\}$ and the Zeeman splitting of the qubits is much larger than the effective qubit-qubit coupling, we can neglect the effect of H_{eff} in this part of the subspace and approximate it by its projection in the space spanned by the vectors $\{|\uparrow,\downarrow\rangle, |\downarrow,\uparrow\rangle\}$

$$H'_{\text{eff}} = H_\sigma + \alpha(\sigma_1^x\sigma_2^x - \sigma_1^y\sigma_2^y) + \beta(\sigma_1^x\sigma_2^y + \sigma_1^y\sigma_2^x), \tag{4.10}$$

where $\alpha = -8\text{Re}(e_1e_2^*)$ and $\beta = -4\text{Re}(d_1e_2^* + d_2e_1^*)$. Within this approximation, the coupling in H'_{eff} and the Zeeman terms now commute. From here we readily see that the stray field components, a_i, b_i, as well as the coefficient c_i do not determine the operation time of the two qubit gates—the operation time depends only on d_i and e_i. To proceed we perform a rotation on the second qubit around the z-axis by an angle $\tan\theta = \beta/\alpha$ and arrive at the Hamiltonian

$$H'_{\text{eff}} = H_\sigma + \sqrt{\alpha^2+\beta^2}(\sigma_1^x\tilde{\sigma}_2^x - \sigma_1^y\tilde{\sigma}_2^y). \tag{4.11}$$

We consider the implementation of the iSWAP gate

$$U_{\text{iSWAP}} = e^{i(\sigma_1^x\tilde{\sigma}_2^x + \sigma_1^y\tilde{\sigma}_2^y)\pi/4}, \tag{4.12}$$

which can be used to implement the CNOT gate [102]. The Hamiltonian H' can be transformed to the desired form by changing the sign of $\sigma_1^x\tilde{\sigma}_2^x$ term. This is achieved with the following sequence [103]

$$U_{\text{iSWAP}} = \sigma_1^y e^{iH_\sigma t} e^{-iH'_{\text{eff}}t}\sigma_1^y, \tag{4.13}$$

where $t = \pi/(4\sqrt{\alpha^2+\beta^2})$. When iSWAP is available, the CNOT gate can be constructed in the standard way [104]

$$U_{CNOT} = e^{-i\frac{\pi}{4}\sigma_1^z} e^{i\frac{\pi}{4}\sigma_2^x} e^{i\frac{\pi}{4}\sigma_2^z} U_{\text{i}SWAP} e^{-i\frac{\pi}{4}\sigma_1^x} U_{\text{i}SWAP} e^{i\frac{\pi}{4}\sigma_2^z}. \tag{4.14}$$

Since H'_{eff} is an approximation of H_{eff}, the above sequence will yield approximate CNOT, U'_{CNOT}, when used with the full the Hamiltonian. The success of the sequences therefore depends on the fidelity of the gates, $F(U'_{CNOT})$. Ideally this would be defined using a minimization over all possible states of two qubits. However, to characterize the fidelity of an imperfect CNOT it is sufficient to consider the following four logical states of two qubits [60]: $|+,\uparrow\rangle, |+,\downarrow\rangle, |-,\uparrow\rangle$, and $|-,\downarrow\rangle$. These are product states which, when acted upon by a perfect CNOT, become the

four maximally entangled Bell states $|\Phi^+\rangle, |\Psi^+\rangle, |\Phi^-\rangle$, and $|\Psi^-\rangle$, respectively. As such, the fidelity of an imperfect CNOT may be defined,

$$F(U'_{\mathrm{CNOT}}) = \min_{i\in\{+,-\},j\in\{0,1\}} |\langle i,j|U^\dagger_{\mathrm{CNOT}}U'_{\mathrm{CNOT}}|i,j\rangle|^2. \tag{4.15}$$

The choice of basis used here ensures that $F(U'_{CNOT})$ gives a good characterization of the properties of U'_{CNOT} in comparison to a perfect CNOT, especially for the required task of generating entanglement. For realistic parameters, with the Zeeman terms two order of magnitude stronger than the qubit-qubit coupling, the above sequence yields fidelity for the CNOT gate of 99.976%.

To compare these values to the thresholds found in schemes for quantum computation, we must first note that imperfect CNOTs in these cases are usually modeled by the perfect implementation of the gate followed by depolarizing noise at a certain probability. It is known that such noisy CNOTs can be used for quantum computation in the surface code if the depolarizing probability is less than 1.1% [20]. This corresponds to a fidelity, according to the definition above, of 99.17%. The fidelities that may be achieved in the schemes proposed here are well above this value and hence, though they do not correspond to the same noise model, we can expect these gates to be equally suitable for fault-tolerant quantum computation.

4.2 Decoherence

In this section we study the dynamics of a single qubit coupled to the ferromagnet. In particular we want to answer the question whether the two-qubit dynamics studied in the previous section is *coherent*, i.e., whether the decoherence time solely due to the dipolar coupling to the ferromagnet is larger than the qubit operation time.

A ferromagnet has two types of fluctuations—longitudinal and transverse ones. The longitudinal noise stems from fluctuations of the longitudinal $S^{\tilde{z}}$ component (we recall that the ferromagnet is polarized along $\tilde{z}$), while the transverse one is related to fluctuations of $S^{\pm}$. In what follows we study these two noise sources separately. The general noise model that describes both types of noise is then given by

$$H = H_{\mathrm{F}} + \frac{\Delta}{2}\sigma^z + \sigma^z \otimes X + \sigma^+ \otimes Y + \mathrm{h.c.}, \tag{4.16}$$

where the ferromagnet operators X (Y) with zero expectation value couple longitudinally (transversally) to the qubit. The noise model given in Eq. (4.16) leads to the following relaxation and decoherence times within Born-Markov approximation [105]

$$T_1^{-1} = S_Y(\omega = \Delta), \tag{4.17}$$

$$T_2^{-1} = \frac{1}{2}T_1^{-1} + S_X(\omega = 0), \tag{4.18}$$

where we defined the fluctuation power spectrum of an operator A in the following way, $S_A(\omega) = \int dt e^{-i\omega t}\{A^\dagger(t), A(0)\}$. In order to obtain expression for the decoherence times we need a specific model for the ferromagnet Hamiltonian, herein taken to be a gapped Heisenberg model $H_F = -J\sum_{\langle \boldsymbol{r},\boldsymbol{r}'\rangle} \boldsymbol{S}_{\boldsymbol{r}} \cdot \boldsymbol{S}_{\boldsymbol{r}'} + \Delta_F \sum_{\boldsymbol{r}} S^z_{\boldsymbol{r}'}$, J being the exchange coupling and Δ_F the excitation gap.

Longitudinal noise

The power spectrum of longitudinal fluctuations is given by the following expression for $\omega \gg T$ (see Appendix 4.C and in particular Eq. (4.85))

$$S_\parallel^{3D}(\omega) = \frac{\alpha\sqrt{\beta\omega}}{2\beta^2 D^3} e^{-\beta\Delta_F} \coth(\beta\omega/2), \tag{4.19}$$

while for $\omega \ll T$ (see Appendix 4.C, Eq. (4.87))

$$S_\parallel^{3D}(\omega) = \frac{\ln(1+n_{\boldsymbol{k}=0})}{16\pi\beta D^3}\omega \coth(\beta\omega/2), \tag{4.20}$$

where $D = 2JS$. We study transverse (Y) and longitudinal (X) coupling separately. In the case of longitudinal coupling we solve the problem exactly while we treat the transverse coupling within the framework of perturbation theory.

Transverse coupling to longitudinal noise

The part of the Hamiltonian that describes transverse coupling to the longitudinal noise reads

$$H = H_F + \sigma^+ \otimes \int d\boldsymbol{r} b_{1,\boldsymbol{r}} S^{\tilde{z}}_{\boldsymbol{r}} + \text{h.c.} \tag{4.21}$$

Using Eq. (4.18) and the inequality

$$S_{\parallel}^{3D}(\omega, \boldsymbol{r}) \leq S_{\parallel}^{3D}(\omega, \boldsymbol{r}=0),$$

we obtain the relaxation time

$$\begin{aligned} T_1^{-1} &= \int d\boldsymbol{r} d\boldsymbol{r}' b_{1,\boldsymbol{r}} b_{1,\boldsymbol{r}'} S_{\parallel}^{3D}(\Delta, \boldsymbol{r} - r') \\ &\leq \int d\boldsymbol{r} d\boldsymbol{r}' b_{1,\boldsymbol{r}} b_{1,\boldsymbol{r}'} S_{\parallel}^{3D}(\Delta, \boldsymbol{r}=0) \\ &= b_1^2 S_{\parallel}^{3D}(\Delta), \end{aligned} \tag{4.22}$$

where expression for $S_{\parallel}^{3D}(\Delta)$ is given in Eq. (4.19) since $\Delta \gg T$. The above expression readily shows that relaxation time can be tailored arbitrarily small by choosing the ratio T/Δ_F sufficiently small.

Longitudinal coupling to longitudinal noise

Here we consider only longitudinal coupling to longitudinal noise thus the Hamiltonian reads

$$H = H_F + \sigma^z \otimes V + \epsilon\, \sigma_z\,, \tag{4.23}$$

with ϵ the qubit splitting and $V = \int d\boldsymbol{r} a_{1,\boldsymbol{r}} S_{\boldsymbol{r}}^{\tilde{z}}$. To simplify the problem further [106], we substitute $S_{\boldsymbol{r}}^{\tilde{z}} \to S_{\boldsymbol{r}}^{\tilde{x}}$ since the latter is linear in magnon operators while the former is quadratic. When the final formula for the decoherence time is obtained we substitute back the power spectrum of $S_{\boldsymbol{r}}^{\tilde{z}}$ instead of $S_{\boldsymbol{r}}^{\tilde{x}}$.

In order to study decoherence we have to calculate the following quantity [106]

$$\begin{aligned} \langle \sigma^-(t) \rangle = e^{i\varepsilon t/\hbar} \langle \sigma^-(0) \rangle \times \\ \times \left\langle \tilde{T} \exp\left(i \int_0^t V dt' \right) T \exp\left(i \int_0^t V dt' \right) \right\rangle\,, \end{aligned} \tag{4.24}$$

with ($\tilde{T}$) T the (anti-) time ordering operator. The average in the above expression can be evaluated using a cluster expansion [107] and since the perturbation V is linear in the bosonic operators, only the second order cluster contributes. Therefore, the final exact result for the time-evolution of $\sigma^-(t)$ reads

$$\langle \sigma^-(t) \rangle = e^{i\varepsilon t/\hbar} \langle \sigma^-(0) \rangle e^{-\frac{1}{2}\int_0^t \int_0^t S(t_2 - t_1) dt_1 dt_2}\,, \tag{4.25}$$

where $S(t) = \langle [V(t), V(0)]_+ \rangle$. After performing the Fourier transformation we obtain

$$\langle \sigma_-(t) \rangle = e^{i\varepsilon t/\hbar} \langle \sigma_-(0) \rangle \times \times \exp\left(-\frac{1}{2} \int \frac{d\omega}{2\pi} S(\omega) \frac{\sin^2(\omega t/2)}{(\omega/2)^2} \right) . \tag{4.26}$$

Note that this expression is of exactly the same form as the one for a *classical* Gaussian noise [108]. Now we substitute back $S^{\tilde{x}}_{\boldsymbol{r}} \to S^{\tilde{z}}_{\boldsymbol{r}}$

$$\langle \sigma^-(t) \rangle = e^{i\varepsilon t/\hbar} \langle \sigma^-(0) \rangle \times \times \exp\left(-\frac{1}{2} \int \frac{d\omega}{2\pi} \int d\boldsymbol{r} d\boldsymbol{r}' a_{1,\boldsymbol{r}} a_{1,\boldsymbol{r}'} S^{3D}_{\parallel}(\omega, \boldsymbol{r} - r') \frac{\sin^2(\omega t/2)}{(\omega/2)^2} \right) . \tag{4.27}$$

For long times $t \gg \hbar/T$ the dynamics is of the form

$$\langle \sigma^-(t) \rangle \sim e^{-a_1^2 T^2 \ln(1+n_{k=0}) t/(8\pi D^3) + i\Delta t}, \tag{4.28}$$

where we have used the inequality $S^{3D}_{\parallel}(\omega, \boldsymbol{r}) \leq S^{3D}_{\parallel}(\omega, \boldsymbol{r} = 0)$. Thus, this type of decoherence can be suppressed by choosing the ratio T/Δ_F sufficiently small.

Transverse noise

The power spectrum of transverse fluctuations of the ferromagnet vanishes for $\omega < \Delta_F$ (see Eqs. (4.75) and (4.73) in Appendix 4.B),

$$S^{3D}_{\perp}(\omega) = 0 , \qquad \omega < \Delta_F , \tag{4.29}$$

$$S^{3D}_{\perp}(\omega) = \frac{S\sqrt{\omega - \Delta_F}}{D^{3/2}} \coth(\beta\omega/2), \quad \omega > \Delta_F. \tag{4.30}$$

Since the transverse fluctuations are gapped and the precession frequency of the qubits is below the gap, this noise source does not contribute in the second order (Born approximation) because only virtual magnons can be excited. In this section we choose the quantization axes such that qubit splitting is along the z-axis, while the ferromagnet is polarized along the x-axis (see Fig. 4.1), this is done solely for simplicity and all the conclusions are also valid for the most general case. The Hamiltonian of the

coupled system is of the form Eq. (4.16) with operators X (Y)

$$X = \frac{i}{2}\int d\boldsymbol{r} c_{\boldsymbol{r}}(S^+_{\boldsymbol{r}} - S^-_{\boldsymbol{r}}), \tag{4.31}$$

$$Y^+ = -\frac{i}{8}\int d\boldsymbol{r}(a_{\boldsymbol{r}}S^+_{\boldsymbol{r}} + b_{\boldsymbol{r}}S^-_{\boldsymbol{r}}), \tag{4.32}$$

with $S^{\pm}_{\boldsymbol{r}} = S^y_{\boldsymbol{r}} \pm iS^z_{\boldsymbol{r}}$ and the definitions

$$a_{\boldsymbol{r}} = B_{\boldsymbol{r}} + 3C_{\boldsymbol{r}} - 6A_{\boldsymbol{r}}, \tag{4.33}$$

$$b_{\boldsymbol{r}} = B_{\boldsymbol{r}} + 3C_{\boldsymbol{r}} + 6A_{\boldsymbol{r}}, \tag{4.34}$$

$$c_{\boldsymbol{r}} = B_{\boldsymbol{r}} - 3A''_{\boldsymbol{r}}, \tag{4.35}$$

where $A_{\boldsymbol{r}}$, $B_{\boldsymbol{r}}$, $C_{\boldsymbol{r}}$ are given by Eqs. (5.24)-(5.26). To proceed further we perform the SW transformation on the Hamiltonian given by Eq. (4.16). We ignore the Lamb and Stark shifts and obtain the effective Hamiltonian

$$H = H_{\rm F} + \frac{\Delta}{2}\sigma^z + \sigma^z \otimes \tilde{X}_2 + \sigma^+ \otimes \tilde{Y}_2^- + \sigma^- \otimes \tilde{Y}_2^+, \tag{4.36}$$

where

$$\tilde{X}_2 = X_2 - \langle X_2\rangle, \tag{4.37}$$

$$\tilde{Y}_2^{\pm} = Y_2^{\pm} - \langle Y_2^{\pm}\rangle, \tag{4.38}$$

with the following notation

$$X_2 = 4(Y^+_{\Delta}Y^- + Y^+Y^-_{\Delta}), \tag{4.39}$$

$$Y_2^+ = 2(Y^+_{\Delta}X - X_0Y^+), \tag{4.40}$$

$$X_{\omega} = \frac{i}{2}\int d\boldsymbol{r}\boldsymbol{r}'\chi_{\perp}(\omega, \boldsymbol{r}-\boldsymbol{r}')c_{\boldsymbol{r}}(S^+_{\boldsymbol{r}'} - S^-_{\boldsymbol{r}'}), \tag{4.41}$$

$$Y^+_{\omega} = -\frac{i}{8}\int d\boldsymbol{r}\boldsymbol{r}'\chi_{\perp}(\omega, \boldsymbol{r}-\boldsymbol{r}')(a_{\boldsymbol{r}}S^+_{\boldsymbol{r}'} + b_{\boldsymbol{r}}S^-_{\boldsymbol{r}'}). \tag{4.42}$$

The model given by Eq. (4.16) yields the following expressions for the relaxation and decoherence times

$$T_1^{-1} = S_{\tilde{Y}_2^-}(\omega = \Delta), \tag{4.43}$$

$$T_2^{-1} = \frac{1}{2}T_1^{-1} + S_{\tilde{X}_2}(\omega = 0). \tag{4.44}$$

After a lengthy calculation we obtain the following expressions for T_1 and T_2 (see Appendix 4.E for a detailed derivation)

$$T_1^{-1} \leq \frac{B^4 S^2 \Delta_F^2}{2D^3} \left(\frac{1}{\Delta_F} + \frac{1}{\Delta_F - \Delta} \right)^2 f\left(\frac{\Delta}{\Delta_F}, \beta \Delta_F \right), \tag{4.45}$$

$$T_2^{-1} \leq \frac{B^4 S^2 \Delta_F^2}{4D^3} \left(\frac{1}{\Delta_F} + \frac{1}{\Delta_F - \Delta} \right)^2 f\left(\frac{\Delta}{\Delta_F}, \beta \Delta_F \right) + \frac{B^4 S^2 \Delta_F^2}{2D^3 (\Delta_F - \Delta)^2} f\left(0, \beta \Delta_F\right), \tag{4.46}$$

with the function $f(x, y)$ defined as follows

$$f(x, y) = \int_{1+x}^{\infty} dz \frac{\sqrt{z-1}}{e^{yz} - 1} \frac{\sqrt{z-x-1}}{e^{y(z-x)} - 1}. \tag{4.47}$$

It is important to note that $f(x, y) \propto e^{-y}$, i.e., we obtain, as for the longitudinal noise, that the effect of transverse fluctuations can be suppressed by choosing the temperature much smaller than the excitation gap of the ferromagnet. As anticipated, Eq. (4.46) shows that the transverse noise becomes more important as the resonance is approached ($\Delta \sim \Delta_F$).

4.3 Estimates

In this section we give numerical estimates for the coherent coupling mediated by the ferromagnet and the associated decoherence times. These estimates are valid for both silicon-based and NV-center qubits.

Let us assume that the qubits lie close to the disc axis at a distance $h = 25\, nm$ below the disc and that the ferromagnet has in-plane polarization (along x-axis), the thickness of the disk is $20\, nm$, its radius $50\, nm$, and the lattice constant 4Å. In this case the stray field reaches values up to $10\, mT$ and this is not detrimental since NV-centers can tolerate such small fields perpendicular to the polarization axis; stronger magnetic fields would destroy the ability to manipulate NV-centers optically [9]. For these cases and when the qubit splitting is brought close to resonance, $\Delta_F - \Delta \approx 10^{-2} \mu eV$, we obtain operation times on the order of tens of nanoseconds when the qubits are separated by a distance of about $1\, \mu m$. The decoherence times T_2 depend strongly on the ratio $k_B T / \Delta_F$ and the additional decoherence source can be made negligible

if this ratio is sufficiently small. For a magnon gap $\Delta_F = 100\,\mu eV$ and a temperature $T = 0.1\,K$, we obtain decoherence times solely due to the coupling to the ferromagnet that are much bigger than the operation times and the typical decoherence times of the qubits.

4.4 Conclusions

We propose a scheme to coherently couple two *atomistic* qubits separated over distances on the order of a micron. We present a sequence for the implementation of the entangling CNOT gate and obtain operation times on the order of a few tens of nanoseconds. We show that there is a regime where all fluctuations of the ferromagnet are under control and the induced decoherence is non-detrimental: this is achieved when the temperature is smaller than the excitation gap of the ferromagnet. The main novel aspect of our proposal is its applicability to the technologically very important silicon qubits and NV-centers to which previous coupling methods do not apply.

4.5 Acknowledgements

We would like to thank A. Yacoby, A. Morello, R. Warburton and T. van der Sar for useful discussions. This work was supported by SNF, NCCR QSIT, and IARPA.

4.A Holstein-Primakoff transformation

For the sake of completeness we derive in this Appendix explicit expressions for the different spin-spin correlators used in this work

$$C^{\alpha\beta}(\omega, \boldsymbol{q}) = \langle S^{\alpha}_{\boldsymbol{q}}(\omega) S^{\beta}_{-\boldsymbol{q}}(0) \rangle \,. \tag{4.48}$$

For this purpose, we make use of a Holstein-Primakoff transformation

$$\begin{aligned} S_i^z &= -S + n_i, \;\; S_i^- = \sqrt{2S}\sqrt{1 - \frac{n_i}{2S}} a_i, \;\; \text{and} \\ S_i^+ &= \left(S_i^-\right)^\dagger, \end{aligned} \tag{4.49}$$

in the limit $n_i \ll 2S$, with a_i satisfying bosonic commutation relations and $n_i = a_i^\dagger a_i$ [109]. The creation operators $a_i^\dagger$ and annihilation operators a_i satisfy bosonic commutation relations and the associated particles are called magnons. The corresponding Fourier transforms are straightforwardly defined as $a_{\boldsymbol{q}}^\dagger = \frac{1}{\sqrt{N}} \sum_i e^{-i\boldsymbol{q}\cdot\boldsymbol{R}_i} a_i$. In harmonic approximation, the Heisenberg Hamiltonian H_F reads

$$H_F \approx \sum_{\boldsymbol{q}} \epsilon_{\boldsymbol{q}} a_{\boldsymbol{q}}^\dagger a_{\boldsymbol{q}} \,, \tag{4.50}$$

where $\epsilon_{\boldsymbol{q}} = \omega_{\boldsymbol{q}} + \Delta_F = 4JS[3 - (\cos(q_x) + \cos(q_y) + \cos(q_z))] + \Delta_F$ is the spectrum for a cubic lattice with lattice constant $a = 1$ and the gap Δ_F is induced by the external magnetic field or anisotropy of the ferromagnet.

4.B Transverse correlators $\langle S_{\boldsymbol{q}}^+(t) S_{-\boldsymbol{q}}^-(0)\rangle$

Let us now define the Fourier transforms in the harmonic approximation

$$\begin{aligned} S_{\boldsymbol{q}}^+ &= \frac{1}{\sqrt{N}} \sum_i e^{-i\boldsymbol{q}\boldsymbol{r}_i} S_i^+ = \frac{\sqrt{2S}}{\sqrt{N}} \sum_i e^{-i\boldsymbol{q}\boldsymbol{r}_i} a_i^\dagger = \sqrt{2S} a_{-\boldsymbol{q}}^\dagger \,, \\ S_{-\boldsymbol{q}}^- &= \frac{1}{\sqrt{N}} \sum_i e^{i\boldsymbol{q}\boldsymbol{r}_i} S_i^- = \frac{\sqrt{2S}}{\sqrt{N}} \sum_i e^{i\boldsymbol{q}\boldsymbol{r}_i} a_i = \sqrt{2S} a_{-\boldsymbol{q}} \,. \end{aligned} \tag{4.51}$$

From this it directly follows that

$$\begin{aligned} C^{+-}(t, \boldsymbol{q}) &= \langle S_{\boldsymbol{q}}^+(t) S_{-\boldsymbol{q}}^-(0)\rangle \\ &= 2S \langle a_{-\boldsymbol{q}}^\dagger(t) a_{-\boldsymbol{q}}\rangle = 2S e^{i\epsilon_{\boldsymbol{q}} t} n_{\boldsymbol{q}} \,, \end{aligned} \tag{4.52}$$

with $\epsilon_{\boldsymbol{q}} \approx D\boldsymbol{q}^2 + \Delta_F$ in the harmonic approximation.

The Fourier transform is then simply given by

$$\begin{aligned} C^{+-}(\omega, \boldsymbol{q}) &= \frac{1}{\sqrt{2\pi}} \int_{-\infty}^{\infty} dt e^{-i\omega t} C^{+-}(t, \boldsymbol{q}) \\ &= \underbrace{\frac{1}{\sqrt{2\pi}} \int_{-\infty}^{\infty} dt e^{i(\epsilon_{\boldsymbol{q}} - \omega)t}}_{\sqrt{2\pi}\delta(\epsilon_{\boldsymbol{q}} - \omega)} 2S n_{\boldsymbol{q}} \\ &= \sqrt{2\pi} 2S \delta(\epsilon_{\boldsymbol{q}} - \omega) \frac{1}{e^{\beta\omega} - 1} \,. \end{aligned} \tag{4.53}$$

The corresponding correlator in real space is then simply given by ($q := |\boldsymbol{q}|$)

$$\begin{aligned} C^{+-}(\omega,\boldsymbol{r}) &= \frac{1}{(2\pi)^{3/2}}\int d\boldsymbol{q}e^{i\boldsymbol{q}\boldsymbol{r}}C^{+-}(\omega,\boldsymbol{q}) \\ &= \frac{\sqrt{2\pi}}{(2\pi)^{3/2}}2S\frac{1}{e^{\beta\omega}-1}\int d\boldsymbol{q}\delta(D\boldsymbol{q}^2+\Delta_F-\omega)e^{i\boldsymbol{q}\boldsymbol{r}} \\ &= \frac{2S}{e^{\beta\omega}-1}\int_{-1}^{1}\int_0^\infty dqdxq^2\delta(Dq^2+\Delta_F-\omega)e^{iqrx} \\ &= \frac{4S}{r}\frac{1}{e^{\beta\omega}-1}\int_0^\infty dqq\delta(Dq^2+\Delta_F-\omega)\sin(qr)\,. \end{aligned} \tag{4.54}$$

Let us now perform the following substitution

$$y = Dq^2, \tag{4.55}$$

which gives for $\omega > \Delta_F$

$$\begin{aligned} C^{+-}(\omega,\boldsymbol{r}) = \frac{4S/r}{2D(e^{\beta\omega}-1)}\int_0^\infty dy\delta(y+\Delta_F-\omega)\times \\ \times\sin\left(\sqrt{\frac{y}{D}}r\right) \\ = \frac{2S}{D}\frac{1}{e^{\beta\omega}-1}\frac{\sin(\sqrt{(\omega-\Delta_F)/D}r)}{r}\,. \end{aligned} \tag{4.56}$$

We remark that

$$C^{+-}(\omega,\boldsymbol{r}) = 0, \quad \omega < \Delta_F. \tag{4.57}$$

We note the diverging behavior of the above correlation function for $\Delta_F = 0$ and $\omega \to 0$, namely

$$\frac{1}{e^{\beta\omega}-1}\frac{\sin\left(\sqrt{\frac{\omega}{D}}r\right)}{r} \to \frac{1}{\sqrt{D}\beta}\frac{1}{\sqrt{\omega}}\,. \tag{4.58}$$

Similarly, it is now easy to calculate the corresponding commutators and anticommutators. Let us define

$$S_\perp(t,\boldsymbol{q}) := \frac{1}{2}\{S^+_{\boldsymbol{q}}(t), S^-_{-\boldsymbol{q}}(0)\}\,. \tag{4.59}$$

It is then straightforward to show that

$$S_\perp(t,\boldsymbol{q}) = Se^{i\epsilon_{\boldsymbol{q}}t}(1+2n_{\boldsymbol{q}})\,, \tag{4.60}$$

and therefore

$$\begin{aligned} S_\perp(\omega,\boldsymbol{q}) &= \frac{S}{\sqrt{2\pi}}\int_{-\infty}^{\infty} e^{i(\epsilon_{\boldsymbol{q}}-\omega)t}(1+2n_{\boldsymbol{q}}) \\ &= S\sqrt{2\pi}\delta(\epsilon_{\boldsymbol{q}}-\omega)\left(1+2\frac{1}{e^{\beta\omega}-1}\right). \end{aligned} \tag{4.61}$$

Following essentially the same steps as the one performed above, we obtain the 3D real space anticommutator for $\omega > \Delta_F$

$$\begin{aligned} S_\perp^{\rm 3D}(\omega,\boldsymbol{q}) &= S\coth(\beta\omega/2)\times \qquad (4.62)\\ &\quad \times\int_{-1}^{1}\int_0^\infty dxdqq^2 e^{iqrx}\delta(\epsilon_{\boldsymbol{q}}-\omega) \\ &= \frac{S}{D}\coth(\beta\omega/2)\frac{\sin(\sqrt{(\omega-\Delta_F)/D}r)}{r}. \end{aligned} \tag{4.63}$$

Let us now finally calculate the transverse susceptibility defined as

$$\chi_\perp(t,\boldsymbol{q}) = -i\theta(t)[S^+_{\boldsymbol{q}}(t), S^-_{-\boldsymbol{q}}(0)]\,. \tag{4.64}$$

As before, in the harmonic approximation, one finds

$$\chi_\perp(t,\boldsymbol{q}) = i\theta(t)2Se^{i\epsilon_{\boldsymbol{q}}t}\,. \tag{4.65}$$

In the frequency domain, we then have

$$\begin{aligned} \chi_\perp(\omega,\boldsymbol{q}) &= \frac{2iS}{\sqrt{2\pi}}\int_0^\infty dt e^{i(\epsilon_{\boldsymbol{q}}-\omega)t-\eta t} \qquad (4.66)\\ &= -\frac{2S}{\sqrt{2\pi}}\frac{1}{\epsilon_{\boldsymbol{q}}-\omega+i\eta}\,, \end{aligned}$$

and thus in the small $\boldsymbol{q}$ expansion

$$\chi_\perp(\omega,\boldsymbol{q}) = -\frac{2S}{\sqrt{2\pi}}\frac{1}{D\boldsymbol{q}^2+\Delta_F-\omega+i\eta}\,. \tag{4.67}$$

In real space, for the three-dimensional case, we obtain

$$\begin{aligned} \chi_\perp^{\rm 3D}(\omega,\boldsymbol{r}) &= -\frac{2S}{\sqrt{2\pi}}\frac{2\pi}{(2\pi)^{3/2}}\int_0^\infty\int_{-1}^1 dxdqq^2\frac{1}{D\boldsymbol{q}^2+\Delta_F-\omega+i\eta}e^{iqrx} \\ &= -\frac{4S}{\sqrt{2\pi}}\frac{2\pi}{(2\pi)^{3/2}}\frac{1}{r}\int_0^\infty dqq\frac{1}{Dq^2+\Delta_F-\omega+i\eta}\sin(qr) \qquad (4.68) \end{aligned}$$

Making use of the Plemelj formula we obtain for $\omega > \Delta_F$

$$\begin{aligned}\chi_\perp^{\rm 3D}(\omega,\boldsymbol{r}) &= -\frac{2S}{\sqrt{2\pi}}\frac{2\pi}{(2\pi)^{3/2}}\frac{1}{r}\int_{-\infty}^{\infty}dqq\frac{1}{Dq^2+\Delta_F-\omega+i\eta}\sin(qr)\\ &= -\frac{2S}{\sqrt{2\pi}}\frac{2\pi}{(2\pi)^{3/2}}\frac{1}{r}P\int_{-\infty}^{\infty}dq\frac{q}{Dq^2+\Delta_F-\omega}\sin(qr)\\ &\quad +i\frac{2S}{\sqrt{2\pi}}\frac{2\pi^2}{(2\pi)^{3/2}}\frac{1}{r}\int_{-\infty}^{\infty}dqq\delta(Dq^2+\Delta_F-\omega)\sin(qr)\\ &= -\frac{S}{D}\frac{\cos(r\sqrt{(\omega-\Delta_F)/D})}{r}+i\frac{S}{2D}\frac{\sin(\sqrt{(\omega-\Delta_F)/D}r)}{r}\,.\end{aligned} \tag{4.69}$$

It is worth pointing out that the imaginary part of the susceptibility vanishes,

$$\chi_\perp^{\rm 3D}(\omega,\boldsymbol{r})'' = 0, \quad \omega < \Delta_F, \tag{4.70}$$

and therefore the susceptibility is purely real and takes the form of a Yukawa potential

$$\chi_\perp^{\rm 3D}(\omega,\boldsymbol{r}) = -\frac{S}{D}\frac{e^{-r/l_F}}{r}, \quad \omega < \Delta_F, \tag{4.71}$$

where

$$l_F = \sqrt{\frac{D}{\Delta_F-\omega}}. \tag{4.72}$$

Note also that the imaginary part of the transverse susceptibility satisfies the well-know fluctuation-dissipation theorem

$$S_\perp^{\rm 3D}(\omega,\boldsymbol{r}) = \coth(\beta\omega/2)\chi_\perp^{\rm 3D}(\omega,\boldsymbol{r})''\,. \tag{4.73}$$

In three dimensions the susceptibility decay as $1/r$, where r is measured in lattice constants. For distances of order of $1\mu m$ this leads to four orders of magnitude reduction.

For quasi one-dimensional ferromagnets such a reduction is absent and the transverse susceptibility reads

$$\chi_\perp^{\rm 1D}(\omega,r) = -\frac{S}{D}l_F e^{-r/l_F}, \quad \omega < \Delta_F, \tag{4.74}$$

where l_F is defined as above and the imaginary part vanishes as above, i.e.,

$$\chi_\perp^{\rm 1D}(\omega,r)'' = 0, \quad \omega < \Delta_F. \tag{4.75}$$

Similarly for $\omega > \Delta_F$ we have

$$\chi_{\perp}^{\mathrm{1D}}(\omega, r) = S\frac{\sin\left(\sqrt{(\omega-\Delta_F)/D}r\right)}{\sqrt{D(\omega-\Delta_F)}}\,, \tag{4.76}$$

and

$$\chi_{\perp}^{\mathrm{1D}}(\omega, r)'' = \frac{S}{2D}\sqrt{\frac{D}{\omega-\Delta_F}}\cos\left(\sqrt{(\omega-\Delta_F)/D}r\right)\,. \tag{4.77}$$

4.C Longitudinal correlators $\langle S^z_{\boldsymbol{q}}(t)S^z_{-\boldsymbol{q}}(0)\rangle$

The longitudinal susceptibility reads

$$\begin{aligned}\chi_{\parallel}(t,\boldsymbol{q}) &= -i\theta(t)[S^z_{\boldsymbol{q}}(t), S^z_{-\boldsymbol{q}}(0)] \\ &= -\theta(t)\frac{1}{N}\sum_{\boldsymbol{q}',\boldsymbol{q}''} e^{it(\epsilon_{\boldsymbol{q}'}-\epsilon_{\boldsymbol{q}'+\boldsymbol{q}})}\langle[a^\dagger_{\boldsymbol{q}'}a_{\boldsymbol{q}'+\boldsymbol{q}}, a^\dagger_{\boldsymbol{q}''}a_{\boldsymbol{q}''-\boldsymbol{q}}]\rangle\,.\end{aligned} \tag{4.78}$$

Applying Wick's theorem and performing a Fourier transform, we obtain the susceptibility in frequency domain

$$\chi_{\parallel}(\omega,\boldsymbol{q}) = -\frac{1}{N}\sum_{\boldsymbol{k}}\frac{n_{\boldsymbol{k}}-n_{\boldsymbol{k}+\boldsymbol{q}}}{\omega-\epsilon_{\boldsymbol{k}+\boldsymbol{q}}+\epsilon_{\boldsymbol{k}}+i\eta}\,, \tag{4.79}$$

where $n_{\boldsymbol{k}}$ is the magnon occupation number given by the Bose-Einstein distribution

$$n_k = \frac{1}{e^{\beta\epsilon_{\boldsymbol{k}}}-1}\,, \tag{4.80}$$

where $\epsilon_{\boldsymbol{k}}$ is again the magnon spectrum ($\epsilon_{\boldsymbol{k}} = \omega_{\boldsymbol{k}} + \Delta_F \approx D\boldsymbol{k}^2 + \Delta_F$ for small k). Note that the longitudinal susceptibility is proportional to $1/S$, due to the fact that $\epsilon_{\boldsymbol{k}} - \epsilon_{\boldsymbol{k}+\boldsymbol{q}} = \omega_{\boldsymbol{k}} - \omega_{\boldsymbol{k}+\boldsymbol{q}} \propto S$.

Since we are interested in the decoherence processes caused by the longitudinal fluctuations, we calculate the imaginary part of $\chi_{\parallel}(\omega,\boldsymbol{q})$ that is related to the fluctuations via the fluctuation-dissipation theorem. Performing a small $\boldsymbol{q}$ expansion and assuming without loss of generality

$\omega > 0$, we obtain for the imaginary part

$$\begin{aligned}
\chi_{\parallel}^{\mathrm{3D}}(\omega,\boldsymbol{q})'' &= \frac{\pi}{(2\pi)^3}\int d\boldsymbol{k}(n_{\boldsymbol{k}}-n_{\boldsymbol{k}+\boldsymbol{q}})\delta(\omega_{\boldsymbol{k}}-\omega_{\boldsymbol{k}+\boldsymbol{q}}+\omega) \\
&= \frac{1}{4\pi}\int_0^\infty dk k^2\int_{-1}^1 dx\left(\frac{1}{e^{\beta(\Delta_F+Dk^2)}-1}-\frac{1}{e^{\beta(\omega+\Delta_F+Dk^2)}-1}\right)\times \\
&\qquad\times\delta(\omega-Dq^2-2Dkqx) \\
&= \frac{1}{4\pi}\int_0^\infty dk k^2\int_{-1}^1 dx\left(\frac{1}{e^{\beta(\Delta_F+Dk^2)}-1}-\frac{1}{e^{\beta(\omega+\Delta_F+Dk^2)}-1}\right)\times \\
&\qquad\times\delta\left(k-\frac{\omega-Dq^2}{2Dqx}\right)\left|\frac{1}{2Dqx}\right| \\
&= \frac{1}{4\pi}\int_{-1}^1 dx\left|\frac{1}{2Dqx}\right|\left(\frac{\omega-Dq^2}{2Dqx}\right)^2\theta\left(\frac{\omega-Dq^2}{2Dqx}\right)\times \\
&\quad\times\left(\frac{1}{e^{\beta\left(\Delta_F+D\left(\frac{\omega-Dq^2}{2Dqx}\right)^2\right)}-1}-\frac{1}{e^{\beta\left(\omega+\Delta_F+D\left(\frac{\omega-Dq^2}{2Dqx}\right)^2\right)}-1}\right) \\
&= \frac{1}{4\pi}\int_0^1 dx\frac{1}{2Dqx}\left(\frac{\omega-Dq^2}{2Dqx}\right)^2\times \\
&\quad\left(\frac{1}{e^{\beta\left(\Delta_F+D\left(\frac{\omega-Dq^2}{2Dqx}\right)^2\right)}-1}-\frac{1}{e^{\beta\left(\omega+\Delta_F+D\left(\frac{\omega-Dq^2}{2Dqx}\right)^2\right)}-1}\right). \qquad (4.81)
\end{aligned}$$

Next, since we are interested in the regime where $\omega \gg T$ (and thus $\beta\omega \gg 1$), we have $n_{\boldsymbol{k}} \gg n_{\boldsymbol{k}+\boldsymbol{q}}$. Furthermore, we approximate the distribution function $n_{\boldsymbol{k}} = \frac{e^{-\beta(\Delta_F+\omega_{\boldsymbol{k}})}}{1-e^{-\beta\Delta_F+\beta\omega_{\boldsymbol{k}}}}$ (this is valid when $\beta\omega_{\boldsymbol{k}} \ll 1$) and arrive at the following expression

$$\begin{aligned}
\chi_{\parallel}^{\mathrm{3D}}(\omega,\boldsymbol{q})'' &= \frac{1}{4\pi}\int_0^1 dx\frac{1}{2Dqx}\left(\frac{\omega-Dq^2}{2Dqx}\right)^2\frac{e^{-\beta\left(\Delta_F+D\left(\frac{\omega-Dq^2}{2Dqx}\right)^2\right)}}{1-e^{-\beta\Delta_F}+\beta D\left(\frac{\omega-Dq^2}{2Dqx}\right)^2} \\
&= -\frac{e^{1-e^{-\beta\Delta_F}-\beta\Delta_F}}{4\beta D^2 q}\mathrm{Ei}\left(e^{-\beta\Delta_F}+\frac{1}{4}\left(-4-\beta Dq^2+2\beta\omega-\frac{\beta\omega^2}{Dq^2}\right)\right), \qquad (4.82)
\end{aligned}$$

where $\mathrm{Ei}(z)$ is the exponential integral function. We also need the the real

space representation obtained after inverse Fourier transformation,

$$\chi_{\parallel}^{\rm 3D}(\omega,\boldsymbol{r})'' = \sqrt{\frac{2}{\pi}}\frac{1}{r}\int_0^\infty dqq\chi_{\parallel}^{\rm 3D}(\omega,q)''\sin(qr)\,. \tag{4.83}$$

In order to perform the above integral we note that the imaginary part of the longitudinal susceptibility, given by Eq. (4.82), is peaked around $q=\sqrt{\omega/D}$ with the width of the peak $(1/\sqrt{\beta D})$ much smaller than its position in the regime we are working in ($\omega \gg T$). For $\boldsymbol{r}=0$, the integration over q can be then performed approximately and yields the following expression

$$\begin{aligned}\chi_{\parallel}^{\rm 3D}(\omega,\boldsymbol{r}=0)'' = \frac{\sqrt{\pi}e^{-e^{-\beta\Delta_F}-3\beta\Delta_F/2}}{2\beta^2D^3}\Big(e^{e^{-\beta\Delta_F}+\beta\Delta_F/2}\\ - e\sqrt{\pi}\sqrt{e^{\beta\Delta_F}-1}\\ \times\ {\rm Erfc}(e^{-\beta\Delta_F/2}\sqrt{e^{\beta\Delta_F}-1})\Big)\sqrt{\beta\omega}\,,\end{aligned} \tag{4.84}$$

where ${\rm Erfc}(z)$ denotes the complementary error function. It is readily observed from the above expression that the longitudinal fluctuations are exponentially suppressed by the gap. Assuming that $\Delta_F \gg T$, we obtain the following simplified expression

$$\chi_{\parallel}^{\rm 3D}(\omega,\boldsymbol{r}=0)'' = \frac{\sqrt{\pi}-e\pi{\rm Erfc}(1)}{2\beta^2D^3}e^{-\beta\Delta_F}\sqrt{\beta\omega}\,. \tag{4.85}$$

We observe that, since $J(\omega)=\chi_{\parallel}(\omega,\boldsymbol{r})''$, the longitudinal noise of the ferromagnet is—as the transverse one—sub-ohmic [105].

It is interesting to obtain the behavior of the longitudinal susceptibility in the opposite limit, when $\beta\omega \ll 1$. In this limit, the difference of the two Boltzmann factors in Eq. (4.81) can be expanded to the lowest order in the small quantity $\beta\omega$,

$$\begin{aligned}\chi_{\parallel}^{3D}(\omega,\boldsymbol{q})'' =& \int_0^1 dx\frac{1}{8\pi Dqx}\left(\frac{\omega-Dq^2}{2Dqx}\right)^2\times\\ &\frac{\beta\omega}{{\rm ch}\left(\beta\Delta_F+\beta D\left(\frac{\omega-Dq^2}{2Dqx}\right)^2\right)-1}\\ =&\frac{\omega}{16\pi D^2q\left(e^{\beta\Delta_F+\frac{\beta(\omega-Dq^2)^2}{4Dq^2}}-1\right)}.\end{aligned} \tag{4.86}$$

In order to calculate the Fourier transform to real space, we note that for $\omega \ll \Delta_F$ the denominator of the above expression depends only weakly on ω, thus we ignore this dependence and obtain the Fourier transform for $\boldsymbol{r} = 0$

$$\chi_{\parallel}^{3D}(\omega)'' = \frac{\ln(1+n_{\boldsymbol{k}=0})}{16\pi\beta D^3}\omega. \tag{4.87}$$

The above formula shows that the longitudinal noise of a ferromagnet at high temperatures ($\beta\omega \ll 1$) behaves as ohmic rather than sub-ohmic bath.

Next we calculate the longitudinal fluctuations for the case of a quasi-one-dimensional ferromagnet ($\Delta_F \gg T$) and obtain

$$\begin{aligned}\chi_{\parallel}^{1D}(\omega, r=0)'' &= \frac{1}{4\pi}\int_{-\infty}^{\infty} dk \int_{-\infty}^{\infty} dq \left(\frac{1}{e^{\beta(\Delta_F + Dk^2)} - 1} \right. \\ &\left. - \frac{1}{e^{\beta(\omega+\Delta_F+Dk^2)} - 1} \right) \delta(\omega - Dq^2 - 2Dkq) \\ &= \int_{-\infty}^{\infty} dk \frac{e^{-\beta D k^2}}{1 - e^{-\beta\Delta_F} + \beta D k^2} \frac{1}{D\sqrt{k^2 + \omega/D}} \\ &= \frac{\gamma}{D\sqrt{\beta\omega}} e^{-\beta\Delta_F}\,, \end{aligned} \tag{4.88}$$

where γ is a numerical factor of order unity.

Note that $S_{\parallel}(\omega, \boldsymbol{r})$ is defined through the fluctuation dissipation theorem as

$$S_{\parallel}(\omega, \boldsymbol{r}) = \coth(\beta\omega/2)\chi_{\parallel}(\omega, \boldsymbol{r})''\,. \tag{4.89}$$

4.D Exchange coupling to the ferromagnet

Exchange coupling

The Hamiltonian we consider is of the following form

$$H = H_F + H_\sigma + A\sum_{\boldsymbol{i}} \boldsymbol{\sigma}_i \cdot \boldsymbol{S}_{\boldsymbol{r}_i}\,, \tag{4.90}$$

where A is the exchange coupling constant between the qubit spins and the ferromagnet. The ferromagnet is assumed to be below the Curie

temperature with the magnetization pointing along the out-of-plane z-direction. The qubit Hamiltonian is assumed to be without splitting initially, that is $H_\sigma^{(0)} = 0$. Nevertheless, since the ferromagnet is in the ordered phase, there exists a first order effect due to coupling to the ferromagnet which gives rise to the term of the form $A\sum_i \sigma_i^z \langle S_{\boldsymbol{r}_i}^z\rangle$. Such a splitting is undesirable if one is interested in *coherent* interaction—we remedy this by coupling the spins to another ferromagnet, albeit with anti-parallel magnetization. Since we allow for some misalignment between orientation of the magnetization of the two ferromagnets, the final Hamiltonian for the qubits in the spin space after taking into account the first order corrections due to coupling to the ferromagnet reads

$$H_\sigma = \frac{1}{2}\Delta \sum_i \sigma_i^x \,. \tag{4.91}$$

The splitting in the x-direction of the qubit (or equivalently along the y-direction) is beneficial since it reduces decoherence due to longitudinal noise of the ferromagnet: the effect of such noise spectrum can significantly influence decoherence times for the case of no splitting of the qubit because the longitudinal noise is gapless.

Coherent coupling

We proceed with the derivation of an effective two-spin interaction Hamiltonian for $A \ll J$ by employing a perturbative Schrieffer-Wolff transformation [97] up to the second order

$$H_{\text{eff}} = H_\sigma + \frac{A^2}{8}\chi_\perp(\Delta)(2\sigma_1^y\sigma_2^y + \sigma_1^z\sigma_2^x + \sigma_1^x\sigma_2^z)\,, \tag{4.92}$$

where we introduced the notation $\chi_\perp(\omega) = \chi_\perp(\omega, L)$ ($L = |\boldsymbol{r}_2 - \boldsymbol{r}_1|$) and $\chi_\perp(\omega, \boldsymbol{r})$ is the transverse real space spin susceptibility of the ferromagnet. Note that we have neglected $\chi_\perp^{\text{3D}}(-\Delta)$ and $\chi_\perp^{\text{3D}}(0)$ in comparison to $\chi_\perp^{\text{1D}}(\Delta)$, as well as the longitudinal susceptibility $\chi_\parallel$ since it is smaller by factor of $1/S$ compared to the transverse one and it is suppressed by temperature. The real space transverse susceptibility of the 3D ferromagnet is given by

$$\chi_\perp^{\text{3D}}(\omega, \boldsymbol{r}) = -\frac{S}{D}\frac{e^{-r/l_F}}{r}, \quad \omega < \Delta_F, \tag{4.93}$$

where Δ_F is the gap induced via applied external magnetic field or due to internal anisotropy of the ferromagnet, $l_F = \sqrt{\frac{D}{\Delta_F - \omega}}$ and $D = 2JS$.

In what follows, we assume that the external gap is always larger than the qubit splitting, $\Delta < \Delta_F$, as this ensures that the transverse noise is not contributing to decoherence in second order since transverse noise is related to the vanishing imaginary part of the transverse susceptibility, $\chi_\perp(\omega)'' = 0$ ($\omega < \Delta_F$). The spatial dependence of the effective two spin coupling given by Eq. (4.93) is of Yukawa type due to presence of the external gap. If we assume a realistic tunnel coupling to the ferromagnet of $100\mu\mathrm{eV}$ [110, 111], the Curie temperature of $550\mathrm{K}$ [as for example for yttrium iron garnet (YIG)] and a gap of $\Delta_F = 100\mu\mathrm{eV}$, and the qubit splitting close to the resonance $\Delta_F - \Delta = 3 \times 10^{-3}\mu\mathrm{eV}$ (corresponding to a magnetic field of about $B = 60\mu\mathrm{T}$) we obtain for the qubit-qubit coupling strength a value on the order of $4 \times 10^{-11}\,\mathrm{eV}$ for a lattice constant of about 4Å. This coupling strength gives rise to the operation times of $50\mu s$—significantly below the relaxation and decoherence times of the spin qubit, $T_1 = 1s$ [64] and $T_2 > 200\mu s$ [65] respectively. Furthermore, the error threshold—defined as the ratio between the two-qubit gate operation time to the decoherence time—we obtain with such an operation time is about 10^{-2}, which is good enough for implementing the surface code error correction [21]. Here we used T_2 instead of T_2^* since spin-echo can be performed together with two-qubit gates [112]. Alternatively, the decoherence time of GaAs qubits can be increased without spin-echo by narrowing the state of the nuclear spins [113, 114].

The dimensionality of the ferromagnet plays an important role—if we assume $10nm$ width of the trench where the ferromagnet is placed, then, for energies below $0.1m\mathrm{eV}$, the ferromagnet behaves as quasi one-dimensional (1D). In this case we obtain

$$\chi_\perp^{\mathrm{1D}}(\omega, r) = -\frac{S}{D} l_F e^{-r/l_F}, \quad \omega < \Delta_F, \tag{4.94}$$

wherefrom it is evident that at distances $r \lesssim l_F$ the susceptibility of a quasi-1D ferromagnet is practically constant in contrast to the 3D case, where a $1/r$ decay is obtained, see Eq. (4.93). Additionally, we require $l_F \lesssim D/(AS) = 2J/A$ for the perturbation theory to be valid. Thus, for the same parameters as above, but without the need to tune very close to the resonance (we set herein $\Delta_F - \Delta = 0.5\mu\mathrm{eV}$, corresponding to about $B = 10m\mathrm{T}$) a coupling strength of $10^{-8}\mathrm{eV}$ is obtained.

For 1D case there is yet another rather promising possibility—to use magnetic semiconductors [115]. These materials are characterized by a particularly low Curie temperature of 30K or below [115], and the distance between the ions that are magnetically ordered via RKKY interac-

tion is about $10 - 100nm$. Such a large lattice constant is very beneficial for the long range coupling—if we take the lattice constant to be $10nm$, the coupling to the ferromagnet $A = 15\mu\text{eV}$ and the qubit splitting close to resonance ($\Delta_F - \Delta = 0.5\mu\text{eV}$, corresponding to about $B = 10m\text{T}$), the qubit-qubit coupling becomes of the order of $1\mu\text{eV}$. Such a coupling strength in turn leads to an error threshold on the order of 10^{-8}. Therefore, even the standard error correction protocol can be used in this case.

Derivation of the effective Hamiltonian (exchange coupling)

Here we give a detailed derivation of the qubit-qubit effective Hamiltonian. As stated above, the total Hamiltonian of the system reads

$$H = H_F + H_\sigma + A\sum_{\boldsymbol{i}}\left(\frac{1}{2}(\sigma_i^+ S_{\boldsymbol{r}_i}^- + \sigma_i^- S_{\boldsymbol{r}_i}^+) + \sigma_i^z S_{\boldsymbol{r}_i}^z\right), \tag{4.95}$$

where we identify the main part as $H_0 = H_F + H_\sigma$ and the small perturbation as the exchange coupling $V = A\sum_{\boldsymbol{i}} \boldsymbol{\sigma}_i \cdot \boldsymbol{S}_{\boldsymbol{r}_i}$. The Hamiltonian of the ferromagnet reads $H_F = -J\sum_{\langle \boldsymbol{r},\boldsymbol{r}'\rangle} \boldsymbol{S}_{\boldsymbol{r}} \cdot \boldsymbol{S}_{\boldsymbol{r}'}$, while the Hamiltonian for the two distant qubits is $H_\sigma = \frac{\Delta}{2}\sum_{i=1,2}\sigma_i^x$.

The second order effective Hamiltonian [97] is given by $H_{\text{eff}}^{(2)} = H_0 + U$, where

$$U = -\frac{i}{2}\lim_{\eta\to 0^+}\int_0^\infty dt e^{-\eta t}[V(t), V], \tag{4.96}$$

where $V(t) = e^{iH_0 t}Ve^{-iH_0 t}$.

We have

$$\sigma_i^+(t) = \frac{1+\cos(\Delta t)}{2}\sigma_i^+ + \frac{1-\cos(\Delta t)}{2}\sigma_i^- - i\sin(\Delta t)\sigma_i^z, \tag{4.97}$$

and $\sigma_i^-(t) = \sigma_i^+(t)^\dagger$.

Recalling that the zz susceptibility can be neglected and that only the transverse susceptibility contributes, we obtain the following result from Eq. (4.96), $U = \lim_{\eta\to 0^+}\int_0^\infty dt e^{-\eta t}\sum_{ij} U_{ij}$

$$\begin{aligned} U_{ij} &= -\frac{iA^2}{8}\left([\sigma_i^-(t)S_{\boldsymbol{r}_i}^+(t), \sigma_j^+ S_{\boldsymbol{r}_j}^-] + \text{h.c.}\right) \\ &= -\frac{iA^2}{8}\left(\sigma_i^-(t)\sigma_j^+[S_{\boldsymbol{r}_i}^+(t), S_{\boldsymbol{r}_j}^-] + \text{h.c.}\right) \end{aligned} \tag{4.98}$$

Finally, by rewriting $\cos(\Delta t) = \frac{e^{i\Delta t}+e^{-i\Delta t}}{2}$, $\sin(\Delta t) = \frac{e^{i\Delta t}-e^{-i\Delta t}}{2i}$, and using the definition of the real space transverse spin susceptibility

$$\chi_\perp(\omega, \boldsymbol{r}_i - \boldsymbol{r}_j) = -i \lim_{\eta\to 0^+} \int_0^\infty dt e^{-(i\omega+\eta)t} [S^+_{\boldsymbol{r}_i}(t), S^-_{\boldsymbol{r}_j}], \tag{4.99}$$

we obtain by inserting Eq. (4.97) into Eq. (4.98)

$$\begin{aligned} U =& \frac{A^2}{8} \sum_{ij} \left(\frac{\chi_\perp(0)}{2} + \frac{\chi_\perp(\Delta) + \chi_\perp(-\Delta)}{4} \right) \sigma_i^- \sigma_j^+ \\ &+ \frac{A^2}{8} \sum_{ij} \left(\frac{\chi_\perp(0)}{2} - \frac{\chi_\perp(\Delta) + \chi_\perp(-\Delta)}{4} \right) \sigma_i^+ \sigma_j^+ \\ &- \frac{A^2}{8} \sum_{ij} \frac{\chi_\perp(\Delta) - \chi_\perp(-\Delta)}{2} \sigma_i^z \sigma_j^+ + \text{h.c.} \end{aligned} \tag{4.100}$$

Since the decay length of the susceptibility $\chi(\omega, \boldsymbol{r})$ is large only close to the resonance, $\Delta_F \sim \Delta$, we can simplify the above equation by neglecting $\chi(-\Delta, \boldsymbol{r})$ and $\chi(0, \boldsymbol{r})$ in comparison to $\chi(\Delta, \boldsymbol{r})$ which is assumed to be close to the resonance. Within this approximation we arrive at Eq. (4.92) of the main text.

4.E Fourth order contributions to decoherence

In this section we determine the effect of the transverse noise in the lowest non-vanishing order due to coupling dipolarly to the ferromagnet. Here we choose quantizations axes such that the qubit splitting is along the z-axis, while the ferromagnet is polarized along x-axis. The Hamiltonian of the coupled system reads

$$H = H_{\rm F} + \frac{\Delta}{2}\sigma^z + \sigma^z \otimes X + \sigma^+ \otimes Y^- + \sigma^- \otimes Y^+, \tag{4.101}$$

where the operator X (Y) that couples longitudinally (transversally) to the qubit is linear in the transverse operators of the ferromagnet

$$X = \frac{i}{2} \int d\boldsymbol{r} c_{\boldsymbol{r}} (S^+_{\boldsymbol{r}} - S^-_{\boldsymbol{r}}), \tag{4.102}$$

$$Y^+ = -\frac{i}{8} \int d\boldsymbol{r} (a_{\boldsymbol{r}} S^+_{\boldsymbol{r}} + b_{\boldsymbol{r}} S^-_{\boldsymbol{r}}), \tag{4.103}$$

with $S^{\pm}_{\boldsymbol{r}} = S^{y}_{\boldsymbol{r}} \pm iS^{z}_{\boldsymbol{r}}$ and the definitions of the coefficients

$$a_{\boldsymbol{r}} = B_{\boldsymbol{r}} + 3C_{\boldsymbol{r}} - 6A_{\boldsymbol{r}}, \tag{4.104}$$
$$b_{\boldsymbol{r}} = B_{\boldsymbol{r}} + 3C_{\boldsymbol{r}} + 6A_{\boldsymbol{r}}, \tag{4.105}$$
$$c_{\boldsymbol{r}} = B_{\boldsymbol{r}} - 3A''_{\boldsymbol{r}}, \tag{4.106}$$
$$A_{\boldsymbol{r}} = \frac{1}{a^3}\frac{r^z r^+}{r^5}\,, \tag{4.107}$$
$$C_{\boldsymbol{r}} = \frac{1}{a^3}\frac{(r^+)^2}{r^5}\,, \tag{4.108}$$
$$B_{\boldsymbol{r}} = \frac{1}{a^3}\frac{1}{r^3}\left(2 - \frac{3r^+r^-}{r^2}\right)\,. \tag{4.109}$$

To proceed further we perform the SW transformation on the Hamiltonian given by Eq. (4.101). We ignore the Lamb and Stark shifts and obtain the effective Hamiltonian

$$H = H_{\rm F} + \frac{\Delta}{2}\sigma^z + \sigma^z \otimes \tilde{X}_2 + \sigma^+ \otimes \tilde{Y}_2^- + \sigma^- \otimes \tilde{Y}_2^+, \tag{4.110}$$

where

$$\tilde{X}_2 = X_2 - \langle X_2 \rangle, \tag{4.111}$$
$$\tilde{Y}_2^{\pm} = Y_2^{\pm} - \langle Y_2^{\pm} \rangle, \tag{4.112}$$

with the following notation

$$X_2 = 4(Y_\Delta^+ Y^- + Y^+ Y_\Delta^-), \tag{4.113}$$
$$Y_2^+ = 2(Y_\Delta^+ X - X_0 Y^+), \tag{4.114}$$
$$X_\omega = \frac{i}{2}\int d\boldsymbol{r}\boldsymbol{r}'\chi_\perp(\omega, \boldsymbol{r}-\boldsymbol{r}')c_{\boldsymbol{r}}(S^+_{\boldsymbol{r}'} - S^-_{\boldsymbol{r}'}), \tag{4.115}$$
$$Y^+_\omega = -\frac{i}{8}\int d\boldsymbol{r}\boldsymbol{r}'\chi_\perp(\omega, \boldsymbol{r}-\boldsymbol{r}')(a_{\boldsymbol{r}}S^+_{\boldsymbol{r}'} + b_{\boldsymbol{r}}S^-_{\boldsymbol{r}'}), \tag{4.116}$$

The model given by Eq. (4.110) yields the following expressions for the relaxation and decoherence times

$$T_1^{-1} = S_{\tilde{Y}_2^-}(\omega = \Delta), \tag{4.117}$$
$$T_2^{-1} = \frac{1}{2}T_1^{-1} + S_{\tilde{X}_2}(\omega = 0), \tag{4.118}$$

where, again, $S_A(\omega) = \int dt e^{-i\omega t}\{A^\dagger(t), A(0)\}$.

After a lengthly calculation we obtain the expressions for $S_{\tilde{X}_2}(\omega=0)$ and $S_{\tilde{Y}_2^-}(\omega=\Delta)$,

$$S_{\tilde{X}_2}(0) = \frac{1}{128}\int d\nu d\boldsymbol{r}_1\boldsymbol{r}_2\boldsymbol{r}_3\boldsymbol{r}_4\boldsymbol{r}_5\boldsymbol{r}_6 C^{-+}(\nu,\boldsymbol{r}_3-\boldsymbol{r}_4)C^{+-}(-\nu,\boldsymbol{r}_1-\boldsymbol{r}_2)\times \tag{4.119}$$

$$\begin{aligned}
&((a_{\boldsymbol{r}_5}a^*_{\boldsymbol{r}_3}+b_{\boldsymbol{r}_3}b^*_{\boldsymbol{r}_1})(a_{\boldsymbol{r}_4}a^*_{\boldsymbol{r}_2}+b_{\boldsymbol{r}_6}b^*_{\boldsymbol{r}_4})\chi_\perp(\Delta,\boldsymbol{r}_1-\boldsymbol{r}_5)\chi_\perp(\Delta,\boldsymbol{r}_2-\boldsymbol{r}_6)+\\
&(a_{\boldsymbol{r}_4}a^*_{\boldsymbol{r}_2}+b_{\boldsymbol{r}_5}b^*_{\boldsymbol{r}_4})(a_{\boldsymbol{r}_1}a^*_{\boldsymbol{r}_3}+b_{\boldsymbol{r}_6}b^*_{\boldsymbol{r}_1})\chi_\perp(\Delta,\boldsymbol{r}_2-\boldsymbol{r}_5)\chi_\perp(\Delta,\boldsymbol{r}_3-\boldsymbol{r}_6)+\\
&(a_{\boldsymbol{r}_6}a^*_{\boldsymbol{r}_2}+b_{\boldsymbol{r}_2}b^*_{\boldsymbol{r}_4})(a_{\boldsymbol{r}_5}a^*_{\boldsymbol{r}_3}+b_{\boldsymbol{r}_3}b^*_{\boldsymbol{r}_1})\chi_\perp(\Delta,\boldsymbol{r}_1-\boldsymbol{r}_5)\chi_\perp(\Delta,\boldsymbol{r}_4-\boldsymbol{r}_6)+\\
&(a_{\boldsymbol{r}_6}a^*_{\boldsymbol{r}_2}+b_{\boldsymbol{r}_2}b^*_{\boldsymbol{r}_4})(a_{\boldsymbol{r}_1}a^*_{\boldsymbol{r}_3}+b_{\boldsymbol{r}_5}b^*_{\boldsymbol{r}_1})\chi_\perp(\Delta,\boldsymbol{r}_3-\boldsymbol{r}_5)\chi_\perp(\Delta,\boldsymbol{r}_4-\boldsymbol{r}_6))\,,
\end{aligned}$$

$$S_{\tilde{Y}_2^-}(\Delta) = \frac{1}{64}\int d\nu d\boldsymbol{r}_1\boldsymbol{r}_2\boldsymbol{r}_3\boldsymbol{r}_4\boldsymbol{r}_5\boldsymbol{r}_6 C^{-+}(\nu,\boldsymbol{r}_3-\boldsymbol{r}_4)C^{+-}(\Delta-\nu,\boldsymbol{r}_1-\boldsymbol{r}_2)\times \tag{4.120}$$

$$\begin{aligned}
&(c_{\boldsymbol{r}_3}c_{\boldsymbol{r}_6}(a_{\boldsymbol{r}_4}b^*_{\boldsymbol{r}_1}+a_{\boldsymbol{r}_5}b^*_{\boldsymbol{r}_4})\chi_\perp(0,\boldsymbol{r}_2-\boldsymbol{r}_6)\chi_\perp(\Delta,\boldsymbol{r}_1-\boldsymbol{r}_5)\\
&-c_{\boldsymbol{r}_3}c_{\boldsymbol{r}_6}(a_{\boldsymbol{r}_5}a^*_{\boldsymbol{r}_2}+b_{\boldsymbol{r}_2}b^*_{\boldsymbol{r}_1})\chi_\perp(0,\boldsymbol{r}_4-\boldsymbol{r}_6)\chi_\perp(\Delta,\boldsymbol{r}_1-\boldsymbol{r}_5)-\\
&c_{\boldsymbol{r}_4}c_{\boldsymbol{r}_6}(a_{\boldsymbol{r}_1}a^*_{\boldsymbol{r}_2}+b_{\boldsymbol{r}_5}b^*_{\boldsymbol{r}_1})\chi_\perp(0,\boldsymbol{r}_3-\boldsymbol{r}_6)\chi_\perp(\Delta,\boldsymbol{r}_2-\boldsymbol{r}_5)\\
&+c_{\boldsymbol{r}_1}c_{\boldsymbol{r}_6}(b_{\boldsymbol{r}_5}a^*_{\boldsymbol{r}_2}+b_{\boldsymbol{r}_2}a^*_{\boldsymbol{r}_3})\chi_\perp(0,\boldsymbol{r}_4-\boldsymbol{r}_6)\chi_\perp(\Delta,\boldsymbol{r}_3-\boldsymbol{r}_5)+\\
&c_{\boldsymbol{r}_4}c_{\boldsymbol{r}_5}(b_{\boldsymbol{r}_3}a^*_{\boldsymbol{r}_2}+b_{\boldsymbol{r}_6}a^*_{\boldsymbol{r}_3})\chi_\perp(0,\boldsymbol{r}_1-\boldsymbol{r}_5)\chi_\perp(\Delta,\boldsymbol{r}_2-\boldsymbol{r}_6)\\
&+c_{\boldsymbol{r}_3}c_{\boldsymbol{r}_4}(a_{\boldsymbol{r}_5}a^*_{\boldsymbol{r}_2}+b_{\boldsymbol{r}_6}b^*_{\boldsymbol{r}_1})\chi_\perp(\Delta,\boldsymbol{r}_1-\boldsymbol{r}_5)\chi_\perp(\Delta,\boldsymbol{r}_2-\boldsymbol{r}_6)-\\
&c_{\boldsymbol{r}_1}c_{\boldsymbol{r}_5}(a_{\boldsymbol{r}_4}a^*_{\boldsymbol{r}_3}+b_{\boldsymbol{r}_6}b^*_{\boldsymbol{r}_4})\chi_\perp(0,\boldsymbol{r}_2-\boldsymbol{r}_5)\chi_\perp(\Delta,\boldsymbol{r}_3-\boldsymbol{r}_6)\\
&-c_{\boldsymbol{r}_1}c_{\boldsymbol{r}_4}(b_{\boldsymbol{r}_6}a^*_{\boldsymbol{r}_2}+b_{\boldsymbol{r}_5}a^*_{\boldsymbol{r}_3})\chi_\perp(\Delta,\boldsymbol{r}_2-\boldsymbol{r}_5)\chi_\perp(\Delta,\boldsymbol{r}_3-\boldsymbol{r}_6)-\\
&c_{\boldsymbol{r}_2}c_{\boldsymbol{r}_5}(a_{\boldsymbol{r}_6}a^*_{\boldsymbol{r}_3}+b_{\boldsymbol{r}_3}b^*_{\boldsymbol{r}_4})\chi_\perp(0,\boldsymbol{r}_1-\boldsymbol{r}_5)\chi_\perp(\Delta,\boldsymbol{r}_4-\boldsymbol{r}_6)\\
&+c_{\boldsymbol{r}_2}c_{\boldsymbol{r}_5}(a_{\boldsymbol{r}_6}b^*_{\boldsymbol{r}_1}+a_{\boldsymbol{r}_1}b^*_{\boldsymbol{r}_4})\chi_\perp(0,\boldsymbol{r}_3-\boldsymbol{r}_5)\chi_\perp(\Delta,\boldsymbol{r}_4-\boldsymbol{r}_6)-\\
&c_{\boldsymbol{r}_2}c_{\boldsymbol{r}_3}(a_{\boldsymbol{r}_6}b^*_{\boldsymbol{r}_1}+a_{\boldsymbol{r}_5}b^*_{\boldsymbol{r}_4})\chi_\perp(\Delta,\boldsymbol{r}_1-\boldsymbol{r}_5)\chi_\perp(\Delta,\boldsymbol{r}_4-\boldsymbol{r}_6)\\
&+c_{\boldsymbol{r}_1}c_{\boldsymbol{r}_2}(a_{\boldsymbol{r}_6}a^*_{\boldsymbol{r}_3}+b_{\boldsymbol{r}_5}b^*_{\boldsymbol{r}_4})\chi_\perp(\Delta,\boldsymbol{r}_3-\boldsymbol{r}_5)\chi_\perp(\Delta,\boldsymbol{r}_4-\boldsymbol{r}_6)+\\
&c_{\boldsymbol{r}_5}c_{\boldsymbol{r}_6}(a_{\boldsymbol{r}_4}a^*_{\boldsymbol{r}_3}+b_{\boldsymbol{r}_3}b^*_{\boldsymbol{r}_4})\chi_\perp(0,\boldsymbol{r}_1-\boldsymbol{r}_5)\chi_\perp(0,\boldsymbol{r}_2-\boldsymbol{r}_6)\\
&-c_{\boldsymbol{r}_5}c_{\boldsymbol{r}_6}(a_{\boldsymbol{r}_4}b^*_{\boldsymbol{r}_1}+a_{\boldsymbol{r}_1}b^*_{\boldsymbol{r}_4})\chi_\perp(0,\boldsymbol{r}_2-\boldsymbol{r}_5)\chi_\perp(0,\boldsymbol{r}_3-\boldsymbol{r}_6)-\\
&c_{\boldsymbol{r}_5}c_{\boldsymbol{r}_6}(b_{\boldsymbol{r}_3}a^*_{\boldsymbol{r}_2}+b_{\boldsymbol{r}_2}a^*_{\boldsymbol{r}_3})\chi_\perp(0,\boldsymbol{r}_1-\boldsymbol{r}_5)\chi_\perp(0,\boldsymbol{r}_4-\boldsymbol{r}_6)\\
&+c_{\boldsymbol{r}_5}c_{\boldsymbol{r}_6}(a_{\boldsymbol{r}_1}a^*_{\boldsymbol{r}_2}+b_{\boldsymbol{r}_2}b^*_{\boldsymbol{r}_1})\chi_\perp(0,\boldsymbol{r}_3-\boldsymbol{r}_5)\chi_\perp(0,\boldsymbol{r}_4-\boldsymbol{r}_6)).
\end{aligned}$$

In order to obtain the lower bound of relaxation and decoherence time, we consider the ferromagnet to be in shape of infinite plane. Furthermore, we are not aiming at performing an exact evaluation of the integrals in Eqs. (4.120)-(4.121), but rather at finding the lower bound for the relaxation and decoherence times. To this end we note that $|C^{+-}(\omega,\boldsymbol{r}-\boldsymbol{r}')|\leq|C^{+-}(\omega,\boldsymbol{r}=0)|$ and arrive at the following inequalities

$$S_{\tilde{X}_2}(0) \leq \frac{B^4}{8(\Delta_F-\Delta)^2}\int_{\Delta_F}^{\infty} d\nu C^{+-}(\nu)^2, \tag{4.121}$$

$$S_{\tilde{Y}_2^-}(\Delta) \leq \frac{B^4}{8}\left(\frac{1}{\Delta_F}+\frac{1}{\Delta_F-\Delta}\right)^2 \times \int_{\Delta_F+\Delta}^{\infty} d\nu C^{+-}(\nu)C^{+-}(\nu-\Delta), \tag{4.122}$$

where we used notation $B=\int d\boldsymbol{r} B_{\boldsymbol{r}}$. Finally we arrive at the expression for the lower bound of the relaxation and decoherence times

$$T_1^{-1} \leq \frac{B^4 S^2 \Delta_F^2}{2D^3}\left(\frac{1}{\Delta_F}+\frac{1}{\Delta_F-\Delta}\right)^2 f\left(\frac{\Delta}{\Delta_F}, \beta\Delta_F\right), \tag{4.123}$$

$$T_2^{-1} \leq \frac{B^4 S^2 \Delta_F^2}{4D^3}\left(\frac{1}{\Delta_F}+\frac{1}{\Delta_F-\Delta}\right)^2 f\left(\frac{\Delta}{\Delta_F}, \beta\Delta_F\right) + \frac{B^4 S^2 \Delta_F^2}{2D^3(\Delta_F-\Delta)^2} f\left(0, \beta\Delta_F\right). \tag{4.124}$$

with the function $f(x,y)$ defined as follows

$$f(x,y) = \int_{1+x}^{\infty} dz \frac{\sqrt{z-1}}{e^{yz}-1}\frac{\sqrt{z-x-1}}{e^{y(z-x)}-1}. \tag{4.125}$$

Assuming the same parameters as in the main text, we obtain decoherence times of about 0.5 hours, while the relaxation time is on the order of 1000 hours. It is worth noting that this result depends sensitively on the ratio Δ_F/T, thus if we assume a temperature of 4K, we obtain $T_1 \geq 200\mu s$ and $T_2 \geq 30\mu s$.

CHAPTER 5

Long-Range Interaction of Spin-Qubits via Ferromagnets

Adapted from:
Luka Trifunovic, Fabio L. Pedrocchi, and Daniel Loss,
"Long-Range Interaction of Singlet-Triplet Qubits via Ferromagnets",
ArXiv: 1305.2451 (2013).

We propose a mechanism of a long-range coherent interaction between two singlet-triplet qubits dipolarly coupled to a dogbone-shaped ferromagnet. An effective qubit-qubit interaction Hamiltonian is derived and the coupling strength is estimated. Furthermore we derive the effective coupling between two spin-$1/2$ qubits that are coupled via dipolar interaction to the ferromagnet and that lie at arbitrary positions and deduce the optimal positioning. We consider hybrid systems consisting of spin-$1/2$ and ST qubits and derive the effective Hamiltonian for this case. We then show that operation times vary between 1MHz and 100MHz and give explicit estimates for GaAs, Silicon, and NV-center based spin qubits. Finally, we explicitly construct the required sequences to implement a CNOT gate. The resulting quantum computing architecture retains all the single qubit gates and measurement aspects of earlier approaches, but allows qubit spacing at distances of order $1\,\mu$m for two-qubit gates, achievable with current semiconductor technology.

5.1 Ferromagnet

We denote by $\boldsymbol{S}_{\boldsymbol{r}}$ the spins (of size S) of the ferromagnet at site $\boldsymbol{r}$ on a cubic lattice and $\boldsymbol{\sigma}_i$ stands for the spin-$1/2$ qubit spins. The ferromagnet Hamiltonian we consider is of the following form

$$H_F = -J \sum_{\langle \boldsymbol{r}, \boldsymbol{r}' \rangle} \boldsymbol{S}_{\boldsymbol{r}} \cdot \boldsymbol{S}_{\boldsymbol{r}'} + \Delta_F \sum_{\boldsymbol{r}} S^z_{\boldsymbol{r}}, \tag{5.1}$$

with $J > 0$ and $\Delta_F = \mu B$, where B is externally applied magnetic field (see Fig. 5.1) and μ is the magnetic moment of the ferromagnet spin. The above Hamiltonian is the three-dimensional (3D) Heisenberg model with the sum restricted to nearest-neighbor sites $\langle \boldsymbol{r}, \boldsymbol{r}' \rangle$. The ferromagnet is assumed to be monodomain and below the Curie temperature with the magnetization pointing along the z-direction.

We would like to stress at this point that even though herein we analyze a specific model for the ferromagnet (Heisenberg model), all our conclusions rely only on the generic features of the ferromagnet susceptibility, i.e., its long-range nature. Furthermore, the gap in the magnon spectrum can originate also from anisotropy. The presence of the gap is an important feature since it suppresses the fluctuations, albeit the susceptibility is cut-off after some characteristic length given by the gap and the frequency at which the ferromagnet is probed.

5.2 Coupling between ST-qubits

The Hamiltonian we consider is of the following form

$$H = H_F + H_\tau + H_I, \tag{5.2}$$

where H_τ is Hamiltonian of the two ST-qubits [63, 116] and H_I is the dipolar coupling between the ferromagnet and the ST-qubits (see below).

Singlet-triplet qubit Hamiltonian

A Singlet-Triplet (ST) qubit is a system that consists of two electrons confined in a double quantum well. Herein we assume that the wells are steep enough so that we can consider only one lowest orbital level of each well. Following Ref. [84], we consider also the spin space of the two

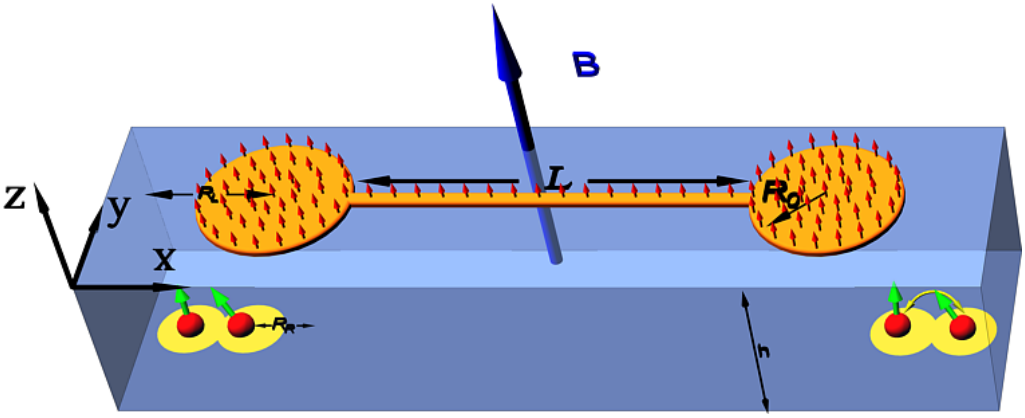

Figure 5.1: Model system consisting of two identical double-QDs in the xy-plane and the dogbone-shaped coupler. The dogbone coupler consists of two ferromagnetic disks of radius R_0 connected by a thin ferromagnetic wire of length L. Each double-QD can accommodate one (two) electrons, defining the spin-$1/2$ (ST-) qubit. Absence of tunneling between the separate double-QD is assumed. Here $R_{\rm L}$ ($R_{\rm R}$) is the in-plane distance between the left (right) well and the corresponding disk center, while h is vertical distance between the QD and the gate. The red arrow on top of the ferromagnet denote the orientation of its magnetization which is assumed to be monodomain.

electrons and write down the total of six basis states

$$\begin{aligned}
|(2,0)S\rangle &= c^\dagger_{\rm L\uparrow}c^\dagger_{\rm L\downarrow}|0\rangle,\\
|(0,2)S\rangle &= c^\dagger_{\rm R\uparrow}c^\dagger_{\rm R\downarrow}|0\rangle,\\
|(1,1)S\rangle &= \frac{1}{\sqrt{2}}\left(c^\dagger_{\rm L\uparrow}c^\dagger_{\rm R\downarrow}-c^\dagger_{\rm L\downarrow}c^\dagger_{\rm R\uparrow}\right)|0\rangle,\\
|T_+\rangle &= c^\dagger_{\rm L\uparrow}c^\dagger_{\rm R\uparrow}|0\rangle,\\
|T_0\rangle &= \frac{1}{\sqrt{2}}\left(c^\dagger_{\rm L\uparrow}c^\dagger_{\rm R\downarrow}+c^\dagger_{\rm L\downarrow}c^\dagger_{\rm R\uparrow}\right)|0\rangle,\\
|T_-\rangle &= c^\dagger_{\rm L\downarrow}c^\dagger_{\rm R\downarrow}|0\rangle,
\end{aligned} \tag{5.3}$$

where $c^\dagger_{\rm L}$ ($c^\dagger_{\rm R}$) creates an electron in the Wannier state $\Phi_{\rm L}$ ($\Phi_{\rm R}$). The Wannier states are $\Phi_{{\rm L},R}=\frac{1}{\sqrt{1-2sg+g^2}}\left(\varphi_{1,2}-g\varphi_{2,1}\right)$, where

$$s=\langle\varphi_1|\varphi_2\rangle=\exp[-\left(a/a_{\rm B}\right)^2]$$

is the overlap of the harmonic oscillator ground state wave functions of the two wells, $a_{\mathrm{B}} = \sqrt{\hbar/m\omega_0}$ is the Bohr radius of a single quantum dot, $\hbar\omega_0$ is the single-particle level spacing, and $2a = l$ is the interdot distance. The mixing factor of the Wannier states is $g = (1 - \sqrt{1 - s^2})/s$. Using these six basis states we can represent the Hamiltonian of the ST-qubits

$$H_0 = \begin{pmatrix} H_{SS} & 0 \\ 0 & H_{\mathrm{T}T,0} \end{pmatrix}. \tag{5.4}$$

In writing the above equation we have neglected the spin-orbit interaction (SOI), thus there are no matrix elements coupling the singlet and triplet blocks. The effect of SOI in ST-qubit was studied in Ref. [84] and no major influence on the qubit spectra was found.

The two qubit states are $|T_0\rangle$ and, in the absence of SOI, the linear combination of the singlet states $|S\rangle = \alpha|(2,0)S\rangle + \beta|(1,1)S\rangle + \gamma|(0,2)S\rangle$, where the coefficients α, β, γ depend on the detuning ε between the two quantum wells. In particular, when $\varepsilon = 0$ we have $|S\rangle = |(1,1)S\rangle$. In what follows, we always consider Hamiltonians only in the qubit subspace, thus the Hamiltonian of two ST-qubits reads

$$H_\tau = -\frac{\Delta}{2}\sum_{i=1,2}\tau_i^z, \tag{5.5}$$

where $\tau^{x,y,z}$ are the Pauli matrices acting in the space spanned by vectors $\{|S\rangle, |T_0\rangle\}$ and Δ is the ST-qubit splitting.

Dipolar coupling to ST-qubit

In this section we derive the dipolar coupling between the ferromagnet and the ST-qubit. To this end we first project the Zeeman coupling to the ST-qubit system on the two-dimensional qubit subspace

$$H_{\mathrm{Z}} = g^*\mu_B\left(\boldsymbol{B}_{\mathrm{L}}\cdot\boldsymbol{S}_{\mathrm{L}} + \boldsymbol{B}_{\mathrm{R}}\cdot\boldsymbol{S}_{\mathrm{R}}\right), \tag{5.6}$$

where $\boldsymbol{B}_{\mathrm{L}}$ ($\boldsymbol{B}_{\mathrm{R}}$) is the magnetic field in the left (right) quantum well, $S^i_{\mathrm{L},R} = (\sigma^i)_{ss'}c^\dagger_{\mathrm{L},R,s}c_{\mathrm{L},R,s'}$ and g^* is the effective Landé factor. After projecting on the qubit space we obtain

$$H_{\mathrm{Z}} = g^*\mu_B(B^z_{\mathrm{L}} - B^z_{\mathrm{R}})\tau^x. \tag{5.7}$$

With this result we are ready to write down the ferromagnet/ST-qubit interaction Hamiltonian

$$H_I = \sum_{i=1,2} g^*\mu_0\mu_B\left(\hat{B}^z_{\mathrm{L}}(i) - \hat{B}^z_{\mathrm{R}}(i)\right)\tau^x_i, \tag{5.8}$$

where index i enumerates ST-qubits, and the magnetic field from the ferromagnet can be express through the integral over the ferromagnet

$$\hat{B}^z_{\mathrm{L},R}(i) = \frac{\mu_0\mu}{4\pi a^3}\int d\boldsymbol{r}(i)_{\mathrm{L},R}\frac{1}{r(i)^3_{\mathrm{L},R}}\times \left(S^z_{\boldsymbol{r}(i)_{\mathrm{L},R}} - \frac{3(\boldsymbol{S}_{\boldsymbol{r}(i)_{\mathrm{L},R}}\cdot\boldsymbol{r}(i)_{\mathrm{L},R})r(i)^z_{\mathrm{L},R}}{r(i)^2_{\mathrm{L},R}}\right), \tag{5.9}$$

where the coordinate system for $\boldsymbol{r}(i)_{\mathrm{L}}$ ($\boldsymbol{r}(i)_{\mathrm{R}}$) is positioned in left (right) quantum well of the i-th qubit.

Effective coupling between two ST-qubits

Given the total Hamitonian, Eq. (5.2), we can easily derive the effective qubit-qubit coupling with help of Schrieffer-Wolff transformation

$$H_{eff} = H_\tau - \lim_{\nu\to 0^+}\frac{i}{2}\int_0^\infty dt e^{-\nu t}\left[H_I(t), H_I\right], \tag{5.10}$$

with $H_I(t) = e^{iH_\tau t}H_I e^{-iH_\tau t}$.

We assume that the radius of the two disks is much smaller than the distance between their centers ($R_0 \ll L$). Within this assumption we can take for the susceptibility between two points at opposite disks the same as the 1D susceptibility. Next we take only on-resonance susceptibility and make use of the expression $\tau^x(\Delta) = \frac{1}{2}(\tau^x + i\tau^y)$, where $\tau^x(\omega)$ is the Fourier transform of $\tau^x(t) = e^{iH_\tau t}\tau^x e^{-iH_\tau t}$. We define the transverse susceptibility in the standard way

$$\chi_\perp(\omega, \boldsymbol{r}_i - \boldsymbol{r}_j) = -i\lim_{\eta\to 0^+}\int_0^\infty dt e^{(-i\omega-\eta)t}[S^+_{\boldsymbol{r}_i}(t), S^-_{\boldsymbol{r}_j}]. \tag{5.11}$$

The longitudinal susceptibility, defined via

$$\chi_\parallel(\omega, \boldsymbol{r}_i - \boldsymbol{r}_j) = -i\lim_{\eta\to 0^+}\int_0^\infty dt e^{(-i\omega-\eta)t}[S^z_{\boldsymbol{r}_i}(t), S^z_{\boldsymbol{r}_j}], \tag{5.12}$$

can be neglected compared to the transverse one because the former is smaller by a factor $1/S$ and is proportional to the magnon occupation number. Therefore the longitudinal susceptibility vanishes at zero temperature, while the is not the case for the transverse susceptibility. We arrive finally at the following expression

$$H_{eff} = H_\tau + \frac{9}{4}\mathcal{B}\chi^{1D}_\perp(\Delta, L)\tau^x_1\tau^x_2, \tag{5.13}$$

where $\mathcal{B} = (\mu_0\mu)^2(g^*\mu_B)^2(A_L^1 - A_R^1)(A_L^2 - A_R^2)/16\pi^2a^6$, $\chi_\perp^{1D}$ is given in Eq. (4.74) and

$$A^i_{\mathrm{L},R} = \int d\boldsymbol{r}(i)_{\mathrm{L},R} \frac{r(i)^-_{\mathrm{L},R} r(i)^z_{\mathrm{L},R}}{r(i)^5_{\mathrm{L},R}}. \tag{5.14}$$

Assuming the dogbone shape of the ferromagnet in the above integral

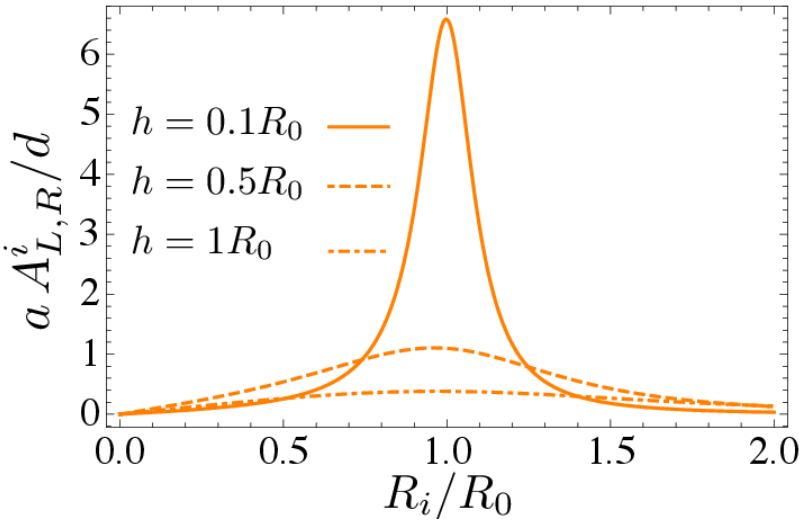

Figure 5.2: Plot of $aA^i_{L,R}/d$ defined through Eq. (5.14) as function of R_i/R_0 for different values of h. We see that the value of $aA^i_{L,R}/d$ is bigger when the ST-qubit is closer to the disk of the dogbone as expected. Furthermore, by placing the right dot at distance R_0 of the disk axis and the left dot on the disk axis, we obtain the strongest value for the effective coupling between the two ST-qubits, see Eq. (5.13).

and integration only over the adjacent disk, we obtain

$$\begin{aligned} A^i_{\mathrm{L},R} \;=\; & \frac{2ihd}{a}\left(\frac{2R^i_{\mathrm{L},R}R_0\left(F(\mathrm{acsc}(w^i_{\mathrm{L},R}), {w^i_{\mathrm{L},R}}^2) - K({w^i_{\mathrm{L},R}}^2)\right)}{3R^i_{\mathrm{L},R}\left((R^i_{\mathrm{L},R}-R_0)^2+h^2\right)\sqrt{(R^i_{\mathrm{L},R}+R_0)^2+h^2}} \right. \\ & \left. + \frac{u^i_{\mathrm{L},R}E({w^i_{\mathrm{L},R}}^2) - u^i_{\mathrm{L},R}E(\mathrm{acsc}(w^i_{\mathrm{L},R}), {w^i_{\mathrm{L},R}}^2)}{3R^i_{\mathrm{L},R}\left((R^i_{\mathrm{L},R}-R_0)^2+h^2\right)\sqrt{(R^i_{\mathrm{L},R}+R_0)^2+h^2}} \right), \end{aligned} \tag{5.15}$$

where R_0 is the disk radius, $R^i_{\mathrm{L},R}$ is the distance from the adjacent disk axis to the left or right quantum well of the i-th qubit, $\mathrm{acsc}(x)$ is the inverse cosecant; $F(x,y)$, $K(x)$ and $E(x,y)$ are the corresponding elliptic

integrals. Furthermore, we introduced the notation $u^i_{\mathrm{L},R} = {R^i_{\mathrm{L},R}}^2 + R_0^2 + h^2$ and $w^i_{\mathrm{L},R} = \sqrt{1 - \frac{4R^i_{\mathrm{L},R}R_0}{(R^i_{\mathrm{L},R}+R_0)^2+h^2}}$, where h is the distance in the z-direction between the ST-qubit plane and the adjacent disk bottom and d is the disk thickness, see Fig. 5.1.

Figure 5.2 illustrates the dependence of the $A^i_{\mathrm{L},R}$ integrals on the position of the quantum wells. Since the coupling constant is given by the difference of this integrals for left and right quantum well, we conclude that the strongest coupling is obtained if one quantum well of the ST-qubit is positioned below the disk center and the other exactly below the edge. Furthermore, when $h \ll R_0$ the value of the integral is strongly peaked around $R \sim R_0$ and this can be exploited as yet another switching mechanism—moving one quantum well away from the edge of the disk.

Sequence for CNOT gate

Two qubits interacting via the ferromagnet evolve according to the Hamiltonian H_{eff}, see Eq. (5.13). The Hamiltonian is therefore the sum of Zeeman terms and qubit-qubit interaction. These terms do not commute, making it difficult to use the evolution to implement standard entangling gates. Nevertheless, since H_τ acts only in the subspace spanned by $\{|\uparrow\uparrow\rangle, |\downarrow\downarrow\rangle\}$ and $\Delta \gg J_{12} = 9\mathcal{B}\chi_\perp(\Delta)/4$, we can neglect the effect of H_{eff} in this part of the space and approximate it by its projection in the space spanned by vectors $\{|\uparrow\downarrow\rangle, |\downarrow\uparrow\rangle\}$

$$H'_{\mathrm{eff}} = H_\tau + J_{12}(\tau_1^x\tau_2^x + \tau_1^y\tau_2^y). \tag{5.16}$$

Within this approximation, the coupling in H'_{eff} and Zeeman terms now commute.

We consider the implementation of the iSWAP gate [103]

$$U_{\mathrm{iSWAP}} = e^{-i(\tau_1^x\tau_2^x+\tau_1^y\tau_2^y)3\pi/4},$$

which can be used to implement the CNOT gate:

$$U_{\mathrm{iSWAP}} = e^{iH_\tau t}e^{-iH'_{\mathrm{eff}}t}, \tag{5.17}$$

where $t = 3\pi/(4J_{12})$. When iSWAP is available, the CNOT gate can be constructed in the standard way [104]

$$U_{CNOT} = e^{-i\frac{\pi}{4}\tau_1^z}e^{i\frac{\pi}{4}\tau_2^x}e^{i\frac{\pi}{4}\tau_2^z}U_{\mathrm{i}SWAP}e^{-i\frac{\pi}{4}\tau_1^x}U_{\mathrm{i}SWAP}e^{i\frac{\pi}{4}\tau_2^z}. \tag{5.18}$$

Since H'_{eff} is an approximation of H_{eff}, the above sequence will yield approximate CNOT, U'_{CNOT}, when used with the full Hamiltonian. The success of the sequences therefore depends on the fidelity of the gates, $F(U'_{CNOT})$. Ideally this would be defined using a minimization over all possible states of two qubits. However, to characterize the fidelity of an imperfect CNOT it is sufficient to consider the following four logical states of two qubits [60]: $|+,0\rangle, |+,1\rangle, |-,0\rangle$, and $|-,1\rangle$. These are product states which, when acted upon by a perfect CNOT, become the four maximally entangled Bell states $|\Phi^+\rangle, |\Psi^+\rangle, |\Phi^-\rangle$, and $|\Psi^-\rangle$, respectively. As such, the fidelity of an imperfect CNOT may be defined,

$$F(U'_{CNOT}) = \min_{i\in\{+,-\},j\in\{0,1\}} |\langle i,j|U^\dagger_{CNOT}U'_{CNOT}|i,j\rangle|^2. \tag{5.19}$$

The choice of basis used here ensures that $F(U'_{CNOT})$ gives a good characterization of the properties of U'_{CNOT} in comparison to a perfect CNOT, especially for the required task of generating entanglement. For realistic parameters, with the Zeeman terms two order of magnitude stronger than the qubit-qubit coupling, the above sequence yields fidelity for the CNOT gate of 99.976%.

To compare these values to the thresholds found in schemes for quantum computation, we must first note that imperfect CNOT's in these cases are usually modelled by the perfect implementation of the gate followed by depolarizing noise at a certain probability. It is known that such noisy CNOT's can be used for quantum computation in the surface code if the depolarizing probability is less than 1.1% [20]. This corresponds to a fidelity, according to the definition above, of 99.17%. The fidelities that may be achieved in the schemes proposed here are well above this value and hence, though they do not correspond to the same noise model, we can expect these gates to be equally suitable for fault-tolerant quantum computation.

5.3 Coupling between spin-$1/2$ qubits

In this section we study the coupling of two spin-$1/2$ quantum dots via interaction with a dog-bone shaped ferromagnet. The Hamiltonian has again the form as in Eq. (5.2) and we allow for splittings of the spin-$1/2$ qubits both along x and z direction,

$$H_\sigma = \frac{\Delta_x}{2}\sum_{i=1,2}\sigma_i^x + \frac{\Delta_z}{2}\sum_{i=1,2}\sigma_i^z\,, \tag{5.20}$$

where $\boldsymbol{\sigma}_i$ are the Pauli operators of the i^{th} spin-$1/2$ quantum dot. Hamiltonian (5.20) is a generalized version of the Hamiltonian [60], where we considered splitting along x only. We present here a detailed derivation of the effective coupling between two quantum dots located at an arbitrary position with respect to the dogbone shaped ferromagnet, i.e., contrary to Ref. [60] we do not assume that the quantum dots are positioned at a highly symmetric point but consider the most general case. This allows us to determine the optimal positioning of the qubit in order to achieve the strongest coupling between the qubits.

The dipolar coupling between the ferromagnet and the spin-$1/2$ qubits is given by

$$H_I = \sum_{i,\boldsymbol{r}} \frac{g^* \mu_0 \mu_B \mu}{4\pi r^3} \left(\boldsymbol{\sigma}_i \cdot \boldsymbol{S}_{\boldsymbol{r}} - \frac{3(\boldsymbol{\sigma}_i \cdot \boldsymbol{r})(\boldsymbol{S}_{\boldsymbol{r}} \cdot \boldsymbol{r})}{r^2} \right) , \tag{5.21}$$

where μ_D is the magnetic moment of the spin-$1/2$ qubit. The explicit expressions for the time evolution of the Pauli operators in Heisenberg picture is

$$\begin{aligned}
\sigma_i^+(t) &= -\frac{1}{\Delta^2}(i\Delta\cos(\Delta t/2) - \Delta_z \sin(\Delta t/2))^2 \sigma_i^+ \\
&\quad -\frac{\Delta_x^2}{2\Delta^2}(\cos(t\Delta) - 1)\sigma_i^- \\
&\quad +\frac{\Delta_x}{\Delta^2}(\Delta_z - \Delta_z \cos(t\Delta) - i\Delta \sin(t\Delta))\sigma_i^z , \\
\sigma_i^z(t) &= \frac{\Delta_x}{2\Delta^2}(\Delta_z - \Delta_z \cos(t\Delta) - i\Delta \sin(t\Delta))\sigma_i^+ \\
&\quad +\frac{\Delta_x}{2\Delta^2}(\Delta_z - \Delta_z \cos(t\Delta) + i\Delta \sin(t\Delta))\sigma_i^- \\
&\quad +\frac{\Delta_z^2 + \Delta_x^2 \cos(t\Delta)}{\Delta^2}\sigma_i^z ,
\end{aligned} \tag{5.22}$$

where we introduced the notation $\Delta = \sqrt{\Delta_x^2 + \Delta_z^2}$. We also assume that $\Delta < \Delta_F$ such that the susceptibility $\chi_\perp(\Delta, \boldsymbol{r})$ is purely real—thus the transverse noise is gapped. By replacing the above expressions in

Eq. (5.10), we obtain the effective qubit-qubit coupling

$$
\begin{aligned}
H_{\text{eff}} = H_\sigma + \frac{(g^*\mu_0\mu_B\mu)^2}{16\pi^2 a^6}\Big(&\frac{9}{8}A_1^*A_2\chi_\perp^{1\text{D}}(\Delta)\sigma_1^z(\Delta)\sigma_2^z \\
&+ \frac{3}{16}(3A_2C_1^*\chi_\perp^{1\text{D}}(\Delta) - B_1A_2^*\chi_\perp^{1\text{D}}(\Delta))\sigma_1^+(\Delta)\sigma_2^z \\
&+ \frac{3}{16}(3A_1C_2^*\chi_\perp^{1\text{D}}(\Delta) - B_2A_1^*\chi_\perp^{1\text{D}}(\Delta))\sigma_1^z(\Delta)\sigma_2^+ \\
&+ \frac{1}{32}(B_1B_2\chi_\perp^{1\text{D}}(\Delta) + 9C_1C_2^*\chi_\perp^{1\text{D}}(\Delta))\sigma_1^-(\Delta)\sigma_2^+ \\
&- \frac{3}{32}(B_1C_2\chi_\perp^{1\text{D}}(\Delta) + B_2C_1\chi_\perp^{1\text{D}}(\Delta))\sigma_1^-(\Delta)\sigma_2^- \\
&+ \text{h.c.}\Big) + 1 \leftrightarrow 2\,,
\end{aligned}
\tag{5.23}
$$

where we have denoted $\chi_\perp^{1D}(\Delta) = \chi_\perp^{1D}(\Delta, L)$ and introduced the follow-

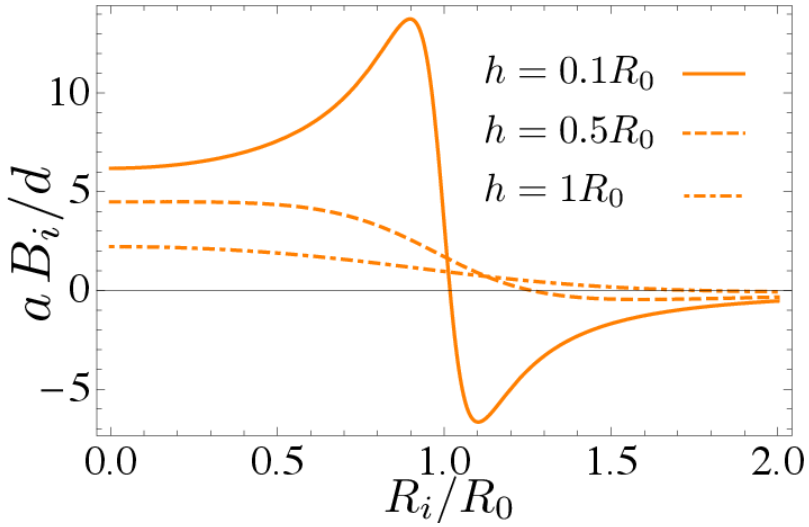

Figure 5.3: Plot of aB_i/d defined in Eq. (5.26) as function of R_i/R_0 for different values of h. The value of the integral increases in general by decreasing the value of h.

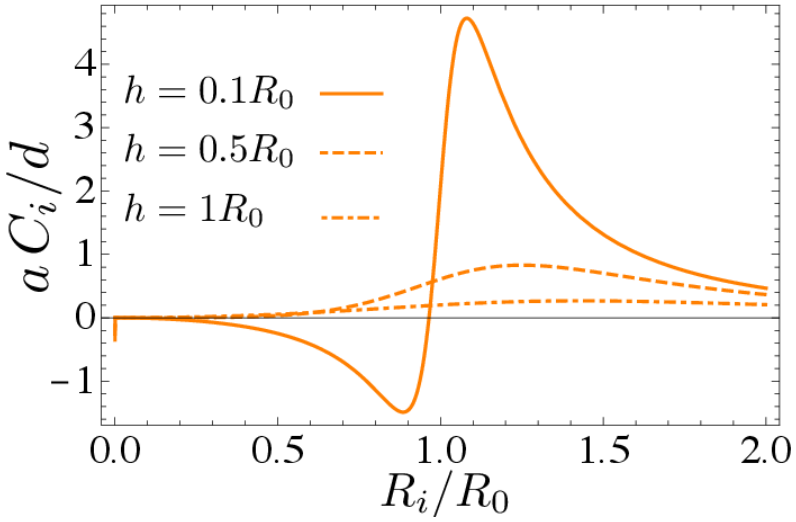

Figure 5.4: Plot of aC_i/d defined in Eq. (5.25) as function of R_i/R_0 for different values of h. The value of the integral is peaked around $R_i \sim R_0$ and it increases in general by decreasing the value of h.

ing notation for the integrals

$$A_i = \int d\boldsymbol{r}_i \frac{r_i^z r_i^+}{r_i^5}\,, \tag{5.24}$$

$$C_i = \int d\boldsymbol{r}_i \frac{(r_i^+)^2}{r_i^5}\,, \tag{5.25}$$

$$B_i = \int d\boldsymbol{r}_i \frac{1}{r_i^3}\left(2 - \frac{3r_i^+ r_i^-}{r_i^2}\right)\,, \tag{5.26}$$

with the coordinate origin for $\boldsymbol{r}_i$ at the i-th qubit and the integration goes over the adjacent disk. We also defined the Fourier transforms of the time evolution of Pauli matrices $\boldsymbol{\sigma}(t) = e^{iH_\sigma t}\boldsymbol{\sigma}e^{-iH_\sigma t}$ as

$$\begin{aligned}\sigma_i^+(\Delta) \;=\; & -\frac{1}{\Delta^2}\left(-\frac{\Delta^2}{4} + \frac{\Delta_z\Delta}{2} - \frac{\Delta_z^2}{4}\right)\sigma_i^+ \\ & + \frac{\Delta_x}{\Delta^2}\left(-\frac{\Delta_z}{2} + \frac{\Delta}{2}\right)\sigma_i^z - \frac{\Delta_x^2}{4\Delta^2}\sigma_i^-\,,\end{aligned}$$

and

$$\begin{aligned}\sigma_i^z(\Delta) \;=\; & \frac{\Delta_x}{2\Delta^2}\left(-\frac{\Delta_z}{2} + \frac{\Delta}{2}\right)\sigma_i^+ + \frac{\Delta_x}{2\Delta^2}\left(-\frac{\Delta_z}{2} - \frac{\Delta}{2}\right)\sigma_i^- \\ & + \frac{\Delta_x^2}{2\Delta^2}\sigma_i^z\,.\end{aligned} \tag{5.27}$$

By assuming a dogbone-shaped ferromagnet and integrating only over the adjacent disk as above, we obtain A_i given in Eq. (5.15) with $R^i_{L,R}$ replaced by R_i since there is now only one spin-$1/2$ qubit below each disk of the dogbone. The remaining integrals yield the following results

$$\begin{aligned} B_i &= -\frac{2d}{3a}\left(\frac{\left(R_i^4+3R_i^2\left(h^2-R_0^2\right)+\left(R_0^2+h^2\right)^2\right)E\left(1-w_i^2\right)}{R_i^2\left(\left(R_i-R_0\right)^2+h^2\right)\sqrt{\left(R_i+R_0\right)^2+h^2}}\right., \\ &\quad \left.-\frac{\left(\left(R_i-R_0\right)^2+h^2\right)\left(R_i^2+2\left(R_0^2+h^2\right)\right)K\left(1-w_i^2\right)}{R_i^2\left(\left(R_i-R_0\right)^2+h^2\right)\sqrt{\left(R_i+R_0\right)^2+h^2}}\right) \\ C_i &= \frac{2d}{a}\frac{\left(\left(R_i-R_0\right)^2+h^2\right)K\left(1-w_i^2\right)-2\left(R_i^2-R_0^2+h^2\right)E\left(1-w_i^2\right)}{\left(\left(R_i-R_0\right)^2+h^2\right)\sqrt{\left(R_i+R_0\right)^2+h^2}}, \end{aligned} \tag{5.28}$$

where $w_i=\sqrt{1-\frac{4R_iR_0}{(R_i+R_0)^2+h^2}}$, R_0 is the radius of each disk, R_i is the distance of the i-th qubit to the adjacent dog bone axis, and R_0 and h are defined as in Sec. 5.2. In deriving Eq. (5.23) we took again only 'on-resonance' terms into account (i.e. we neglected $\chi_\perp^{\rm 1D}(0)$ and $\chi_\perp^{\rm 1D}(-\Delta)$). Furthermore we assumed, as above, that the susceptibility between two points on different disks of the dogbone is well approximated by the 1D transverse susceptibility. In the limit where each quantum dot lies on the vertical axis going through the center of each cylinder of the dogbone, the axial symmetry leads to $A_1=A_2=C_1=C_2=0$, $B_1=B_2=B$, and with $\Delta_z=0$ we recover the result

$$H_{\rm eff}=H_\sigma+\frac{\left(g^*\mu_0\mu_B\mu\right)^2}{16\,\pi^2a^6}\frac{B^2}{32}\chi_\perp^{1D}(\Delta)(2\sigma_1^y\sigma_2^y+\sigma_1^z\sigma_2^x+\sigma_1^x\sigma_2^z) \tag{5.29}$$

derived in Ref. [60]. The analysis carried out herein assumes arbitrary positioning of the qubit and allow us to determine the optimal positioning for the strongest coupling. To this end, we analyze integrals $A_i,\ B_i,\ C_i$, see Figs. 5.2-5.4. It is readily observed that the coupling strength increases as the vertical distance between the qubit and coupler plane, h, decreases. Additionally, we observe that the strongest coupling strength is obtained when the qubit is positioned below the edge of the adjacent disk.

The derived coupling is valid for any dogbone-like shape of the ferromagnet, i.e., it is not crucial to assume disk shape.

Sequence for CNOT gate

The effective Hamiltonian derived in previous section, Eq. (5.23), can be re-expressed in the following form

$$H_{eff} = \frac{(g^*\mu_0\mu_B\mu)^2}{16\pi^2 a^6}\chi_\perp^{1D}(\Delta, L)\boldsymbol{\sigma}_1^T \cdot \hat{\mathcal{H}} \cdot \boldsymbol{\sigma}_2 + \frac{1}{2}\boldsymbol{\Delta} \cdot (\boldsymbol{\sigma}_1 + \boldsymbol{\sigma}_2), \tag{5.30}$$

with $\boldsymbol{\Delta} = (\Delta_x, 0, \Delta_z)^T$ and $\hat{\mathcal{H}}$ being the symmetric matrix with all entries being non-zero. The question now arises how to construct the CNOT gate sequence for such a general Hamiltonian. We tackle this problem by taking first the quantization axis to be along the total magnetic field acting on the two qubits and denote by $\tilde{\boldsymbol{\sigma}}_i$ Pauli matrix vector with respect to this new quantization axis. The Hamiltonian now reads

$$H_{eff} = \frac{(g^*\mu_0\mu_B\mu)^2}{16\pi^2 a^6}\chi_\perp^{1D}(\Delta, L)\,\tilde{\boldsymbol{\sigma}}_1^T \cdot \hat{\tilde{\mathcal{H}}} \cdot \tilde{\boldsymbol{\sigma}}_2 + \frac{1}{2}\Delta(\tilde{\sigma}_1^z + \tilde{\sigma}_2^z), \tag{5.31}$$

where the components of the matrix $\hat{\tilde{\mathcal{H}}}$ are given in Appendix 5.A.

We proceed further along the lines presented in Sec. 5.2, i.e., we project the rotated Hamiltonian, Eq. (5.31), on the subspace spanned by vectors $\{|\tilde{\uparrow}\tilde{\downarrow}\rangle, |\tilde{\downarrow}\tilde{\uparrow}\rangle\}$. This procedure yields the following result

$$H'_{eff} = \tilde{J}_{12}(\tilde{\sigma}_1^x\tilde{\sigma}_2^x + \tilde{\sigma}_1^y\tilde{\sigma}_2^y) + \Delta(\tilde{\sigma}_1^z + \tilde{\sigma}_2^z), \tag{5.32}$$

$\tilde{J}_{12} = \frac{(\mu_0 g^*\mu_B\mu)^2}{(4\pi)^2 a^6}\frac{\chi_\perp^{1D}(\Delta,L)}{32}\tilde{A}_{12}$. The dimensionless constant $\tilde{A}_{12}$ is defined through the following expression

$$\begin{aligned}\tilde{A}_{12} = &\frac{{\Delta_x}^2\left(36A_1A_2 + (B_1 + 3C_1)(B_2 + 3C_2)\right)}{16\Delta^2} \\ &+ \frac{6\Delta_x\Delta_z\left(A_2(B_1 - 3C_1) + A_1(B_2 - 3C_2)\right)}{16\Delta^2} \\ &+ \frac{2\Delta_z(B_1B_2 + 9C_1C_2)(\Delta + \Delta_z)}{16\Delta^2}.\end{aligned} \tag{5.33}$$

The projected Hamiltonian in Eq. (5.32) is identical to the one already considered in Sec. 5.2, Eq. (5.16). Thus the CNOT gate sequence can be obtained in exactly same way, namely via Eqs. (5.17) and (5.18).

Similar to the previously studied case of ST-qubits, the CNOT gate sequence described in this section is only approximate one. For realistic parameters, with the Zeeman terms two order of magnitude stronger

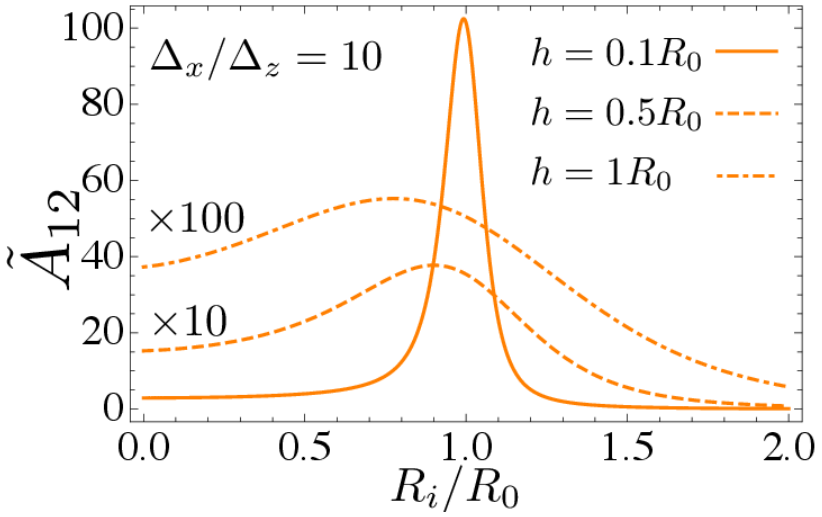

Figure 5.5: Plot of $\tilde{A}_{12}$ defined in Eq. (5.33) as function of R_i/R_0 for different values of h, assuming $R_1 = R_2$ and $\Delta_x = 10\Delta_z$. The value of the integral is peaked around $R_i \sim R_0$ and it increases in general by decreasing the value of h.

than the qubit-qubit coupling, this approximate sequence yields fidelity for the CNOT gate similar to the one previously found in Sec. 5.2.

We now use Eq. (5.33) to determine the optimal positioning of the qubits in order to obtain shortest possible gate operation times. If we assume that the qubit splitting is predominantly along the x-axis ($\Delta_x \gg \Delta_z$), we obtain the behavior illustrated in Fig. 5.5. We conclude that for all values of h the optimal positioning is below the edge of the adjacent disk. It is interesting to note that when $h \ll R_0$ one can obtain more than two orders of magnitude enhancement compared to the positioning previously studied in Ref. [60]. In the opposite limit, $\Delta_x \ll \Delta_z$, we observe behavior illustrated in Fig. 5.6. When also $h \ll R_0$ we recover the same optimal positioning as before—below the edge of the disk, while when $h \sim R_0$, positioning the qubit anywhere below the disk yields approximately same coupling strength.

5.4 Coupling between spin-$1/2$ and ST-qubits

In the previous sections we have considered the coupling of both spin-$1/2$ and ST qubits individually. Since each setup has its own advantages

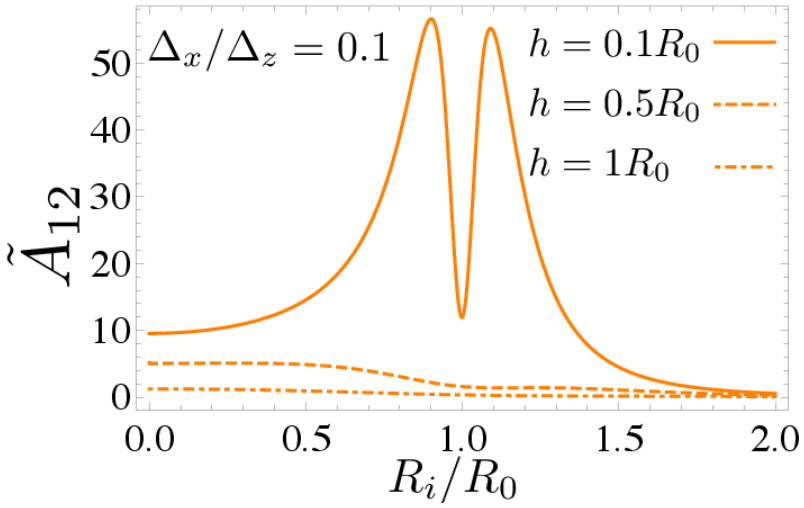

Figure 5.6: Plot of $\tilde{A}_{12}$ defined in Eq. (5.33) as function of R_i/R_0 for different values of h, assuming $R_1 = R_2$ and $\Delta_x = 0.1\Delta_z$. The value of the integral is peaked around $R_i \sim R_0$ only for $h \ll R_0$ and it increases in general by decreasing the value of h.

and challenges, it is interesting to show these qubits can be cross-coupled to each other and thus that hybrid spin-qubits can be formed. This opens up the possibility to take advantage of the 'best of both worlds.

The Hamiltonian of such a hybrid system reads

$$H = H_F + H_\sigma + H_\tau + H_I, \tag{5.34}$$

where the first three term on left-hand side are given by omitting the summation over i in Eqns. (5.1), (5.20) and (5.5), respectively. The interaction term H_I has the following form

$$\begin{aligned} H_I = &\sum_{\boldsymbol{r}} \frac{g^* \mu_0 \mu_B \mu}{4\pi r^3} \left(\boldsymbol{\sigma} \cdot \boldsymbol{S}_{\boldsymbol{r}} - \frac{3(\boldsymbol{\sigma} \cdot \boldsymbol{r})(\boldsymbol{S}_{\boldsymbol{r}} \cdot \boldsymbol{r})}{r^2} \right) \\ &+ g^* \mu_B \left(\hat{B}^z_{\mathrm{L}} - \hat{B}^z_{\mathrm{R}} \right) \tau^x_i, \end{aligned} \tag{5.35}$$

with $\hat{B}_{\mathrm{L},R}$ being given in Eq. (5.9) when index i is omitted. Continuing along the lines of the previous sections, we perform the second order SW transformation and obtain the effective coupling between the qubits

$$H_{eff} = \frac{3(\mu_0 g^* \mu_B \mu)^2}{256\pi^2 a^6} \chi_\perp^{\mathrm{1D}}(\Delta) \left(\mathrm{Re}[3A(A_L - A_R)^*]\tau^x\sigma^z(\Delta) + (C^*(A_L - A_R) - 3B(A_L - A_R)^*)\tau^x\sigma^+(\Delta) + \mathrm{h.c}\right) + \{\sigma^i(\Delta) \to \sigma^i, \tau^x \to \tau^x(\Delta)\}, \quad (5.36)$$

where $A_{\mathrm{L},R}$ and A are calculated in Eq. (5.15), while B and C are given in Eq. (5.28).

Similarly as in the previous sections, we find that the optimal coupling for the hybrid case is obtained when the spin-$1/2$ qubit is positioned below the edge of one of the two discs while one quantum well of the ST-qubit is positioned below the other disc center with the other well being below the disc edge.

5.5 Validity of the effective Hamiltonian

We discuss herein the validity of the effective Hamiltonian derived in Sec. 5.2 and Sec. 5.3.

Special care has to be taken for the validity of the perturbation theory employed herein, since we are working close to resonance, i.e., $\Delta - \Delta_F$ has to be small but still much larger than the coupling of a qubit to an individual spin of the ferromagnet. For the perturbation theory to be valid we also require the tilt of each ferromagnet spin to be sufficiently small (i.e. $\langle S_{\boldsymbol{r}}^{\pm}\rangle \ll 1$). The tilt of the central spin of the ferromagnetic disk can be estimated by the integral over the dogbone disk D

$$\langle S_{\boldsymbol{r}}^{\pm}\rangle = \int_D \chi_\perp(\boldsymbol{r}) B_\perp(\boldsymbol{r})\,. \quad (5.37)$$

Using cylindrical coordinates we then obtain

$$\langle S_{\boldsymbol{r}}^{\pm}\rangle \sim \frac{\mu_0\mu_B^2}{2a}\int_0^R \rho d\rho \frac{1}{(\rho^2+h^2)^{3/2}}\frac{S}{D\rho}, \quad (5.38)$$

where $\frac{S}{D\rho}$ is the spatial decay of the transversal susceptibility and $\frac{1}{(\rho^2+h^2)^{3/2}}$ is the decay of the dipolar field causing the perturbation of the ferromagnet. Even though each spin is just slightly tilted, we obtain a sizable coupling due to big number of spins involved in mediating the coupling.

5.6 Switching mechanisms

In this section we briefly discuss possible switching *on/off* mechanisms. These include changing the splitting of the qubits and moving them spatially. The former mechanism is based on the dependence of the susceptibility decay length on frequency [60] see Eq. (4.74,). It is enough to detune the qubit splitting by less then a percent to switch the qubit-qubit coupling effectively off. This is particularly feasible for the ST-qubits where qubit splitting can be controlled by all electrical means. Furthermore, the ST-qubits coupling can be switched off also by rotating them such that $A_{\mathrm{L}} = A_{\mathrm{R}}$, see Eq. (5.14).

The spin-$1/2$ qubits can be switched either by detuning its splitting off-resonance with the magnon gap Δ_F or by moving them away from the dogbone disk, see Figs. 5.5-5.6.

5.7 Coupling strengths and operation times

In Tables 5.1 and 5.2 we present a summary of the effective coupling strengths and operation times that can be obtained in the proposed setup. We assume that the qubits are separated by a distance of $1\mu m$ and we give the remaining parameters in the table captions.

The column captions correspond to four experimentally relevant setups considered in this work (GaAs ST and spin-$1/2$ quantum dots, silicon-based quantum dots, and NV-centers). The row captions denote respectively the vertical distance h between the qubit and the disk of the ferromagnet, the difference between the qubit splitting Δ and the internal splitting Δ_F of the ferromagnet (given in units of energy and in units of magnetic field), the obtained effective qubit-qubit interaction, and the corresponding operation time.

The operation times obtained in Tables 5.1 and 5.2 are significantly below the relaxation and decoherence times of the corresponding qubits. Indeed, for GaAs quantum dots $T_1 = 1s$ (see Ref. [64]), and $T_2 > 200\mu s$ (see Ref. [65]), respectively. Here we compare to T_2 instead of T_2^* since spin-echo can be performed together with two-qubit gates [112]. Alternatively, the T_2^* of GaAs qubits can be increased without spin-echo by narrowing the state of the nuclear spins [113, 114].

For silicon-based qubits decoherence time up to $T_2 \approx 200\mu s$ is achievable [48] Finally decoherence times of $T_2^*. \approx 20\mu s$ and $T_2 \approx 1.8ms$ have been obtained for N-V centers in diamond [11].

Table 5.1: The parameters used to obtain the numbers below are: Landé factor of the ferromagnet $g_F = 2$; disk radius $R_0 = 50nm$; disk thickness $d = 20nm$; Curie temperature $T = 550K$ and thus exchange coupling $J/k_B \approx 824K$; lattice constant of the ferromagent $a = 4$Å. We consider the case $\Delta_x \ll \Delta_z$.

$\Delta_x \ll \Delta_z$	GaAs ST QD $\lvert g^*\rvert = 0.4$	GaAs ST QD $\lvert g^*\rvert = 0.4$	GaAs spin-1/2 QD $\lvert g^*\rvert = 0.4$
Distance h	$50\,nm$	$50\,nm$	$50\,nm$
Splitting $\Delta_F - \Delta$	$1\,\mu eV$ $(43.2\,mT)$	$0.5\mu eV$ $(21.6mT)$	$10^{-2}\,\mu eV$ $(0.4\,mT)$
Coupling strength (CS)	$1.4 \times 10^{-9}\,eV$	1.4×10^{-8}	$2 \times 10^{-10}\,eV$
Operation time (OS)	$470\,ns$	$47ns$	$3.3\,\mu s$

$\Delta_x \ll \Delta_z$	Silicon-based QD	NV-center
Distance h	$25\,nm$	$5\,nm$
Splitting $\Delta_F - \Delta$	$10^{-2}\,\mu eV\,(0.1\,mT)$	$10^{-1}\,\mu eV\,(0.9\,mT)$
Coupling Strength (CS)	$2.4 \times 10^{-8}\,eV$	$1.8 \times 10^{-8}\,eV$
Operation Time (OT)	$27.4\,ns$	$36.6\,ns$

Table 5.2: We use the same parameters as in Table 5.1 but consider the case $\Delta_x \gg \Delta_z$.

$\Delta_x \gg \Delta_z$	GaAs spin-1/2 QD $\lvert g^*\rvert = 0.4$	Silicon-based QD $\lvert g^*\rvert = 2$	NV-center $\lvert g^*\rvert = 2$
Distance h	$50\,nm$	$25\,nm$	$5\,nm$
Splitting $\Delta_F - \Delta$	$10^{-2}\,\mu eV$ $(0.4\,mT)$	$10^{-2}\,\mu eV$ $(0.1\,mT)$	$10^{-1}\,\mu eV$ $(0.9\,mT)$
Coupling strength	$1.2 \times 10^{-10}\,eV$	$1.8 \times 10^{-8}\,eV$	$3.6 \times 10^{-8}\,eV$
Operation time	$5.5\,\mu s$	$36.6\,ns$	$18.3\,ns$

In Table 5.3, we summarize the obtained coupling strengths and operation times obtained when a ST-qubit is cross coupled with a spin-1/2 qubit.

We have verified that the tilting of the ferromagnet spins given in Eq. (5.38) remains small. The biggest tilt we obtain (for $h = 5\,nm$) is $\langle S^{\pm}_{\boldsymbol{r}} \rangle \approx 10^{-7} \ll 1$. Thus all the result are within the range of validity of the perturbation theory.

Table 5.3: We use the same parameters as in Table 5.1 and choose the splitting $\Delta_F - \Delta = 10^{-2}\,\mu eV$ for the ST-qubit (the splitting of the other qubit is taken from Table 5.1) to determine the coupling strengths and operation times achieved in the hybrid case. The column caption of the table labels GaAs ST-QD, while the row captions label the three other qubit systems, considered in this work, to which it can be hybridized. The left panel corresponds to the case $\Delta_x \ll \Delta_z$ while the right panel corresponds to $\Delta_x \gg \Delta_z$.

$\Delta_x \ll \Delta_z$	GaAs ST QD	
	Coupling strength	Operation time
GaAs spin-$1/2$ QD	$1.7 \times 10^{-9}\,eV$	$387\,ns$
Silicon-based QD	$1.8 \times 10^{-8}\,eV$	$36.6\,ns$
NV-center	$1.6 \times 10^{-8}\,eV$	$41.1\,ns$

$\Delta_x \gg \Delta_z$	GaAs ST QD	
	Coupling strength	Operation time
GaAs spin-$1/2$ QD	$1.3 \times 10^{-9}\,eV$	$506\,ns$
Silicon-based QD	$1.6 \times 10^{-8}\,eV$	$41.1\,ns$
NV-center	$2.2 \times 10^{-8}\,eV$	$29.9\,ns\,ns$

5.8 Conclusions

We have proposed and studied a model that allows coherent coupling of distant spin qubits. The idea is to introduce a piece of ferromagnetic material between qubits to which they couple dipolarly. A dogbone shape of the ferromagnet is the best compromise since it allows both strong coupling of the qubits to the ferromagnet and long-distance coupling because of its slowly decaying 1D spin-spin susceptibility. We have derived an effective Hamiltonian for the qubits in the most general case where the qubits are positioned arbitrarily with respect to the dogbone. We have calculated the optimal position for the effective qubit-qubit coupling to be strongest and estimated it. For both the singlet-triplet (ST) and spin-$1/2$ qubits, interaction strengths of $10^{-2}\mu eV$ can be achieved. Since decoherence effects induced by the coupling to the ferromagnet are negligible [60], we obtain error thresholds of about 10^{-4} for ST-qubits and for spin-$1/2$ qubits. In both cases this is good enough to implement the surface code error correction [21]. Finally, for both types of qubits we have explicitly constructed the sequence to implement a CNOT gate achievable with a fidelity of more than 99.9%

Our analysis is general and is not restricted to any special types of qubits as long as they couple dipolarly to the ferromagnet. Furthermore, the only relevant quantity of the coupler is its spin-spin susceptibility. Hence, our analysis is valid for any kind of coupler (and not just a ferromagnet) that has a sufficiently slowly decaying susceptibility.

This quantum computing architecture retains all the single qubit gates and measurement aspects of earlier approaches, but allows qubit spacing at distances of order 1 μm for two- qubit gates, achievable with the state-of-the-art semiconductor technology.

5.9 Acknowledgment

We would like to thank A. Yacoby, A. Morello, and C. Kloeffel for useful discussions. This work was supported by the Swiss NSF, NCCR QSIT, and IARPA.

5.A Rotated Hamiltonian for CNOT gate

Here we give the general form of the matrix $\hat{\tilde{H}}$ entering Eq. (5.31).

$$\begin{aligned}\tilde{\mathcal{H}}_{12} &= \frac{3\Delta_z\Delta_z^-(C_2''(-6\Delta_x A_1' + B_1\Delta_z^- + 3C_1'\Delta_z^+) + 2\Delta_x A_1''(B_2+3C_2'))}{32\Delta^3} \\ &\quad \frac{6\Delta_z\Delta_z^- C_1''(B_2\Delta_z^- - 3C_2'\Delta_z^+) + 3\Delta_x i\,(12A_2\Delta\Delta_x A_1^* - 12A_1\Delta\Delta_x A_2^*)}{64\Delta^3} \\ &\quad + \frac{\Delta_x\,(-4\Delta_x A_1'(B_2+3C_2) + 4A_1B_2\Delta_x + \Delta_z^-\,(3C_1C_2^* + 2i(B_1C_2'' + B_2C_1'')))}{64\Delta^3} \\ &\quad + \frac{3\Delta_x i\,(12A_1\Delta_x^2 C_2' + 3C_1^*\Delta_z^-(2A_2\Delta - C_2\Delta_x) + (2B_1\Delta A_2''\Delta_z^- + 3iC_1\Delta A_2^*\Delta_z^-))}{64\Delta^3},\end{aligned} \tag{5.39}$$

$$\begin{aligned}\tilde{\mathcal{H}}_{13} &= \frac{2\left(\Delta_z^z(B_2\Delta_x(B_1-3C_1')-3B_1(2\Delta_z A_2'+\Delta_x C_2'))-6B_2\Delta_x^2 A_1'\right)}{64\Delta^2}\\ &+\frac{9\Delta_x C_2^*(2A_1\Delta_x+C_1\Delta-C_1\Delta_z)+9C_1^*\Delta_z^-(2A_2\Delta_z+C_2\Delta_x)}{64\Delta^2}\\ &+\frac{18\Delta_x A_1^*(2A_2\Delta_z+C_2\Delta_x)+18\Delta_z A_2^*(2A_1\Delta_x+C_1\Delta-C_1\Delta_z)}{64\Delta^2}\,,\end{aligned} \tag{5.40}$$

$$\begin{aligned}\tilde{\mathcal{H}}_{23} &= \frac{3i\left(2i(\Delta_x(\Delta_z^-(B_1C_2''+B_2C_1'')+2iB_2\Delta_x A_1')+2iB_1\Delta_z A_2'\Delta_z^-)\right)}{64\Delta^2}\\ &+\frac{12i\left(A_1B_2\Delta_x^2+A_2B_1\Delta_z\Delta_z^-\right)+9i\Delta_x C_2^*(2A_1\Delta_x-C_1\Delta+C_1\Delta_z)}{64\Delta^2}\\ &+\frac{3i\left(6\Delta_z A_2^*(-2A_1\Delta_x-C_1\Delta+C_1\Delta_z)-6\Delta_x A_1^*(C_2\Delta_x-2A_2\Delta_z)\right)}{64\Delta^2}\\ &+\frac{3i\left(3C_1^*\Delta_z^-(2A_2\Delta_z+C_2\Delta_x)\right)}{64\Delta^2}\,,\end{aligned} \tag{5.41}$$

$$\begin{aligned}\tilde{\mathcal{H}}_{11} &= \frac{2(6B_2\Delta_x\Delta_z A_1'-\Delta_z^-(6B_1\Delta_x A_2'+B_2\Delta_z(B_1-3C_1')-3B_1\Delta_z C_2'))}{32\Delta^2}\\ &+\frac{18\Delta_x A_2^*(2A_1\Delta_x+C_1\Delta-C_1\Delta_z)-9C_1^*\Delta_z^-(C_2\Delta_z-2A_2\Delta_x)}{32\Delta^2}\\ &+\frac{18\Delta_x A_1^*(2A_2\Delta_x-C_2\Delta_z)+9\Delta_z C_2^*(-2A_1\Delta_x-C_1\Delta+C_1\Delta_z)}{32\Delta^2},\end{aligned} \tag{5.42}$$

$$\begin{aligned}\tilde{\mathcal{H}}_{22} &= -\frac{9C_2^*(2A_1\Delta_x-C_1\Delta+C_1\Delta_z)+18C_2\Delta_x A_1^*+9C_2C_1^*\Delta_z^-}{32\Delta^2}\\ &+\frac{2(6B_2\Delta_x A_1'+\Delta_z^-(B_1(B_2+3C_2')+3B_2C_1'))}{32\Delta^2}\,,\end{aligned} \tag{5.43}$$

$$\tilde{\mathcal{H}}_{33} = 0\,, \tag{5.44}$$

and the rest of the components $\tilde{\mathcal{H}}_{ij}$ are obtain from $\tilde{\mathcal{H}}_{ji}$ by exchanging $i \leftrightarrow j$.

Part II

Weak magnetic field amplification for room-temperature magnetometry

CHAPTER 6

Introduction

Magnetic resonance techniques not only provide powerful imaging tools that have revolutionized medicine, but they have a wide spectrum of applications in other fields of science like biology, chemistry, neuroscience, and physics [117, 118]. In order to resolve structures on the nanometer scale and thus image individual molecules, however, one needs to go beyond conventional magnetometric techniques. In particular, standard nuclear magnetic resonance (NMR) and magnetic resonance imaging (MRI) experiments detect magnetic fields through the current induced inside a coil according to Faraday's law; unfortunately induction-based detection is not sensitive enough to allow resolution in the sub-micrometer regime [119].

Over the last years, a lot of experimental effort has been put into improving magnetic detection schemes. At present, Hall-sensors and SQUID sensors are among the most sensitive magnetic field detectors [120, 121]. Furthermore, a great deal of success has been achieved with magnetic resonance force microscopy, where the force between a magnetic tip and the magnetic moment under investigation is exploited to detect single electron-spins, achieving a resolution of a few cubic nanometers [122, 123, 124]. On the other hand, the very low temperatures that are required in such schemes represent a considerable drawback to imaging systems in many biological environments.

NV-center spins also provide very good candidates for magnetometry, boosting sensitivities up to a few $\mathrm{nT}/\sqrt{\mathrm{Hz}}$ at room temperature [13, 14, 15, 16, 17, 18] and sub-nanometer spatial resolution, permitting three-dimensional imaging of nanostructures [14]. These results are realizable

due to the amazingly long decoherence times of NV-centers at room temperature and the ability to noninvasively engineer an NV-magnetometer very close to the magnetic sample. Although impressive, current state-of-the-art technology [19] is unable to detect a single nuclear spin; achieving such sensitivity would revolutionize magnetic imaging in chemical and biological systems by facilitating atomic resolution of molecules.

In this work, we propose an experimental realization of NV-magnetometers which could increase present NV-center sensitivities by four orders magnitude at room temperature; this unprecedented amplification of sensitivity forecasts magnetometers capable of detecting individual nuclear spins. This can be achieved by introducing a ferromagnetic particle between the spin that needs to be detected, which henceforth we call a qubit,[1] and the NV-magnetometer. When excited on resonance by the driven qubit, the macroscopic ferromagnetic spin begins to precess which, in turn, amplifies the magnetic field felt by the NV-center. By resonantly addressing the qubit and using a ferromagnetic resonator as a lever, our setup, in contrast to existing schemes, is particularly advantageous because, due to the large amplification of sensitivity, the nuclear spin need not lie within a few nanometers of the surface [125] but rather can be detectable at a distance of 30 nm, and, while related existing schemes rely on the *quantum* nature of a mediator spin [126], our proposal is *fully classical*. With these novelties, our scheme provides chemically sensitive spin detection.

[1]We emphasize that we denote the target magnetic moment by 'qubit' solely for the purpose of convenience in nomenclature and that our scheme does not rely on the quantum nature of the magnetic moment we aim to measure.

CHAPTER 7

High-efficiency resonant amplification of weak magnetic fields for single spin magnetometry

Adapted from:
Luka Trifunovic, Fabio L. Pedrocchi, Silas Hoffman, Patrick Maletinsky, Amir Yacoby, and Daniel Loss
"High-efficiency resonant amplification of weak magnetic fields for single spin magnetometry",
Nature Nanotechnology **10**, 541 (2015)

Magnetic resonance techniques not only provide powerful imaging tools that have revolutionized medicine, but they have a wide spectrum of applications in other fields of science like biology, chemistry, neuroscience, and physics. However, current state-of-the-art magnetometers are unable to detect a single nuclear spin unless the tip-to-sample separation is made sufficiently small. Here, we demonstrate theoretically that by placing a ferromagnetic particle between a nitrogen-vacancy (NV) magnetometer and a target spin, the magnetometer sensitivity is improved dramatically. Using materials and techniques already experimentally available, our proposed setup is sensitive enough to detect a single nuclear spin within ten milliseconds of data acquisition at room temperature. The sensitivity is practically unchanged when the ferromagnet surface to the target spin separation is smaller than the ferromagnet lateral dimensions; typically about a tenth of a micron. This scheme further benefits when used for NV ensemble measurements, enhancing sensitivity by an additional three orders of magnitude. Our proposal opens the door for nanoscale nuclear magnetic resonance (NMR) on biological material under ambient conditions.

7.1 Setup

The standard experimental setup, yielding the most accurate NV-magnetometers [14]), consists of an NV-center near the target qubit and two distinct microwave sources that independently control the NV-center and qubit so that double electron-electron (electron-nuclear) resonance, DEER (DENR), can be performed. We extend this setup by including a macrospin ferromagnetic particle (FM) between the NV-magnetometer and the qubit we want to measure, see Fig. 7.1. A recent experiment [127, 128] demonstrates that there is no significant quenching of the NV-center photoluminescence in the presence of the FM. On the other hand, due to the stray field of the FM, the qubit energy-splitting, and therefore the frequency (ω_s) at which the qubit responds resonantly, is strongly modified; one needs first to characterize the FM stray field in order to be able to control the qubit by, in our case, applying π-pulses.[1] Treating the ferromagnet as a single classical spin, the Hamiltonian of this system is [130, 131]

$$H = KV(1 - m_z^2) + M_F V b m_z - \mu_s \boldsymbol{n}_s(t) \cdot \mathbb{B}_F \boldsymbol{m}, \tag{7.1}$$

[1] Instead of performing the qubit control resonantly, one can make use of 'adiabatic passage' [129] wherein triangular pulses are applied in lieu of square pulses. In such a setup, knowledge of the exact value of the qubit Zeeman splitting, and therefore the FM stray field, is not needed.

where $\boldsymbol{m}$ is the normalized magnetization of the FM, M_F the saturation magnetization of the FM, and V its volume. We assume uniaxial anisotropy in the FM with the anisotropy constant, $K > 0$, composed of both shape and crystalline anisotropy, with an easy axis along z. An external magnetic field b is applied along the z axis. The magnetic moment of the qubit is μ_s and $\boldsymbol{n}_s(t)$ is its polarization at time t. The 3×3-matrix $\mathbb{B}_F$ is defined as $(\mathbb{B}_F)_{ij} = \boldsymbol{B}_F^j(\boldsymbol{r}_s)\cdot\boldsymbol{e}_i$, where $\boldsymbol{B}_F^j(\boldsymbol{r}_s)$ is the stray field produced by the FM at the position of the qubit, $\boldsymbol{r}_s$, when the FM is polarized along the j-axis for $j = x$, y, or z. The Hamiltonian of the qubit is not explicitly written as its polarization is completely determined by the externally applied static and time-dependent microwave field and the stray field of the FM. For example, in equilibrium the ground state of the qubit is polarized along the total static field acting on it $\boldsymbol{n}_s = (\boldsymbol{b} \pm \boldsymbol{B}_F^z)/|\boldsymbol{b} \pm \boldsymbol{B}_F^z|$ when $m_z = \pm1$. Although in the following we take V small enough to approximate the FM as a monodomain, our analysis and therefore our results are amenable to including the effects of magnetic texture.

Using two independent microwave sources we apply a train of π-pulses first to the qubit and subsequently a Carr-Purcell-Meiboom-Gill (CPMG) pulse sequence [132, 133] to the NV-center, see Fig. 7.2. As the qubit is pulsed it will drive the FM at the frequency of the pulse sequence π/τ, τ being the time between the application of two subsequent π-pulses. When π/τ is close to the ferromagnetic resonance (FMR) frequency, ω_F, the response of the FM becomes large and one obtains a large amplification of the magnetic field felt by the NV-center. The pulses are applied to the qubit only until the FM reaches steady state precession. We also allow for a possible time offset, ξ, between the pulse sequences applied to the qubit and the NV-center, see Fig. 7.2. Here, ξ may be chosen to compensate for the phase difference between the driving of the qubit and the response of the FM, thus maximizing the sensitivity of our magnetometry scheme. Since the microwave field applied to the qubit is a sequence of π-pulses, the polarization is simply $\boldsymbol{n}_s(t) = \boldsymbol{n}_s f_\tau(t)$, where $f_\tau(t)$ may take the values ±1 according to the pulse sequence. It is worth noting that even though we excite the FMR with the inhomogeneous dipolar field of the qubit, only the lowest Kittel mode is excited since for a small FM higher modes are separated by an energy gap that exceeds the perturbation amplitude. Therefore the macrospin approximation used in Eq. (7.1) is justified.

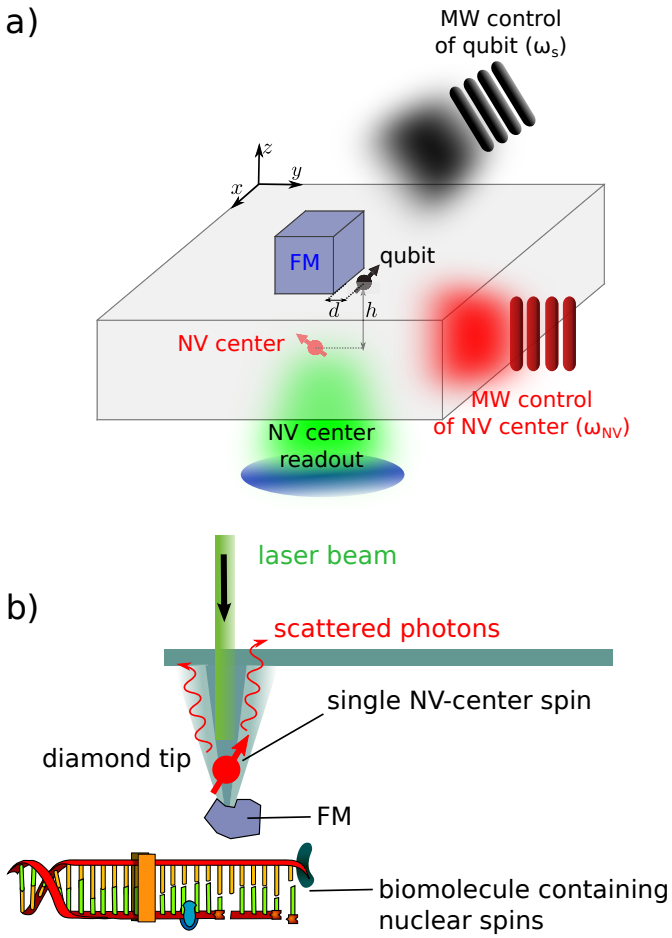

Figure 7.1: Panel a) shows a detailed illustration of the setup considered. The abbreviation "FM" denotes the ferromagnetic particle that is placed on top of the diamond surface that contains the NV-center (red) which is used as magnetometer. Close to the top surface of the FM lies the qubit (black) we want to measure. The setup also includes separate microwave (MW) controls of the qubit (black) and NV-center (red) with resonance frequencies ω_s and $\omega_{\rm NV}$, respectively. The ferromagnetic resonance frequency ω_F is assumed to be different from both ω_s and $\omega_{\rm NV}$. The NV-center is read out optically with a green laser. A slightly modified version of the setup with the NV-center and the FM on a tip is illustrated in panel b); for simplicity we have omitted the two driving fields in this panel.

7.2 Proposed magnetometer sensitivity

We now consider our particular scenario wherein a FM is introduced at a distance d from the qubit and h from the NV-center (Fig. 7.1). In this case, both the accumulated phase and the dephasing of the NV-center are modified by the presence of the FM. Because the sensitivity of our magnetometry scheme crucially depends on the series of pulses applied to the NV-center and qubit, here we detail the pulse sequence, see Fig. 7.2. First we apply, on the qubit only, N' π-pulses separated by a time interval τ, for a total time of $t' = N'\tau$—during this time the FM reaches steady state precession. Next we initialize the NV-center in state $|0\rangle$, which takes time t_p that is on the order of few hundreds of nanoseconds. Then, a $\pi/2$ pulse is applied to the NV-center allowing it to accumulate the phase from the FM tilt stray field. Consequently, a series of N π-pulses are applied to both the NV-center and qubit for a total interrogation time $t_i = N\tau$. Finally we apply to the NV-center a $\pi/2$-pulse which is, in general, along an axis in the plane orthogonal to the NV-center axis and different from the first $\pi/2$-pulse by an angle θ. The probability that the NV-center occupies the state $|0\rangle$ or $|1\rangle$ after the pulse sequence is now a function of the accumulated phase $\varphi_{\rm NV}(t_i)$

$$p(n|\varphi_{\rm NV}(t_i)) = \frac{1}{2}\left(1 + n\cos(\varphi_{\rm NV}(t_i) + \theta)e^{-\langle(\delta\varphi_{\rm NV}(t_i))^2\rangle}\right). \tag{7.2}$$

Here, $n = \pm 1$ are the two possible outcomes when the state of the NV-center is measured, $\langle(\delta\varphi_{\rm NV}(t_i))^2\rangle$ is the dephasing of the NV-center, and $\langle\cdots\rangle$ is the expectation value in the Gibbs state. Because the accumulated phase itself depends on the value of the qubit magnetic moment μ_s, a measurement of the NV-center is a measurement of μ_s. The variance in the measured value of the NV-center can be reduced by repeating the measurement $\mathcal{N}$ times (Fig. 7.2). Because typically $t' \ll \mathcal{N}t_i$ and therefore $t' + \mathcal{N}t_i \approx \mathcal{N}t_i$, the total measurement time is marginally prolonged by the initial pulse sequence that initialized the tilt of the FM.

Given Eq. (7.2), one may show quite generally that the sensitivity of the NV-magnetometer is given by

$$S = \frac{1}{R\sqrt{\eta}}\min_{t_i}\left[\frac{e^{\langle(\delta\varphi_{\rm NV}(t_i))^2\rangle}\sqrt{t_i + t_p}}{|\partial\varphi_{\rm NV}(t_i)/\partial\mu_s|}\right], \tag{7.3}$$

which defines the minimum detectable magnetic field for a given total measurement time. Here, R, the measurement contrast, is the relative

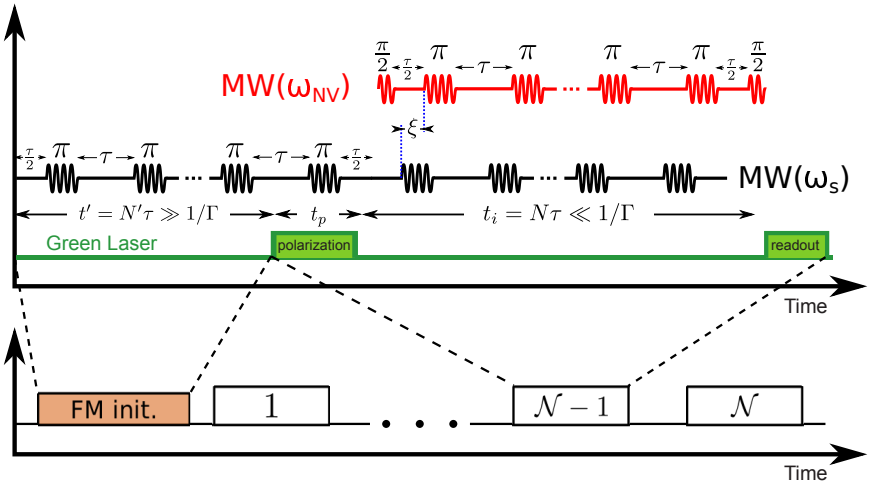

Figure 7.2: The pulse sequence that we apply to the qubit (black) and to the NV-center spin (red). The pulse sequence $f_\tau(t)$ that consists of N (N is even) is applied to both spins, with the time offset ξ, during the interrogation time $t_i = N\tau$. The measurement is repeated $\mathcal{N}$ times until the desired precision is achieved, as illustrated on the bottom panel. The sequence section denoted by "FM init" with duration $t' = N'\tau$ is the time during which the precession of the FM is being developed. We assume that the frequencies ω_s, $\omega_{\rm NV}$, and ω_F are all sufficiently different from each other. The green laser is applied to the NV-center for initialization (polarization) and read-out. The total measurement time is $t'+\mathcal{N}t_i \approx \mathcal{N}t_i$.

difference in detected signal depending on spin-projection of the NV-center spin, and η is the detection efficiency which takes into account that many measurements have to be performed in order to detect a photon [134]. A detailed derivation of Eq. (7.3) can be found in Supplementary Information, Sec. II. The sensitivity is small (*i.e.*, 'good') when the NV-center dephasing is small while the accumulated phase is large. When the qubit is directly coupled to the NV-center (without the FM) the dephasing time of the NV-center is given by $T_2 \sim 200$ μs [135, 136] so that $\langle(\delta\varphi_{\rm NV}(t_i))^2\rangle = (t_i/T_2)^2$.

As we show in Supplementary Information, Sec. IV, given the pulse sequence described above, when $\Gamma t' \gg 1$ and $\Gamma t_i \ll 1$, where Γ is the linewidth of the ferromagnet, there is a *resonant* response of the FM while the NV-center picks up *non-resonant* noise. As such, the ratio of the dephasing to the accumulated phase of the qubit is minimized thereby optimizing the sensitivity. We henceforth take $\Gamma t' \gg 1 \gg \Gamma t_i$ in the remainder

of the text.

The accumulated phase is formally

$$\varphi_{\rm NV}(t_i) = \gamma_{\rm NV} \int_0^{t_i} B_{\rm NV}(t'') f_\tau(t'') dt'' \,, \tag{7.4}$$

where $\gamma_{\rm NV}$ is the gyromagnetic ratio of the NV. $B_{\rm NV} \equiv \left| \boldsymbol{B}^-_{F,\rm NV} \cdot \boldsymbol{n}_{\rm NV} \right|$ where $\boldsymbol{B}^\pm_{F,\rm NV} = \boldsymbol{B}^x_F(\boldsymbol{r}_{\rm NV}) \pm i\boldsymbol{B}^y_F(\boldsymbol{r}_{\rm NV})$ [$\boldsymbol{B}^\pm_{F,s} = \boldsymbol{B}^x_F(\boldsymbol{r}_s) \pm i\boldsymbol{B}^y_F(\boldsymbol{r}_s)$] is a complex combination of the magnetic stray-field for the FM polarization along the x and y axes at the position of the NV-center (qubit), $\boldsymbol{r}_{NV}$ ($\boldsymbol{r}_s$), and $\boldsymbol{n}_{\rm NV}$ is the NV-center polarization axis. We note that $\boldsymbol{B}^\pm_{F,\rm NV} \cdot \boldsymbol{n}_{\rm NV}$ ($\boldsymbol{B}^\pm_{F,s} \cdot \boldsymbol{n}_s$) is the FM-NV (FM-qubit) coupling constant.

Within the linear response regime and using the pulse sequence described above and optimally choosing ξ, the expression for the phase accumulated by the NV-center when $\tau = (2k+1)\pi/\omega_F$, [2] for $k = 0, 1, \ldots$, is

$$\varphi_{\rm NV}(t_i) = \frac{4\mu_s \gamma \gamma_{\rm NV} |\boldsymbol{B}^+_{F,s} \cdot \boldsymbol{n}_s| |\boldsymbol{B}^-_{F,\rm NV} \cdot \boldsymbol{n}_{\rm NV}|}{\pi^2 (2k+1)^2 M_F V \Gamma} t_i \,, \tag{7.5}$$

where γ is the gyromagnetic ratio of the FM. k is defined such that the resonantly driven FM undergoes $2k+1$ half-periods between consecutive π-pulses applied to the NV-center. In the optimal case we have $k = 0$ so that τ is half the period of precession of the ferromagnet. The details of the derivation of Eq. 7.5 can by found in Supplementary Information, Sec. IV. It is readily observed from the above equation that $\varphi_{\rm NV}(t_i) \sim 1/\Gamma$ which is proportional to the AC magnetic susceptibility of the FM on resonance; thus we indeed obtain a resonant response as anticipated. Even though the phase $\varphi_{\rm NV}$ accumulated due to the FM tilt is large, the angle of the FM tilt is small ($\sim 10^{-3}$ if the qubit is a nuclear spin) because $M_F V \gg \mu_s$. Therefore, we can neglect the effects of the backaction of the FM tilt on the qubit, because the stray field modulation induced by the tilt is small compared to the qubit Rabi amplitude and far detuned from the qubit Larmor precession frequency (i.e. $\omega_F \neq \omega_s$). Thus, the qubit is polarized along the total field $\boldsymbol{n}_s = (\boldsymbol{B}^z_F + \boldsymbol{b})/|\boldsymbol{B}^z_F + \boldsymbol{b}|$; the scalar product $\boldsymbol{B}^+_{F,s} \cdot \boldsymbol{n}_s$ is nonzero only if the stray field of the FM tilt has a component along $\boldsymbol{n}_s$ at the position of the qubit, see Fig. 7.3. We address the optimal geometry and position of the qubit relative to the FM in Methods, Sec. 7.5.

[2] The Fourier transform of the CPMG pulse sequence has peaks at frequencies $(2k+1)\pi/\tau$

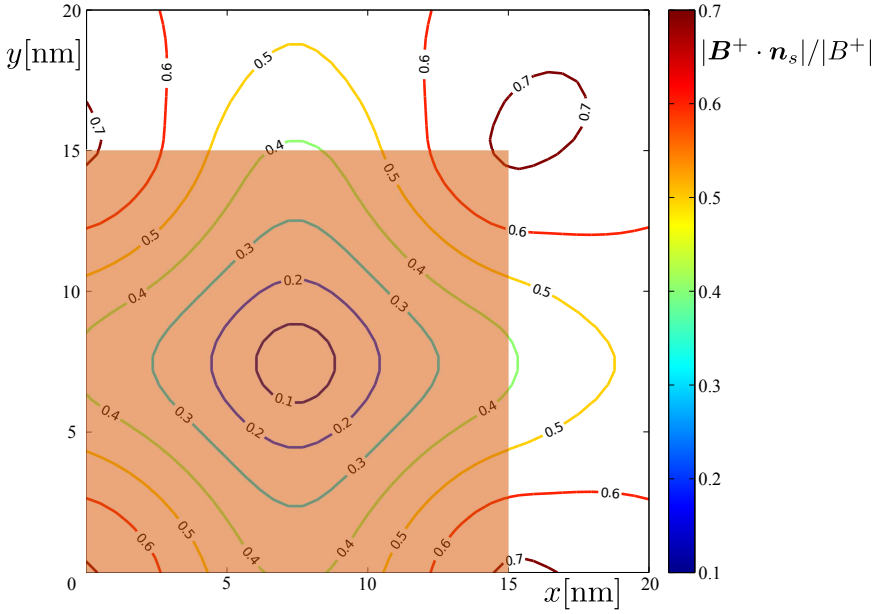

Figure 7.3: Contour plot of the quantity $|\boldsymbol{B}^+ \cdot \boldsymbol{n}_s|/|B^+|$ in the xy-plane that is 2 nm above the upper face of the cube. We assume the FM cube (orange square) has a side length of $L = 15$ nm. The values of the stray fields are obtained from OOMMF micromagnetic simulations, taking into account the demagnetizing field.

The relevant dephasing is the maximum of the inherent dephasing of the NV-center, $(t_i/T_2)^2$, and the dephasing due to the coupling to the FM [132],

$$\beta(t_i, \tau) = \gamma_{\rm NV}^2 \int_0^{t_i} ds S(s) \int_0^{t_i - s} dt'' f_\tau(t'') f_\tau(t'' + s). \tag{7.6}$$

Here $S(s) = \langle B_{\rm NV}(s) B_{\rm NV}(0) \rangle$ is the autocorrelation function of the FM noise. Again taking $\tau = (2k+1)\pi/\omega_F$, we show in Supplementary Information, Sec. IV B that

$$\beta(t_i, \tau) = \frac{4\gamma\gamma_{\rm NV}^2 |\boldsymbol{B}_{F,\rm NV}^+ \cdot \boldsymbol{n}_{\rm NV}|^2 k_B T}{\pi^2 (2k+1)^2 M_F V \omega_F} t_i^2 \equiv (t_i/T_2')^2 \,, \tag{7.7}$$

where T_2' (T_2) is the decoherence time of the NV-center caused by the FM. Because $\beta(t_i, \tau) \sim 1/\omega_F \sim S(\omega = 0)$, the NV-center indeed accumulates non-resonant noise.

The value of the NV-center decoherence rate when the FM volume is chosen as small as possible (see Eq. 7.9) becomes $T_2'^{-1} \sim \gamma_{\rm NV} |\boldsymbol{B}_{F,\rm NV}^+ \cdot \boldsymbol{n}_{\rm NV}|$.

Furthermore, since the optimal interrogation time is $t_i \sim T_2'$, we obtain that for typical values of the FM stray field we are in the limit $t_i \ll t_p$. After substituting $\langle(\delta\varphi_{\rm NV}(t_i))^2\rangle = \beta(t_i,\tau)$ and $\varphi_{\rm NV}(t_i)$ from Eq. (7.5) and Eq. (7.7) into Eq. (7.3) and performing the minimization over the interrogation time in Eq. (7.3), we find the sensitivity S_A of our magnetometry scheme

$$S_A = \frac{1}{R\sqrt{\eta}} \frac{\pi e^{\frac{1}{2}}(2k+1) M_F V \Gamma}{\sqrt{2}\gamma |\boldsymbol{B}^{+}_{F,s} \cdot \boldsymbol{n}_s|} \sqrt{\frac{\gamma k_B T t_p}{M_F V \omega_F}}. \tag{7.8}$$

The best sensitivity is obtained when one half-period of the FM oscillation occurs over the timescale τ, *i.e.*, $k = 0$. In practice, experimental limitations, such as limitations to the qubit Rabi frequency, bound τ and therefore k from below. Thus, in order to achieve the resonance, one has to use $k \gg 0$ (at the expense of sensitivity) or to tune the FMR frequency as described in the following subsection. We note that since the sensitivity in Eq. 7.8 scales as $S_A \sim \Gamma$, using low loss FM materials like Yttrium Iron Garnet (YIG) is crucial for achieving high sensitivities.

A few comments are in order regarding the obtained expression for the sensitivity in Eq. 7.8. First, we note that S_A is completely independent of the FM-NV coupling constant $|\boldsymbol{B}^{\pm}_{F,\rm NV} \cdot \boldsymbol{n}_{\rm NV}|$—this behavior holds as long as the stray field at position of the NV is not too weak, since otherwise a weak FM-NV coupling leads to long T_2' and thus we are no longer in the limit $t_i \ll t_p$ and thus Eq. 7.8 is no longer valid. Therefore, S_A depends only on d but not on h (see Fig. 7.1). Having a magnetometer with the sensitivity that is independent of the NV positioning [3] is particularly advantageous for NV ensemble measurements since we can place many NV-centers that would all have the same sensitivity (though different optimal interrogation times) and thus obtain significant improvement of the total sensitivity. Finally, S_A depends on the FM-qubit coupling constant and therefore depends on d. But herein, rather than having a sensitivity that has cubic dependence on the tip-to-sample separation, we have only weak dependence on d since the FM stray field is not changed much as long as $d \ll L \equiv V^{1/3}$ (see Methods, Sec. 7.5). The spatial resolution of our scheme does not differ from the standard NV-magnetometry resolution [14]. In practice the spatial resolution for detection of an isolated spin is determined by the ratio between the magnetic field gradient and the target qubit linewidth. In the case of interacting spins there is a broadening caused by homonuclear dipolar interaction, thus the techniques such

[3] We stress that this statement is true only in region of space near the FM where $T_2' \ll t_p$, i.e., where the FM stray field is bigger that the threshold value $B_{\rm th} \sim 1$ Gauss.

as magic angle spinning (MAS) should be used [137]. Since MAS is usually performed by spinning the sample in a static magnetic field which is impractical for our scheme, one can use rotating magnetic fields [138] instead, with the frequency different from ω_{NV}, ω_F and ω_s for performing MAS.

While the electron spin in a NV-center can be driven at GHz frequencies [139, 140], the same driving field for a proton spin would yield Rabi frequency in the MHz range. Thus, the FMR frequency needs to be tuned to meet the resonance critieria. The method to achieve such a tuning is described in Methods, Sec. 7.5. The idea is to use the metastable state of the FM which has frequency that can be lowered by applying an external magnetic field, see Fig. 7.4. In order for the FM to remain in the metastable state during the measurement time, the FM volume must satisfy

$$V \gtrsim \frac{\gamma k_B T}{M_F \omega_F^+} |\ln \alpha|, \tag{7.9}$$

In case of minimal volume, the sensitivity reads

$$S_A = \frac{1}{R\sqrt{\eta}} \frac{\pi(2k+1)\alpha\sqrt{e|\ln\alpha|t_p} k_B T}{\sqrt{2}|\boldsymbol{B}_{F,s}^+ \cdot \boldsymbol{n}_s|} \,. \tag{7.10}$$

As noted earlier, the sensitivity of our scheme does not depend on the FM-NV coupling constant. Thus, we can take advantage of this fact to obtain an improvement of sensitivity by a factor of $\sqrt{N_{\rm NV}}$, when $N_{\rm NV}$ NV-centers are used for the detection. We present a detailed discussion in Sec. 7.5 of the Methods.

Estimates

In this section we give estimates for the sensitivity S_A for two cases: with and without tuning of the FMR frequency (to MHz range). We also provide the estimates for the case when an NV ensemble is used for the measurement. For all the estimates provided in the following, we assume room temperature and that the FM material is YIG, so that $\alpha \sim 10^{-5}$, $\mu_0 M_F = 0.185$ T, and $K/M_F = 60$ mT [141]. For simplicity but without loss of generality, we assume that the FM has the shape of a cube for the estimates given below. For a cube and in the macrospin approximation there is no contribution from shape anisotropy.

If we tune the FMR frequency to MHz range the minimum FM volume V according to Eq. (7.9) corresponds to a cube with side $L = 210$ nm.

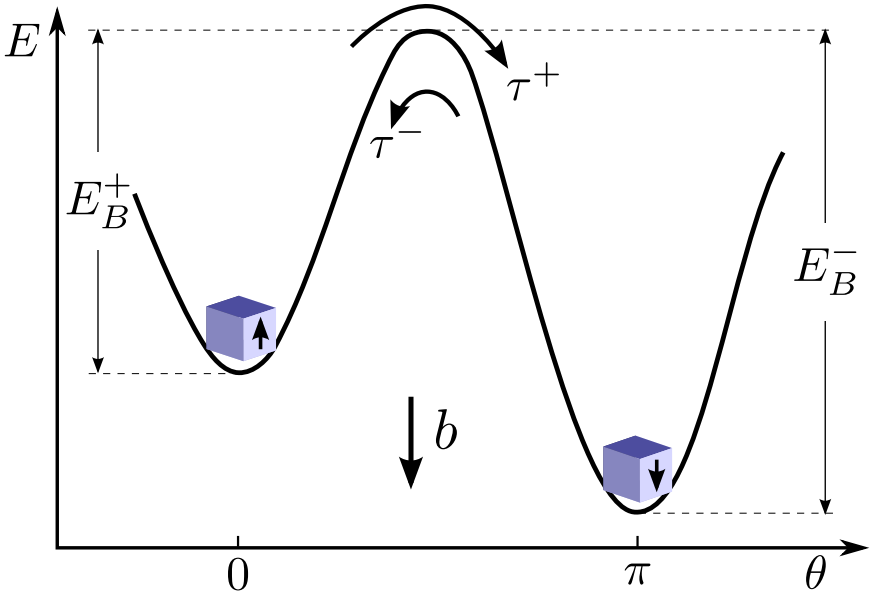

Figure 7.4: The FM energy when an external field $b/b_a = 0.2$ is applied, *i.e.*, the first two terms from the right-hand side of Eq. (7.1) of the main text, as a function of θ, where $m_z = \cos\theta$. The metastable state at $\theta = 0$ has smaller FMR frequency compared to the case with no external field. The tunneling time τ^+ from the metastable state has to be longer than the measurement time. We note that $E_B^+ = M_F V(b_a - b)$.

We note that since $t_i \ll t_p \ll \tau$ (see Fig. 7.2) one essentially performs DC magnetometry with the NV. Furthermore, S_A being weakly dependent on d for $d \ll L$ means that we can increase the "FM surface"-to-"target spin" separation up to values of hundred nanometers practically without decreasing the sensitivity S_A. Taking $t_p \sim 300$ ns and estimating $R\sqrt{\eta}$ [13], we obtain $S_A = 0.13\mu_N/\sqrt{\text{Hz}}$, where μ_N is the nuclear magneton. Thus, our magnetometry scheme can detect a single nuclear spin within ten milliseconds of data acquisition at room temperature. For comparison, standard NV-magnetometry setups with the state-of-the-art magnetic field sensitivity [142] $S = 4.3$ nT$/\sqrt{\text{Hz}}$ needs a $\sim$100 times smaller tip-to-sample separation [143, 144] of 2.5 nm in order to achieve the same magnetic moment sensitivity.

For the electron spin, the minimal FM volume V according to Eq. (7.9) corresponds to a cube with side $L = 21$ nm in this case. Using the same parameters as in the previous paragraph we obtain $S_A = 0.32\mu_N/\sqrt{\text{Hz}}$.

Typical values of the stray fields at the position of the qubit and NV-

center in the limit $d, h \ll L$ for YIG are on the order of a few hundreds of Gauss. The presence of a magnetic field perpendicular to the NV-center axis can significantly limit the read-out fidelity of the NV-center, it was found that fields up to 100 Gauss can be tolerated [9]. Since the sensitivity S_A does not depend on the FM-NV coupling constant, the NV should be placed in the region where the stray field $B_{F,\mathrm{NV}}$ is less than 100 Gauss but bigger than the threshold value B_{th}, i.e., 1 Gauss $< B_{F,\mathrm{NV}} < 100$ Gauss. For $|\boldsymbol{B}^{\pm}_{F,\mathrm{NV}} \cdot \boldsymbol{n}_{\mathrm{NV}}| \sim 10$ Gauss, the decoherence time of the NV is $T_2' \sim 100$ ns [see Eq. (7.7)], which is also the value of the optimal interrogation time. Thus, because the signal amplification in our scheme far exceeds the effect of the additional decoherence it induces, even shallow NV-centers [136, 135] or dense ensembles of NV-centers [134] with relatively short decoherence time can be used and significantly outperform long-lived NV-centers (without the FM).

Finally, we give the estimates for the case of the FMR tuned to the MHz range and for measurements with ensembles of NV-centers. As experimentally demonstrated [145], NV ensembles with a separation of about 10 nm between neighboring NV-centers can be achieved. Such NV ensembles have $T_2^* \sim 100$ ns, but this property, as noted in the previous paragraph, does not affect the sensitivity of our scheme. We can distribute the NV-centers in the volume where the stray field satisfies $B_{F,\mathrm{NV}} > B_{\mathrm{th}}$ and such a volume can be estimated to be a cube with side length of 1 μm. Therefore, $N_{\mathrm{NV}} \sim 10^6$ which yields an unprecedented sensitivity of $\tilde{S}_A = 0.13 \times 10^{-3} \mu_N / \sqrt{\mathrm{Hz}}$.

7.3 Conclusions

We have proposed and analyzed, both analytically and numerically, a modification of a standard NV-magnetometry setup that yields a significant improvement of NV-magnetometer sensitivity—the obtained sensitivity is practically unchanged as long as the ferromagnet surface to the target spin separation is smaller than the ferromagnet lateral dimensions which is typically about a tenth of a micron. Our scheme is based on a ferromagnetic particle, placed in close proximity to a sensing NV-center spin. The qubit spin to be detected is then used to resonantly drive the large macrospin of the FM giving rise to a strong, amplified stray field acting on the NV-magnetometer. Compared to the existing schemes that use the quantum nature of an intermediate spin for improving sensitivity [126], we stress that our scheme is fully classical and thus should be

easily realizable at room temperature—all the ingredients of our scheme are already demonstrated in separate experiments [139, 140, 14, 146, 128, 127, 147].

The magnetometric scheme including a ferromagnetic particle proposed here is a step forward to a more accurate magnetic field measurement. In particular, it enables the detection of a single nuclear spin at distances that are noninvasive to the system under study. Therefore, the proposed room temperature magnetometry scheme opens up new venues for future analyses of previously inaccessible biological and chemical systems.

7.4 Acknowledgments

We would like to thank H. Fanghor for sharing his expertise about micromagnetic simulations. This work was supported by the SNF, NCCR QSIT, IARPA, DARPA QuASAR programs and the MURI QuISM. F. L. P. is grateful for support from the Alexander von Humboldt foundation.

7.5 Methods

Tuning the FMR frequency

It has been demonstrated experimentally [139, 140] that the electron spin of NV-centers can be coherently driven at GHz frequency. For a proton spin, however, the same drive would yield Rabi oscillations in the MHz range. Because typical FMR frequencies are in GHz range, ω_F needs to be reduced in order for the proton Rabi frequency to be on resonance with the FMR.

One way to decrease ω_F is to apply an external magnetic field antiparallel to $\boldsymbol{m}$ [148], whereby there is a metastable state when $b < b_a$, with $b_a = K/M_F$ the FM (crystalline and shape) anisotropy field. In Fig. 7.4, we plot the energy of the FM as a function of angle θ of the magnetization with respect to the easy axis, according to Eq. (7.1) of the main text. It is straightforward to show that the FMR frequency in the metastable state is $\omega_F^+ = \gamma(b_a - b)$. On the other hand, the ferromagnet will relax to the thermal state on a timescale τ^+ given by the Arrhenius law $\tau^+ = \tau_0 e^{E_B^+/k_B T}$, where $\tau_0 \sim 1/\omega_F^+$ is the attempt time. We can insure that the FM is initialized in the metastable state by first measuring the direction of the magnetization, applying an external magnetic field $\boldsymbol{b}$ antiparallel to $\boldsymbol{m}$

and checking subsequently that the FM magnetization direction is unchanged, which can be done under hundred picoseconds [149, 150, 151].

In order for the ferromagnet to remain in the metastable state while the measurement is being performed, we require $\tau^+ \gg 1/\Gamma$. Indeed, the total measurement time T should be larger than the FMR initialization time $t' \gg 1/\Gamma$, and smaller than Arrhenius' timescale $\tau^+ \gtrsim T$, see Fig. 7.2 in the main text. Thus, if we want to tune ω_F^+ to a certain value and work at room temperature, the Arrhenius law suggests that the FM volume must satisfy

$$V \gtrsim \frac{\gamma k_B T}{M_F \omega_F^+} |\ln \alpha|, \tag{7.11}$$

in order for the metastable state lifetime to be bigger than the measurement time. Here $\alpha = \Gamma/\omega_F^+$ is the Gilbert damping of the FM. Substituting Eq. (7.9) for the minimal volume into Eq. (7.8) of the main text we obtain

$$S_A = \frac{1}{R\sqrt{\eta}} \frac{\pi(2k+1)\alpha\sqrt{e|\ln\alpha|t_p} k_B T}{\sqrt{2}|\boldsymbol{B}_{F,s}^+ \cdot \boldsymbol{n}_s|} \tag{7.12}$$

Compared to the sensitivity in Eq. (7.8) of the main text, the above expression is independent of the FMR frequency ω_F and the FM volume V. Thus, irrespective of the choice of the frequency we work at, the same value for the sensitivity S_A is obtained. Furthermore, the only dependence on the volume is incorporated in the stray fields but, as shown in Sec. 7.5, this dependence is weak in the limit $d \ll L$. The volume in Eq. (7.9) is implicitly bounded from above in order to remain in the regime where the macrospin approximation is valid.

An alternative setup to achieve resonance between the qubit and FM is to place the NV-center and the FM on a cantilever [152] with resonance frequency in the GHz range. By driving the cantilever, we alleviate the necessity of driving the qubit at FMR frequency as the qubit field is modulated by the oscillations of the cantilever. Since the dipolar field of the qubit decays rapidly with distance, the modulation of the qubit field achieved in this scheme is almost as big as when the qubit is driven via a microwave field (the previously described scheme for which the sensitivity estimates are given). Therefore, we conclude that the estimates for the sensitivity S_A given in Sec. 7.2 still hold in that case.

FM geometry and demagnetizing fields

In the absence of an external magnetic field, the qubit aligns along the stray field direction of the FM, while the FM spins are aligned along the easy axis. Because $M_F V \gg \mu_s$, the FM tilt induced by the qubit is negligible. Therefore, the qubit will align along the direction of the stray field produced by the FM. However, for most geometries of the FM and positions of the qubit, the FM-qubit coupling constant is almost zero, i.e. $|\boldsymbol{B}^{+}_{F,s} \cdot \boldsymbol{n}_s| \sim \boldsymbol{B}^{x,y}_{F,s} \cdot \boldsymbol{B}^{z}_{F,s} \sim 0$, and therefore the sensitivity is bad $S_A^{-1} \sim 0$. In the following discussion, we consider our ferromagnet to be a cube of side L, but our conclusions can be straightforwardly generalized to other geometries. To gain insight into the direction and strength of the stray field, we use the well-known analogy between the stray field of a homogeneously magnetized body and an electric field produced by surface charges. Specifically, we may consider the surfaces of the cube to have charge density $\sim M_F \, \boldsymbol{m} \cdot \boldsymbol{s}$, where $\boldsymbol{s}$ is the vector normal to the surface of the cube. Therefore, when the position of the qubit is very close to the center of the FM surface which is perpendicular to the polarization direction (here assumed along z-axis), $\boldsymbol{B}^{z}_{F,s}$ points along the z-axis. Similarly, $\boldsymbol{B}^{x}_{F,s}$ and $\boldsymbol{B}^{y}_{F,s}$ are almost aligned with the x and y axes close to the surface, respectively. Therefore, in these positions, $\boldsymbol{B}^{x,y}_{F,s} \cdot \boldsymbol{B}^{z}_{F,s} \sim 0$. However, this is not true near the edges of the ferromagnet. Therefore, in order to obtain a sensitive magnetometer, one needs, first, a ferromagnet with edges and, second, to position the qubit close to the edges. One may show analytically and numerically (see Fig. 7.3) that $|\boldsymbol{B}^{+} \cdot \boldsymbol{n}_s|/|B^{+}|$ close to the edges is about an order of magnitude bigger than close to the face center and that it has local maxima close to the cube's corners.

In evaluating $\boldsymbol{B}^{x,y,z}_{F,s}$, we assume that the FM is homogeneously magnetized as, in cubic geometry, one can find an analytical formula for the stray field in this case (see Supplementary Information, Sec. V). However, it is important to note that due to demagnetizing fields (arising from dipole-dipole interactions in the FM), the FM ground-state is not homogeneous but rather "flowerlike" [153]. Specifically, the canting of the spins close to the edges is more pronounced [154], which modifies the FM stray field close to the edges. To account for the effects of the demagnetizing fields, we perform micromagnetic simulations in OOMMF. [4] In Fig. 7.3 we plot $|\boldsymbol{B}^{+} \cdot \boldsymbol{n}_s|/|B^{+}|$ in the xy-plane that is 2 nm above the upper face of the cube. We find that the inclusion of demagnetizing fields changes our value of $\boldsymbol{B}^{x,y,z}_{F,s}$ by only $\sim 1\%$ as compared to the uniformly

[4] The code is available at http://math.nist.gov/oommf

magnetized cube. Therefore, we expect the analytical expression for the stray field to be valid for our choice of parameters.

Because the sensitivity S_A depends on d only through the stray field at the position of the qubit, herein we detail this dependence and show that the sensitivity of our magnetometry scheme is practically unchanged as d is varied. The stray field close to the cube edge (in comparison to L) is equivalent to the electric field of a set of infinite line charges. Therefore, there is a logarithmic dependence of the stray field on the distance to the edge, d, of the cube in units of L so that the sensitivity S_A is only weakly dependent on d.

NV ensemble measurements

As noted earlier, the sensitivity of our scheme S_A does not depend on the FM-NV coupling constant. Such behavior of the sensitivity is in stark contrast to the cubic dependence on the tip-to-sample separation of typical NV-magnetometer sensitivity. This property of S_A is very useful if we want to perform the measurements with an ensemble of NV-centers since all of them would have the same sensitivity irrespective of the actual value of the FM-NV coupling constant. Thus, we obtain an improvement of sensitivity by a factor of $\sqrt{N_{\rm NV}}$, where $N_{\rm NV}$ is the number of NV-centers in the ensemble. In our scheme $N_{\rm NV}$ is the maximum number of NV-centers that we can place in the region of space around the FM where the stray field value is above the threshold $B_{\rm th}$.

As the FM volume is increased, the sensitivity is decreased as $S_A \sim \sqrt{V}$ see Eq. 7.8. Nevertheless, in case of an NV ensemble measurement, increasing V leads to an increase of $N_{\rm NV}\ V$. Thus, for ensemble measurements our scheme does not loose sensitivity when the FM volume is increased, but rather the sensitivity is logarithmically improved due to increasing the FM-qubit coupling constant. The possibility of having a large FM without loss of sensitivity is important since it can be experimentally more feasible to work with micron-sized FMs.

7.A Cramer-Rao Bound

For the sake of completeness, we review here the proof of the Cramer-Rao bound,

$$\langle(\delta\hat{\mu}_s)^2\rangle \geq 1/F(\mu_s), \tag{7.13}$$

that we use to derive the sensitivity expression in Eq. (7.3) of the main text.

The Fisher information of the parameter estimator $\hat{\mu}_s$ is given by

$$F(\mu_s) = -\sum_{n=\pm 1} p(n|\mu_s) \frac{\partial^2 \ln(p(n|\mu_s))}{\partial \mu_s^2} \,. \tag{7.14}$$

The Cramer-Rao bound follows from the trivial identity

$$0 = \sum_{n_1} \cdots \sum_{n_{\mathcal{N}}} p(n_1|\mu_s) \ldots p(n_{\mathcal{N}}|\mu_s) \Delta\hat{\mu}_s, \tag{7.15}$$

where $\Delta\hat{\mu}_s = \hat{\mu}_s(n_1, \ldots, n_{\mathcal{N}}) - \langle\hat{\mu}_s\rangle$. Taking the derivative of this identity with respect to μ_s and using the fact that the estimator $\hat{\mu}_s$ does not depend explicitly on μ_s, we obtain

$$\sum_{n_1} \cdots \sum_{n_{\mathcal{N}}} p(n_1|\mu_s) \ldots p(n_{\mathcal{N}}|\mu_s) \left(\sum_{k=1}^{\mathcal{N}} \frac{\partial \ln p(n_k|\mu_s)}{\partial \mu_s} \right) \Delta\hat{\mu}_s = \frac{d\langle\hat{\mu}_s\rangle}{d\mu_s}. \tag{7.16}$$

Furthermore, for the unbiased estimator, $\langle\hat{\mu}_s\rangle = \mu_s$ and thus the right-hand side of Eq. (7.16) is equal to 1. Finally, applying the Schwarz inequality, $\mathrm{cov}(X,Y)^2 \geq \mathrm{var}(X)\mathrm{var}(Y)$, to the above equation yields the Cramer-Rao bound, Eq. (7.13).

7.B Sensitivity of an NV-center

The variance of any estimator $\hat{\mu}_s$ of the unknown parameter μ_s satisfies the Cramer-Rao inequality Eq. (7.13). Using the probability distribution from Eq. (7.2) of the main text, we obtain

$$F(\mu_s) = \frac{(\partial\varphi_{\mathrm{NV}}(t_i)/\partial\mu_s)^2 \sin^2(\varphi_{\mathrm{NV}}(t_i)+\theta)}{e^{2\langle(\delta\varphi_{\mathrm{NV}}(t_i))^2\rangle} - \cos^2(\varphi_{\mathrm{NV}}(t_i)+\theta)} \,. \tag{7.17}$$

Thus, a bigger Fisher information $F(\mu_s)$ leads to a more accurate value of the estimator $\hat{\mu}_s$.

For DC magnetometry we typically have $\varphi_{\mathrm{NV}}(t_i) = \gamma_{\mathrm{NV}}(B_0 + B)t_i \equiv t_i/T'$ and $\langle(\delta\varphi_{\mathrm{NV}}(t_i))^2\rangle = t_i/T_2^*$, where $\gamma_{\mathrm{NV}}B_0 = 2.87$GHz is the zero-field splitting of the NV-center and T_2^* is typically on the order of a few microseconds. The field we want to measure is $B = \mu_0\mu_s/(4\pi d^3)$, with d the distance between the qubit and the NV-center. Consider the scenario

$T' \ll T_2$ which is valid for DC magnetometry. In such a situation, one may choose an interrogation time maximizing $\sin^2[\varphi_{\rm NV}(t_i)+\theta]$ and minimizing $\cos^2[\varphi_{\rm NV}(t_i)+\theta]$ in Eq. (7.17). This is independent of the angle θ which we set to zero without loss of generality. Thus instead of maximizing the Fisher information from Eq. (7.17), we need only to maximize its envelope function,

$$\tilde{F}(\mu_s) = (\partial\varphi_{\rm NV}(t_i)/\partial\mu_s)^2 e^{-2\langle(\delta\varphi_{\rm NV}(t_i))^2\rangle}\,. \tag{7.18}$$

Repeating the measurement $\mathcal{N} = T/(t_p+t_i)$ times (t_p is the initialization time) reduces the variance by a factor $1/\mathcal{N}$. The Cramer-Rao bound (7.13) then leads to $\langle(\delta\hat{\mu}_s)^2\rangle \geq \frac{1}{\mathcal{N}F(\mu_s)}$. The minimal value of the magnetic moment $\tilde{\mu}_s(t_i,T)$ (that can be resolved within measurement time T and interrogation time t_i) is determined by the one for which the mean value is equal to its standard deviation,

$$\tilde{\mu}_s(t_i,T) = \frac{1}{\sqrt{\mathcal{N}F(\tilde{\mu}_s)}}\,. \tag{7.19}$$

We finally obtain the sensitivity

$$S = \frac{1}{R\sqrt{\eta}}\min_{t_i}\left[\frac{e^{\langle(\delta\varphi_{\rm NV}(t_i))^2\rangle}\sqrt{t_i+t_p}}{|\partial\varphi_{\rm NV}(t_i)/\partial\mu_s|}\right]. \tag{7.20}$$

As mentioned in the main text, R is the measurement contrast and η is the detection efficiency; [134] these quantities take into account that the measurement has to be performed many times in order to detect a photon.

The situation for AC magnetometry is different, here

$$\varphi_{\rm NV}(t_i) = \lambda\gamma_{NV}Bt_i \equiv t_i/T', \tag{7.21}$$

while we still have $\langle(\delta\varphi_{\rm NV}(t_i))^2\rangle = t_i/T_2$. (Note that the constant of proportionality λ depends on the specific pulse sequence applied.) In typical situations, the AC magnetic field is small and $T' \gg T_2$. In such scenario, and for vanishing angle θ, the accumulated phase will never reach a value of $\pi/2$ and one needs to maximize the Fisher information (7.17), not only its envelope. In this limit, we obtain a very different expression for the sensitivity, and, in particular, the expression is in units of "magnetic moment"/$\mathrm{Hz}^{\frac{1}{4}}$ (see Sec. 7.C). Fortunately, such result can be improved: one may take a nonzero value of the angle θ such that the expression $\varphi_{\rm NV}(t_i)+\theta = \pi/2$ within the interrogation time. In this case, the sensitivity takes the form (7.20), improving the sensitivity.

7.C AC sensitivity for $\theta = 0$

The goal of this appendix is to derive the expression for the AC sensitivity when the angle θ between the two $\pi/2$-pulses, applied at the beginning and at the end of the sequence, is zero. This calculation is presented for the sake of completeness, however, this is not the expression we use to derive sensitivity of our magnetometry scheme. As mentioned in the main text, for AC magnetometry we have

$$\varphi_{\rm NV}(t_i) \propto \gamma_{\rm NV} B t_i \equiv t_i/T', \tag{7.22}$$

$$\langle (\delta\varphi_{\rm NV}(t_i))^2 \rangle = t_i/T_2, \tag{7.23}$$

where the constant of proportionality depends on the specific pulse sequence applied. It is important to note that here only the AC field component that matches the frequency of the pulse sequence contributes (*i.e.*, there is no contribution from B_0). When the magnitude of the AC driving field is small, we are in the limit of $T' \gg T_2$. As noted above, in this regime the accumulated phase $\varphi_{\rm NV}(t_i)$ will not reach the value of $\pi/2$ and thus the full Fisher information needs to be maximized. Namely, we maximize

$$F(\mu_s) = \frac{(\partial\varphi_{\rm NV}(t_i)/\partial\mu_s)^2 \sin^2(\varphi_{\rm NV}(t_i)+\theta)}{e^{2\langle(\delta\varphi_{\rm NV}(t_i))^2\rangle} - \cos^2(\varphi_{\rm NV}(t_i)+\theta)}\,. \tag{7.24}$$

Therefore,

$$\sqrt{\langle(\delta\hat{\mu}_s)^2\rangle} \geq \frac{\sqrt{e^{2\langle(\delta\varphi_{\rm NV}(t_i))^2\rangle} - \cos^2(\varphi_{\rm NV}(t_i))}\sqrt{t_p+t_i}}{\sqrt{T}|\sin(\varphi_{\rm NV}(t_i))\partial\varphi_{\rm NV}(t_i)/\partial\mu_s|}. \tag{7.25}$$

In contrast to the result obtained [126] [which is similar to the one obtained in Eq. (7.18)], the Fisher information in Eq. (7.25) depends on the estimation parameter μ_s. The minimal value of the magnetic moment $\tilde{\mu}_s(t_i, T)$ (that can be resolved within measurement time T and interrogation time t_i) is again determined as the one for which the mean value is equal to its standard deviation, Eq. (7.19). Therefore, using the fact that $\varphi_{\rm NV}(t_i)$ depends linearly on μ_s and that for typical interrogation time $\varphi_{\rm NV}(t_i) \ll 1$ and assuming $t_p \ll t_i$, we find an approximate solution to Eq. (7.19). Minimizing over the interrogation time, we obtain

$$\begin{aligned}\tilde{\mu}_s(T) &\equiv \min_{t_i}\left[\tilde{\mu}_s(t_i,T)\right] \\ &= \min_{t_i}\left[\frac{(e^{2\langle(\delta\varphi_{\rm NV}(t_i))^2\rangle}-1)^{\frac{1}{4}}}{|\partial\varphi_{\rm NV}(t_i)/\partial\mu_s|}\left(\frac{t_i}{T}\right)^{\frac{1}{4}}\right].\end{aligned} \tag{7.26}$$

Now, if we remove the dependence on the total measurement time from the above expression, we obtain the quantity that describes the magnetic moment sensitivity in units of "magnetic moment"/$\mathrm{Hz}^{\frac{1}{4}}$, *i.e.*,

$$S = \frac{1}{R\sqrt{\eta}} \min_{t_i} \left[\frac{(e^{2\langle(\delta\varphi_{\mathrm{NV}}(t_i))^2\rangle} - 1)^{\frac{1}{4}} t_i^{\frac{1}{4}}}{|\partial\varphi_{\mathrm{NV}}(t_i)/\partial\mu_s|} \right] . \tag{7.27}$$

7.D Calculation of $\varphi_{NV}(t_i)$ and $\beta(t_i, \tau)$

The goal of this appendix is to give a detailed derivation of Eqs. (7.5) and (7.7) of the main text that are central to our work. The former describes the phase accumulated by the NV-magnetometer, while the latter the variance of this accumulated phase.

Within linear response, the accumulated phase is

$$\varphi_{\mathrm{NV}}(t_i) = \frac{\mu_s \gamma \gamma_{\mathrm{NV}}}{M_F V} \mathrm{Re}\left[i X_\xi(t_i, t') \left(\boldsymbol{B}^+_{F,s} \cdot \boldsymbol{n}_s \right) \left(\boldsymbol{B}^-_{F,\mathrm{NV}} \cdot \boldsymbol{n}_{\mathrm{NV}} \right) \right] , \tag{7.28}$$

where ξ ($|\xi| \leq \tau$) is the time offset between the CPMG pulse sequence applied to the qubit and the NV-center. We have introduced the following notation,

$$\begin{aligned} X_\xi(t_i, t') =& \int_0^{t'} ds e^{-\Omega s} \int_0^{t_i} dt'' f_\tau(t'') f_\tau(t'' - s - \xi) + e^{-\Omega t'} \int_0^{t_i} ds e^{-\Omega s} p_\tau(s, t; \xi) \\ \equiv& \tilde{X}_\xi(t_i, t') + e^{-\Omega t'} Y_\xi(t_i), \end{aligned} \tag{7.29}$$

with $\Omega = i\omega_F + \Gamma$ and $p_\tau(s, t_i; \xi) = \int_0^{t_i - s} dt'' f_\tau(t'' - \xi) f_\tau(t'' + s)$. After performing the integral in Eq. (7.29) and using $t_i = N\tau$, $t' = N'\tau$, we obtain

$$\tilde{X}_\xi(N\tau, N'\tau) = e^{-\Omega\xi}\Big[\tilde{X}_{\xi=0}(N\tau, N'\tau) - (1-e^{-\Omega t'})\frac{\Omega\tau - 2 + e^{-\Omega\xi}(2+2\Omega\xi-\Omega\tau)}{\Omega^2}N\Big], \quad (7.30)$$

$$\tilde{X}_{\xi=0}(N\tau, N'\tau) = \frac{(1-e^{-N'\Omega\tau})N(2+e^{\Omega\tau}(\Omega\tau-2)+\Omega\tau)}{\Omega^2(1+e^{\Omega\tau})}, \quad (7.31)$$

$$Y_{\xi=0}(N\tau) = -\frac{4\mathrm{sh}^4(\Omega\tau/4)}{\Omega^2\mathrm{ch}^2(\Omega\tau/2)} + \frac{2+\Omega\tau+(\Omega\tau-2)e^{\Omega\tau}}{\Omega^2(1+e^{\Omega\tau})}N + \frac{(e^{\Omega\tau/2}-1)^4}{\Omega^2(1+e^{\Omega\tau})^2}e^{-N\Omega\tau}. \quad (7.32)$$

Since we want the qubit to perturb the ferromagnet within a narrow frequency window around the FMR (*i.e.*, narrower than the FMR linewidth Γ), we require that $\Gamma t' \gg 1$. In this limit, the expression for $X_\xi(t_i, t')$ is significantly simplified

$$X_\xi(N\tau, N'\tau) = e^{-\Omega\xi}\left[\tilde{X}_{\xi=0}(N\tau, N'\tau) - \frac{\Omega\tau - 2 + e^{-\Omega\xi}(2+2\Omega\xi-\Omega\tau)}{\Omega^2}N\right],$$
$$\tilde{X}_{\xi=0}(N\tau, N'\tau) \approx X_{\xi=0}(N\tau) \equiv \frac{N(2+e^{\Omega\tau}(\Omega\tau-2)+\Omega\tau)}{\Omega^2(1+e^{\Omega\tau})}. \quad (7.33)$$

The expression for dephasing can be obtained from [132]

$$\beta(t_i, \tau) = \gamma_{\mathrm{NV}}^2 \int_0^{t_i} ds \langle B_{\mathrm{NV}}(s) B_{\mathrm{NV}}(0)\rangle p_\tau(s, t_i; \xi = 0). \quad (7.34)$$

Furthermore,

$$\langle B_{\mathrm{NV}}(t) B_{\mathrm{NV}}(0)\rangle = |\boldsymbol{B}^+_{F,\mathrm{NV}} \cdot \boldsymbol{n}_{\mathrm{NV}}|^2 \mathrm{Re}[\langle m^+(t) m^-(0)\rangle]. \quad (7.35)$$

In the limit $M_F V(b_a \pm b) \gg k_B T$ ($b_a = K/M_F$ is the anisotropy field) one obtains the following expression for the fluctuations of the ferromagnet,

$$\langle m^+(t) m^-(0)\rangle = \frac{2k_B T}{M_F V(b_a \pm b)} e^{-i\omega_F t - \Gamma|t|}. \quad (7.36)$$

Combining equations (7.34-7.36) we finally obtain

$$\beta(N\tau, \tau) = \frac{2\gamma_{\mathrm{NV}}^2 |\boldsymbol{B}^+_{F,\mathrm{NV}} \cdot \boldsymbol{n}_{\mathrm{NV}}|^2 k_B T}{M_F V(b_a \pm b)} Y'_{\xi=0}(N\tau). \quad (7.37)$$

On-resonance case $\tau = (2k+1)\pi/\omega_F$

The Fourier transform of the CPMG sequence depicted in Fig. 7.2 has peaks at frequencies $(2k+1)\pi/\tau$. Thus we have a resonant behavior whenever this frequency matches ω_F. Assuming $\Gamma t' \gg 1$ and $\omega_F \gg (2k+1)\Gamma$ leads to the following expression for $X_\xi(t_i)$, namely

$$X_\xi(N) = \left[-\frac{4N}{(2k+1)\pi\Gamma\omega_F} + i\frac{\left((2k+1)^2\pi^2 - 8\right)N}{(2k+1)\pi\omega_F^2}\right] e^{-i\psi}, \tag{7.38}$$

where $\psi = \omega_F\xi$. Assuming $\omega_F \gg (2k+1)^2\pi^2\Gamma$, we can neglect the second term in the bracket in Eq. (7.38) and obtain the expression for the phase accumulated by the NV-center during the interrogation time t_i,

$$\varphi_{\rm NV}(t_i) = \frac{4\mu_s\gamma\gamma_{\rm NV}{\rm Im}\left[e^{-i\psi}(\boldsymbol{B}^+_{F,s}\cdot\boldsymbol{n}_s)(\boldsymbol{B}^-_{F,{\rm NV}}\cdot\boldsymbol{n}_{\rm NV})\right]}{\pi^2(2k+1)^2M_FV\Gamma}t_i\,. \tag{7.39}$$

Next, we choose the time offset ξ (*i.e.*, ψ) such that $\varphi_{\rm NV}(t_i)$ in the above equation is maximized

$$\psi = \arg\left[(\boldsymbol{B}^+_{F,s}\cdot\boldsymbol{n}_s)(\boldsymbol{B}^-_{F,{\rm NV}}\cdot\boldsymbol{n}_{\rm NV})\right] \tag{7.40}$$

we obtain

$$\varphi_{\rm NV}(t_i) = \frac{4\mu_s\gamma\gamma_{\rm NV}|\boldsymbol{B}^+_{F,s}\cdot\boldsymbol{n}_s||\boldsymbol{B}^-_{F,{\rm NV}}\cdot\boldsymbol{n}_{\rm NV}|}{\pi^2(2k+1)^2M_FV\Gamma}t_i\,. \tag{7.41}$$

Assuming that the optimal interrogation time satisfies $\Gamma t_i \ll 1$, we arrive at the following expression for $Y'_{\xi=0}(t_i)$, namely

$$\begin{aligned} Y'_{\xi=0}(N) &= \frac{2N}{\omega_F^3}\left[\left((2k+1)\pi - 4(-1)^k\right)\Gamma + N\omega_F\right] \\ &\sim \frac{2N^2}{\omega_F^2}. \end{aligned} \tag{7.42}$$

The above expression yields the following variance of the phase accumulated by the NV-center

$$\beta(t_i,\tau) = \frac{4\gamma\gamma_{\rm NV}^2|\boldsymbol{B}^+_{F,{\rm NV}}\cdot\boldsymbol{n}_{\rm NV}|^2k_BT}{\pi^2(2k+1)^2M_FV\omega_F}t_i^2\,. \tag{7.43}$$

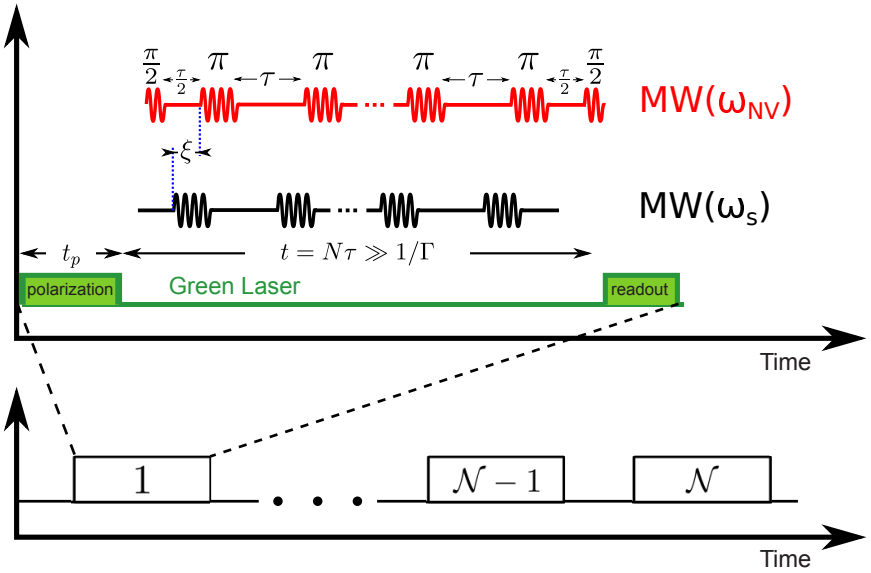

Figure 7.5: One obvious choice for the pulse sequence applied to the qubit (black) and the NV-center spin (red) that does not yield good magnetometer sensitivity. The pulse sequence $f_\tau(t)$ that consists of $2N$ pulses is applied to both spins, with the time offset ξ, during the interrogation time t. The measurement is repeated $\mathcal{N}$ times until the desired precision is achieved, as illustrated on the bottom panel. We assume that the frequencies ω_s, $\omega_{\rm NV}$, and ω_F are all different.

Pulse sequence applied: a matter of timescales

Here we elucidate the importance of the different duration of the pulse sequences applied to the qubit and the NV-center. We analyze what happens to the sensitivity of our scheme when both the pulse sequences have the same duration, see Fig. 7.5. Performing the Fourier transform of Eq. (7.34), one obtains

$$\begin{aligned}\beta(t_i,\tau) =&\gamma_{\rm NV}^2|\boldsymbol{B}_{F,\rm NV}^+\cdot\boldsymbol{n}_{\rm NV}|^2\int\frac{d\omega}{2\pi}\langle m_-(t)m_+(0)\rangle_\omega\frac{F(\omega t_i)}{\omega^2}\\ \approx&\gamma_{\rm NV}^2|\boldsymbol{B}_{F,\rm NV}^+\cdot\boldsymbol{n}_{\rm NV}|^2\langle m_-(t)m_+(0)\rangle_{\omega_F}\int\frac{d\omega}{2\pi}\frac{F(\omega t_i)}{\omega^2}\\ =&\gamma_{\rm NV}^2|\boldsymbol{B}_{F,\rm NV}^+\cdot\boldsymbol{n}_{\rm NV}|^2\langle m_-(t)m_+(0)\rangle_{\omega_F}t_i\\ \equiv&t_i/T_2'\,.\end{aligned}\tag{7.44}$$

Here the subscript ω_F refers to the Fourier transform evaluated at frequency ω_F. We assume that the filter function $F(\omega t_i)$ is centered around

the frequency ω_F (on-resonance case) and that it is much narrower than the FMR linewidth, *i.e.*, $\Gamma t_i \gg 1$—this is exactly the opposite limit from the one assumed to arrive at Eq. (7.7). The accumulated phase is given in Eq. (7.5), and thus the magnetic moment sensitivity in this case reads

$$\tilde{S}_A = \frac{1}{R\sqrt{\eta}} \frac{\pi^2}{4i\,|\boldsymbol{B}^+_{F,s} \cdot \boldsymbol{n}_s|} \frac{\sqrt{\langle m_-(t) m_+(0)\rangle_{\omega_F}}}{\chi_\perp(\omega_F)}, \tag{7.45}$$

where $\chi_\perp(\omega) = \gamma/\left[M_F V(\omega_F - \omega + i\Gamma)\right]$. The above expression does not yields good sensitivity, since we do not only excite the FM resonantly but also the NV-center picks up the resonant noise. If we rewrite Eq. (7.7) in the form $\beta(t_i, \tau) \equiv (t_i/T_2'')^2$, we can understand that the decoherence times in the two considered limits differ from each other by many orders of magnitude, namely

$$\frac{T_2''}{T_2'} = \frac{\Gamma}{\pi\gamma_{\rm NV}|\boldsymbol{B}^+_{F,\rm NV} \cdot \boldsymbol{n}_{\rm NV}|} \sqrt{\frac{M_F V \omega_F}{\gamma k_B T}} \gg 1. \tag{7.46}$$

7.E Stray field from a uniformly magnetized cuboid

In this section we review the analytical formulas giving the stray field of a uniformly magnetized cuboid of side lengths L_x, L_y, and L_z, see Fig. 7.7. As mentioned in the main text, the magnetic field $\mathbf{B}(\mathbf{r})$ at a point $\mathbf{r} = (x, y, z)$ outside of the cuboid can be calculated from the expression for the electric field originating from charges uniformly distributed on the surfaces of the cuboid perpendicular to the magnetization [155, 156], see Fig. 7.7. For the sake of simplicity, we assume that the magnetization direction points either along x, y, or z. The expression for the stray field is then

$$\mathbf{B}^\delta(\mathbf{r}) = \frac{\mu_0\, M_F}{4\pi} \int_0^{L_\alpha} d\alpha \int_0^{L_\beta} d\beta \left\{ \frac{\mathbf{r} - \mathbf{r}^{\alpha\beta}_\delta}{|\mathbf{r} - \mathbf{r}^{\alpha\beta}_\delta|^3} - \frac{\mathbf{r} - \mathbf{r}^{\alpha\beta}_{\bar{\delta}}}{|\mathbf{r} - \mathbf{r}^{\alpha\beta}_{\bar{\delta}}|^3} \right\} \tag{7.47}$$

for $\delta = x, y, z$. Here, α and β are the directions perpendicular to δ, *i.e.*, $\mathbf{r}^{\alpha\beta}_x = (L_x, \alpha, \beta)$, $\mathbf{r}^{\alpha\beta}_y = (\alpha, L_y, \beta)$, and $\mathbf{r}^{\alpha\beta}_z = (\alpha, \beta, L_z)$, and $r^{\alpha\beta}_{\bar{\delta}} = r^{\alpha\beta}_\delta\,|_{L_\delta = 0}$.

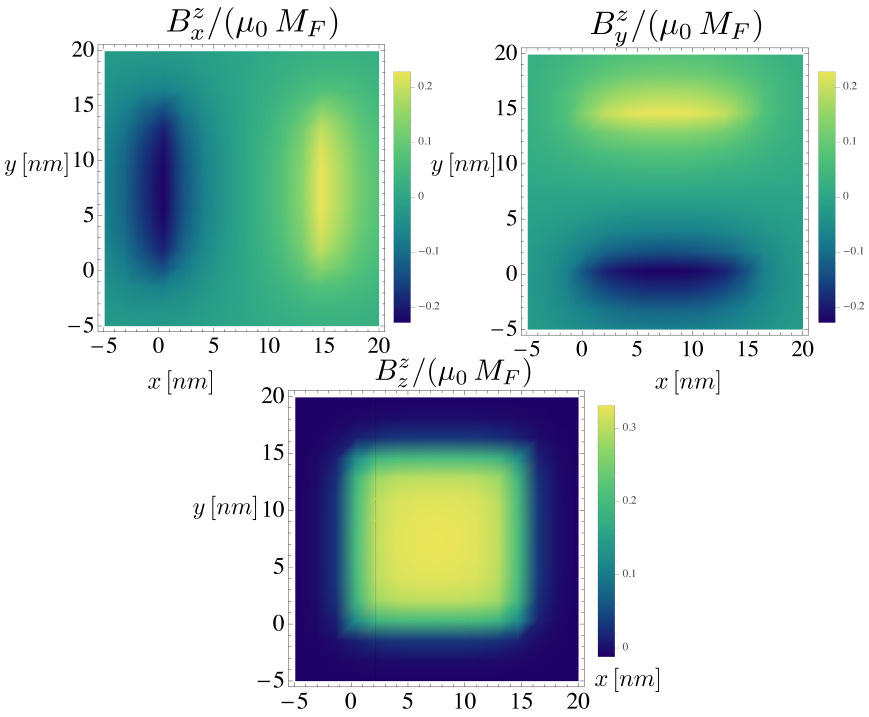

Figure 7.6: Plot of the stray field components normalized to the magnetic saturation: $B_x^z(x, y, z = 16\,\text{nm})/(\mu_0 M_F)$, $B_y^z(x, y, z = 16\,\text{nm})/(\mu_0 M_F)$, and $B_z^z(x, y, z = 16\,\text{nm})/(\mu_0 M_F)$ for a cube of side length $L = 15\,\text{nm}$. Because the origin of our coordinate system is at the center of the cube, this is a plot of the stray field at a distance of $1\,\text{nm}$ from the upper surface of the cube.

The integrals in Eq. (7.47) can be evaluated analytically [155, 156].

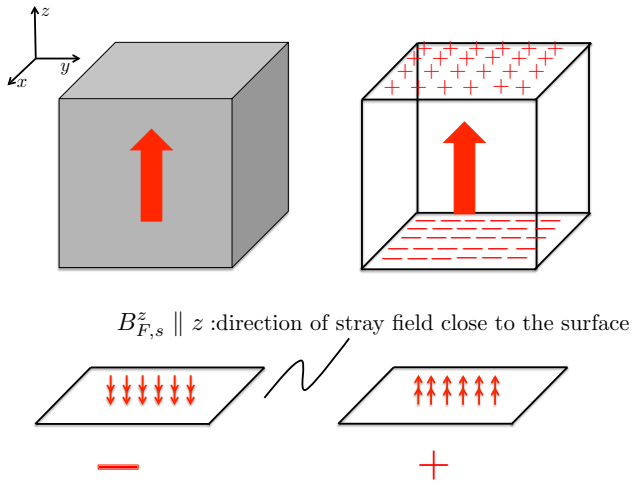

Figure 7.7: Schematic representation of the ferromagnetic particle polarized along the z axis. The stray field produced by a uniformly magnetized cube can be calculated by adding the electric field produced from the negatively charged bottom plane to the electric field produced by the positively charged upper plane. Close to the surfaces and away from the edges, the stray field points mostly along z. Only close to the edges the transverse components become significant.

When the cuboid is magnetized along z, one obtains

$$B^x_x(x,y,z) = \frac{\mu_0 M_F}{4\pi}\{f(x,y,z) - f(x,y-L_y,z) \\ -f(x-L_x,y,z) + f(x-L_x,y-L_y,z)\} \tag{7.48}$$

$$B^x_y(x,y,z) = \frac{\mu_0 M_F}{4\pi}\{f(y,x,z) - f(y-L_y,x,z) \\ -f(y,x-L_x,z) + f(y-L_y,x-L_x,z)\} \tag{7.49}$$

$$B^x_z(x,y,z) = \frac{\mu_0 M_F}{4\pi}\{g(x,y,L_z,z) - g(x,y-L_y,L_z,z) \\ -g(x-L_x,y,L_z,z) + g(x-L_x,y-L_y,L_z,z) \\ -g(x,y,0,z) + g(x,y-L_y,0,z) \\ +g(x-L_x,y,0,z) - g(x-L_x,y-L_y,0,z)\}\ . \tag{7.50}$$

Here

$$f(a,b,z) = \log\left(\frac{\sqrt{a^2+(z-L_z)^2}(b+\sqrt{a^2+b^2+z^2})}{\sqrt{a^2+z^2}(b+\sqrt{a^2+b^2+(z-L_z)^2})}\right), \tag{7.51}$$

$$g(a,b,c,z) = \arctan\left(\frac{a\,b}{(z-c)\sqrt{a^2+b^2+(z-c)^2}}\right). \tag{7.52}$$

The analytical expressions for $\mathbf{B}^{y,z}(\mathbf{r})$ are found similarly.

For the sake of illustration, we plot in Fig. 7.6 the three components of $\mathbf{B}^z$ as function of x and y for a cube of size $L = L_x = L_y = L_z = 15\,\text{nm}$ at a distance of $1\,\text{nm}$ above the upper face.

Part III

End states in one-dimensional systems

CHAPTER 8

Introduction

Over the last decades a number of proposals have been made for solid-state implementations of a quantum computer. Among these, electron spins in GaAs quantum dots [1, 82] are most promising candidates with unusually long coherence times [157]. Such dots contain typically many levels which are filled according to Hund's rule. Thus, the condition for a spin-qubit, which requires the presence of only a single unpaired electron, becomes challenging [82], and the scalability of such an approach is still an open problem. Herein we propose a simple setup, involving periodically modulated gates on top of a quantum wire, which eventually results in an effective double dot system. Due to the spatial modulation of the gate voltage the energy spectrum of the quantum wire acquires a charge density wave (CDW) gap. Recently, similarly modulated setups have been discussed with focus on metal-insulator transitions [158] and transport properties in an infinite-wire superlattice [159]. Here, we show that the modulated quantum wire supports localized, fractionally charged states at each end of the wire, known as Tamm-Shockley bound states [160, 161], with their energies lying inside the gap. These end wave-functions are well protected from the continuum and can host stable spin-qubits.

The previously described fractionally charged end-states are related to the field of topological quantum computing that has emerged in recent years as a promising alternative to standard quantum computing schemes (such as previously described spin-qubit based quantum computing). The main difference in this approach to quantum computing as compared to other schemes is that some of the universal quantum

gates are performed by braiding topological excitations in the solid state systems, thus this approach provides, in principle, an error-free implementation of some of the universal quantum gates. Within this field of research, the study of Majorana fermions (MFs) that emerge as end-states in various solid-state systems has recently attracted a lot of attention [24, 25, 26, 27, 28, 29, 30]. In particular, the possibility of realizing them as zero-energy states localized at the end of one-dimensional systems—so-called Majorana end states (MES).

It was shown that the scheme to induce the fractional Tamm-Shockley bound states can be modified by assuming the simultaneous presence of Rashba spin-orbit interaction (SOI) and uniform and spatially periodic magnetic field which produce gapped phases with a rich phase diagram, including a reentrance behavior of MFs and a complementary phase characterized by fractionally charged fermions (FF) [34]. Similarly to MFs, these fractional fermion states can exhibit non-Abelian braiding statistics [35], but they exist both with and without superconductivity.

We first consider one-dimensional discrete and continuum models and find a number of remarkable features for the end states resulting from the CDW modulation. In particular, using exact numerical diagonalization of the discrete open chain we analyze the stability of these states in the presence of a random potential and find that for weak disorder the end states remain stable. For the continuum model we consider a periodically modulated potential of the form $\Delta_0 \cos(k_{CDW}x + \vartheta)$, where Δ_0 is the strength of the potential, k_{CDW} the CDW vector, and ϑ a constant phase. For $\vartheta = \pi/2$, the CDW phase supports zero energy bound states which are remarkably robust to position dependent fluctuations in Δ_0. We also show that for $\vartheta = \pi/2$ the model maps to the Jackiw-Rebbi model for massive Dirac fermions with midgap bound states [162]. We treat interactions via fermionic and bosonic techniques and find that they primarily renormalize the gap and decrease the localization length. We consider end states in a ring-geometry by connecting them directly via tunnel junction. The Aharanov-Bohm oscillation in such rings exhibits an unusual 4π periodicity, providing a striking signature of the existence of end states. Finally, we show that the two opposite end states serve as effective double quantum dot which can be used to implement quantum computing gates for spin-qubits.

Next, we analyze the experimental signature of MFs in transport setups. The experimental search [31, 32, 33] of MFs predicted to occur in condensed matter systems is challenging due to the fact that MFs are characterized by zero coupling to electromagnetic fields. Only an indi-

rect identification is possible, in particular via a zero-bias conductance peak (ZBP) [163, 164]. However, such features are not an unambiguous demonstration of MFs. The same ZBPs can be induced by different mechanisms, including the Kondo effect [165], Andreev bound states [166], weak antilocalization and reflectionless tunneling [167].

A typical experimental setup [31, 32, 33] consists of a semiconducting nanowire with Rashba spin-orbit interaction (SOI) deposited on or coated with a bulk s-wave superconductor (S) on one end and contacted through a tunnel barrier by a normal lead, on the other end. Part of the nanowire is in a superconducting state induced by proximity effect.

The transition to the topological phase controlled by a magnetic field B is accompanied by a closing and reopening of the excitation gap [25, 26, 27, 28, 29, 30]. The topological phase persists for all B-fields above a critical $B_{\rm c}$ in a one-band model, while it could have a finite upper critical field in a multiband model, where bands cross at large fields and hybridization of MFs takes place. However, in experiments one typically explores regimes where only one band undergoes a transition [31, 32, 33]. For a topological section of finite length $L_\star$, the MFs at each end with localization length $\xi_{\rm M}$ depending on B can overlap, leading to splitting of the ZBP at strong B-fields.

The experiments [31, 32, 33] show features which are *partially* consistent with the existence of MFs. However, *quantitative* agreement with the theory is still missing. To fill in this gap, we perform numerical calculations of the two-terminal conductance G in a hybrid structure, referred to as NSS′ setup which closely models the experiment. Here, G is calculated within the standard scattering theory [168], with the help of the recursive Green's function techniques [169]. This allows us to model a complex structure close to experiment that is not amenable to analytical approaches.[1]

To be specific, we focus on InSb nanowires [31, 32] and we use as a primary reference the experiment [31]. Nonidealities such as multiple occupied subbands, disorder, finite width of electrostatic barriers, finite coherence lengths, and nonzero temperature are taken into account.

Our study reveals important features not emphasized so far. For this, the presence of the bulk superconductor turns out to be decisive. We summarize here our main findings. In our NSS′ setup, the gap-edge con-

[1]Note that the SW region is not grounded in typical experiments while the mean-field formalism adopted here implies this assumption. Such difference can be accounted for through a modified formula for the conductance, and leads to small corrections [168, 170].

ductance peak decreases in intensity for increasing B, a feature that is also not captured by simpler models. Further, in some regimes the closing of the gap becomes visible in the conductance, while it does not in an NS setup. We find oscillations of the ZBP as a function of B and explain their origin. We argue that disorder is unlikely to be the explanation of the observed ZBPs. Further, we show that the tunnel barrier plays an important role for the visibility of peaks. Finally, according to our results the experimental dI/dV behavior seems to point to a SOI strength larger than the one reported.

Finally, we study the transport and noise characteristics of FFs that have not been investigated so far, i.e., we address the question of finding transport signatures related to FFs in non-superconducting Rashba NWs, which we regard as one of the most promising setups for the observation of FFs.

To carry out our analysis, we consider the NW contacted by two normal (N) leads at its two ends. We find that the FF phase is identified in a distinctive way by a series of features in the conductance behavior of the junction. The fractional charge of the bound states, however, cannot be directly demonstrated by standard two-terminal measurements.

CHAPTER 9

Localized end states in density modulated quantum wires and rings

Adapted from:
Suhas Gangadharaiah, Luka Trifunovic, and Daniel Loss
"Localized end states in density modulated quantum wires and rings",
Phys. Rev. Lett. **108**, 136803 (2012)

We study finite quantum wires and rings in the presence of a charge density wave gap induced by a periodic modulation of the chemical potential. We show that the Tamm-Shockley bound states emerging at the ends of the wire are stable against weak disorder and interactions, for discrete open chains and for continuum systems. The low-energy physics can be mapped onto the Jackiw-Rebbi equations describing massive Dirac fermions and bound end states. We treat interactions via the continuum model and show that they increase the charge gap and further localize the end states. In an Aharonov-Bohm ring with weak link, the bound states give rise to an unusual 4π-peridodicity in the spectrum and persistent current as function of an external flux. The electrons placed in the two localized states on the opposite ends of the wire can interact via exchange interactions and this setup can be used as a double quantum dot hosting spin-qubits.

Figure 9.1: The figure shows a quantum wire (black) of length L with negatively charged gates (blue) forming a superlattice potential. Due to the induced charge density modulation a bound state at each wire end can emerge.

9.1 Lattice model

The typical lattice model for 1D spin-less fermions in the presence of CDW modulation is described by [1]

$$H = -t\sum_{j=1}^{N-1}\left[c_{j+1}^{\dagger}c_j + \text{h.c.}\right] + \Delta\sum_{j=1}^{N}\cos\left[2k_{CDW}ja + \vartheta\right]c_j^{\dagger}c_j, \tag{9.1}$$

where c_j is a fermion operator at the site j, N is the total number of lattice sites, $t > 0$ is the hopping integral, $\Delta > 0$ the CDW gap, k_{CDW} the CDW wave-vector, a the lattice constant and ϑ is an arbitrary phase. The energy spectrum under the constraint of open boundary conditions is obtained by exact numerical diagonalization and we find that the criterion for the existence of bound states depends on the sign of the potential at the beginning and end sites. For illustrative purposes we have considered $k_{CDW} = \pi/4a$ and $\vartheta = \pi/2$, this choice corresponds to negative potential at the initial two sites with the overall profile given by $\Delta\sum_{j=1}^{N}\cos\left[j\pi/2 + \pi/2\right] \equiv \Delta(-1, 0, 1, 0, -1, ...)$. If the phase of the potential is chosen such that one end of the wire has positive whereas the other end has negative potential then only one end state is obtained. On the other hand, for a reflection symmetric potential profile about the center of a long wire (with both ends having negative potential), there will be two degenerate mid-gap states, ψ_R and ψ_L, localized at the right and left boundaries *resp.*, being the well-known Tamm-Shockley states [160, 161]. Fig. 9.2(a) shows the spectrum of an 320 site chain. Reducing the wire length causes exponentially small splitting in the energies of the bound states, with the new states described by the symmetric

[1] For simplicity we omit here the spin indexes, since the $\uparrow$ and $\downarrow$ spin channels are independent and this leads only to an additional degeneracy.

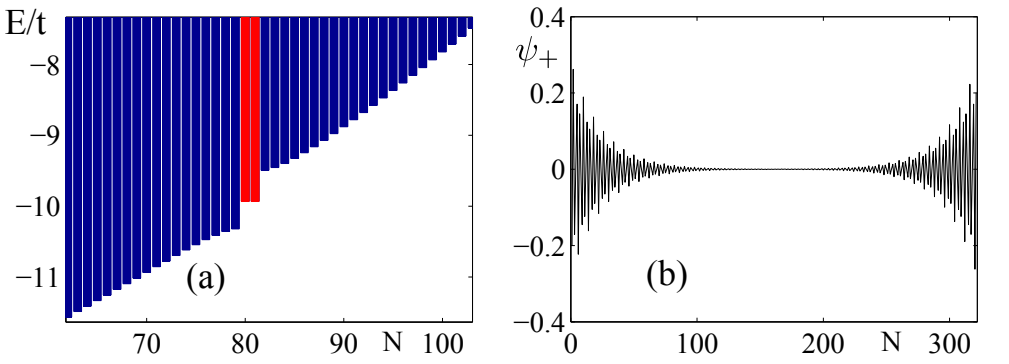

Figure 9.2: (a) The part of the spectra around the gap of the Hamiltonian given by Eq. (9.1), obtained by exact diagonalization. The red bars denote two almost degenerate bound (midgap) states. We have chosen for the parameters $t = 7$, $\Delta = 0.8$, and $N = 320$. (b) One of two bound states. Plotted here is $\psi_+ = \psi_L + \psi_R$, where $\psi_{L,R}$ are states localized at the left (right) end of the wire.

and anti-symmetric combination of ψ_R and ψ_L. We obtain the bound states to be in the middle of the gap only when $\vartheta = \pi/2$ and $t \gg \Delta$.

9.2 Disorder effects

For realistic systems, some degree of random disorder is unavoidable. To study this effect in our lattice model, we add a random on-site potential $\sum_i V_i c_i^\dagger c_i$. Here, V_i is taken according to a Gaussian distribution with zero mean and standard deviation γ. Fig. 9.3 depicts the linear dependence of the root-mean-square $\sqrt{\sigma[E_i]}$ of the i-th energy level ($i = 1 \ldots N$, i.e., for all energy levels) on the standard deviation of the random disorder potential [2]. Since the slopes of the bound states are less than 1, we conclude that the end states remain gapped even for disorder strengths comparable to the gap (Δ). As γ is increased, Anderson localization sets in. We also observe as γ is increased that the end states begin to mix with other (spatially) nearby localized states, thus effectively causing the end states to be more delocalized. Additionally, it is readily observed from Fig. 9.3 that the end states are more affected by disorder compared to all the con-

[2] We note that a Kolmogorov-Smirnov test shows that the eigenenergies are not normally distributed.

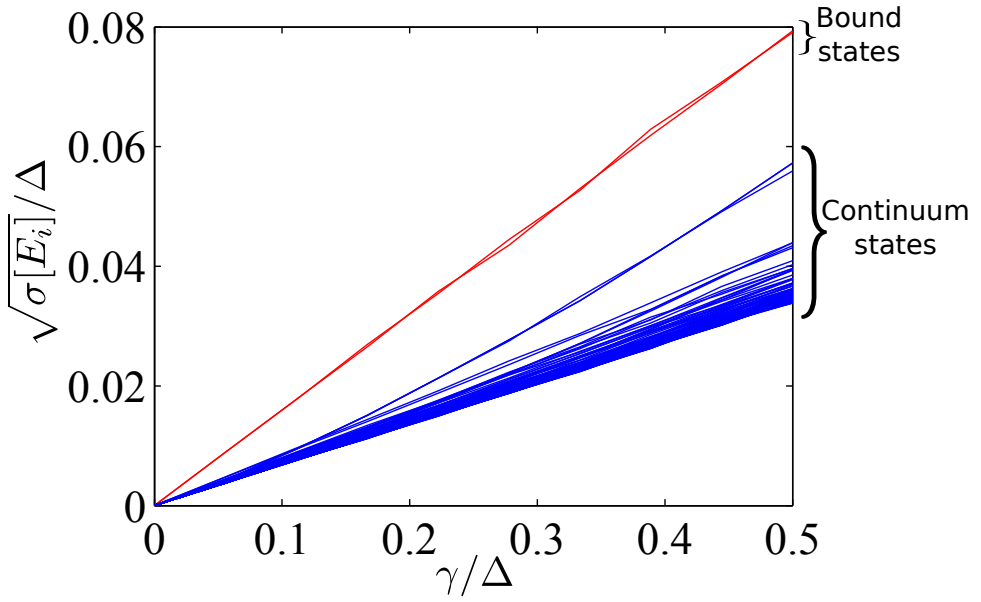

Figure 9.3: The dependence of the root-mean-square value $\sqrt{\sigma[E_i]}$ of the i-th energy level ($i = 1 \ldots N$, i.e., for all energy levels) on the standard deviation of the random disorder potential.

tinuum states. The ratio thereof depends on ξ/L, since this difference is coming from the spatial localization of the end states. For a weak disorder, the aforementioned dependence is linear, while for a strong disorder the dependence becomes more complicated due to the emergence of Anderson localization.

So far we have considered a particular realization of the lattice model. We next consider the continuum case, this limit describes the low-energy physics of a large class of one-dimensional lattice models with CDW (or superlattice) modulation. Recently, there has been intense activity on exotic quantum matter, such as Majorana fermions (chargeless) [171, 172, 173, 174, 175, 176, 177, 178, 179, 180, 181] and massless Weyl fermions [182, 183] among others. Here, we will show that our setup allows for the realization of the Jackiw-Rebbi Hamiltonian [162], describing a massive Dirac fermion of charge $1/2$ as end state.

9.3 Continuum model

We consider a quantum wire in the presence of a gate-induced potential with periodicity $\lambda_{CDW} = 2\pi/k_{CDW}$. For carrier densities smaller than the intraband energy gap only the lowest subband is occupied. The physics of the fermion mode Ψ_σ ($\sigma =\uparrow,\downarrow$ is the spin index) in the lowest subband is described in terms of the slowly varying right $\mathcal{R}_\sigma(x)$ and left $\mathcal{L}_\sigma(x)$ parts and is expressed as $\Psi_\sigma(x) = \mathcal{R}_\sigma(x)e^{ik_F x} + \mathcal{L}_\sigma(x)e^{-ik_F x}$. For an open wire, the boundary condition $\Psi_\sigma(x = 0) = 0$ imposes the constraint [184, 185], $\mathcal{R}_\sigma(x) = -\mathcal{L}_\sigma(-x)$. Thus, the Hamiltonian can be expressed in terms of right movers only.

The non-interacting Hamiltonian can be written as a sum of two parts, $H_0 = H_0^{(1)} + H_0^{(2)}$, where the kinetic part can be expressed in terms of only the right moving fermions (the original range $[0, L]$ now becomes $[-L, L]$) and is given by (summation on the spin indices is assumed)

$$H_0^{(1)} = -iv_F \int_{-L}^{L} dx \mathcal{R}_\sigma^\dagger(x)\partial_x \mathcal{R}_\sigma(x) \tag{9.2}$$

and the CDW term by

$$H_0^{(2)} = \Delta_0 \int_0^L dx \cos(2k_{CDW}x + \vartheta)\Psi_\sigma^\dagger(x)\Psi_\sigma(x), \tag{9.3}$$

with ϑ being a constant phase factor. Thus

$$H_0 = (1/2) \int_{-L}^{L} dx \mathbf{R}_\sigma^\dagger \mathcal{H}_0 \mathbf{R}_\sigma, \tag{9.4}$$

where $\mathbf{R}_\sigma(x) = [\mathcal{R}_\sigma(x), \mathcal{R}_\sigma(-x)]^T$ and the Hamiltonian density $\mathcal{H}_0$ for each spin is the same and given by

$$\mathcal{H}_0 = -iv_F\tau_z\partial_x + m_1(x)\tau_x + m_2(x)\tau_y, \tag{9.5}$$

where

$$\begin{aligned} m_1(x) &= -\cos[2\delta k x + \vartheta \mathrm{sgn}(x)]\Delta_0/2, \\ m_2(x) &= \sin[2\delta k x + \vartheta \mathrm{sgn}(x)]\Delta_0/2, \end{aligned} \tag{9.6}$$

and $\delta k = k_{CDW} - k_F$. If $\delta k = 0$ and the charge-density wave vanishes at the boundary, i.e., $\vartheta = \pi/2$, then it is easy to verify that $\mathcal{H}_0$ satisfies the 'chiral symmetry' [186] $\mathcal{P}\mathcal{H}_0 = -\mathcal{H}_0\mathcal{P}$ ($\mathcal{P}$ is a complex conjugation

operator). Moreover, the eigenvalue equation ($\mathcal{H}_0\psi_\sigma = \epsilon\psi_\sigma$) of the chiral symmetric $\mathcal{H}_0$ is related to the Jackiw-Rebbi equation describing massive fermions, [3]

$$\mathcal{H}^{JR}\psi^{JR} = [\tau_z\partial_x + m\text{sgn}(x)]\psi^{JR} = \epsilon\tau_x\psi^{JR}, \tag{9.7}$$

via the transformation, $\psi^{JR} = \mathcal{U}^{-1}\tau_y\psi$ and $\mathcal{H}^{JR} = \mathcal{U}^{-1}\mathcal{H}_0\tau_y\mathcal{U}$, where $\mathcal{U} = \exp(i\boldsymbol{\tau}\cdot\hat{n}2\pi/3)$ and $\hat{n} = (\hat{i}+\hat{j}+\hat{k})/\sqrt{3}$. Here, $\tau_{x,y,z}$ denote Pauli matrices acting on the spinor $\mathbf{R}_\sigma(x)$. Solving the eigenvalue equation for $L \gg v_F/\Delta_0$ one obtains exponentially decaying bound states $\psi_\sigma \sim \exp[-(\Delta_0/2v_F)x]$ and $\psi_\sigma \sim \exp[-(\Delta_0/2v_F)(L-x)]$ at $x = 0$ and $x = L$. Away from the chiral symmetry point ($\vartheta \neq \pi/2$) bound states still exist as long as $\sin\vartheta > 0$, with the eigenstates given by

$$\psi_\sigma \sim \exp[-i(\Delta_0\exp[-i\vartheta]/2v_F)x] \tag{9.8}$$
$$\psi_\sigma \sim \exp[-i(\Delta_0\exp[-i\vartheta]/2v_F)(L-x)]. \tag{9.9}$$

For infinite wires the eigenvalues are degenerate and given by

$$\epsilon = -\Delta_0\cos(\vartheta)/2. \tag{9.10}$$

However, finite length introduces overlap between the end states leading to an exponentially small splitting in the energy (see below and Fig. 9.4).

In a realistic quantum wire the gap $\Delta(x)$ and the phase $\vartheta(x)$ will invariably be position dependent. Assuming this dependence to be weak, the correction in lowest order in $\delta(x)/\Delta_0 \ll 1$ is given by,

$$\delta\epsilon \;=\; -\frac{\Delta_0}{4v_F}\int_0^\infty dx\delta(x)\sin 2\vartheta(x)e^{-\Delta_0\sin[\vartheta_0]x/v_F}, \tag{9.11}$$

where $\langle\delta(x)\rangle = 0$ and $\langle\vartheta(x)\rangle = \langle\vartheta_0 + \delta\vartheta(x)\rangle = \vartheta_0$, and they both vary slowly on the Fermi wavelength $\lambda_F = 2\pi/k_F$. Thus, $\delta\epsilon \ll \Delta_0$, and the bound states remain stable to weak perturbations.

9.4 Interaction effects

In the following, we consider the effect of repulsive interactions on the end states. For simplicity, we consider spinless fermions with $k_F = k_{CDW}$

[3] The fractional charge $1/2$ of the end states are seen only in the continuum model [162] but not in the lattice model. This difference is coming from subtracting an infinite Fermi sea when passing to the continuum model.

and $\vartheta = \pi/2$. As usual in 1D, the interactions can be split into forward and back scattering parts. The former

$$H_F = \pi v_F g_4 \int_0^L dx(:J_R J_R: + :J_L J_L:), \tag{9.12}$$

where $J_R = \mathcal{R}^\dagger(x)\mathcal{R}(x)$ and $J_L = \mathcal{L}^\dagger(x)\mathcal{L}(x)$, is responsible for the velocity renormalization [187], $v = v_F(1+g_4)$. On the other hand, the backscattering part given by

$$H_B = \pi v_F g_2 \int_0^L dx:J_L J_R:, \tag{9.13}$$

renormalizes the gap at the lowest order in interaction. The mean-field gap $\tilde{\Delta}(x) \propto g_2 v_F \langle \mathcal{R}(x)\mathcal{R}^\dagger(-x)\rangle$ adds to the externally induced gap

$$m_2(x) = \text{sgn}(x)\Delta_0/2. \tag{9.14}$$

We note that similar to $m_2(x)$, $\Delta(0_+) = -\Delta(0_-)$. This can be seen by invoking the boundary condition, $\mathcal{R}(x) = -\mathcal{L}(-x)$, and by expressing $\mathcal{R}(x) = \exp(i\sqrt{4\pi}\phi_R)$ and $\mathcal{L}(x) = \exp(-i\sqrt{4\pi}\phi_L)$ in terms of the bosonic fields $\phi_R(x)$ and $\phi_L(x)$ which themselves satisfy [185]

$$\sqrt{4\pi}\phi_R(0) = -\sqrt{4\pi}\phi_L(0) + \pi. \tag{9.15}$$

Thus, for weak interactions the bound states retain the same form as for the non-interacting case but with renormalized velocity and gap. To estimate the gap size we evaluate the self-energy, $\hat{\Sigma}$, using the unperturbed Green's function for an infinite wire, $G_0(i\omega, k) = (i\omega - v_F k\tau_z - \Delta_0\tau_y/2)^{-1}$. In leading order, the gap renormalizes to

$$(\Delta_0/2)[1 + (g_2/4)\ln[\text{min}(\Lambda, v_F L^{-1})/\Delta_0]], \tag{9.16}$$

where Λ is the band width. Thus, the localization length, given by $\xi = (2v_F/\Delta_0)\{1 + g_4 - (g_2/4)\ln[v_F/L\Delta_0]\}$, reduces with interaction. In other words, due to the repulsive interaction between the continuum and the end states, the latter states get squeezed.

The renormalization of the gap can be more rigorously analyzed via bosonization. Using standard procedures [188], we obtain the following form for the bosonic Lagrangian

$$\mathfrak{L}(x,t) = \sum_{\nu=c,s}\Big[\frac{1}{2v_\nu K_\nu}(\partial_t\phi_\nu)^2 - \frac{v_\nu}{2K_\nu}(\partial_x\phi_\nu)^2\Big] \tag{9.17}$$
$$+\frac{v_F}{2\pi a^2}\sum_{\eta=\uparrow,\downarrow} y_\eta \sin[\sqrt{4\pi}\phi_\eta - 2\delta kx - \vartheta],$$

where the subscripts c, s refer to charge and spin, *resp.* The $\partial_x \phi_{c/s}$ field describes the charge/spin density fluctuations and $\theta_{c/s}$ is the conjugated field, and $\phi_{\uparrow,\downarrow} = (\phi_c \pm \phi_s)/\sqrt{2}$. The Luttinger liquid parameters $K_{c/s}$ and velocities $v_{c/s}$ encode interactions, and $y_{\uparrow,\downarrow} = a\Delta_0/v_F$. The sine term denotes the coupling of up and down spin fermions with the external potential. As before, we assume $\delta k = 0$. In general, there are two additional terms: one of them arises due to backscattering between opposite spin electrons and is given by $\cos(\sqrt{8\pi}\phi_s)$, and the other, $\cos(4\sqrt{\pi}\phi_c - 4k_F x)$, describes the Umklapp scattering. However, both can be neglected as the two operators flow to zero under a renormalization group (RG) treatment.

The scaling dimensions of $\sin(\sqrt{4\pi}\phi_{\uparrow,\downarrow})$, $d_{\uparrow,\downarrow} = (K_c + K_s)/2 \approx 1$, indicate that near commensurability ($\delta k v_F/\Delta_0 \ll 1$) the sine terms are strongly relevant. The parameters $y_{\uparrow,\downarrow}$ have an identical flow [so as to preserve the $SU(2)$ symmetry, this also implies $K_s = 1$] towards the strong coupling regime and yields an effective localization length $\xi \sim a(a\Delta_0/v_F)^{2/(K_c-3)}$ for the bound state. Thus as before the role of the interactions is to reinforce the externally induced gap. We note that under RG additional terms of the type $\partial_i\phi_c\partial_i\phi_s$ (where $i = x, \tau$) are generated, however, they are marginal and leave the essential physics unaltered.

9.5 Detection

A viable approach for detecting the energy splitting between the bound states is through persistent current measurements. For this the wire should be in a ring geometry so that the end states are connected together via a tunnel junction and also large enough such that the energy splitting between the bound states is small yet the overlap of the localized wavefunctions remain non-zero. Such a set-up can enclose magnetic flux Φ inducing Aharonov-Bohm (AB) oscillations in a mesoscopic (phase-coherent) regime. Next consider a single electron placed in one of the bound states. The effective Hamiltonian for the spinless fermion in terms of the orthogonal symmetric, $|+\rangle$, and anti-symmetric, $|-\rangle$, states can thus be written

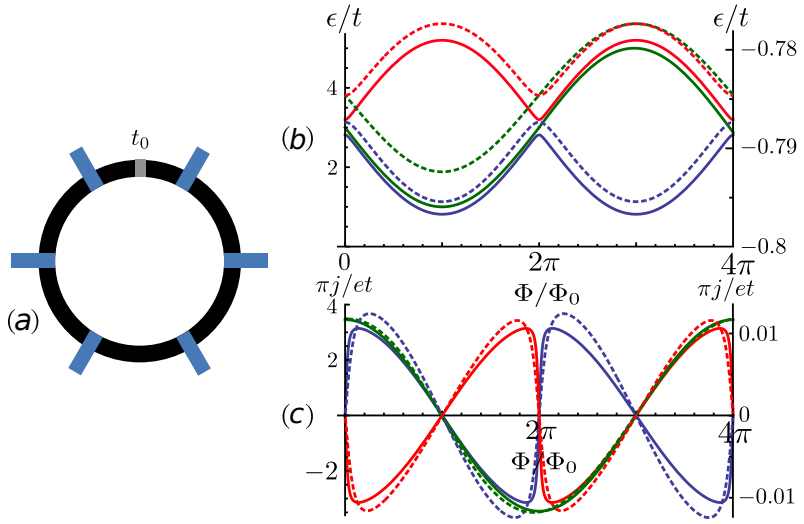

Figure 9.4: (a) Quantum wire (black) in an Aharonov-Bohm-ring geometry with negatively charged gates (blue). The bound states are localized on either side of the weak link (grey) of strength t_0. The energy (b) and persistent current $j = -\partial F/\partial\Phi$ (c) dependence on the flux Φ/Φ_0 are plotted with the solid curves for the effective model (Eq. (9.18)) and with the dashed curves for the lattice model (Eq. (9.1)). The parameters for the red and blue solid curves correspond to $\delta/t_0 = 2.2$ and $(\epsilon_+ + \epsilon_-)/t_0 = 6.2$, and for the green curve to $\delta/t_0 = 2.0$ and $(\epsilon_+ + \epsilon_-)/t_0 = 6.0$ (see Eq. (9.19)). While for the dashed curves the parameters are $\Delta/t_0 = 3.85$ (red and blue) and $\Delta/t_0 = 4.54$ (green). The ratio $\Delta/t = 0.5$ and $N = 50$ is the same for all three dashed curves. Here, t_0 is chosen such that we have a degeneracy at $\Phi/\Phi_0 = 2\pi$. Assuming only the lower bound state is filled, the persistent current shows an unusual 4π-periodicity as function of Φ/Φ_0.

as [4]

$$H = \sum_{\eta=\pm} \Big[\epsilon_\eta + \eta t_0 \cos\Big(\frac{\Phi}{\Phi_0}\Big)\Big] |\eta\rangle\langle\eta| + i t_0 \sin\Big(\frac{\Phi}{\Phi_0}\Big) \times \Big[|-\rangle\langle+| - |+\rangle\langle-|\Big], \tag{9.18}$$

where $\Phi_0 = h/e$ is the flux quantum, ϵ_+ (ϵ_-) the energy of the symmetric (anti-symmetric) mode, and the tunneling across the weak link is associated with a factor $\nu t_0 \exp(i\mu\Phi/\Phi_0)$, where $\nu, \mu = \pm 1$ and t_0 the tunneling amplitude. For (anti-) clockwise tunneling we have $\mu = +(-)$, while the sign of ν depends on the relative sign between the wave-functions across the weak link. The energy eigenvalues are

$$\epsilon_{1/2} = \frac{1}{2}\big(\epsilon_- + \epsilon_+ \pm \sqrt{4t_0^2 + \delta^2 - 4t_0\delta\cos[\Phi/\Phi_0]}\big), \tag{9.19}$$

where $\delta = |\epsilon_+ - \epsilon_-|$. At $\Phi/\Phi_0 = 2\pi$ the separation between the two eigenvalues is minimal and given by $|2t_0 - \delta|$. For large separations, the energy levels exhibit the usual 2π dependence on the flux Φ/Φ_0. In contrast, for a flux sweep-rate ω larger than $|2t_0 - \delta|$ a scenario emerges wherein an electron placed in one of the levels can jump to the second level and come back to the original one after a second 2π phase, thus exhibiting an unusual 4π-periodicity in the persistent current, $j = -\partial F/\partial\Phi$, where F is the free energy [189]. By independently varying t_0 and ω the splitting δ can be estimated. For typical values $t_0 \sim \delta \sim 10\mu$eV we estimate $j \sim 0.1$nA, which is of measurable size [190, 191]. For the observation, the phase-coherence length L_ϕ of the ring needs to exceed L. For GaAs rings, we note that $L_\phi \gtrsim \mu$m for sub-Kelvin temperatures [190, 191].

The effective model, Eq. (9.18), does not take into account the contribution arising from the filled Fermi sea of continuum states. However, when the number of continuum states below the gap is even—the states come in pairs with mutually canceling contributions to the current. On the other hand, when this number is odd, the topmost filled continuum state contributes to the current. Nevertheless, the amplitude of the persistent current, due to the end and continuum states, scale differently with the lattice length N—the latter behaves like $1/N$, while the former like $\delta \sim e^{-\xi/Na}$. Thus, for chains with $N \gg 1$ and $\Delta \sim \hbar v_F/Na$, the persistent current will be dominated by the end states and our effective

[4] For simplicity we omit here the spin indexes, since the $\uparrow$ and $\downarrow$ spin channels are independent and this leads only to an additional degeneracy

description fully applies. The dashed curves in Fig. 9.4 include contributions from the bound states as well as the filled Fermi sea. Indeed we have confirmed that the contributions from the continuum states are two orders of magnitude less compared to those from the bound states. Finally, for the spinfull case, the amplitude of j simply doubles, whereas the periodicity remains unchanged.

9.6 Effective quantum dot

Similar to the discrete quantum dot states, the presence of spinful, CDW-induced, localized states in the quantum wire opens up an intriguing possibility for the realization of a quantum computer device. These states are well separated from the continuum and can be filled by tuning the chemical potential to the end state level. We note that these 'quantum dots' contain automatically only one orbital level, and no individual gates are needed to tune them into a single electron regime. Due to incomplete screening there will be half-filling, i.e., only one state on either end will be filled. This is simply because once one of the energy levels on either end is filled, to fill the remaining two levels requires additional energy to overcome the Coulomb repulsion. The physics of the half-filled state is described by the usual Hubbard model, $H = -t\sum_{\sigma=\uparrow,\downarrow}(c^{\dagger}_{\sigma,R}c_{\sigma,L} + h.c.) + U\sum_{i=L,R} n_{\uparrow,i}n_{\downarrow,i}$, where t is the tunneling amplitude and U is the onsite repulsion. For the energy hierarchy $\Delta \gg U \gg t$ the effective Hamiltonian acquires the Heisenberg form, $H = J\boldsymbol{S}_R \cdot \boldsymbol{S}_L$, where $J = 4t^2/U$. The effective exchange coupling J can be controlled by changing the gate potential which determines the overlap between the left and right end modes and hence the tunneling amplitude t. We note that for weak overlap, t is small and U large making the J to be small, whereas for strong overlap the opposite is true. [5] By switching on and off the exchange constant in an appropriate sequence, the essential operations of the quantum dot, both the 'swap' and 'square-root-of-swap' operations can be performed, which, together with two single spin-qubit operations, enables the fundamental XOR gate [1].

Finite overlap between the right and the left end states can be ensured if their localization length ξ is on the order of the wire length L. This restriction yields an estimate for the strength of the periodically modulated external voltage, $\Delta_0 \sim \Lambda(a/L)^{(3-K_c)/2}$, where $\Lambda \sim v_F/a$ is the band

[5] We note that because of the gap between the bound state and the continuum, Kondo physics does not play a role.

width. A GaAs quantum wire with length $L \sim 1\mu$m with approximately $10 - 20$ gates requires a Fermi wave-length $\lambda_F \sim 50$nm. And with the parameters [192], $\Lambda \sim 0.2$eV, $K_c = 0.8$, and lattice spacing $a \approx 5$Å, we obtain $\Delta_0 \sim 0.04$meV. Thus, the upper bound for temperatures are in the achievable range of a few hundred milli-Kelvin.

9.7 Conclusions

We have shown that a CDW gap in a quantum wire can lead to bound states at the ends of the wire which are stable against weak disorder and interactions. They map to massive Dirac fermions desrcibed by the Jackiw-Rebbi model. In an AB-ring, the bound states lead to an unusual 4π-periodicity in the persistent current. Finally, the two opposite end states serve as effective double quantum dot which can be used to implement quantum computing gates for spin-qubits.

9.8 Acknowledgements

We acknowledge discussions with K. Damle, C. Klöffel, D. Rainis, B. Röthlisberger, D. Stepanenko, and V. Tripathi. This work is supported by the Swiss NSF, NCCR Nanoscience and NCCR QSIT, DARPA, and IARPA.

CHAPTER 10

Realistic transport modeling for a superconducting nanowire with Majorana fermions

Adapted from:
Diego Rainis, Luka Trifunovic, Jelena Klinovaja, and Daniel Loss
"Realistic transport modeling for a superconducting nanowire with Majorana fermions",
Phys. Rev. B **87**, 024515 (2013)

Motivated by recent experiments searching for Majorana fermions (MFs) in hybrid semiconducting-superconducting nanostructures, we consider a realistic tight-binding model and analyze its transport behavior numerically. In particular, we take into account the presence of a superconducting contact, used in real experiments to extract the current, which is usually not included in theoretical calculations. We show that important features emerge that are absent in simpler models, such as the shift in energy of the proximity gap signal, and the enhanced visibility of the topological gap for increased spin-orbit interaction. We find oscillations of the zero bias peak as a function of the magnetic field and study them analytically. We argue that many of the experimentally observed features hint at an actual spin-orbit interaction larger than the one typically assumed. However, even taking into account all the known ingredients of the experiments and exploring many parameter regimes for MFs, we are not able to reach full agreement with the reported data. Thus, a different physical origin for the observed zero-bias peak cannot be excluded.

10.1 Model

We consider a two-dimensional rectangular nanowire of length L along the $\hat{\boldsymbol{x}}$ direction and lateral extension W in the $\hat{\boldsymbol{y}}$ direction. All the plots presented in this manuscript refer to 4-subband wires ($W = 4$), but we have conducted similar simulations for $W = 1, 2, 8$ as well, noting only quantitative changes in the relative strength of the different dI/dV features (besides the known peculiarity of the one-band case, where some features are absent).

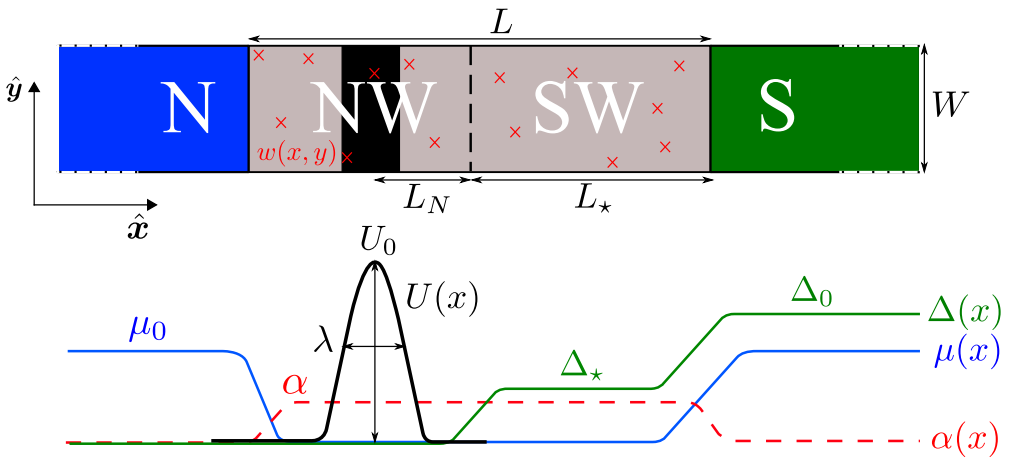

Figure 10.1: The schematics of the NSS′ geometry setup we consider in this work (top panel). The nanowire (gray) is connected on the left to a semi-infinite normal lead (N, blue) and on the right to a semi-infinite bulk s-wave superconducting lead (S, green). It consists of a normal section (NW, gray), where a potential barrier $U(x)$ (black) is created, and a proximity-induced superconducting nanowire section (SW, gray). We allow for static disorder $w(x, y)$ (red crosses) in the nanowire. The spatial dependence of the parameters entering the Hamiltonian in Eq. (10.1) is qualitatively depicted in the bottom panel.

The tight-binding Hamiltonian (lattice constant a) describing the dif-

ferent sections of the setup has the form

$$\begin{aligned} H = & \sum_{\boldsymbol{m},\boldsymbol{d}} c^\dagger_{\boldsymbol{m}+\boldsymbol{d},\alpha} \left[-t\delta_{\alpha\beta} - i\bar{\alpha}_{\boldsymbol{m}} (\hat{\boldsymbol{x}} \cdot \boldsymbol{d}) \sigma^y_{\alpha\beta} \right] c_{\boldsymbol{m},\beta} \\ & + \sum_{\boldsymbol{m}} c^\dagger_{\boldsymbol{m},\alpha} \left[(\epsilon_{\boldsymbol{m}} - \mu_0)\delta_{\alpha\beta} - \frac{g_{\boldsymbol{m}}}{2} \mu_{\mathrm{B}} B_x \sigma^x_{\alpha\beta} \right] c_{\boldsymbol{m},\beta} \\ & + \sum_{\boldsymbol{m}} \Delta_{\boldsymbol{m}} \left(c^\dagger_{\boldsymbol{m},\uparrow} c^\dagger_{\boldsymbol{m},\downarrow} + \mathrm{H.c.} \right), \end{aligned} \tag{10.1}$$

where $t = \hbar^2/(2ma^2)$ is the hopping amplitude (set to 1 and taken as an energy unit) and $\bar{\alpha}$ is the spin-flip hopping amplitude, related to the physical SOI parameter by $\bar{\alpha} = \alpha/2a$ and to the SOI energy by $E_{\mathrm{so}} = \bar{\alpha}^2/t$. Here and in the remainder of the paper we are neglecting transverse spin-orbit coupling, but we have checked that the introduction of a small finite transverse SOI is not affecting qualitatively our results. We made the assignment $t = 10$ meV, which corresponds to taking $a \simeq 15$ nm, and realistic sizes ($\sim \mu$m) are then amenable to reasonable computations. The sums run over all lattice sites $\boldsymbol{m}$ and nearest neighbors $(\boldsymbol{m} + \boldsymbol{d})$. Implicit summation over repeated spin indices is assumed. The constant μ_0 is chosen to set the common chemical potential to the zero-field bottom of the topmost band and depends on the number of subbands (i.e. on W). Further, $\epsilon_{\boldsymbol{m}} = -\mu_{\boldsymbol{m}} + U_{\boldsymbol{m}} + w_{\boldsymbol{m}}$ accounts for local variations of the chemical potential, for the tunnel-barrier potential $U_{\boldsymbol{m}}$, and includes an on-site random potential $w_{\boldsymbol{m}}$ which models Anderson disorder. The tunnel barrier has a Gaussian profile with height U_0 and width λ. The external magnetic field $\boldsymbol{B}$ points along the nanowire axis ($\hat{\boldsymbol{x}}$) and induces a Zeeman splitting $2V_{\mathrm{Z}} = g_{\boldsymbol{m}}\mu_{\mathrm{B}}B$. Finally, Δ is the pairing amplitude and can either account for the native superconductivity in the bulk s-wave superconducting lead (Δ_0) or for the proximity-induced pairing in the nanowire ($\Delta_\star$), as exemplified in Fig. 10.1. All the above quantities are taken to be site-dependent along the $\hat{\boldsymbol{x}}$ direction (except $w_{\boldsymbol{m}}$, which is taken to be completely random), so that we can model different parts of the setup. The normal lead is characterized by

$$\begin{aligned} & \bar{\alpha} = 0,\ \mu \simeq -\mu_0 \ (\text{i.e. metallic regime}), \\ & g = 2,\ w_{\boldsymbol{m}} = 0,\ \Delta_{\boldsymbol{m}} = 0. \end{aligned} \tag{10.2}$$

The nanowire is characterized by finite $\bar{\alpha} = \bar{\alpha}_{\mathrm{R}}$, chemical potential $\mu \simeq 0$ close to the bottom of the topmost band, $g = 50$ appropriate for InSb nanowires, and $\Delta_{\boldsymbol{m}}$ varying from 0 in the normal section to $\Delta_\star$ in the

proximized section. The nanowire is adiabatically connected to a metallic superconducting lead with

$$\begin{aligned} &\bar{\alpha} = 0,\ \mu \simeq -\mu_0, \\ &g = 2,\ w_{\boldsymbol{m}} = 0,\ \Delta_{\boldsymbol{m}} = \Delta_0 \geq \Delta_\star. \end{aligned} \tag{10.3}$$

In a simpler model the nanowire is semi-infinite, without external superconductor, referred to as NS geometry. This corresponds to taking the superconducting lead to be identical to the nanowire, with a single pairing amplitude $\Delta_\star$. In such a configuration, the second MF is always moved to infinity, and the ZBP is locked to zero for all $B > B_{\rm c}$, whereby the topological transition occurs at the "bulk" critical field $(g\mu_{\rm B}/2)B_{\rm c} = \sqrt{\Delta_\star^2 + \mu^2}$ [25, 26, 27, 28, 29, 30]. We will sometimes switch to this NS configuration in order to connect with previous studies [193, 194, 195, 196, 197, 198, 199, 200] and to understand the effect of the bulk superconductor.

In the actual experiments, and in a fully microscopic theoretical simulation, the nanowire has zero pairing everywhere, and the effective gap $\Delta_\star$ is generated by the coupling to the bulk superconductor. Usually one can forget about the superconductor and work with a wire with given $\Delta_\star$. However, in the considered setup the bulk S is still playing a role, since current is extracted through it, and it is therefore substantially modifying the dI/dV behavior (not simply by singling out the Andreev reflection contribution of an NS calculation). It would be different in the case of transport across a proximity wire placed on a superconductor that is not used as a contact (NSN geometry).

Our setup aims exactly at taking this fact into account: The proximity effect is included in an effective fashion (not microscopically), but we do have two different pairing regions that electrons have to cross. Still, with the sequential geometry of Fig. 10.1 we are slightly simplifying here the experimental setup [31, 32, 33], where the nanowire is side-contacted, or top-contacted, and the current does not follow a straight path.

First we note that the value of the SOI α in the experiments is not known [201], since the only available measurements have been performed in a different setup, where the SOI was likely modified. Similarly, the proximity pairing amplitude is not directly accessible, and one can only deduce it from the dI/dV behavior. Thus, it becomes interesting and even necessary to consider regimes with different SOI strengths, or different proximity pairing amplitudes.

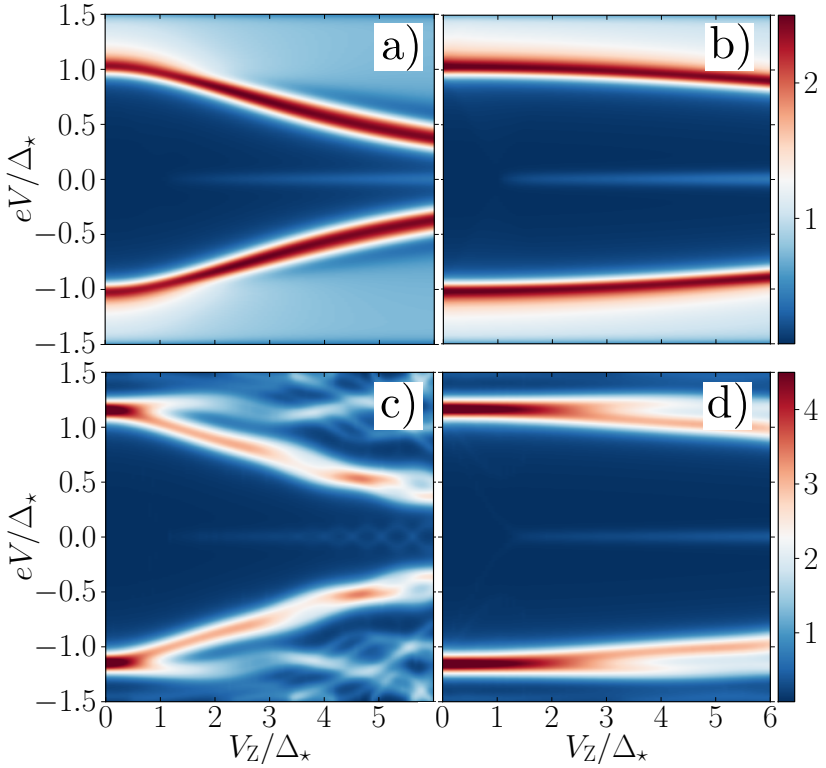

Figure 10.2: Effect of larger SOI strength, clean case. We plot here the differential conductance dI/dV evaluated as a function of bias voltage V and Zeeman energy V_Z. Panels (a) and (b) refer to the NS configuration, while (c) and (d) refer to the NSS′ setup. The parameters used here correspond to: $\Delta_\star = 250$ μeV, $\Delta_0 = 2.1$ meV (only NSS′), $\mu_0 = -3.8$ meV, $U_0 = 45$ meV, $\lambda = 1$ nm (narrow barrier), $L_N = 0$, $L_\star = 3$ μm (only NSS′) and $\mu = 0$, which corresponds to a bulk critical $V_Z^c = \Delta_\star$. For the case of InSb, the plotted range $V_Z = 0 - 6\Delta_\star$ corresponds to $B = 0 - 1$ T. Temperature is set to $T = 75$ mK. $\alpha = 0.2$ eV·Å(left column). $\alpha = 0.8$ eV·Å(right column). Larger SOI yields a slower closing of the k_F-gap $\Delta_{k_F}(B)$, in both configurations, where k_F is the Fermi momentum. Notice that in the NSS′ case the k_F-gap signal decreases in intensity as the magnetic field is increased.

10.2 Discussion

The first important point we want to make is that by assuming that the actual SOI is larger than the reported one (e.g., $\alpha = 0.2$ eV·Å, or $E_{so} = 50$ μeV [31]), one can get a substantial improvement in the calculated

dI/dV behavior, with features more similar to experiments [31, 32, 33]. In other words, the measured data suggest a stronger SOI. In particular, we observe the following facts.

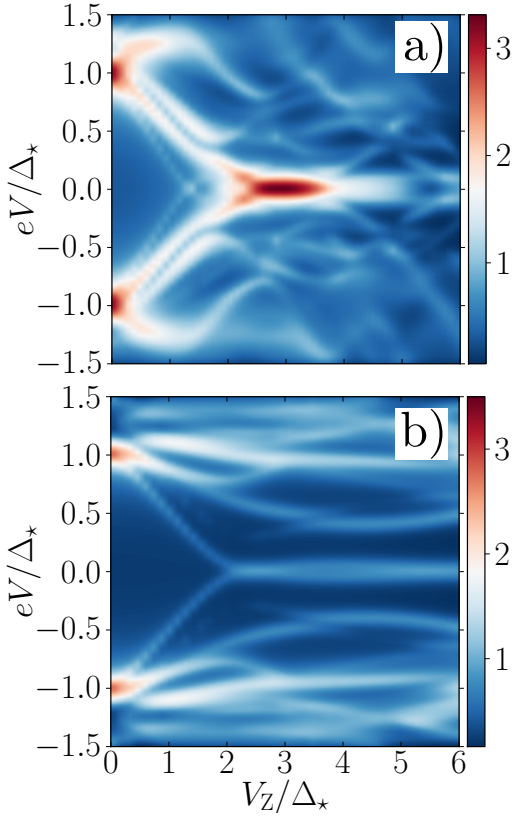

Figure 10.3: Effect of larger SOI strength on disorder, NSS′ case. The parameter values are the same as in Fig. 10.2. In addition, a realistic disorder $w_{\boldsymbol{m}} \in [-3, 3]$ meV (corresponding to a mean free path $\ell_{\rm mfp} \simeq 150$ nm [201]) is included over the entire nanowire length $L \simeq 2.5$ μm. We do not average over disorder configurations. (a) $\alpha = 0.2$ eV·Å. (b) $\alpha = 0.8$ eV·Å. In the weak SOI regime, the disorder lowers or destroys the gap relative to lower subbands, bringing many supra-gap states down, close to the Fermi level, where they cluster in some cases into a finite-extension ZBP, like in panel (a). Such clustering is, however, removed for stronger SOI [201], see panel (b).

(1) Under the assumption that the measured ZBP [31, 32, 33] arises from MFs, we conclude that $\mu \simeq 0$ in the topological section, since the ZBP emerges already at small B, $\frac{1}{2} g \mu_{\rm B} B \simeq \Delta_\star$ for $g = 50$.

However, such a small μ, together with the reported SOI values [31], would generate a rapid closing of the $k_{\rm F}$-gap $\Delta_{k_{\rm F}}$ as a function of B. This is indeed what we find in our transport calculations for $\mu \simeq 0$, $\alpha = 0.2$ eV·Å, both in the NS and NSS′ setup, see Figs. 10.2(a) and 10.2(c), respectively. Note that in the NS case the ZBP stays at zero for all fields, whereas in the NSS′ case the ZBP exhibits an oscillating splitting (see below). In the same figure we show that a stronger SOI gives a better agreement with the measured $\Delta_{k_{\rm F}}(B)$, both in the NS setup [194], see panel (b), and in the NSS′ setup, shown in panel (d). Note that this latter SOI effect, which answers the issue raised in point (iv) above, is independent of the nature of the observed ZBP.

As already observed elsewhere [196], the considered regime of $\mu \simeq 0$ is characterized by an invisible gap closing, probably due to pretransition wave functions which are delocalized throughout the wire, with little weight close to the probed edges. At finite temperature we observe this behavior both in the NS and in the NSS′ setups. On can thus state that issue (i) has been settled.

(2) When realistic Anderson disorder is included in the model, the closing of the gap becomes visible again even in the $\mu \simeq 0$ regime [197, 201, 198], reintroducing a discrepancy with experiments [31, 32, 33]. Disorder in a nanowire with *weak* SOI causes a number of subgap states to appear, some of which cluster around zero energy and possibly give rise to a nontopological ZBP, more markedly for finite μ [201]. Such states are coming from other subbands, for which the effective minigap gets reduced in the presence of disorder. This is substantiated by the fact that the ZBP in Fig. 10.3(a) has a conductance peak larger than $2e^2/h$, implying that it cannot come from the Andreev signal of a single band. For stronger SOI, the effect of disorder gets suppressed, and fewer subgap states are observed (see Fig. 10.3), more compatibly with the experimental evidence [31, 32, 33]. Due to the same mechanism, also the strong ZBP feature of Fig. 10.3(a) disappears, though. Thus, disorder is unlikely to explain the ZBP structure observed in experiments.

(3) As a consequence of the finite length of the topological section ($L_\star$) and of the B dependence of $k_{\rm F}$, we observe that the ZBP splitting exhibits oscillations of increasing amplitude as B is swept, see Fig. 10.4(a) [203]. To explain this, we recall that in the weak-SOI limit the MF wave function has an exponentially decaying envelope with localization length $\xi_{\rm M}$ and a fast-oscillating part $\sim \sin(k_{\rm F}x)$ [202]. If the magnetic field exceeds a critical value $B_{\rm c}^{**} = B_{\rm c}^{**}(\alpha, L_\star)$ (see Fig. 10.5), the two end-MFs overlap and split away from zero energy. Since $\xi_{\rm M}$ increases with B [25, 26, 27, 28,

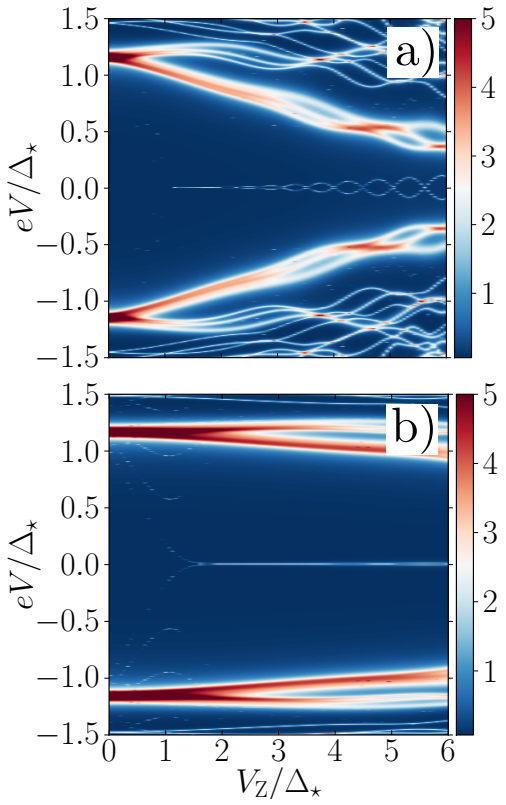

Figure 10.4: Same parameters as in Fig. 10.2, without disorder and at $T = 0$. Only the wire length is slightly smaller, $L_\star = 2.2\,\mu$m. (a) $\alpha = 0.2$ eV·Å. Note the oscillations of the ZBP, for explanations see text. (b) $\alpha = 0.8$ eV·Å. For larger SOI, the oscillations become visible at higher magnetic field (B_c^{**} increases), and with large enough SOI strength the gap closing becomes partially visible, even for the considered case of $\mu \simeq 0$, while it is not visible in an NS setup with the same parameters. The dI/dV peaks coming from the gap-closing have, however, very small width and they get washed out by realistic temperatures.

29, 30, 202], so does the splitting. However, if $k_F L_\star$ becomes an integer multiple of π as a function of B, the ZBP splitting returns to zero, leading to oscillations with a period given by

$$\delta(V_Z/\Delta_\star) = \frac{\pi\hbar}{L_\star\Delta_\star}\sqrt{\frac{2V_Z}{m}} = \frac{\pi a}{L_\star}\frac{\sqrt{tV_Z}}{\Delta_\star}\,, \tag{10.4}$$

where m is the band mass and a the lattice constant. Using parameter values corresponding to Fig. 10.4, $t/\Delta_\star = 40$, $L_\star/a = 200$, we obtain quan-

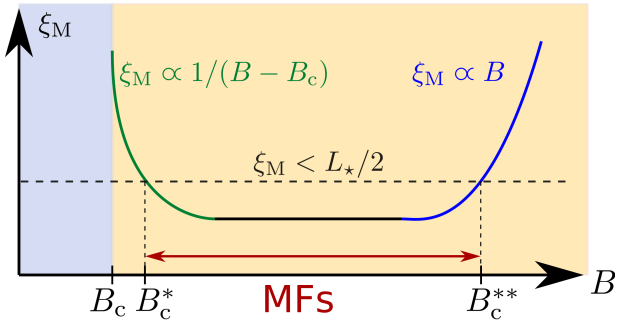

Figure 10.5: Schematic dependence of the MF localization length ξ_M on magnetic field B. According to the theory for a one-band semi-infinite nanowire [30, 29], a MF emerges when the magnetic field exceeds a critical value $B_c = 2\sqrt{\Delta_\star^2 + \mu^2}/g\mu_B$, and the system goes from the non-topological (gray) to the topological (yellow) regime. However, for a nanowire of finite length $L_\star$, due to overlap of the MFs from each end, the additional approximate condition for the observation of a MF is $\xi_M < L_\star/2$. Considering typical dependences of ξ_M on magnetic field [202], we predict that the MF should be observed for $B_c^* < B < B_c^{**}$, where the critical fields B_c^* and B_c^{**} are defined through $\xi_M(B_c^*) \approx \xi_M(B_c^{**}) \approx L_\star/2$ (cf. Fig. 10.4).

titative agreement with the simulated ZBP oscillations. Since the critical field B_c^{**} increases with SOI [202], the ZBP splitting and related oscillations occur at larger fields. In other words, the presence or absence of the oscillations in a given range of magnetic field values is determined by the strength α of the SOI and by the ratio $\xi_M(\alpha)/L_\star$. The former fixes the form of the MF wave function, the latter determines whether the two MF bound states are overlapping in a significant way or not. This explains why in Fig. 10.4(b), where strong SOI has been adopted, oscillations are starting at higher B (barely visible).

Note that these oscillations are quite robust against temperature effects, see Fig. 10.2(c). Such behavior of the ZBP is quite remarkable and provides an additional possible signature to identify MFs experimentally. One can argue at this point that the absence of oscillations in the experimentally observed ZBPs [31, 33] represents an additional hint for strong SOI.

We note in passing that in the NSS′ setup the SOI affects the visibility of the gap closing, see Fig. 10.4. Again, one can explain this behavior by invoking the changing spatial profile of the wave functions close to the

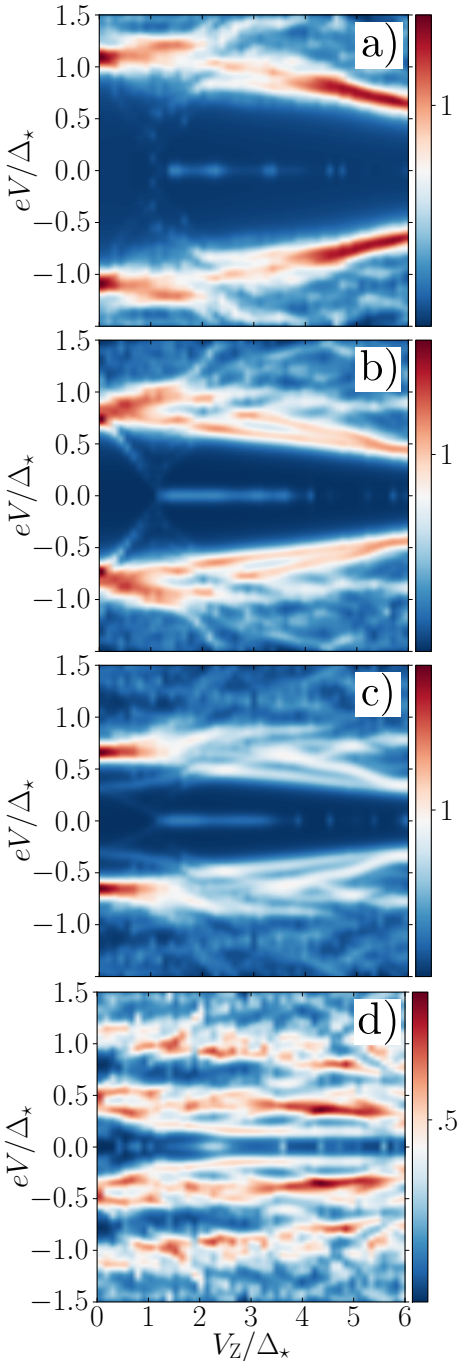

Figure 10.6: Dependence of the conductance behavior on the normal-region length L_N. Panels (a)-(d) correspond to $L_N = 0, 0.3, 0.6, 1.5\,\mu$m, respectively. The other parameters are chosen as in Fig. 10.2, apart from: $\lambda = 20$ nm, $L_\star = 3\,\mu$m, $\alpha = 0.4$ eV·Å, $w_m \in [-1.2, 1.2]$ meV ($\ell_{mfp} \simeq 1\,\mu$m). Temperature is set to $T = 75$ mK, as before. Note the evolution of the proximity peak towards lower energies and the appearance of a second peak at the largest values of L_N [panel (d)].

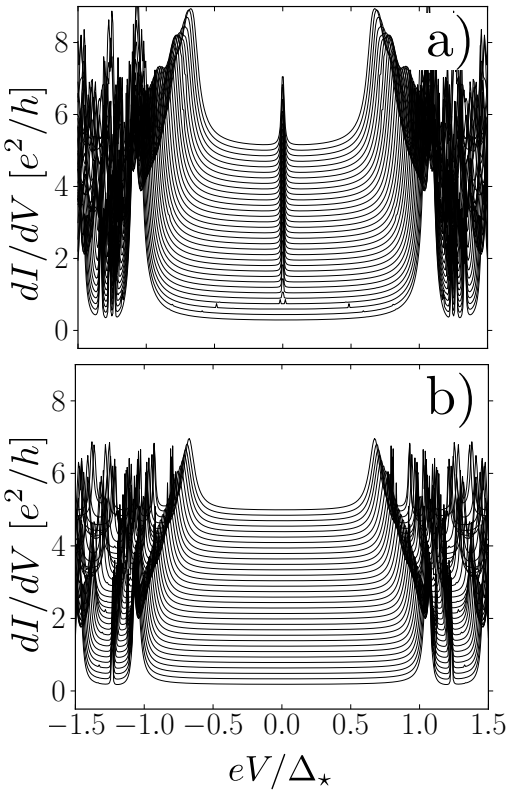

Figure 10.7: Role of the tunnel barrier $U(x)$. The parameters are chosen as in the previous figures, different curves refer to different magnetic field values, ranging from 0 to $6\Delta_\star = 1.5\,\text{meV}$ ($= 1\,\text{T}$ for $g = 50$), in steps of $0.2\,\Delta_\star$. Here we kept $T = 0$ in order to show the effect of the barrier smoothness alone. a) Gaussian tunnel barrier with width $\lambda = 1$ nm (essentially, a δ-function). The Majorana-induced ZBP is fully visible, with maximal weight $dI/dV = 2e^2/h$ at the largest magnetic fields. The closing of the gap is, however, nearly absent. b) Same system, but with $\lambda = 50$ nm, a value closer to the experimental situation. Gap-closing and ZBP are completely absent (the adopted energy resolution δE is much smaller than the realistic $k_\text{B}T$).

wire edge for different SOI values, together with the finite length of the wire. The same effect is not manifested in the case of the NS setup (infinite wire length).

Next we address further issues that have received less attention in the literature so far.

(4) The position of the proximity gap $\Delta_{k_F}(B = 0)$ as observed in the dI/dV curves is in general different from $\Delta_\star$ inserted in the Hamiltonian, Eq. (10.1). This observation is important, since it means that deducing the proximity gap from the conductance curves is not a correct procedure [31, 33]. Such an energy shift can be due to the presence of a normal section of finite length L_N between tunnel barrier and NS interface. More precisely, the observed peak moves to *lower* bias voltages for larger L_N. By increasing L_N, one can move the conductance peak deeper inside the gap and eventually even introduce additional peaks when $L_N \gtrsim \xi = \hbar v_F/(\pi\Delta_\star)$, similarly to the case of McMillan-Rowell resonances [204]. This behavior is summarized in Fig. 10.6. Alternatively, in the NSS′ configuration the peak corresponding to $\Delta_\star$ itself can be viewed as a subgap resonance of the larger gap Δ_0, and its position can be changed by varying the distance $L_\star$ of the N-S interface from the S-S′ interface. In this case, the peak moves to $larger$ energies for decreasing $L_\star$, see, e.g., Fig. 10.2(c) and 10.2(d), and Fig. 10.4, where the dI/dV peak is above $\Delta_\star$ due to the finite wire length [compare with Figs. 10.2(a) and 10.2(b)].

(5) In both NS and NSS′ configurations, the tunnel barrier plays an important role — it determines the transmission of each transport channel, which in turn sets the width of the subgap resonances [204] (without changing their height). Introduction of temperature smears the resonances while preserving their weight, which implies a reduction of the height in correspondence to the barrier-induced reduction of the width. This explains the very small value of the ZBP in experiments, and answers to issue (iii). If the resonance width becomes smaller than the temperature, the resonance is essentially invisible [201]. Consequently, if the barrier is wide enough, no subgap features are present in the dI/dV curve. If the tunnel barrier is chosen to be sharp (like in many analytical and numerical calculations), all the states present in the nanowire could become visible. However, that is not a realistic choice, since a typical barrier in experiments has a characteristic width of ~ 50 nm. For such values we already observe a momentum filtering [194], leading in some cases to a complete disappearance of MF signatures, see Fig. 10.7. Again, introducing disorder can make the aforementioned subgap features reappear. Therefore, it is the combined effect of barrier shape, SOI, and disorder strength that determines the final visibility of MFs.

10.3 Conclusions

In summary, by numerically simulating a more realistic setup than before, we have obtained new features in the transport that are similar to the ones observed in experiments. However, even after considerable effort, we do not reproduce all such features in a single configuration, and we still lack a satisfactory agreement with experiments. In particular, the exact shape of the measured ZBP is not very compatible with the picture of MFs that form and then split as a function of magnetic field. Thus, either the theoretical model is still incomplete, or a different physical origin for the observed ZBP [31, 32, 33] is to be considered. More precisely, from our findings it seems possible that in the experiments the MF features are essentially invisible and the observed ZBP is coming from some different coexisting phenomenon, like Kondo effect, which seems indeed to yield a similar behavior in some situations [205].

10.4 Acknowledgments

We thank Fabio Pedrocchi for useful discussions and Fabio Taddei for support with the numerics. This work has been supported by the Swiss NSF, NCCR Nanoscience, NCCR QSIT, and the EU project SOLID.

CHAPTER 11

Transport signatures of fractional Fermions in Rashba nanowires

Adapted from:
Diego Rainis, Arijit Saha, Jelena Klinovaja, Luka Trifunovic, and Daniel Loss
"Towards a realistic transport modeling in a superconducting nanowire with Majorana fermions",
Phys. Rev. Lett. **112**, 196803 (2014)

We theoretically study transport through a semiconducting Rashba nanowire (NW) in the presence of uniform and spatially modulated magnetic fields. The system is fully gapped, and the interplay between the spin orbit interaction and the magnetic fields leads to fractionally charged fermion (FF) bound states of Jackiw-Rebbi type at each end of the nanowire. We investigate the transport and noise behavior of a N/NW/N system, where the wire is contacted by two normal leads (N), and we look for possible signatures that could help in the experimental detection of such states. We find that the differential conductance and the shot noise exhibit a subgap structure which fully reveals the presence of the FF state. Alternatively, another confirmation of the presence of the FFs is provided by a conductance measurement in an Aharonov-Bohm (AB) setup, where the FFs are responsible for double-periodic oscillations. Our predictions can be tested in InSb/InAs nanowires and are within reach of the present technology.

11.1 Model

We consider a semiconducting NW of length L along the $\hat{x}$ direction, in the presence of long the $\hat{z}$ direction and a magnetic field that includes a uniform ($\boldsymbol{B}$) and a spatially periodic component ($\boldsymbol{B}_n$). The NW continuum Hamiltonian is given by $H_0 = \frac{1}{2}\int \mathrm{d}x \Psi^\dagger(x)\mathcal{H}_0\Psi(x)$, where $\Psi = (\Psi_\uparrow, \Psi_\downarrow)^{\mathrm{T}}$, $\Psi_\sigma(x)$ is the annihilation operator for a spin-σ electron at position x. The Hamiltonian density is of the form

$$\mathcal{H}_0 = -\hbar^2\partial_x^2/2m - \mu - i\alpha\sigma^z\partial_x \,, \tag{11.1}$$

with m the electron band mass, α the oefficient, and μ the chemical potential. The spectrum of $\mathcal{H}_0$ consists of two parabolas centered at the SOI momenta $\pm k_{\mathrm{so}} = \pm m\alpha/\hbar^2$. The magnetic field leads to the Zeeman term

$$\mathcal{H}_z = g\mu_{\mathrm{B}}[\boldsymbol{B} + \boldsymbol{B}_n(x)] \cdot \boldsymbol{\sigma}\ /2 \,, \tag{11.2}$$

where g is the Landé g-factor and μ_B the Bohr magneton. Chosen along the $\hat{x}$ direction, $\boldsymbol{B}$ opens a gap $\Delta_z = g\mu_{\mathrm{B}}B/2$ at $k = 0$. The oscillating field $\boldsymbol{B}_n(x)$ is oriented along $\hat{y}$, $\boldsymbol{B}_n = \hat{y}B_n \sin(4k_{\mathrm{so}}x + \theta)$ (but other equivalent configurations are possible [34]). It couples the two exterior branches of the spectrum, and opens up a gap $\Delta_n = g\mu_{\mathrm{B}}B_n/4$. Such a field can be generated externally, by an array of nanomagnets placed in proximity to the wire [206, 207, 208], or internally, *e.g.*, by the hyperfine field of ordered nuclear spins inside the nanowire [209].

In our analysis, we are assuming that the nergy $\epsilon_{\mathrm{so}} = m\alpha^2/2\hbar^2$ is the largest energy scale in the NW. In this strong-egime, we follow the procedure described in Refs. [210, 202], which allows us to linearize $\mathcal{H}_0$ around $k = 0$ ("interior branch") and $k = \pm 2k_{\mathrm{so}}$ ("exterior branches"). For $\mu = 0$, one obtains the spectrum around $k = 0$ and $k = \pm 2k_{\mathrm{so}}$ as $E_m^2 = (\alpha k)^2 + \Delta_m^2$, with $\Delta_m = \Delta_z, \Delta_n$ for $m = i, e$. In such situation the system is fully gapped, with no propagating modes at subgap energies, $|E| < \min\{\Delta_z, \Delta_n\}$. However, there can be localized edge states, FFs, in the gap [34]. For example, in a semi-infinite geometry there is one bound state, localized at the nanowire end, with energy

$$E_{\mathrm{FF}} = \frac{\Delta_z\Delta_n \sin\theta}{\sqrt{\Delta_z^2 + \Delta_n^2 - 2\Delta_z\Delta_n\cos\theta}} \,. \tag{11.3}$$

The angle θ encodes the boundary condition for the oscillating field at the nanowire edge. The FF state exists only if the following relation is satisfied: $\cos\theta < \min\{\Delta_z, \Delta_n\}/\max\{\Delta_z, \Delta_n\} \leq 1$, see Fig. 11.1.

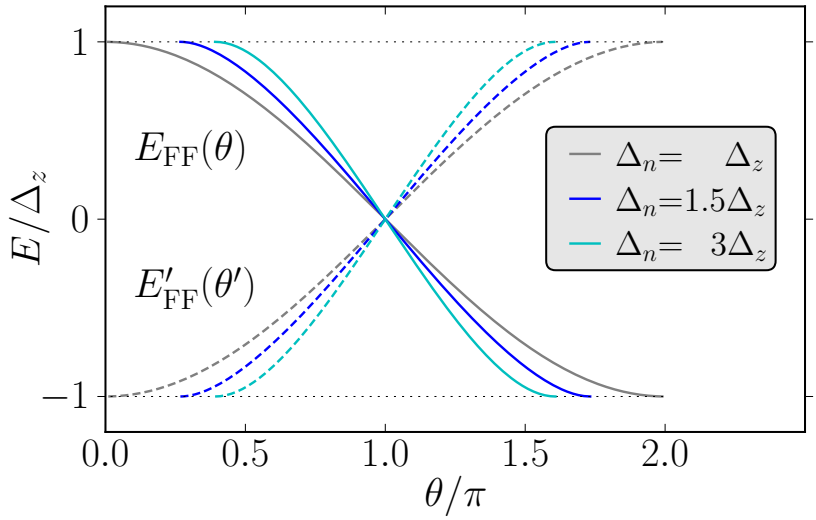

Figure 11.1: Energies $E_{\rm FF}(\theta)$ and $E'_{\rm FF}(\theta')$ of the left (full lines) and right (dashed lines) FF bound state, for $L \to \infty$, for different gap values, as evaluated from the analytical result Eq. (11.3). The angle θ' describes the right-end boundary condition for $\boldsymbol{B}_n$ and is given by $\theta + 4k_{\rm so}L$. Here we chose symmetric boundary conditions $\theta' = \theta + n\pi$, in which case the two FF energies vanish for $\theta = \pi$, merging into the continuum at $E = \min\{\Delta_z, \Delta_n\}$, in correspondence of $\bar{\theta} = \bar{\theta}(\Delta_z/\Delta_n)$.

The non-interacting, spin-degenerate left and right leads (l =L,R) are described by the Hamiltonian density $\mathcal{H}_l = -\hbar^2\partial_x^2/2m - \mu_l$. At each lead/wire interface we insert a barrier, modeled with a δ-function in the wave-function-matching analysis and with a rectangular-shaped potential in the tight-binding (TB) calculations. In the latter, more realistic case, one observes that if the barrier between NW and N sections is high enough the FFs are localized entirely in the NW section, see Figs. 11.2c)-d), and the spectra of NW and N section are decoupled, as in Fig. 11.2a). However, if the barrier is reduced, the left FF wave function (WF) can leak out in the N region and hybridize with the local WFs, see Figs. 11.2e)-f) and the red spectrum in Fig. 11.2b).

11.2 Method

To study the transport through the semiconducting NW of length L we employ an $\mathbb{S}$-matrix formalism [211, 212, 213, 214], where we match WFs

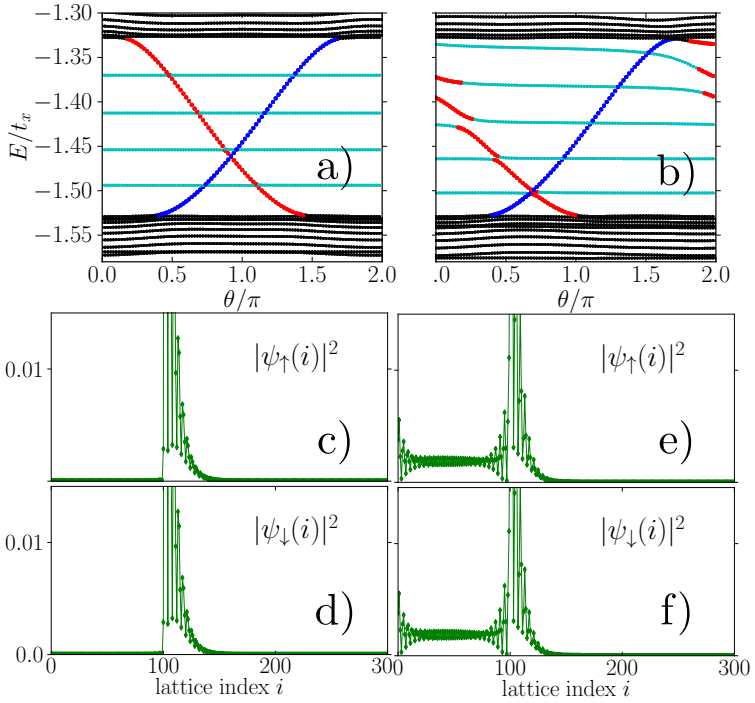

Figure 11.2: Tight-binding numerical results for a nanowire with a normal/fractional-fermion (N/FF) junction, with FF bound states in the FF phase. $\Delta_z = 0.2t_x$ and $\Delta_n = 0.1t_x$ (t_x hopping parameter). The rotating field B_n is present only in the FF section of length $L_{\rm T}$, with $L_{\rm T} = 3L_{\rm N}$ and $L_{\rm N} = 100$. At the N-FF interface there is a rectangular barrier of width $L_b = L_{\rm T}/50$, and height $V = 5t_x$ (left column) or $V = t_x$ (right column). a)-b): TB energy spectrum $E_n(\theta)$. Inside the bulk gap, delimited by continuum states (black dots), there are two FF bound states, localized at the left (red dots) and right end (blue dots). In addition, there are states localized in the N section (cyan dots). c)-f): Probability densities $|\psi_\sigma(x)|^2$ of the left FF state at $\theta = 0.6\pi$ [c),d)] and $\theta = 0.1\pi$ [e),f)]. If the barrier is high, the FF is completely localized in the FF section [c),d)], and, as a result, the FF spectrum shows no hybridization [a)] and is fully consistent with Eq. (11.3). For lower barrier, the left FF leaks out in the normal section [e),f)] and gets hybridized with the N-region subgap states [b)].

and associated probability currents [215, 216, 217] at each wire/lead interface to find the differential conductance and the shot noise in the presence of the FFs state. Depending on the choice of the spin-polarization axis in the leads, one observes different types of behavior in the spin-resolved transport coefficients $\mathbb{S}_{\sigma\sigma'}$. With the given configuration of SOI and magnetic fields, the most natural choice (provided by the eigenbasis of $\mathbb{t}^\dagger\mathbb{t}$) is to work with y-polarized electrons. We then consider incoming plane-wave WFs with wave vector $k_l = \sqrt{2m(\mu_l + E)/\hbar^2}$, and a nanowire WF that in the strong-imit reads $\psi_{\rm NW} = a\psi_i^+ + b\psi_i^- + c\psi_e^+ + d\psi_e^-$, where $\psi_{i/e}^\pm$ are the four solutions (internal/external branches, right/left movers) at energy E, given by

$$\psi_i^\pm(x) = \left(\frac{\left[E \pm \sqrt{E^2 - \Delta_z^2}\right]}{\Delta_z}, 1 \right) e^{\pm i k_z x}, \tag{11.4}$$

$$\psi_e^\pm(x) = \left(\frac{e^{i\theta}\left[E \mp \sqrt{E^2 - \Delta_n^2}\right]}{\Delta_n} e^{-2ik_{\rm so}x}, e^{2ik_{\rm so}x} \right) e^{\pm i k_n x},$$

where $\hbar k_z = \sqrt{E^2 - \Delta_z^2}/\alpha$ and $\hbar k_n = \sqrt{E^2 - \Delta_n^2}/\alpha$ are the momenta at energy E associated to internal and external branches [34]. The definitions for k_z and k_n apply both above and below the gap, where they become purely imaginary and describe evanescent modes, whose linear combination gives rise to our FF bound states.

11.3 Results

Here we present the results of our numerical analysis on transport through the SOI-coupled NW. For finite wire length, the two FF end states have a finite overlap, determined by their localization length(s)

$$\xi_{z,n}(E) \simeq \hbar\alpha/\sqrt{\Delta_{z,n}^2 - E^2}. \tag{11.5}$$

For long wires, $L \gg \xi_z, \xi_n$, the two FF states are well decoupled, and each of them has an energy approximately given by the semi-infinite wire result Eq. (11.3), see Fig. 11.1.

In Fig. 11.3, which contains the main result of this paper, we show that the transport behavior in the long-wire regime nicely follows the spectrum $E_{\rm FF}(\theta)$, provided a suitable parameter configuration is chosen.

More precisely, in order to probe in transport the unperturbed wire spectrum one needs, as usual, to operate in the tunnel regime, i.e., to have small wire-leads coupling. This is usually implemented by adding a strong potential barrier at the N/NW interfaces. However, this method has the drawback of yielding bound state energies shifted to lower values, proportionally to the wire-lead coupling, see Figs. 11.3a) and 11.3b). There is another method which allows one to make the bound state signature visible, without the need of introducing a potential barrier at the interfaces. It amounts to choosing very different Fermi energies (and hence different k_{F}'s) in the wire and in the leads (or in different portions of the wire). The momentum mismatch has then a filtering effect, and the intrinsic properties of the wire are probed without altering the $E(\theta)$ spectra (the level broadening is of course still present, decreasing for larger momentum mismatches), see Figs. 11.3c) and 11.3d). We stress that it is necessary to tune μ_l in order to make the bound state signatures visible in dI/dV. For a generic value of μ_l the momentum filtering acts either ineffectively or too effectively, erasing also the signature of the FF bound state.

In Fig. 11.3 we also show the behavior of the spin-flip reflection coefficient $R_{\uparrow\downarrow}$ as a function of energy and angle θ, in panels b) and d). One immediately notices that $R_{\uparrow\downarrow}$ exhibits a striking and evident signature of the left bound state, with a peak that almost perfectly traces its spectrum $E_{\mathrm{FF}}(\theta)$. Quite intuitively, no influence of the right bound state appears in the behavior of $R_{\uparrow\downarrow}$, apart from at energies very close to the gap, where $\xi_{z,n}$ increase significantly, and from the anticrossing at small energies, where the two branches hybridize and $R_{\uparrow\downarrow} \simeq 0$ (consistent with the fact that at those points $T_{\uparrow}$ is enhanced to 1). Therefore, if one is able to perform spin-polarized measurements yielding both $R_{\uparrow\uparrow}$ and $R_{\uparrow\downarrow}$, one should obtain a clear signature of the FF bound state when its energy (jointly set by Δ_z, Δ_n, θ) is matched by the applied bias. The additional possibility of tuning θ (*i.e.* by shifting the FF section of the wire) would grant the access to the full $E_{\mathrm{FF}}(\theta)$ behavior, an even stronger confirmation for the presence of the FF bound states.

Further experimental identification of the FFs is possible via noise measurements. We have calculated the shot noise $S \propto \mathrm{tr}\left(r^{\dagger} r t^{\dagger} t\right)$ and the Fano factor $F \propto S/I$, both for spin-polarized and spin-unpolarized transport, and shown that they indeed carry signatures of the FFs, as argued in the Supplementary Material.

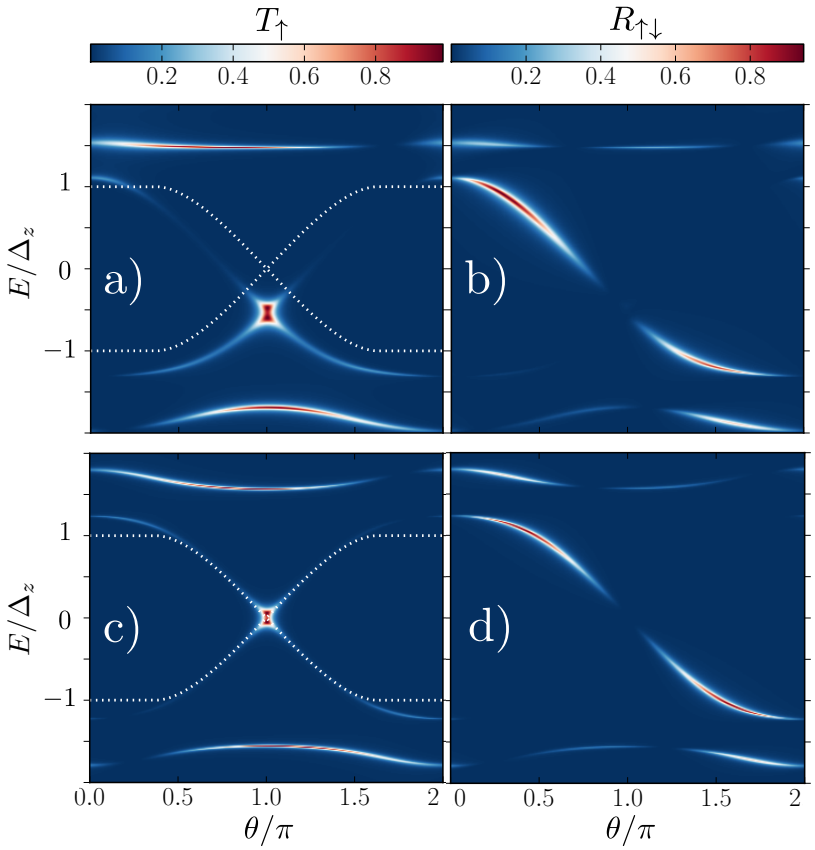

Figure 11.3: The coefficients $T_\uparrow = T_{\uparrow\uparrow} + T_{\uparrow\downarrow}$ [a) and c)] and $R_{\uparrow\downarrow}$ [b) and d)] are plotted in the E-θ plane, as evaluated in two different regimes. Panels a) and b) refer to the high-barrier (λ_1=λ_2=10α), small-μ_l limit ($k_l \simeq k_{\rm so}/2$). Panels c) and d) are instead obtained in the zero-barrier, large-μ_l limit ($k_l \simeq 100 k_{\rm so}$), which yields an equivalent degree of decoupling, but does not shift the bound state spectra, as highlighted by the white dotted lines, which correspond to Eq. (11.3). The other parameter values are $\Delta_z = \epsilon_{\rm so}/10$, $\Delta_n = \epsilon_{\rm so}/5$, $L \simeq 3\xi_z(0)$.

Aharonov-Bohm effect

As anticipated above, all the described transport signatures give indirect evidence for FFs that only stem from their peculiar energy position behavior within the gap.

In order to obtain a more robust and elegant demonstration of the presence of the FFs we envision an Aharonov-Bohm setup, as depicted in Fig. 11.4. When the energy of incoming electrons matches the energy of the overlapping FFs, a new dependence of the conductance on an applied flux Φ having a double period arises. This effect appears due to presence of the degenerate FFs that enable interference between the paths that enclose half flux. We performed numerical tight-binding calculations, by using the Kwant code [218], and obtained the two-terminal conductance $G(\Phi, V)$ as function of Φ and voltage V. Its Fourier transform with respect to Φ, $G(\nu, V)$, shows the presence of the doubled periodicity (additional peaks at $\nu = 1/2, 3/2, ...$) only when V matches the midgap energy of the FFs, see Fig. 11.5. In the Supplementary Material, besides the description of the adopted tight-binding framework, we present a simple analytical model that shows how the presence of the two degenerate FF bound states induces 4π-periodic oscillations as a function of Φ in $G(\Phi, V)$. Thus, measurement of $G(\Phi, V)$ would yield a clear evidence of the fractional charge nature of the subgap states in the proposed system.

11.4 Experimental feasibility

The transport measurements we propose are within reach of present experimental techniques. Given that the most challenging ingredient is the creation of a strong enough spatially modulated field, and the need to use large-g-factor semiconductors in order to achieve sizable Zeeman couplings, we are proposing to use large-g-factor InAs ($|g| \simeq 15$), InGaAs ($|g| \simeq 12$), and InSb wires ($|g| \simeq 51$), or less standard materials, like $InSb_{1-x}N_x$ and $GaAs_{1-x}N_x$, with g-factors of several hundreds [219]. Moreover, our setup can exhibit effects due to strain, confinement, and interactions, which are known to significantly modify g [220, 221, 222, 223, 224, 225]. Taking typical magnetic fields generated by nanomagnets, $B_n \simeq 50$ mT [208], we obtain for InSb $\Delta_n \simeq 40$ μeV, corresponding to $\simeq 0.5$ K. It is convenient to choose similar values also for $\boldsymbol{B}$, so that the two gaps are comparable and the bound state can be observed for a large range of θ (see Fig. 11.1), whose exact value in a measurement can be

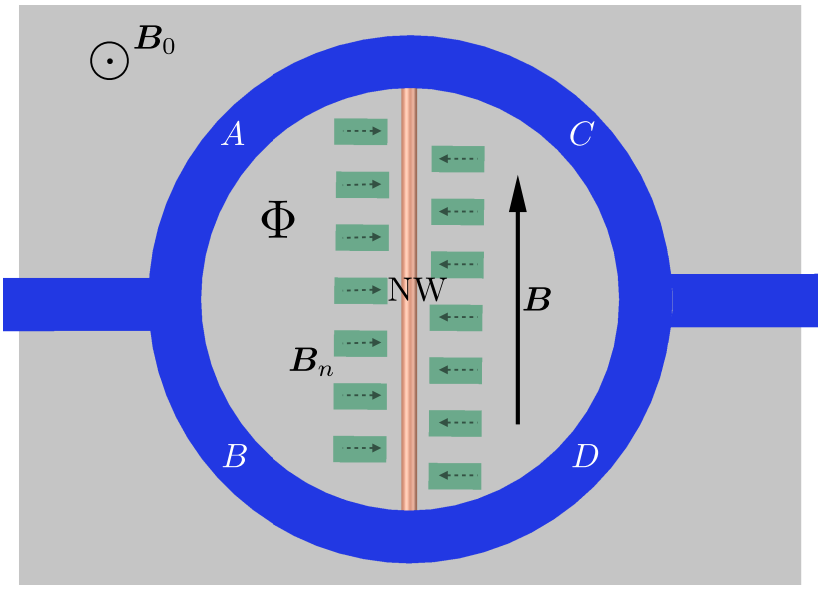

Figure 11.4: Aharonov-Bohm setup where the NW (pink, light gray) hosting a FF at each end connects the two arms of the AB ring (blue, black). When μ lies within the NW gap, only standard AB oscillations in the conductance $G(\Phi)$ as function of flux Φ (generated by a perpendicular magnetic field B_0) appear, whereas when resonance with the degenerate FFs is reached, G exhibits new oscillations with *doubled* period, see Fig. 11.5

not easy to control. As explained above, the tuning of μ in the wire is achieved via an underlying gate, while the tunnel barriers are created by gate fingers or by the wire-lead interfaces themselves. The nergy in InSb wires is $\simeq 50$ μeV, so that the above numbers would indeed place the experiment in the strong-egime. Corresponding estimates for $\xi_z(0)$ give us $\simeq 0.5$ μm, and thus an optimal wire length of $L \simeq 1.5$ μm. Finally, the requirement that B_n couples the $\pm 2k_{\rm so}$ branches translates into having the nanomagnets separated by $2\pi/4k_{\rm so} \simeq 300$ nm.

11.5 Conclusions

We have studied the transport properties of a Rashba NW that, under appropriate conditions, supports subgap FF states bound to the wire ends. We have shown that there are regimes where conductance and shot noise measurements reveal the FF presence. The fractional charge

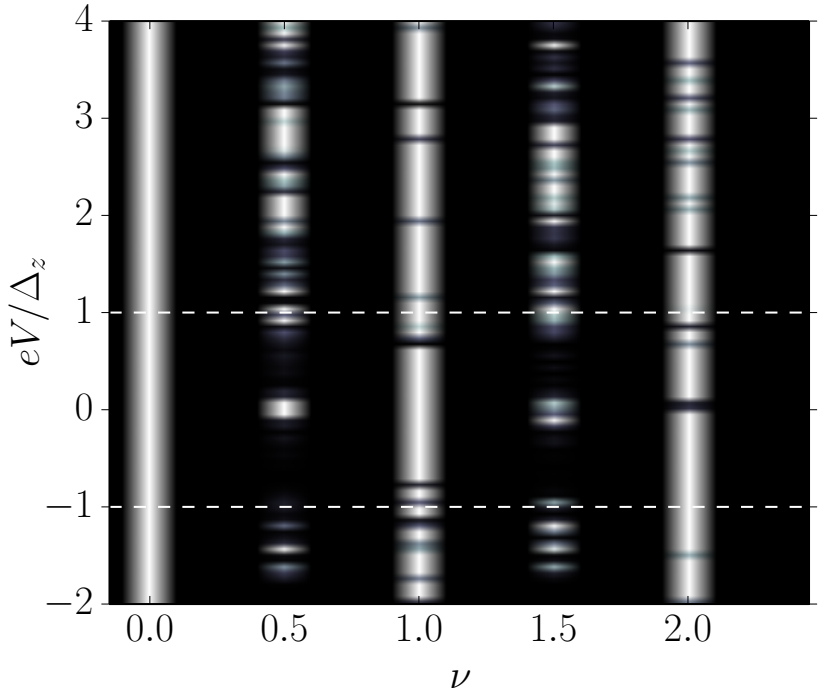

Figure 11.5: The dependence of the conductance $G(\nu, V)$ (in arbitrary units) on frequency ν (conjugate to Φ/Φ_0) of the AB-oscillations and applied voltage V for the AB-ring shown in Fig. 11.4. For V within the gap of the wire (white dashed lines), the doubled periodicity (giving rise to additional conductance peaks at $\nu = 1/2, 3/2, ...$) is observed only when V matches the energy of the midgap FFs.

of the FF bound states can be further confirmed by an Aharonov-Bohm experiment exhibiting double-periodic conductance oscillations.

11.6 Acknowledgements

We thank R. Tiwari for discussions, X. Waintal and M. Wimmer for help with the numerics, and the Swiss NSF, the NCCR QSIT, and the EU project SOLID for support.

Bibliography

[1] D. Loss and D. DiVincenzo, "Quantum computation with quantum dots," *Phys. Rev. A*, vol. 57, p. 120, Jan. 1998.

[2] L. P. Kouwenhoven, D. G. Austing, and S. Tarucha, "Few-electron quantum dots," *Rep. Prog. Phys.*, vol. 64, no. 6, p. 701, 2001.

[3] R. Hanson, L. P. Kouwenhoven, J. R. Petta, S. Tarucha, and L. M. K. Vandersypen, "Spins in few-electron quantum dots," *Rev. Mod. Phys.*, vol. 79, pp. 1217–1265, Oct 2007.

[4] C. Kloeffel and D. Loss, "Prospects for spin-based quantum computing in quantum dots," *Annual Review of Condensed Matter Physics*, vol. 4, no. 1, pp. 51–81, 2013.

[5] D. P. DiVincenzo, "Topics in Quantum Computers," *eprint arXiv:cond-mat/9612126*, Dec. 1996.

[6] J. M. Elzerman, R. Hanson, L. H. Willems van Beveren, B. Witkamp, L. M. K. Vandersypen, and L. P. Kouwenhoven, "Single-shot readout of an individual electron spin in a quantum dot," *Nature*, vol. 430, no. 6998, pp. 431–435, 2004.

[7] J. Wrachtrup and F. Jelezko, "Processing quantum information in diamond," *Journal of Physics: Condensed Matter*, vol. 18, no. 21, p. 807, 2006.

[8] P. Neumann, J. Beck, M. Steiner, F. Rempp, H. Fedder, P. R. Hemmer, J. Wrachtrup, and F. Jelezko, "Single-shot readout of a single nuclear spin," *Science*, vol. 329, no. 5991, pp. 542–544, 2010.

[9] J.-P. Tetienne, L. Rondin, P. Spinicelli, M. Chipaux, T. Debuisschert, J.-F. Roch, and V. Jacques, "Magnetic-field-dependent photodynamics of single nv defects in diamond: an application to quali-

tative all-optical magnetic imaging," *New J. of Phys.*, vol. 14, no. 10, p. 103033, 2012.

[10] A. Gruber, A. Dräbenstedt, C. Tietz, L. Fleury, J. Wrachtrup, and C. v. Borczyskowski, "Scanning confocal optical microscopy and magnetic resonance on single defect centers," *Science*, vol. 276, no. 5321, pp. 2012–2014, 1997.

[11] G. Balasubramanian, P. Neumann, D. Twitchen, M. Markham, R. Kolesov, N. Mizuochi, J. Isoya, J. Achard, J. Beck, J. Tissler, V. Jacques, P. R. Hemmer, F. Jelezko, and J. Wrachtrup, "Ultralong spin coherence time in isotopically engineered diamond," *Nat Mater*, vol. 8, no. 5, pp. 383–387, 2009.

[12] T. Gaebel, M. Domhan, I. Popa, C. Wittmann, P. Neumann, F. Jelezko, J. R. Rabeau, N. Stavrias, A. D. Greentree, S. Prawer, J. Meijer, J. Twamley, P. R. Hemmer, and J. Wrachtrup, "Room-temperature coherent coupling of single spins in diamond," *Nat Phys*, vol. 2, no. 6, pp. 408–413, 2006.

[13] H. J. Mamin, M. Kim, M. H. Sherwood, C. T. Rettner, K. Ohno, D. D. Awschalom, and D. Rugar, "Nanoscale nuclear magnetic resonance with a nitrogen-vacancy spin sensor," *Science*, vol. 339, no. 6119, pp. 557–560, 2013.

[14] M. S. Grinolds, M. Warner, K. D. Greve, Y. Dovzhenko, L. Thiel, R. L. Walsworth, S. Hong, P. Maletinsky, and A. Yacoby, "Sub-nanometre resolution in three-dimensional magnetic resonance imaging of individual dark spins," *Nat. Nano.*, vol. 9, pp. 279–284, Apr. 2014.

[15] T. Staudacher, F. Shi, S. Pezzagna, J. Meijer, J. Du, C. A. Meriles, F. Reinhard, and J. Wrachtrup *Science*, vol. 339, no. 6119, pp. 561–563, 2013.

[16] L. Rondin, J. P. Tetienne, T. Hingant, J. F. Roch, P. Maletinsky, and V. Jacques, "Magnetometry with nitrogen-vacancy defects in diamond," *Rep. Prog. Phys.*, vol. 77, no. 5, p. 056503, 2014.

[17] G. Waldherr, J. Beck, P. Neumann, R. S. Said, M. Nitsche, M. L. Markham, D. J. Twitchen, J. Twamley, F. Jelezko, and J. Wrachtrup, "High-dynamic-range magnetometry with a single nuclear spin in diamond," *Nat Nano*, vol. 7, no. 2, pp. 105–108, 2012.

[18] L. C. Bassett, F. J. Heremans, D. J. Christle, C. G. Yale, G. Burkard, B. B. Buckley, and D. D. Awschalom, "Ultrafast optical control of orbital and spin dynamics in a solid-state defect," *Science*, 2014.

[19] P. Maletinsky, S. Hong, M. S. Grinolds, B. Hausmann, M. D. Lukin, R. L. Walsworth, M. Loncar, and A. Yacoby, "A robust scanning diamond sensor for nanoscale imaging with single nitrogen-vacancy centres," *Nat. Nano*, vol. 7, no. 5, pp. 320–324, 2012.

[20] D. S. Wang, A. G. Fowler, and L. C. L. Hollenberg, "Surface code quantum computing with error rates over 1%," *Phys. Rev. A*, vol. 83, p. 020302, Feb 2011.

[21] R. Raussendorf and J. Harrington, "Fault-tolerant quantum computation with high threshold in two dimensions," *Phys. Rev. Lett.*, vol. 98, p. 190504, May 2007.

[22] F. Wilczek, "Quantum mechanics of fractional-spin particles," *Phys. Rev. Lett.*, vol. 49, pp. 957–959, Oct 1982.

[23] R. Streater and I. Wilde, "Fermion states of a boson field," *Nuclear Physics B*, vol. 24, no. 3, pp. 561 – 575, 1970.

[24] S. Fujimoto, "Topological order and non-abelian statistics in noncentrosymmetric s-wave superconductors," *Phys. Rev. B*, vol. 77, no. 22, p. 220501, 2008.

[25] M. Sato, Y. Takahashi, and S. Fujimoto, "Non-abelian topological order in s-wave superfluids of ultracold fermionic atoms," *Phys. Rev. Lett.*, vol. 103, no. 2, p. 020401, 2009.

[26] J. D. Sau *et al.*, "Generic new platform for topological quantum computation using semiconductor heterostructures," *Phys. Rev. Lett.*, vol. 104, no. 4, p. 040502, 2010.

[27] M. Sato, Y. Takahashi, and S. Fujimoto, "Non-abelian topological orders and majorana fermions in spin-singlet superconductors," *Phys. Rev. B*, vol. 82, no. 13, p. 134521, 2010.

[28] J. Alicea, "Majorana fermions in a tunable semiconductor device," *Phys. Rev. B*, vol. 81, no. 12, p. 125318, 2010.

[29] R. M. Lutchyn, J. D. Sau, and S. Das Sarma, "Majorana fermions and a topological phase transition in semiconductor-superconductor heterostructures," *Phys. Rev. Lett.*, vol. 105, p. 077001, 2010.

[30] Y. Oreg, G. Refael, and F. von Oppen, "Helical liquids and majorana bound states in quantum wires," *Phys. Rev. Lett.*, vol. 105, p. 177002, 2010.

[31] V. Mourik *et al.*, "Signatures of majorana fermions in hybrid superconductor-semiconductor nanowire devices," *Science*, vol. 336, p. 1003, 2012.

[32] M. T. Deng, C. L. Yu, G. Y. Huang, M. Larsson, P. Caroff, and H. Q. Xu, "Anomalous zero-bias conductance peak in a nb–insb nanowire–nb hybrid device," *Nano Letters*, vol. 12, no. 12, pp. 6414–6419, 2012.

[33] A. Das, Y. Ronen, Y. Most, Y. Oreg, M. Heiblum, and H. Shtrikman, "Zero-bias peaks and splitting in an al-inas nanowire topological superconductor as a signature of majorana fermions," *Nat Phys*, vol. 8, no. 12, pp. 887–895, 2012.

[34] J. Klinovaja, P. Stano, and D. Loss, "Transition from fractional to majorana fermions in rashba nanowires," *Phys. Rev. Lett.*, vol. 109, p. 236801, 2012.

[35] J. Klinovaja and D. Loss, "Fractional fermions with non-abelian statistics," *Phys. Rev. Lett.*, vol. 110, p. 126402, 2013.

[36] F. Jelezko, T. Gaebel, I. Popa, A. Gruber, and J. Wrachtrup, "Observation of coherent oscillations in a single electron spin," *Phys. Rev. Lett.*, vol. 92, p. 076401, Feb 2004.

[37] F. Jelezko, T. Gaebel, I. Popa, M. Domhan, A. Gruber, and J. Wrachtrup, "Observation of coherent oscillation of a single nuclear spin and realization of a two-qubit conditional quantum gate," *Phys. Rev. Lett.*, vol. 93, p. 130501, Sep 2004.

[38] L. Childress, M. V. Gurudev Dutt, J. M. Taylor, A. S. Zibrov, F. Jelezko, J. Wrachtrup, P. R. Hemmer, and M. D. Lukin, "Coherent dynamics of coupled electron and nuclear spin qubits in diamond," *Science*, vol. 314, no. 5797, pp. 281–285, 2006.

[39] M. V. G. Dutt, L. Childress, L. Jiang, E. Togan, J. Maze, F. Jelezko, A. S. Zibrov, P. R. Hemmer, and M. D. Lukin, "Quantum register based on individual electronic and nuclear spin qubits in diamond," *Science*, vol. 316, no. 5829, pp. 1312–1316, 2007.

[40] R. Hanson, V. V. Dobrovitski, A. E. Feiguin, O. Gywat, and D. D. Awschalom, "Coherent dynamics of a single spin interacting with an adjustable spin bath," *Science*, vol. 320, no. 5874, pp. 352–355, 2008.

[41] P. Neumann, N. Mizuochi, F. Rempp, P. Hemmer, H. Watanabe, S. Yamasaki, V. Jacques, T. Gaebel, F. Jelezko, and J. Wrachtrup, "Multipartite entanglement among single spins in diamond," *Science*, vol. 320, no. 5881, pp. 1326–1329, 2008.

[42] L. Jiang, J. S. Hodges, J. R. Maze, P. Maurer, J. M. Taylor, D. G. Cory, P. R. Hemmer, R. L. Walsworth, A. Yacoby, A. S. Zibrov, and M. D. Lukin, "Repetitive readout of a single electronic spin via quantum logic with nuclear spin ancillae," *Science*, vol. 326, no. 5950, pp. 267–272, 2009.

[43] G. D. Fuchs, V. V. Dobrovitski, D. M. Toyli, F. J. Heremans, and D. D. Awschalom, "Gigahertz dynamics of a strongly driven single quantum spin," *Science*, vol. 326, no. 5959, pp. 1520–1522, 2009.

[44] P. Neumann, J. Beck, M. Steiner, F. Rempp, H. Fedder, P. R. Hemmer, J. Wrachtrup, and F. Jelezko, "Single-shot readout of a single nuclear spin," *Science*, vol. 329, no. 5991, pp. 542–544, 2010.

[45] B. B. Buckley, G. D. Fuchs, L. C. Bassett, and D. D. Awschalom, "Spin-light coherence for single-spin measurement and control in diamond," *Science*, vol. 330, no. 6008, pp. 1212–1215, 2010.

[46] E. Togan, Y. Chu, A. Trifonov, L. Jiang, J. Maze, L. Childress, M. Dutt, A. Sorensen, P. Hemmer, A. Zibrov, and M. Lukin, "Quantum entanglement between an optical photon and a solid-state spin qubit," *Nature*, vol. 466, no. 7307, pp. 730–734, 2010.

[47] L. Robledo, L. Childress, H. Bernien, B. Hensen, P. F. Alkemade, and R. Hanson, "High-fidelity projective read-out of a solid-state spin quantum register," *Nature*, vol. 477, no. 7366, pp. 574–578, 2011.

[48] J. J. Pla, K. Y. Tan, J. P. Dehollain, W. H. Lim, J. J. L. Morton, F. A. Zwanenburg, D. N. Jamieson, A. S. Dzurak, and A. Morello, "High-fidelity readout and control of a nuclear spin qubit in silicon," *arXiv:1302.0047*, Jan. 2013.

[49] J. J. Pla, K. Y. Tan, J. P. Dehollain, W. H. Lim, J. J. L. Morton, D. N. Jamieson, A. S. Dzurak, and A. Morello, "A single-atom electron spin qubit in silicon," *Nature*, vol. 489, pp. 541–545, Sept. 2012.

[50] V. Dobrovitski, G. Fuchs, A. Falk, C. Santori, and D. Awschalom, "Quantum control over single spins in diamond," *Ann. Rev. Condens. Matter Phys.*, vol. 4, no. 1, pp. 23–50, 2013.

[51] M.-S. Choi, C. Bruder, and D. Loss, "Spin-dependent josephson current through double quantum dots and measurement of entangled electron states," *Phys. Rev. B*, vol. 62, p. 13569, Nov. 2000.

[52] A. Wallraff, D. I. Schuster, A. Blais, L. Frunzio, R.-S. Huang, J. Majer, S. Kumar, S. M. Girvin, and R. J. Schoelkopf, "Strong coupling of a single photon to a superconducting qubit using circuit quantum electrodynamics," *Nature*, vol. 431, no. 7005, pp. 162–167, 2004.

[53] L. Childress, A. S. Sørensen, and M. D. Lukin, "Mesoscopic cavity quantum electrodynamics with quantum dots," *Phys. Rev. A*, vol. 69, p. 042302, Apr 2004.

[54] Y. Rikitake and H. Imamura, "Decoherence of localized spins interacting via RKKY interaction," *Phys. Rev. B*, vol. 72, p. 033308, July 2005.

[55] G. Burkard and A. Imamoglu, "Ultra-long-distance interaction between spin qubits," *Phys. Rev. B*, vol. 74, p. 041307, Jul 2006.

[56] C. Flindt, A. S. Sørensen, and K. Flensberg, "Spin-orbit mediated control of spin qubits," *Phys. Rev. Lett.*, vol. 97, p. 240501, Dec. 2006.

[57] M. Trif, V. N. Golovach, and D. Loss, "Spin-spin coupling in electrostatically coupled quantum dots," *Phys. Rev. B*, vol. 75, p. 085307, Feb. 2007.

[58] M. Trif, V. N. Golovach, and D. Loss, "Spin dynamics in inas nanowire quantum dots coupled to a transmission line," *Phys. Rev. B*, vol. 77, p. 045434, Jan 2008.

[59] K. Flensberg and C. M. Marcus, "Bends in nanotubes allow electric spin control and coupling," *Phys. Rev. B*, vol. 81, p. 195418, May 2010.

[60] L. Trifunovic, O. Dial, M. Trif, J. R. Wootton, R. Abebe, A. Yacoby, and D. Loss, "Long-distance spin-spin coupling via floating gates," *Phys. Rev. X*, vol. 2, p. 011006, Jan. 2012.

[61] M. D. Shulman, O. E. Dial, S. P. Harvey, H. Bluhm, V. Umansky, and A. Yacoby, "Demonstration of entanglement of electrostatically coupled singlet-triplet qubits," *Science*, vol. 336, pp. 202–205, Apr. 2012.

[62] M. Leijnse and K. Flensberg, "Coupling spin qubits via superconductors," *Phys. Rev. Lett.*, vol. 111, p. 060501, Aug 2013.

[63] J. Levy, "Universal quantum computation with spin-1/2 pairs and heisenberg exchange," *Phys. Rev. Lett.*, vol. 89, no. 14, p. 147902, 2002.

[64] S. Amasha, K. MacLean, I. P. Radu, D. M. Zumbühl, M. A. Kastner, M. P. Hanson, and A. C. Gossard, "Electrical control of spin relaxation in a quantum dot," *Phys. Rev. Lett.*, vol. 100, p. 046803, Jan. 2008.

[65] H. Bluhm, S. Foletti, I. Neder, M. Rudner, D. Mahalu, V. Umansky, and A. Yacoby, "Dephasing time of gaas electron-spin qubits coupled to a nuclear bath exceeding 200μs," *Nat. Phys.*, vol. 7, no. 2, pp. 109–113, 2011.

[66] J. R. Petta, A. C. Johnson, J. M. Taylor, E. A. Laird, A. Yacoby, M. D. Lukin, C. M. Marcus, M. P. Hanson, and A. C. Gossard, "Coherent manipulation of coupled electron spins in semiconductor quantum dots," *Science*, vol. 309, no. 5744, pp. 2180–2184, 2005.

[67] F. H. L. Koppens, K. C. Nowack, and L. M. K. Vandersypen, "Spin echo of a single electron spin in a quantum dot," *Phys. Rev. Lett.*, vol. 100, p. 236802, Jun 2008.

[68] R. Brunner, Y.-S. Shin, T. Obata, M. Pioro-Ladrière, T. Kubo, K. Yoshida, T. Taniyama, Y. Tokura, and S. Tarucha, "Two-qubit gate of combined single-spin rotation and interdot spin exchange in a double quantum dot," *Phys. Rev. Lett.*, vol. 107, p. 146801, 2011.

[69] A. M. Childs, H. L. Haselgrove, and M. A. Nielsen, "Lower bounds on the complexity of simulating quantum gates," *Phys. Rev. A*, vol. 68, p. 052311, 2003.

[70] R. Raussendorf and J. Harrington, "Fault-tolerant quantum computation with high threshold in two dimensions," *Phys. Rev. Lett.*, vol. 98, p. 190504, 2007.

[71] M. Trif, F. Troiani, D. Stepanenko, and D. Loss, "Spin-electric coupling in molecular magnets," *Phys. Rev. Lett.*, vol. 101, p. 217201, Nov 2008.

[72] I. H. Chan, R. M. Westervelt, K. D. Maranowski, and A. C. Gossard, "Strongly capacitively coupled quantum dots," *Appl. Phys. Lett.*, vol. 80, no. 10, p. 1818, 2002.

[73] I. Chan, P. Fallahi, R. Westervelt, K. Maranowski, and A. Gossard, "Capacitively coupled quantum dots as a single-electron switch," *Physica E*, vol. 17, no. 0, pp. 584 – 588, 2003.

[74] F. Kuemmeth, S. Ilani, D. C. Ralph, and P. L. McEuen, "Coupling of spin and orbital motion of electrons in carbon nanotubes," *Nature*, vol. 452, pp. 448–452, Mar. 2008.

[75] Y. Hu, H. O. H. Churchill, D. J. Reilly, J. Xiang, C. M. Lieber, and C. M. Marcus, "A ge/si heterostructure nanowire-based double quantum dot with integrated charge sensor," *Nat. Nanotech.*, vol. 2, p. 622, 2007.

[76] D. Stepanenko and G. Burkard, "Quantum gates between capacitively coupled double quantum dot two-spin qubits," *Phys. Rev. B*, vol. 75, p. 085324, Feb. 2007.

[77] A. C. Johnson, J. R. Petta, J. M. Taylor, A. Yacoby, M. D. Lukin, C. M. Marcus, M. P. Hanson, and A. C. Gossard, "Triplet-singlet spin relaxation via nuclei in a double quantum dot," *Nature*, vol. 435, no. 7044, pp. 925–928, 2005.

[78] J. Sten, "Ellipsoidal harmonics and their application in electrostatics," *J. Electrostatics*, vol. 64, pp. 647–654, Sept. 2006.

[79] G. Burkard, D. Loss, and D. P. DiVincenzo, "Coupled quantum dots as quantum gates," *Phys. Rev. B*, vol. 59, p. 2070, Jan. 1999.

[80] J. H. Van Vleck, "Paramagnetic relaxation times for titanium and chrome alum," *Phys. Rev.*, vol. 57, pp. 426–447, Mar 1940.

[81] V. N. Golovach, A. Khaetskii, and D. Loss, "Phonon-induced decay of the electron spin in quantum dots," *Phys. Rev. Lett.*, vol. 93, p. 016601, Jun 2004.

[82] R. Hanson, L. P. Kouwenhoven, J. R. Petta, S. Tarucha, and L. M. K. Vandersypen, "Spins in few-electron quantum dots," *Rev. Mod. Phys.*, vol. 79, p. 1217, Oct. 2007.

[83] R. Zak, B. Rothlisberger, S. Chesi, and D. Loss, "Quantum computing with electron pins in quantum dots," *Riv. Nuovo Cimento*, vol. 33, pp. 345–399, June 2010.

[84] D. Stepanenko, M. Rudner, B. I. Halperin, and D. Loss, "Singlet-triplet splitting in double quantum dots due to spin-orbit and hyperfine interactions," *Phys. Rev. B*, vol. 85, p. 075416, Feb 2012.

[85] D. P. DiVincenzo, "Fault-tolerant architectures for superconducting qubits," *Phys. Scr.*, vol. T137, p. 014020, 2009.

[86] F. H. L. Koppens, C. Buizert, K. J. Tielrooij, I. T. Vink, K. C. Nowack, T. Meunier, L. P. Kouwenhoven, and L. M. K. Vandersypen, "Driven coherent oscillations of a single electron spin in a quantum dot," *Nature*, vol. 442, p. 766, 2006.

[87] V. N. Golovach, M. Borhani, and D. Loss, "Electric-dipole-induced spin resonance in quantum dots," *Phys. Rev. B*, vol. 74, p. 165319, 2006.

[88] K. C. Nowack, F. H. L. Koppens, Y. V. Nazarov, and L. M. K. Vandersypen, "Coherent control of a single electron spin with electric fields," *Science*, vol. 318, p. 1430, 2007.

[89] S. Nadj-Perge, S. M. Frolov, E. P. A. M. Bakkers, and L. P. Kouwenhoven, "Spin-orbit qubit in a semiconductor nanowire," *Nature*, vol. 468, p. 1084, 2011.

[90] C. Fasth, F. A., L. Samuleson, V. N. Golovach, and D. Loss, "Direct measurement of the spin-orbit interaction in a two-electron inas nanowire quantum dot," *Phys. Rev. Lett.*, vol. 98, p. 266801, 2007.

[91] C. Kloeffel, M. Trif, and D. Loss, "Strong spin-orbit interaction and helical hole states in ge/si nanowires," *Phys. Rev. B*, vol. 84, p. 195314, Nov 2011.

[92] D. V. Bulaev, B. Trauzettel, and D. Loss, "Spin-orbit interaction and anomalous spin relaxation in carbon nanotube quantum dots," *Phys. Rev. B*, vol. 77, p. 235301, 2008.

[93] H. O. H. Churchill, A. J. Bestwick, J. W. Harlow, J. Kuemmeth, D. Marcos, C. H. Stwertka, S. K. Watson, and C. M. Marcus, "Electron–nuclear interaction in 13c nanotube double quantum dots," *Nat. Phys.*, vol. 5, p. 321, 2009.

[94] J. Klinovaja, M. J. Schmidt, B. Braunecker, and D. Loss, "Helical modes in carbon nanotubes generated by strong electric fields," *Phys. Rev. Lett.*, vol. 106, p. 156809, 2011.

[95] J. Fischer and D. Loss, "Dealing with decoherence," *Science*, vol. 324, no. 5932, pp. 1277–1278, 2009.

[96] F. Marquardt and V. A. Abalmassov, "Spin relaxation in a quantum dot due to nyquist noise," *Phys. Rev. B*, vol. 71, p. 165325, Apr. 2005.

[97] S. Bravyi, D. DiVincenzo, and D. Loss, "Schrieffer-wolff transformation for quantum many-body systems," *Ann. Phys.*, vol. 326, no. 10, pp. 2793 – 2826, 2011.

[98] C. Kittel, "On the theory of ferromagnetic resonance absorption," *Phys. Rev.*, vol. 73, pp. 155–161, Jan 1948.

[99] H. Watanabe and H. Murayama, "Unified description of nambu-goldstone bosons without lorentz invariance," *Phys. Rev. Lett.*, vol. 108, p. 251602, Jun 2012.

[100] M. Sparks, "Ferromagnetic resonance in thin films. i. theory of normal-mode frequencies," *Phys. Rev. B*, vol. 1, pp. 3831–3856, May 1970.

[101] I. Lee, Y. Obukhov, G. Xiang, A. Hauser, F. Yang, P. Banerjee, D. V. Pelekhov, and P. C. Hammel, "Nanoscale scanning probe ferromagnetic resonance imaging using localized modes," *Nature*, vol. 466, no. 7308, pp. 845–848, 2010.

[102] M. A. Nielsen and I. L. Chuang, *Quantum Computation and Quantum Information*. Cambridge University Press, 1 ed., Jan. 2004.

[103] A. Imamoglu, D. D. Awschalom, G. Burkard, D. P. DiVincenzo, D. Loss, M. Sherwin, and A. Small, "Quantum information processing using quantum dot spins and cavity qed," *Phys. Rev. Lett.*, vol. 83, pp. 4204–4207, Nov 1999.

[104] T. Tanamoto, K. Maruyama, Y. X. Liu, X. Hu, and F. Nori, "Efficient purification protocols using iSWAP gates in solid-state qubits," *Phys. Rev. A*, vol. 78, p. 062313, Dec 2008.

[105] D. P. DiVincenzo and D. Loss, "Rigorous born approximation and beyond for the spin-boson model," *Phys. Rev. B*, vol. 71, p. 035318, Jan. 2005.

[106] Y. Makhlin and A. Shnirman, "Dephasing of solid-state qubits at optimal points," *Phys. Rev. Lett.*, vol. 92, p. 178301, Apr. 2004.

[107] A. A. Abrikosov, L. P. Gorkov, and I. E. Dzyaloshinski, *Methods of Quantum Field Theory in Statistical Physics*. Dover, 1975.

[108] Y. Makhlin, G. Schön, and A. Shnirman, "Dissipative effects in josephson qubits," *Chem. Phys.*, vol. 296, pp. 315–324, Jan. 2004.

[109] W. Nolting and A. Ramakanth, *Quantum Theory of Magnetism*. Springer, 2009.

[110] J. Hauptmann, J. Paaske, and P. Lindelof, "Electric-field-controlled spin reversal in a quantum dot with ferromagnetic contacts," *Nat. Phys.*, vol. 4, no. 5, pp. 373–376, 2008.

[111] L. Hofstetter, A. Geresdi, M. Aagesen, J. Nygård, C. Schönenberger, and S. Csonka, "Ferromagnetic proximity effect in a ferromagnet˘quantum-dot˘superconductor device," *Phys. Rev. Lett.*, vol. 104, p. 246804, Jun 2010.

[112] K. Khodjasteh and L. Viola, "Dynamically error-corrected gates for universal quantum computation," *Phys. Rev. Lett.*, vol. 102, p. 080501, Feb 2009.

[113] X. Xu, W. Yao, B. Sun, D. G. Steel, A. S. Bracker, D. Gammon, and L. J. Sham, "Optically controlled locking of the nuclear field

via coherent dark-state spectroscopy," *Nature*, vol. 459, no. 7250, pp. 1105–1109, 2009.

[114] I. T. Vink, K. C. Nowack, F. H. L. Koppens, J. Danon, Y. V. Nazarov, and L. M. K. Vandersypen, "Locking electron spins into magnetic resonance by electron-nuclear feedback," *Nat. Phys.*, vol. 5, no. 10, pp. 764–768, 2009.

[115] H. Ohno, D. Chiba, F. Matsukura, T. Omiya, E. Abe, T. Dietl, Y. Ohno, and K. Ohtani, "Electric-field control of ferromagnetism," *Nature*, vol. 408, no. 6815, pp. 944–946, 2000.

[116] J. Klinovaja, D. Stepanenko, B. I. Halperin, and D. Loss, "Exchange-based cnot gates for singlet-triplet qubits with spin-orbit interaction," *Phys. Rev. B*, vol. 86, p. 085423, Aug 2012.

[117] R. Ernst, G. Bodenhausen, and A. Wokaun, *Nuclear Magnetic Resonance in One and Two Dimensions*. Oxford: Oxford Univ. Press, 1987.

[118] P. Hemmer, "Toward molecular-scale mri," *Science*, vol. 339, no. 6119, pp. 529–530, 2013.

[119] J. A. Sidles, "Noninductive detection of singleproton magnetic resonance," *Applied Physics Letters*, vol. 58, no. 24, pp. 2854–2856, 1991.

[120] E. Ramsden, *Hall-Effect Sensors, Second Edition: Theory and Application*. Amsterdam ; Boston: Newnes, 2 edition ed., Mar. 2006.

[121] M. E. Huber, N. C. Koshnick, H. Bluhm, L. J. Archuleta, T. Azua, P. G. Björnsson, B. W. Gardner, S. T. Halloran, E. A. Lucero, and K. A. Moler, "Gradiometric micro-squid susceptometer for scanning measurements of mesoscopic samples," *Rev. Sci. Instrum.*, vol. 79, no. 5, 2008.

[122] C. L. Degen, M. Poggio, H. J. Mamin, C. T. Rettner, and D. Rugar, "Nanoscale magnetic resonance imaging," *Proc. Natl Acad. Sci. USA*, vol. 106, no. 5, pp. 1313–1317, 2009.

[123] M. Poggio and C. L. Degen, "Force-detected nuclear magnetic resonance: recent advances and future challenges," *Nanotechnology*, vol. 21, no. 34, p. 342001, 2010.

[124] P. Peddibhotla, F. Xue, H. I. T. Hauge, S. Assali, E. P. A. M. Bakkers, and M. Poggio, "Harnessing nuclear spin polarization fluctuations in a semiconductor nanowire," *Nat Phys*, vol. 9, no. 10, pp. 631–635, 2013.

[125] M. Loretz, S. Pezzagna, J. Meijer, and C. L. Degen, "Nanoscale nuclear magnetic resonance with a 1.9-nm-deep nitrogen-vacancy sensor," *App. Phys. Lett.*, vol. 104, no. 3, 2014.

[126] M. Schaffry, E. M. Gauger, J. J. L. Morton, and S. C. Benjamin, "Proposed spin amplification for magnetic sensors employing crystal defects," *Phys. Rev. Lett.*, vol. 107, p. 207210, Nov. 2011.

[127] T. van der Sar, F. Casola, R. Walsworth, and A. Yacoby, "Nanometre-scale probing of spin waves using single electron spins," *arXiv:1410.6423*, Oct. 2014.

[128] C. S. Wolfe, V. P. Bhallamudi, H. L. Wang, C. H. Du, S. Manuilov, R. M. Teeling-Smith, A. J. Berger, R. Adur, F. Y. Yang, and P. C. Hammel, "Off-resonant manipulation of spins in diamond via precessing magnetization of a proximal ferromagnet," *Phys. Rev. B*, vol. 89, p. 180406, May 2014.

[129] G. D. Fuchs, G. Burkard, P. V. Klimov, and D. D. Awschalom, "A quantum memory intrinsic to single nitrogen-vacancy centres in diamond," *Nat. Phys*, vol. 7, no. 10, pp. 789–793, 2011.

[130] E. C. Stoner and E. P. Wohlfarth, "A mechanism of magnetic hysteresis in heterogeneous alloys," *Phil. Trans. R. Soc. A*, vol. 240, no. 826, pp. 599–642, 1948.

[131] L. Trifunovic, F. L. Pedrocchi, and D. Loss, "Long-distance entanglement of spin qubits via ferromagnet," *Phys. Rev. X*, vol. 3, p. 041023, Dec 2013.

[132] Cywiński, R. M. Lutchyn, C. P. Nave, and S. Das Sarma, "How to enhance dephasing time in superconducting qubits," *Phys. Rev. B*, vol. 77, p. 174509, May 2008.

[133] G. de Lange, Z. H. Wang, D. Ristè, V. V. Dobrovitski, and R. Hanson, "Universal dynamical decoupling of a single solid-state spin from a spin bath," *Science*, vol. 330, no. 6000, pp. 60–63, 2010.

[134] V. M. Acosta, E. Bauch, M. P. Ledbetter, C. Santori, K.-M. C. Fu, P. E. Barclay, R. G. Beausoleil, H. Linget, J. F. Roch, F. Treussart, S. Chemerisov, W. Gawlik, and D. Budker, "Diamonds with a high density of nitrogen-vacancy centers for magnetometry applications," *Phys. Rev. B*, vol. 80, p. 115202, Sep 2009.

[135] K. Ohno, F. Joseph Heremans, L. C. Bassett, B. A. Myers, D. M. Toyli, A. C. Bleszynski Jayich, C. J. Palmstrom, and D. D. Awschalom, "Engineering shallow spins in diamond with nitrogen delta-doping," *App. Phys. Lett.*, vol. 101, no. 8, p. 082413, 2012.

[136] B. A. Myers, A. Das, M. C. Dartiailh, K. Ohno, D. Awschalom, D., and C. Bleszynski Jayich, A., "Probing surface noise with depth-calibrated spins in diamond," *Phys. Rev. Lett.*, vol. 113, p. 027602, Jul 2014.

[137] G. Puentes, G. Waldherr, P. Neumann, G. Balasubramanian, and J. Wrachtrup, "Efficient route to high-bandwidth nanoscale magnetometry using single spins in diamond," *Sci. Rep.*, vol. 4, 2014.

[138] P. London, P. Balasubramanian, B. Naydenov, L. P. McGuinness, and F. Jelezko, "Strong driving of a single spin using arbitrarily polarized fields," *Phys. Rev. A*, vol. 90, p. 012302, Jul 2014.

[139] G. D. Fuchs, V. V. Dobrovitski, D. M. Toyli, F. J. Heremans, and D. D. Awschalom, "Gigahertz dynamics of a strongly driven single quantum spin," *Science*, vol. 326, pp. 1520–1522, Nov. 2009.

[140] J. Yoneda, T. Otsuka, T. Nakajima, T. Takakura, T. Obata, M. Pioro-Ladrière, H. Lu, C. Palmstrøm, A. C. Gossard, and S. Tarucha, "Fast Electrical Control of Single Electron Spins in Quantum Dots with Vanishing Influence from Nuclear Spins," *arXiv:1411.6738*, Nov. 2014.

[141] N. L. Schryer and L. R. Walker, "The motion of 180 domain walls in uniform dc magnetic fields," *J. App. Phys.*, vol. 45, no. 12, p. 5406, 1974.

[142] G. Balasubramanian, P. Neumann, D. Twitchen, M. Markham, R. Kolesov, N. Mizuochi, J. Isoya, J. Achard, J. Beck, J. Tissler, V. Jacques, P. R. Hemmer, F. Jelezko, and J. Wrachtrup, "Ultralong spin coherence time in isotopically engineered diamond," *Nat. Mater*, vol. 8, no. 5, pp. 383–387, 2009.

[143] M. Loretz, T. Rosskopf, J. M. Boss, S. Pezzagna, J. Meijer, and C. L. Degen, "Single-proton spin detection by diamond magnetometry," *Science*, 2014.

[144] A. O. Sushkov, I. Lovchinsky, N. Chisholm, R. L. Walsworth, H. Park, and M. D. Lukin, "Magnetic resonance detection of individual proton spins using quantum reporters," *Phys. Rev. Lett.*, vol. 113, p. 197601, Nov 2014.

[145] V. M. Acosta, E. Bauch, M. P. Ledbetter, C. Santori, K.-M. C. Fu, P. E. Barclay, R. G. Beausoleil, H. Linget, J. F. Roch, F. Treussart, S. Chemerisov, W. Gawlik, and D. Budker, "Diamonds with a high density of nitrogen-vacancy centers for magnetometry applications," *Phys. Rev. B*, vol. 80, p. 115202, Sep 2009.

[146] E. Schäfer-Nolte, L. Schlipf, M. Ternes, F. Reinhard, K. Kern, and J. Wrachtrup, "Tracking Temperature Dependent Relaxation Times of Individual Ferritin Nanomagnets with a Wide-band Quantum Spectrometer," *ArXiv e-prints*, June 2014.

[147] E. Schäfer-Nolte, L. Schlipf, M. Ternes, F. Reinhard, K. Kern, and J. Wrachtrup, "Tracking temperature-dependent relaxation times of ferritin nanomagnets with a wideband quantum spectrometer," *Phys. Rev. Lett.*, vol. 113, p. 217204, Nov 2014.

[148] D. O. Smith, "Static and dynamic behavior of thin permalloy films," *J. App. Phys.*, vol. 29, no. 3, pp. 264–273, 1958.

[149] J. Lotze, H. Huebl, R. Gross, and S. T. B. Goennenwein, "Spin hall magnetoimpedance," *Phys. Rev. B*, vol. 90, p. 174419, Nov 2014.

[150] M. Julliere, "Tunneling between ferromagnetic films," *Phys. Lett. A*, vol. 54, no. 3, pp. 225 – 226, 1975.

[151] K.-J. Lee, A. Deac, O. Redon, J.-P. Nozieres, and B. Dieny, "Excitations of incoherent spin-waves due to spin-transfer torque," *Nat. Mater*, vol. 3, pp. 877–881, Dec 2004.

[152] J. Teissier, A. Barfuss, P. Appel, E. Neu, and P. Maletinsky, "Strain coupling of a nitrogen-vacancy center spin to a diamond mechanical oscillator," *Phys. Rev. Lett.*, vol. 113, p. 020503, Jul 2014.

[153] A. Aharoni, *Introduction to the Theory of Ferromagnetism*. Oxford ; New York: Oxford University Press, 2 edition ed., Mar. 2001.

[154] V. N. Samofalov, D. P. Belozorov, and A. G. Ravlik, "Strong stray fields in systems of giant magnetic anisotropy magnets," *Physics-Uspekhi*, vol. 56, p. 269, Mar. 2013.

[155] J. Norpoth, S. Dreyer, and C. Jooss, "Straightforward field calculations for uniaxial hard magnetic prisms: stray field distributions and dipolar coupling in regular arrays," *J. Phys. D: Appl. Phys.*, vol. 41, p. 025001, 2008.

[156] R. Engel-Herbert and T. Hesjedal, "Calculation of the magnetic stray field of a uniaxial magnetic domain," *J. Appl. Phys.*, vol. 97, p. 074504, 2005.

[157] H. Bluhm, S. Foletti, I. Neder, M. Rudner, D. Mahalu, V. Umansky, and A. Yacoby, "Dephasing time of gaas electron-spin qubits coupled to a nuclear bath exceeding 200[thinsp][mu]s," *Nat Phys*, vol. 7, no. 2, pp. 109–113, 2011.

[158] M. Malard, I. Grusha, G. I. Japaridze, and H. Johannesson, "Modulated rashba interaction in a quantum wire: Spin and charge dynamics," *Phys. Rev. B*, vol. 84, p. 075466, Aug 2011.

[159] G. Thorgilsson, J. C. Egues, D. Loss, and S. I. Erlingsson, "Rashba spin orbit interaction in a quantum wire superlattice," *Phys. Rev. B*, vol. 85, p. 045306, Jan 2012.

[160] I. Tamm *Phys. Z. Soviet Union*, vol. 1, pp. 733–733, 1932.

[161] W. Shockley, "On the surface states associated with a periodic potential," *Phys. Rev.*, vol. 56, pp. 317–323, Aug 1939.

[162] R. Jackiw and C. Rebbi, "Solitons with fermion number $1/2$," *Phys. Rev. D*, vol. 13, pp. 3398–3409, Jun 1976.

[163] K. Sengupta *et al.*, "Midgap edge states and pairing symmetry of quasi-one-dimensional organic superconductors," *Phys. Rev. B*, vol. 63, no. 14, p. 144531, 2001.

[164] J. Sau *et al.*, "Non-abelian quantum order in spin-orbit-coupled semiconductors: Search for topological majorana particles in solid-state systems," *Phys. Rev. B*, vol. 82, p. 214509, 2010.

[165] S. Sasaki *et al.*, "Kondo effect in an integer-spin quantum dot," *Nature*, vol. 405, p. 764, 2000.

[166] M. Zareyan, W. Belzig, and Y. V. Nazarov, "Superconducting proximity effect in clean ferromagnetic layers," *Phys. Rev. B*, vol. 65, p. 184505, 2002.

[167] B. J. van Wees *et al.*, "Excess conductance of superconductor-semiconductor interfaces due to phase conjugation between electrons and holes," *Phys. Rev. Lett.*, vol. 69, p. 510, 1992.

[168] C. Lambert and R. Raimondi, "Phase-coherent transport in hybrid superconducting nanostructures," *J. Phys.: Condens. Matter*, vol. 10, p. 901, 1998.

[169] A. MacKinnon, "The calculation of transport properties and density of states of disordered solids," *Z. Phys. B*, vol. 59, p. 385, 1985.

[170] M. Anatram and S. Datta, "Current fluctuations in mesoscopic systems with andreev scattering," *Phys. Rev. B*, vol. 53, p. 16390, 1996.

[171] A. Y. Kitaev, "Unpaired majorana fermions in quantum wires," *Phys.-Usp.*, vol. 44, p. 131, 2001.

[172] O. Motrunich, K. Damle, and D. A. Huse, "Dynamics and transport in random quantum systems governed by strong-randomness fixed points," *Phys. Rev. B*, vol. 63, p. 134424, Mar 2001.

[173] J. D. Sau, S. Tewari, R. M. Lutchyn, T. D. Stanescu, and S. Das Sarma, "Non-abelian quantum order in spin-orbit-coupled semiconductors: Search for topological majorana particles in solid-state systems," *Phys. Rev. B*, vol. 82, p. 214509, Dec 2010.

[174] Y. Oreg, G. Refael, and F. von Oppen, "Helical liquids and majorana bound states in quantum wires," *Phys. Rev. Lett.*, vol. 105, p. 177002, Oct 2010.

[175] F. Hassler, A. R. Akhmerov, C.-Y. Hou, and C. W. J. Beenakker, "Anyonic interferometry without anyons: how a flux qubit can read out a topological qubit," *New J. Phys.*, vol. 12, no. 12, p. 125002, 2010.

[176] A. C. Potter and P. A. Lee, "Multichannel generalization of kitaev's majorana end states and a practical route to realize them in thin films," *Phys. Rev. Lett.*, vol. 105, p. 227003, Nov 2010.

[177] J. Alicea, Y. Oreg, G. Refael, F. von Oppen, and M. Fisher, "Non-abelian statistics and topological quantum information processing in 1d wire networks," *Nature Phys.*, vol. 7, pp. 412–412, 2011.

[178] S. Gangadharaiah, B. Braunecker, P. Simon, and D. Loss, "Majorana edge states in interacting one-dimensional systems," *Phys. Rev. Lett.*, vol. 107, p. 036801, Jul 2011.

[179] M. Duckheim and P. W. Brouwer, "Andreev reflection from noncentrosymmetric superconductors and majorana bound-state generation in half-metallic ferromagnets," *Phys. Rev. B*, vol. 83, p. 054513, Feb 2011.

[180] E. M. Stoudenmire, J. Alicea, O. A. Starykh, and M. P. Fisher, "Interaction effects in topological superconducting wires supporting majorana fermions," *Phys. Rev. B*, vol. 84, p. 014503, Jul 2011.

[181] D. Sticlet, C. Bena, and P. Simon, "Spin and majorana polarization in topological superconducting wires," *Phys. Rev. Lett.*, vol. 108, p. 096802, Mar 2012.

[182] X. Wan, A. M. Turner, A. Vishwanath, and S. Y. Savrasov, "Topological semimetal and fermi-arc surface states in the electronic structure of pyrochlore iridates," *Phys. Rev. B*, vol. 83, p. 205101, May 2011.

[183] A. A. Burkov and L. Balents, "Weyl semimetal in a topological insulator multilayer," *Phys. Rev. Lett.*, vol. 107, p. 127205, Sep 2011.

[184] M. Fabrizio and A. O. Gogolin, "Interacting one-dimensional electron gas with open boundaries," *Phys. Rev. B*, vol. 51, pp. 17827–17841, Jun 1995.

[185] S. Eggert and I. Affleck, "Magnetic impurities in half-integer-spin heisenberg antiferromagnetic chains," *Phys. Rev. B*, vol. 46, pp. 10866–10883, Nov 1992.

[186] A. P. Schnyder, S. Ryu, A. Furusaki, and A. W. W. Ludwig, "Classification of topological insulators and superconductors in three spatial dimensions," *Phys. Rev. B*, vol. 78, p. 195125, Nov 2008.

[187] A. A. N. A. O. Gogolin and A. M. Tsvelik, *Bosonization and Strongly Correlated Systems*. University Press, Cambridge, 1998.

[188] T. Giamarchi, *Quantum Physics in One Dimension*. Oxford: University Press, 2004.

[189] D. Loss, "Parity effects in a luttinger liquid: Diamagnetic and paramagnetic ground states," *Phys. Rev. Lett.*, vol. 69, pp. 343–346, Jul 1992.

[190] D. Mailly, C. Chapelier, and A. Benoit, "Experimental observation of persistent currents in gaas-algaas single loop," *Phys. Rev. Lett.*, vol. 70, pp. 2020–2023, Mar 1993.

[191] H. Bluhm, N. C. Koshnick, J. A. Bert, M. E. Huber, and K. A. Moler, "Persistent currents in normal metal rings," *Phys. Rev. Lett.*, vol. 102, p. 136802, Mar 2009.

[192] O. Auslaender, A. Yacoby, R. de Picciotto, K. Baldwin, L. Pfeiffer, and K. West, "Tunneling spectroscopy of the elementary excitations in a one-dimensional wire," *Science*, vol. 295, pp. 825–825, 2002.

[193] D. Chevallier, D. Sticlet, P. Simon, and C. Bena, "Mutation of andreev into majorana bound states in long ns and sns junctions," *Phys. Rev. B*, vol. 85, p. 235307, 2012.

[194] E. Prada, P. San-Jose, and R. Aguado, "Transport spectroscopy of ns nanowire junctions with majorana fermions," *Phys. Rev. B*, vol. 86, p. 180503, Nov 2012.

[195] C.-H. Lin, J. D. Sau, and S. Das Sarma, "Zero-bias conductance peak in majorana wires made of semiconductor/superconductor hybrid structures," *Phys. Rev. B*, vol. 86, p. 224511, Dec 2012.

[196] T. D. Stanescu, S. Tewari, J. D. Sau, and S. Das Sarma, "To close or not to close: The fate of the superconducting gap across the topological quantum phase transition in majorana-carrying semiconductor nanowires," *Phys. Rev. Lett.*, vol. 109, p. 266402, Dec 2012.

[197] F. Pientka, G. Kells, A. Romito, P. W. Brouwer, and F. von Oppen, "Enhanced zero-bias majorana peak in the differential tunneling conductance of disordered multisubband quantum-wire/superconductor junctions," *Phys. Rev. Lett.*, vol. 109, p. 227006, Nov 2012.

[198] D. Bagrets and A. Altland, "Class d spectral peak in majorana quantum wires," *Phys. Rev. Lett.*, vol. 109, p. 227005, Nov 2012.

[199] D. I. Pikulin, J. P. Dahlhaus, M. Wimmer, H. Schomerus, and C. W. J. Beenakker, "A zero-voltage conductance peak from weak antilocalization in a majorana nanowire," *New Journal of Physics*, vol. 14, no. 12, p. 125011, 2012.

[200] D. Chevallier, D. Sticlet, P. Simon, and C. Bena, "Effects of finite superconducting coherence lengths and of phase gradients in topological sn and sns junctions and rings," *Phys. Rev. B*, vol. 87, p. 165414, Apr 2013.

[201] J. Liu, A. C. Potter, K. T. Law, and P. A. Lee, "Zero-bias peaks in the tunneling conductance of spin-orbit-coupled superconducting wires with and without majorana end-states," *Phys. Rev. Lett.*, vol. 109, p. 267002, Dec 2012.

[202] J. Klinovaja and D. Loss, "Composite majorana fermion wave functions in nanowires," *Phys. Rev. B*, vol. 86, p. 085408, 2012.

[203] M. Cheng, R. M. Lutchyn, V. Galitski, and S. Das Sarma, "Splitting of majorana-fermion modes due to intervortex tunneling in a $p_x + ip_y$ superconductor," *Phys. Rev. Lett.*, vol. 103, p. 107001, Aug 2009.

[204] J. M. Rowell and W. L. McMillan, "Electron interference in a normal metal induced by superconducting contracts," *Phys. Rev. Lett.*, vol. 16, pp. 453–456, Mar 1966.

[205] E. J. H. Lee, X. Jiang, R. Aguado, G. Katsaros, C. M. Lieber, and S. De Franceschi, "Zero-bias anomaly in a nanowire quantum dot coupled to superconductors," *Phys. Rev. Lett.*, vol. 109, p. 186802, Oct 2012.

[206] M. Kjaergaard, K. Wölms, and K. Flensberg, "Majorana fermions in superconducting nanowires without spin-orbit coupling," *Phys. Rev. B*, vol. 85, p. 020503, 2012.

[207] J. Klinovaja and D. Loss, "Giant spin-orbit interaction due to rotating magnetic fields in graphene nanoribbons," *Phys. Rev. X*, vol. 3, p. 011008, 2013.

[208] B. Karmakar *et al.*, "Controlled coupling of spin-resolved quantum hall edge states," *Phys. Rev. Lett.*, vol. 107, p. 236804, 2011.

[209] B. Braunecker, P. Simon, and D. Loss, "Nuclear magnetism and electron order in interacting one-dimensional conductors," *Phys. Rev. B*, vol. 80, p. 165119, 2009.

[210] B. Braunecker, G. I. Japaridze, J. Klinovaja, and D. Loss, "Spin-selective peierls transition in interacting one-dimensional conductors with spin-orbit interaction," *Phys. Rev. B*, vol. 82, p. 045127, 2010.

[211] C. J. Lambert, "Generalized landauer formulae for quasi-particle transport in disordered superconductors," *J. Phys.: Condens. Matter*, vol. 3, no. 34, p. 6579, 1991.

[212] C. J. Lambert, V. C. Hui, and S. J. Robinson, "Multi-probe conductance formulae for mesoscopic superconductors," *J. Phys.: Condens. Matter*, vol. 5, no. 25, p. 4187, 1993.

[213] C. J. Lambert and R. Raimondi, "Phase-coherent transport in hybrid superconducting nanostructures," *J. Phys.: Condens. Matter*, vol. 10, no. 5, p. 901, 1998.

[214] Y. M. Blanter and M. Büttiker, "Shot noise in mesoscopic conductors," *Phys. Rep.*, vol. 336, pp. 1–166, 2000.

[215] L. W. Molenkamp, G. Schmidt, and G. E. W. Bauer, "Rashba hamiltonian and electron transport," *Phys. Rev. B (R)*, vol. 64, p. 121202, 2001.

[216] V. A. Sablikov, A. A. Sukhanov, and Y. Y. Tkach, "Equilibrium edge spin currents in two-dimensional electron systems with spin-orbit interaction," *Phys. Rev. B*, vol. 78, p. 153302, 2008.

[217] V. A. Sablikov and Y. Y. Tkach, "Evanescent states in two-dimensional electron systems with spin-orbit interaction and spin-dependent transmission through a barrier," *Phys. Rev. B*, vol. 76, p. 245321, 2007.

[218] C. Groth, M. Wimmer, A. Akhmerov, and X. Waintal, "Kwant: a software package for quantum transport," *arXiv:1309.2926*,. http://kwant-project.org/.

[219] X. W. Zhang, W. J. Fan, S. S. Li, and J. B. Xia, "Giant and zero electron g factors of dilute nitride semiconductor nanowires," *Appl. Phys. Lett.*, vol. 90, no. 19, p. 193111, 2007.

[220] A. A. Kiselev, E. L. Ivchenko, and U. Rössler, "Electron g factor in one- and zero-dimensional semiconductor nanostructures," *Phys. Rev. B*, vol. 58, pp. 16353–16359, 1998.

[221] T. Nakaoka, T. Saito, J. Tatebayashi, and Y. Arakawa, "Size, shape, and strain dependence of the g factor in self-assembled in(ga)as quantum dots," *Phys. Rev. B*, vol. 70, p. 235337, 2004.

[222] Y. Lin, J. Nitta, T. Koga, and T. Akazaki, "Electron g factor in a gated ingaas channel with double inas-inserted wells," *Physica E*, vol. 21, pp. 656 – 660, 2004.

[223] C. E. Pryor and M. E. Flatté, "Landé g factors and orbital momentum quenching in semiconductor quantum dots," *Phys. Rev. Lett.*, vol. 96, p. 026804, 2006.

[224] S. Csonka *et al.*, "Giant fluctuations and gate control of the g-factor in inas nanowire quantum dots," *Nano Lett.*, vol. 8, no. 11, pp. 3932–3935, 2008.

[225] H. A. Nilsson *et al.*, "Giant, level-dependent g factors in insb nanowire quantum dots," *Nano Lett.*, vol. 9, no. 9, pp. 3151–3156, 2009.